UNIVERSIDAD TÉCNICA FEDERICO SANTA MARÍA
DEPARTAMENTO DE INFORMÁTICA
VALPARAÍSO - CHILE

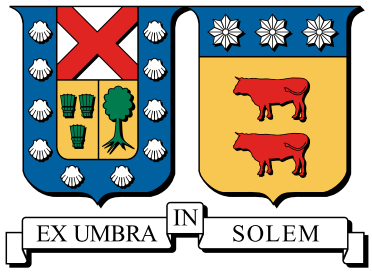

A High-Performance Implementation of a Simplified Coupled Wildfire-Atmosphere Mathematical Model

Daniel Eduardo San Martín Reyes

Thesis presented in partial fulfillment of the requirements for the degree of
Doctor en Ingeniería Informática

Advisor: Claudio Torres, Ph.D.
Internal national member: Roberto León, Ph.D.
External national member: Andrés Fuentes, Ph.D.
External international member: Timothy Sauer, Ph.D.
External international member: Orlando Ayala, Ph.D.
Committee Chair: Mauricio Solar, Ph.D.

November 6, 2025

CONSTANCIA DE VALIDACIÓN Y CONFIDENCIALIDAD DE MONOGRAFÍA A REPOSITORIO ACADÉMICO

1.- IDENTIFICACIÓN DEL TRABAJO ACADÉMICO

Tipo de monografía (marcar una opción): ☐ Memoria o trabajo de título ☒ Tesis de Postgrado

Título del trabajo: A High-Performance Implementation of a Simplified Coupled Wildfire-Atmosphere Mathematical Model

Nombre del candidato(a): Daniel Eduardo San Martín Reyes

Carrera / Grado: Doctorado en Ingeniería Informática

Campus: Casa Central Valparaíso **Departamento:** Informática

2.- VALIDACIÓN DEL PROFESOR GUÍA/DIRECTOR DE TESIS

Yo, Claudio Esteban Torres López, en mi calidad de profesor(a) guía/director(a) del trabajo académico mencionado anteriormente **DEJO CONSTANCIA** que:

- He revisado esta versión del documento y corresponde a la versión final aprobada del trabajo.
- El trabajo cumple con los requisitos académicos y de formato establecidos por la institución.

3.- EVALUACIÓN DE CONFIDENCIALIDAD POR PROPIEDAD INDUSTRIAL (marcar una opción)

☒ El trabajo **NO contiene** información que amerite confidencialidad y puede ser publicado de inmediato en repositorio con acceso abierto.

☐ El trabajo **CONTIENE** información con potenciales implicancias de propiedad industrial o intelectual y requiere un periodo de confidencialidad (**embargo**) por **(marcar una opción)**:

☐ 6 meses ☐ 12 meses ☐ 2 años ☐ 3 años ☐ 5 años ☐ 10 años

Fundamentación de la necesidad de confidencialidad (obligatorio si se solicita embargo):

_____

_____

_____

4.- FIRMAS

Profesor(a) guía o director(a) de memoria o tesis:

Fecha: 06/11/2025 **Firma:** Claudio E. Torres

Estudiante o Candidato(a):

Fecha: 05/11/2025 **Firma:** _____

Este formulario debe ser insertado como página 2 de la memoria o tesis, completado y firmado por estudiante y profesor(a) antes de la entrega en portal PRISMA de Biblioteca USM.

THESIS TITLE:

A High-Performance Implementation of a Simplified Coupled Wildfire-Atmosphere Mathematical Model

AUTHOR:

Daniel Eduardo San Martín Reyes

Thesis presented in partial fulfillment of the requirements for the degree of Doctor en Ingeniería Informática of the Universidad Técnica Federico Santa María.

Claudio Torres, Ph.D. _____
Advisor

Roberto León, Ph.D. _____
Internal national member

Andrés Fuentes, Ph.D. _____
External national member

Timothy Sauer, Ph.D. _____
External international member

Orlando Ayala, Ph.D. _____
External international member

Mauricio Solar, Ph.D. _____
Committee Chair

Valparaíso, Chile.
November 6, 2025.

To everyone involved in this process.

Acknowledgments

This thesis was supported by ANID-Subdirección de Capital Humano/Doctorado Nacional/2019-21191017, ANID PIA/APOYO AFB230003 Centro Científico Tecnológico de Valparaíso - CCTVal, and Programa de Iniciación a la Investigación Científica (PIIC) from Dirección de Postgrado y Programas, Universidad Técnica Federico Santa María, Chile.

Powered@NLHPC: This thesis was partially supported by the supercomputing infrastructure of the NLHPC (CCSS210001).

Resumen

Los incendios forestales representan una problemática ambiental global con fuerte impacto en Chile, donde cada año se pierden miles de hectáreas de bosques. Este fenómeno provoca pérdida de biodiversidad, degradación del aire, alteración de los ciclos hídricos y daños graves a los ecosistemas, generando además impactos económicos y sociales. A nivel mundial, cerca del 75% de los incendios tienen origen humano; en Chile, según la CONAF, el 99,7% son causados por acción o negligencia humana. Entre 1963 y 2024 se registraron más de 283.000 incendios, con más de 4 millones de hectáreas afectadas.

Con el fin de comprender y mitigar esta problemática, se han desarrollado diversos modelos matemáticos y herramientas computacionales. La presente investigación se enfoca en los modelos de propagación físicos acoplados, los cuales integran la dinámica de la atmósfera baja con la propagación del fuego, incorporando además los efectos de retroalimentación entre ambos procesos.

A pesar de la existencia de múltiples implementaciones de estos modelos, solo una fracción se encuentra disponible en formato de código abierto. Este proyecto propone un método numérico y desarrolla una implementación de código abierto basada en un modelo físico simplificado y en técnicas de dinámica de fluidos computacional. Dada la naturaleza del algoritmo, la implementación se realizará en unidades de procesamiento gráfico (GPU) con el objetivo de reducir los tiempos de las simulaciones numéricas. De este modo, se busca facilitar estudios intensivos sobre incendios forestales, alcanzando tiempos de ejecución considerablemente menores en comparación con implementaciones en CPU.

Keywords: Modelamiento Acoplado Atmósfera-fuego, Computación Científica, Métodos Numéricos, GPU.

Abstract

Wildfires represent a global environmental problem with a strong impact in Chile, where thousands of hectares of forest are lost every year. This phenomenon causes loss of biodiversity, air degradation, disruption of hydrological cycles, and severe damage to ecosystems, while also generating significant economic and social impacts. Worldwide, around 75% of forest fires are of human origin; in Chile, according to the National Forest Corporation (CONAF), 99.7% are caused by human action or negligence. Between 1963 and 2024, more than 283,000 fires were recorded, with more than 4 million hectares affected.

To understand and mitigate this problem, several mathematical models and computational tools have been developed. This research focuses on coupled physical propagation models, which integrate the dynamics of the lower atmosphere with fire spread, also incorporating the feedback effects between the two phenomena.

Despite the existence of multiple implementations of these models, only a fraction is accessible in open source format. This project proposes a numerical method and develops an open-source implementation based on a simplified physical model and computational fluid dynamics techniques. Given the nature of the algorithm, the implementation will be carried out on Graphics Processing Units (GPUs) to reduce numerical simulation times. Thus, the project seeks to enable intensive studies of wildfires, achieving significantly shorter execution times compared to CPU-based implementations.

Keywords: Coupled Atmosphere-wildfire Modeling, Scientific Computing, Numerical Methods, GPU.

Contents

List of Figures

List of Tables

List of Algorithms

Chapter 1

Introduction

Wildfires represent a persistent global problem in the modern era, which is increasing due to the impacts of climate change (Di Virgilio et al., 2019; Xu et al., 2020; Zhuang, Fu, Santer, Dickinson, & Hall, 2021). Human actions are estimated to contribute approximately 75% of all wildfires (World Wide Fund & Boston Consulting Group, 2020). Between 1992 and 2020, approximately 85% of wildfires in the United States were attributed to human causes (Short, 2022), and this proportion increased to 89% from 2017 to 2021 (Hoover & Hanson, 2022). The historical stats for the United States are shown in Figure 1.1.

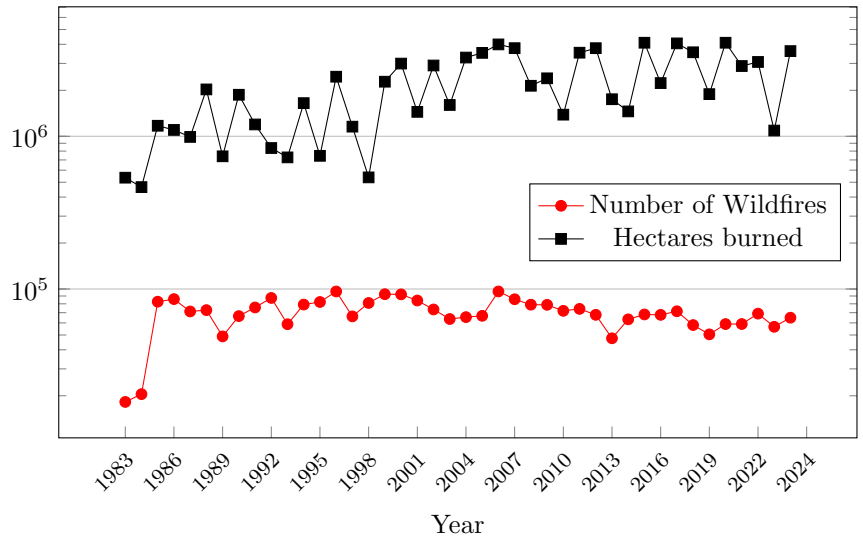

Figure 1.1: Historical data of wildfires in U.S from 1983 to 2024 (National Interagency Fire Center, 2025).

In a local context, the situation is equally or more severe; for example, in Chile, 99.7% of wildfires are attributed to human activities (CONAF, 2025b). Figure 1.2 presents the historical trends of wildfires in Chile.

According to Tyukavina et al. (2022), between 2001 and 2021, wildfires resulted in a cumulative loss of 132 million hectares of forest worldwide, the year of the peak

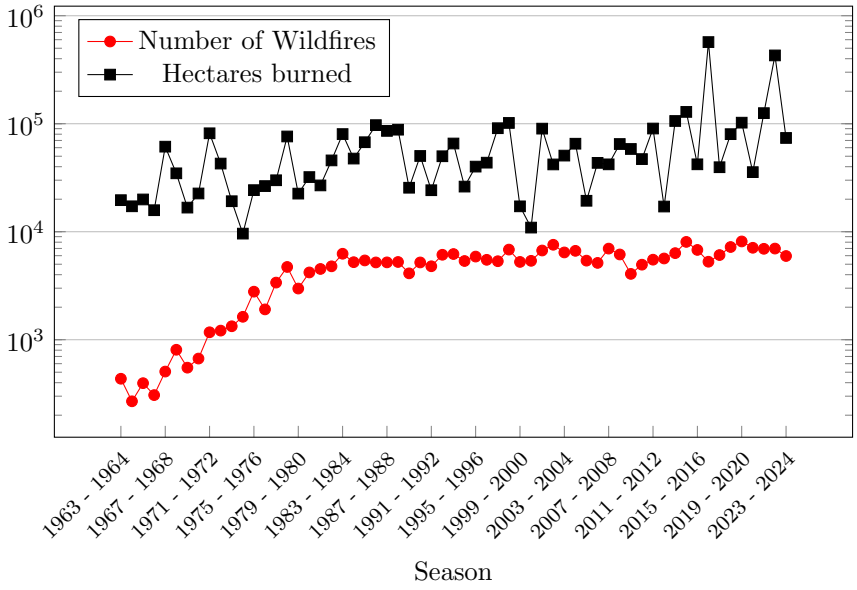

Figure 1.2: Historical data of wildfires in Chile from 1963 to 2024 (CONAF, 2025a).

loss of tree cover due to fires was 2021, when 10.6 million hectares were lost, which is approximately 37% of the total loss of tree cover for that year. The consequences of forest fires include the harm to natural resources, pollution, monetary cost, and even human deaths, among others (Liu, Lei, Gao, Chen, & Xie, 2021). As a result, the scientific community has dedicated considerable effort to studying this phenomenon for many years. Since it remains an unresolved challenge, substantial funding is continuing to be directed towards its exploration (U.S. National Science Foundation, 2025; European Court of Auditors, 2025).

One of the principal strategies to improve the comprehension of this phenomenon is the application of mathematical modeling and numerical computation (Pastor, Zárate, Planas, & Arnaldos, 2003). Wildfire modeling presents significant complexity as it involves multiple scales, including chemical kinetics, heat transfer, and fluid dynamics (Finney, McAllister, Grumstrup, & Forthofer, 2021; Speer & Goodrick, 2022; Himoto, 2022). It is an interdisciplinary domain that integrates methodologies from meteorology, ecology, engineering, and computer science to investigate the initiation and propagation of fires and their interaction with meteorological and other environmental conditions (Finney et al., 2021). Such models employ a synthesis of historical datasets, satellite imagery, and meteorological forecasts to estimate the spread and intensity of a wildfire (Wegrzynski, Lipecki, & Krajewski, 2018). These predictions facilitate informed decision making by fire managers about response strategies and are instrumental in strategic planning for potential wildfires. In addition, these models serve as evaluation tools for assessing the efficacy of various fire management strategies and examining the repercussions of fires on ecological systems and human communities (Finney et al., 2021; Meacham & McNamee, 2023). In general, wildfire modeling is an indispensable tool for the management and mitigation of wildfire

impacts on social structures.

Two main modeling approaches are identified as physical and empirical (Sullivan, 2009a, 2009b). Physical wildfire models are based on the fundamental laws of physics, including energy conservation, mass balance, and fluid dynamics, to simulate the behavior of wildfires (Sullivan, 2009a). These models consider various factors that influence the spread of the fire, such as wind, temperature, humidity, and fuel moisture content. Mathematical equations are utilized within these models to represent the transfer of thermal energy, smoke, and other gases, as well as the dynamics of the fire front. Physical models can provide detailed information on the spread and intensity of a fire and predict the propagation of the fire under varying weather conditions. In contrast, empirical models are derived from historical data and observations of actual fire events (Sullivan, 2009b). These models employ statistical methods to interpret the available data, identifying patterns based on weather, topography, and fuel conditions to predict the spread of the fire. Empirical models are generally more straightforward to implement compared to physical models, requiring fewer input data for predictions. Nevertheless, they may lack the precision of physical models, particularly in forecasting fire behavior in unusual or extreme conditions. Both modeling approaches have specific advantages and drawbacks, and their utilization depends on the particular needs and resources available in a given scenario. In particular, this thesis will focus on coupled wildfire-atmosphere physical models.

A primary issue associated with these types of models is the extensive computational cost of performing numerical experiments, which presents significant challenges in the simulation of large-scale fires due to their demanding computational requirements (Wegrzynski et al., 2018; Bakhshaii & Johnson, 2019; Silva et al., 2022). Many of these challenges arise from the complexity of the simulated domain, the mechanisms of heat transfer primarily associated with radiation, and the pressure problem solver used for fine meshes, particularly in a three-dimensional domain. Consequently, numerous models developed are dependent on high-performance computing (HPC) frameworks (Bakhshaii & Johnson, 2019). These technologies mainly include OpenMP, implemented for shared memory multi-threaded programming CPU, and MPI, for distributed parallel programming (K. McGrattan & Miles, 2016). Although these tools substantially accelerate code execution, they present challenges in designing algorithms that efficiently leverage hardware resources.

The primary objective of this research is to develop a simplified coupled mathematical model of wildfires that, in terms of computational resource requirements, holds an intermediary position between physical and empirical models while incorporating as many details as feasible. Additionally, this research aims to deliver an open source high-performance computing solution that takes advantage of the capabilities of Graphics Processing Units (GPUs) to enhance computational efficiency and reduce processing times. The justification for GPUs is their ability to run models on a workstation, leveraging their computational power, but maintaining a simplified approach due to memory constraints. This aims to distinguish itself from exist-

ing coupled atmosphere-fire models that predominantly utilize HPC technologies to speed up CPU-based computations. Table 1.1 shows the comparison of CPU and GPU for HPC acceleration.

Table 1.1: HPC hardware comparison.

	Memory [GB]	**Cores [#]**	**Frequency [GHz]**
GPU	$5 - 100$	> 2000	$1 - 2$
CPU Node	$100 - 1000$	$10 - 48$	$2 - 3$
Cluster	> 10000	> 1000	> 3

1.1 Antecedents and Motivation

The numerical simulation of wildfires underlying this research began in 2018 with the implementation of a simplified two-dimensional physical model based on the work of Asensio and Ferragut (2002), presented in "Ngen-Kütral: Toward an Open Source Framework for Chilean Wildfire Spreading" (San Martín & Torres, 2018). This study used a Finite Difference Method combined with a Runge–Kutta time integration scheme to solve a convection–diffusion–reaction system, providing a first approximation of the dynamics of spreading wildfires. Building on this foundation, "Exploring a Spectral Numerical Algorithm for Solving a Wildfire Mathematical Model" (San Martín & Torres, 2019) investigated the use of spectral differentiation techniques with Fast Fourier Transform to approximate spatial derivatives more efficiently. Both contributions laid the groundwork for the author's master's thesis, "Open-source Framework for Chilean Wildfire Spreading and Effects Analysis" (San Martin, 2021).

In the doctoral context, research expanded toward high-performance computing with the first GPU-based implementation in Python, presented in "2D Simplified Wildfire Spreading Model in Python: From NumPy to CuPy" (San Martin & Torres, 2023). This study demonstrated that the numerical algorithm could be executed on GPUs with minimal code modifications. The implementation was later enhanced using *CUDA C*, resulting in the publication "A GPU Numerical Implementation of a 2D Simplified Wildfire Spreading Model" (San Martin & Torres, 2024), which emphasized the potential of GPUs to run multiple simulation scenarios in parallel.

However, these earlier models may lack fidelity in extreme scenarios because they did not account for atmosphere–fire interactions, a key driver of wildfire dynamics. This limitation motivated the development of a coupled mathematical framework capable of capturing both fire propagation and atmospheric feedback. At the computational level, the research continued to focus on GPU architectures, given their demonstrated efficiency in reducing simulation times, making large-scale and more realistic wildfire simulations feasible.

1.2 Document Structure

This thesis is organized as follows:

- Chapter 2 reviews the state-of-the-art in wildfire modeling approaches. It highlights key contributions in coupled wildfire-atmosphere models, with emphasis on their main components and implementation features.
- Chapter 3 introduces the thesis proposal, outlining the working hypotheses, their implications, and the expected contributions derived from this research.
- Chapter 4 presents the conceptual basis of the wildfire model, describing its main components and the corresponding mathematical formalization.
- Chapter 5 details the numerical algorithm used to approximate the mathematical model, including both theoretical considerations and a description of the numerical methods that form the foundation of the proposed algorithm.
- Chapter 6 describes the computational implementation, considering both CPU and GPU architectures. Particular emphasis is placed on showcasing the algorithm's compatibility with GPU execution while analyzing the performance achieved compared to the CPU version.
- Chapter 7 presents the results of the simulations and illustrates potential applications of the developed model.
- Finally, Chapter 8 summarizes the findings of the thesis and outlines possible directions for future research.

Chapter 2

State of the Art

Wildfire modeling has evolved significantly over the past decades, with various approaches designed to capture the complex interactions between fire behavior and atmospheric dynamics. Current state-of-the-art models range from physics-based and computational fluid dynamics (CFD) frameworks to coupled atmosphere-fire systems and operational tools aimed at real-time decision-making. This chapter reviews the most relevant contributions in each category, highlighting their underlying physical assumptions, numerical strategies, and intended applications. The discussion provides a foundation for understanding the motivations and limitations that guide the development of the simplified yet efficient model proposed in this thesis.

2.1 Wildfire Modeling

Wildfires are complex phenomena that involve the interaction of various environmental, meteorological, and topographical factors (Finney et al., 2021; Speer & Goodrick, 2022; Himoto, 2022). Modeling these events is essential for understanding their behavior, predicting their spread, and implementing effective mitigation strategies (Meacham & McNamee, 2023).

Fire behavior is significantly affected by fuel properties, such as the type, moisture content, and spatial arrangement of vegetation. Fuel models take these elements into account to estimate fuel availability and combustibility (Finney et al., 2021). Weather conditions, including wind speed, wind direction, temperature, and relative humidity, are essential to determine the spread rate and intensity of the fire (Bakhshaii & Johnson, 2019; Finney et al., 2021). Advanced models often integrate real-time weather data to improve accuracy (Wegrzynski & Lipecki, 2018). Topography features such as slope, elevation, and aspect affect fire behavior by influencing heat transfer and wind patterns (Finney et al., 2021). Steep slopes can accelerate the spread of fire, whereas valleys can act as barriers or conduits (Opie, 2020). Fire spread mechanisms, such as radiation, convection, and spotting, are fundamental to modeling. Understanding these dynamics helps in simulating the progression of the fire front (Drysdale, 2011). The human factor is also an important component

in the modeling of wildfires. Anthropogenic activities, such as changes in land use and firefighting efforts, also play a role in the modeling of wildfires (Meacham & McNamee, 2023).

Regarding modeling approaches, there are several ways to classify them, but in general they could be grouped into:

1. **Empirical Models**: These models rely on statistical relationships derived from historical fire data. They are fairly straightforward and computationally efficient; however, they might not generalize well to atypical conditions (Sullivan, 2009b; Silva et al., 2022).

2. **Physics-Based Models**: These models simulate fire behavior by solving the equations that govern combustion, heat transfer, and fluid dynamics. Although more accurate, they require significant computational resources and detailed input data (Sullivan, 2009a; Silva et al., 2022).

3. **Hybrid Models**: Combining empirical and physics-based approaches, hybrid models aim to balance accuracy and computational efficiency. They often use empirical rules to guide simulations based on physics (Silva et al., 2022).

4. **Machine Learning Approaches**: Recent advances in artificial intelligence have enabled the development of data-driven models that leverage large datasets to predict fire behavior. These models can identify complex patterns and interactions that traditional approaches may overlook (Andrianarivony & Akhloufi, 2024).

5. **Integrated Models**: These models integrate wildfire simulations with atmospheric models to examine feedback mechanisms, specifically how wildfires affect and are affected by local and regional meteorological patterns (Silva et al., 2022).

The following references provide a more in-depth look at wildfire modeling. Pastor et al. (2003) present a review of the wildfire models and software developed from 1940 to 2002. Sullivan presents a detailed description of the physical and empirical models developed between 1990 and 2007 (Sullivan, 2009a, 2009b, 2009c). The authors in Wegrzynski et al. (2018) provide a review that highlights the importance of wind in wildfire modeling. Bakhshaii and Johnson (2019) contrast the coupled atmosphere-fire models, presenting their capabilities and limitations. Finally, Silva et al. (2022) present an extensive review of the literature on fire behavior modeling, including the history of modeling approaches and the new trends in this area.

This study will focus on physics-based models, specifically coupled models, which consider the interplay between the lower atmosphere and fire spread, taking into account the dynamics of both phenomena. The following section discusses the most pertinent models related to this topic.

2.2 Coupled Models

The objective of this work is to develop a coupled, yet computationally efficient physical model to simulate fire-atmosphere interactions in forest fire scenarios. This model aims to capture the essential dynamics of fire spread and its feedback with atmospheric processes, while maintaining a level of simplification that ensures practical applicability and reduced computational cost. In this context, the following section reviews state-of-the-art modeling approaches that integrate fire behavior with atmospheric dynamics, providing the foundation and motivation for the methodology proposed in this study.

2.2.1 Fire Dynamics Simulator

The *Fire Dynamics Simulator* (FDS) is a computational fluid dynamics (CFD) model developed by the U.S. National Institute of Standards and Technology (NIST), specifically designed to simulate fire behavior and its interaction with the surrounding environment (K. B. McGrattan et al., 2025). It is widely used for research, fire safety analysis, and training applications, providing high-resolution numerical simulations of fire dynamics, including combustion, heat transfer, and smoke transport.

FDS solves the low-Mach number form of the Navier-Stokes equations, which eliminates acoustic wave propagation from the dynamics and makes the method efficient for low-speed buoyancy-driven flows, such as fire plumes (Rehm & Baum, 1978). The governing system includes the continuity equation for mass conservation, the momentum equation for fluid flow and buoyancy, and the energy equation for heat transfer and temperature evolution (K. McGrattan et al., 2012). Combustion is represented using a mixture fraction approach, which reduces the complexity of chemical kinetics by describing the mixing of fuel and oxidizer. Heat transfer is modeled through all three modes: convection between gases and surfaces, conduction within solids, and thermal radiation, which is approximated by solving a simplified radiative transport equation (RTE). Solid-phase pyrolysis and material degradation are described by separate energy conservation equations, which are coupled with the gas-phase model. The transport of smoke and other combustion products is incorporated through advection-diffusion equations. Turbulence is treated with Large Eddy Simulation using an implicit filtering approach (K. B. McGrattan et al., 2025).

In terms of numerical methods, FDS employs a structured grid and a second-order accurate Finite Difference Method to discretize the governing equations. Temporal integration is performed with a fractional step method combined with an explicit second-order Runge-Kutta scheme, while radiative transfer is solved with the Finite Volume Method (K. B. McGrattan et al., 2025). The solver uses a fast direct pressure method, which reduces computational time compared to iterative approaches. The implementation is open source, with parallelization supported through OpenMP and the Message Passing Interface (MPI), enabling simulations ranging from small laboratory-scale fires to large building-scale scenarios (K. B. McGrattan & Forney, 2025).

The *Wildland-Urban Interface Fire Dynamics Simulator* (WFDS) is an extension of the FDS developed to model wildland and wildland-urban interface fires (Mell, Jenkins, Gould, & Cheney, 2007). It incorporates a physical wildfire spread model and a semi-coupled fire-atmosphere representation to capture interactions between fire fronts and ambient wind fields. Like its parent model, WFDS is fully three-dimensional, physics-based, and relies on the low-Mach number approximation for computational efficiency. The model is particularly suited to short-duration fire simulations where resolving coupled fire-atmosphere dynamics is essential.

2.2.2 FIRETEC

FIRETEC is a physics-based wildfire behavior model developed at Los Alamos National Laboratory (LANL) (R. Linn, Reisner, Colman, & Winterkamp, 2002). It is designed to simulate the three-dimensional interactions between fire, vegetation, and the surrounding atmosphere by solving the governing equations of fluid dynamics, heat transfer, and combustion in a coupled framework. The model emphasizes the role of fine-scale physical processes, such as turbulence, radiative heat transfer, and vegetation heterogeneity, in shaping fire behavior.

The governing equations include the continuity equation for mass conservation, the momentum equations to capture buoyancy-driven and turbulent flows, the energy equation to model heat transfer, and species transport equations to track combustion products such as water vapor and carbon dioxide (Dupuy et al., 2011). Combustion is described using simplified chemical reaction mechanisms, representing pyrolysis of vegetation, oxidation of char, and burning of hydrocarbons (R. Linn, 1997). The heat release rate is determined by the availability of fuel and oxygen, as well as by local thermodynamic conditions. FIRETEC incorporates all three heat transfer mechanisms: conduction, convection, and radiation. Vegetation is modeled as a porous medium with varying fuel properties (e.g., density, moisture content, and spatial distribution), which strongly influence the spread and intensity of the fire. Turbulence is represented with sub-grid-scale models to account for the effects of eddies and vortices that cannot be explicitly resolved.

Numerically, FIRETEC employs the Finite Difference Method for discretization of the governing equations, ensuring the conservation of mass, momentum, and energy in computational cells (R. Linn et al., 2002). It uses variable-resolution grids to refine the solution in regions of active combustion while reducing computational demand elsewhere. Explicit time integration is applied to capture the fast dynamics of fire spread and atmosphere–fire coupling. This framework allows the model to resolve the spatial and temporal evolution of wildfires under the influence of wind, terrain, and heterogeneous fuel distributions.

The coupled HIGRAD/FIRETEC system links the High Gradient Flow Solver (HIGRAD) (Smolarkiewicz & Margolin, 1997; Reisner, Wynne, Margolin, & Linn, 2000) with the FIRETEC fire model, both developed at LANL. HIGRAD provides the atmospheric flow solver, while FIRETEC represents the physics of fire. The fire model uses a simplification of combustion reactions through ensemble-averaged

processes, including pyrolysis, char burning, hydrocarbon oxidation, and soot combustion in the presence of oxygen. The coupling ensures that fire-induced buoyancy alters the local atmospheric flow at the microscale, which in turn feeds back into the fire spread.

According to R. Linn (1997), the system of equations of FIRETEC was originally solved using the Finite Difference Method. Later, Reisner et al. (2000) describe the coupled HIGRAD/FIRETEC system as being solved with second-order accuracy in both space and time using the Method of Averages (Nadiga, Hecht, Margolin, & Smolarkiewicz, 1997). This semi-coupled framework is suitable for small-scale fire studies over short time periods, where resolving microscale fire–atmosphere interactions is essential.

2.2.3 FIRESTAR

FIRESTAR is a physics-based model of wildfire behavior designed to explore the essential processes behind fire spread in wildland settings, highlighting the complex interaction between fluid dynamics and combustion physics (Morvan & Dupuy, 2004; Morvan, Dupuy, Rigolot, & Valette, 2006; Morvan, Hoffman, Rego, & Mell, 2011). This model provides three-dimensional simulations, initially in a two-dimensional domain (Morvan & Dupuy, 2004), clarifying the mechanisms of fire propagation, environmental factors and the interaction between fire and its environment, which makes it highly beneficial for studying fire behavior under laboratory conditions and natural wildland scenarios (Morvan, Accary, Meradji, Frangieh, & Bessonov, 2018; Frangieh, Accary, Morvan, Méradji, & Bessonov, 2020).

At its core, FIRESTAR solves the Navier–Stokes equations for turbulent reacting flows, coupled with the conservation equations for mass, momentum, energy, and chemical species (Morvan et al., 2018). Numerical discretization is performed using the Finite Volume Method on structured 3D Cartesian grids, using the QUICK scheme for convective terms and central difference for diffusion terms (Morvan et al., 2018; Frangieh et al., 2020). In terms of time integration, an adaptive time-stepping strategy based on the third-order Euler scheme is used to improve numerical stability and computational efficiency, which is especially critical for resolving fast transient processes such as flame spread and heat transfer (Morvan et al., 2018; Frangieh et al., 2020). The radiative transport equation is solved using the Discrete Ordinate Method. The coupling between velocity and pressure is ensured by using the PISO algorithm (Morvan et al., 2018). Turbulence is addressed through the Unsteady Reynolds Average and Large Eddy Simulation methods, which enable the explicit resolution of large-scale flow structures and fire-induced vortices, critical for the capture of dynamic fire behavior (Frangieh et al., 2020).

The model accommodates boundary conditions tailored to both laboratory and wildland contexts, including adjustable wind profiles, fuel bed properties, and terrain slopes, all parameterizable by the user to replicate diverse fire scenarios (Frangieh et al., 2020).

FIRESTAR is primarily implemented in Fortran, a language chosen for its com-

putational efficiency in large-scale scientific simulations (Accary, Bessonov, Fougère, Meradji, & Morvan, 2007). The software architecture supports parallel execution using OpenMP, facilitating scalable performance on modern high-performance computing clusters and multi-core workstations (Accary et al., 2007; Morvan et al., 2018; Frangieh et al., 2020). For demanding simulations, FIRESTAR recommends hardware configurations featuring multicore CPUs and computing clusters with ample RAM, typically several gigabytes per simulation, to effectively manage high-resolution 3D grids (Accary et al., 2007).

2.2.4 OpenFOAM

OpenFOAM (Open Source Field Operation and Manipulation) is an open source computational fluid dynamics (CFD) toolkit that offers extensive flexibility to simulate complex physical phenomena, including fluid flow, heat transfer, chemical reactions, and multiphysics interactions (Greenshields, 2025).

OpenFOAM solves the Navier–Stokes equations together with conservation laws for mass, momentum, energy, and turbulence in their integral form using the Finite Volume Method (Greenshields & Weller, 2022; Greenshields, 2025). Fluxes are evaluated across cell faces to ensure conservation, with user-selectable schemes available for time, convection, and diffusion discretization. Equation solvers, algorithms, and relaxation factors are configurable at runtime, and additional source terms can be introduced through its modular structure (Greenshields, 2025). Turbulence is modeled with both Reynolds-Averaged Navier–Stokes and Large Eddy Simulation approaches, whose transport equations are derived directly from the Navier–Stokes equations and discretized within the same Finite Volume Method framework. The configuration system, combined with the principles of conservation, flux consistency, and stability, makes OpenFOAM a flexible tool for a wide range of CFD applications (Greenshields & Weller, 2022).

Within wildfire research, OpenFOAM has become a versatile platform to simulate fire dynamics through discretization of finite volumes, adaptive mesh refinement, and parallel computing, allowing models with high resolution and resource intensive (Greenshields & Weller, 2022; Greenshields, 2025; Lapointe et al., 2021). It has been applied to study the combustion of vegetative fuels, including pyrolysis, flame development, energy release, and pollutant formation (Houssami et al., 2016; El Houssami, Lamorlette, Morvan, Hadden, & Simeoni, 2018), as well as heat transfer by conduction, convection, and radiation in complex terrains (Y. Wang, Chatterjee, & de Ris, 2011; K. Zhang, Verma, Trouvé, & Lamorlette, 2020).

Wildfire-induced fluid dynamics and turbulence are addressed using Large Eddy Simulation in the FireFOAM solver, capturing buoyancy-driven motion, plumes, and fire-atmosphere interactions (Ghaderi, Ghodrat, & Sharples, 2021; Ghodrat, Edalati-Nejad, & Simeoni, 2022). The combination with atmospheric models and customized boundary conditions further enables the study of feedback mechanisms, local meteorology, and smoke dispersion (Ghodrat, Edalati-nejad, Simeoni, Dlugogorski, & Masri, 2023).

The open-source nature of OpenFOAM fosters wildfire-specific extensions for variables such as humidity, fuel moisture, terrain slope, while interoperability with experiments improves validation (Houssami et al., 2016; El Houssami et al., 2018; Kamma, Loksupapaiboon, Phromjan, & Suvanjumrat, 2025). Its HPC compatibility, including distributed parallelization, supports large-scale fire spread simulations with fine resolution, making OpenFOAM a key tool to advance in wildfire risk assessment and mitigation strategies (Lapointe et al., 2021).

2.3 Other Models

The following section introduces alternative modeling techniques that are crucial to consider because of their significance in wildfire simulation.

2.3.1 Weather Models

Weather models link meteorological processes with fire behavior to account for the influence of wind, temperature, and humidity on wildfire dynamics. Unlike fully coupled fire–atmosphere models, which resolve fine-scale two-way feedback between fire and local weather, weather models typically operate at larger spatial and temporal scales, providing boundary and forcing conditions that drive fire spread. Generally, these models use a hybrid approach, integrating physics-driven weather models with simplified physical or empirical models to account for fire spread. This sub-section discusses relevant models that employ this approach.

CAWFE

The Coupled Atmosphere–Wildland Fire–Environment (CAWFE) model was developed at the National Center for Atmospheric Research (NCAR) to advance integrated wildfire simulation (Clark, Jenkins, Coen, & Packham, 1996a, 1996b; Clark, Coen, & Latham, 2004; Coen, 2005). CAWFE is recognized as the first successful attempt to combine an atmospheric model directly with a fire behavior module, providing a framework for the detailed study of interactions between weather and fire dynamics (Clark et al., 1996a, 1996b). The initial generation achieved this by coupling the Clark–Hall mesoscale atmospheric model with a quasi-physical, tracer-based fire spread representation, allowing simulation of fine-scale meteorological and fire processes within a unified system (Clark et al., 1996a, 1996b).

At its computational core, CAWFE employs three-dimensional primitive equations of motion and thermodynamics, allowing it to resolve convective dynamics and represent ambient meteorological conditions on spatial scales from millimeters to megameters (Clark et al., 2004). The current version consists of two major components: a numerical weather prediction model and a semi-physical fire module, which is fully coupled and dynamically interactive with atmospheric processes even

as wildland fire phenomena typically occur at scales much smaller than the atmospheric grid size (Coen, 2005). The fire module explicitly simulates the progression of the flaming front, post-frontal heat release, and surface and crown fire behavior, calculating sensible and latent heat fluxes in tandem with the weather model (Coen, 2005).

This design enables the CAWFE model to capture both small, localized fires and extensive, landscape-scale wildland fire events, supporting research on the influence of meteorological conditions on fire spread, intensity, and ecological impact (Clark et al., 1996a, 2004; Coen, 2005).

WRF-FIRE

The WRF-FIRE model couples the Weather Research and Forecasting (WRF) model (Patton & Coen, 2004; Mandel, Beezley, & Kochanski, 2011; Coen et al., 2013) with a fire behavior module to provide an integrated framework for simulating fire–atmosphere interactions. Developed as an advancement over the fifth-generation NCAR/Penn State Mesoscale Model, WRF is an open-source, community-supported atmospheric model widely used for applications across multiple scales, from tens of meters to tens of kilometers. The Advanced Research WRF system within WRF supports a diverse range of purposes, including real-time forecasting, research studies, coupled model simulations, regional climate investigations, and data assimilation efforts, all benefiting from its computational parallelization capabilities (Patton & Coen, 2004; Mandel et al., 2011).

The fire module in WRF-FIRE draws inspiration from the CAWFE model, adopting a quasi-physical approach to represent fire spread (Coen et al., 2013). The coupling between the fire and atmospheric components occurs by exchange of winds, temperature, and moisture from the lowest levels of the WRF model, where the vertical resolution can be adjusted according to simulation needs, into the fire behavior module. Fire propagation is implemented using the level-set method, which efficiently captures the evolving shape of the fire front. Temporal integration within the fire module uses a second-order Runge-Kutta scheme while spatial discretization employs the Finite Difference method incorporating central, backward, and forward differencing, as well as first-order essentially non-oscillatory schemes to maintain numerical stability and accuracy (Mandel et al., 2011).

The atmospheric dynamics of WRF are solved in time using an explicit third-order Runge-Kutta method, with spatial discretization based on Finite Difference methods. This structure allows for an accurate and stable simulation of meteorological processes coupled with fire spread. Furthermore, the entire WRF-FIRE system is implemented as open-source software, allowing researchers and practitioners to customize and extend the model to address specific wildfire scenarios and scientific questions (Patton & Coen, 2004; Coen et al., 2013).

ARPS/DEVS-FIRE

The ARPS/DEVS-FIRE model couples the Advanced Regional Prediction System (ARPS) (Xue, Droegemeier, & Wong, 2000; Xue et al., 2001) with the DEVS-FIRE fire spread model (Dahl, Xue, Hu, & Xue, 2015; Ntaimo, Zeigler, Khargharia, & Vasconcelos, 2004; Hu, Sun, & Ntaimo, 2012), integrating atmospheric prediction capabilities with wildfire simulation. ARPS was developed at the Center for Analysis and Prediction of Storms at the University of Oklahoma and is a sophisticated system aimed at simulating severe weather and atmospheric processes. The DEVS-FIRE component is a raster-based fire spread model that conceptualizes the fire front as a progression of grid-cell interactions rather than as a continuous front line, making it a quasi-physical approach to simulating surface fire spread (Dahl et al., 2015; Ntaimo et al., 2004).

Unlike fully coupled fire-atmosphere models, the fire spread in ARPS/DEVS-FIRE treats weather inputs as external data provided to the fire model rather than dynamically coupling fire fluxes and emissions within atmospheric simulations. As such, ARPS itself does not possess integrated solvers for fire spread, heat fluxes, or emission processes necessary for fully parallelized simulations (Dahl et al., 2015). A key limitation of this coupling approach is the reliance on external data exchange between the two models, which involves input/output operations that tend to be slower than internal data passing mechanisms, resulting in longer computational times (Dahl et al., 2015).

Despite these challenges, the ARPS/DEVS-FIRE system includes data assimilation functionality designed to enhance simulation accuracy by incorporating observational data during the modeling process, improving the reliability of fire behavior predictions (Dahl et al., 2015). This integration allows researchers to leverage the strengths of both atmospheric and fire spread modeling in a complementary fashion, albeit with some performance trade-offs due to the coupling strategy.

ForeFire/Meso-NH

The ForeFire/Meso-NH modeling system couples the Meso-NH atmospheric model with the ForeFire wildfire spread model, allowing integrated simulations of meteorology and fire dynamics. Meso-NH, developed by the Centre National de Recherche Météorologique and the Laboratoire d'Aérologie, is an anelastic and non-hydrostatic model designed to resolve atmospheric processes on scales from the meso-gamma (approximately 1 km) to the microscale (approximately 10 m). By filtering out acoustic waves, it focuses computational resources on capturing the meteorological phenomena most relevant to wildfire–atmosphere interactions (Lafore et al., 1998).

The ForeFire component adopts a quasi-physical approach to wildfire spread, representing the flame front as a radiating panel that propagates normal to the fireline. It employs a Lagrangian front-tracking method to capture complex fireline geometries and temporal evolution with high precision (Balbi, Morandini, Silvani, Filippi, & Rinieri, 2009). The coupling between Meso-NH and ForeFire is achieved

through bilinear interpolation of wind, temperature, and humidity fields from the atmospheric model to the fire model. In turn, fire-induced fluxes of heat and water vapor are imposed at the surface in Meso-NH, allowing the atmosphere to respond dynamically to the fire (Filippi et al., 2011).

This coupled system provides a powerful framework for investigating the fire and atmosphere interactions at mesoscale resolutions. By integrating dynamic meteorological conditions with physically based fire propagation, ForeFire/Meso-NH enables researchers to explore wildfire behavior under diverse environmental scenarios, assess feedback mechanisms between fires and the atmosphere, and achieve high spatial and temporal fidelity in wildfire simulations.

2.3.2 Operational Models

This subsection introduces the operational wildfire models, which prioritize computational efficiency and rapid execution over fine-scale process fidelity. In contrast to coupled fire–atmosphere models, these approaches do not explicitly resolve two-way interactions between fire dynamics and atmospheric processes. Instead, they rely on empirical or semi-empirical formulations to predict fire spread, enabling shorter simulation times and reduced computational requirements. As a result, operational models are widely applied in real-time forecasting and decision-support systems, when both speed and practicality are essential.

FlamMap

FlamMap is a desktop fire analysis application developed by the U.S. Forest Service Fire Behavior Research Team. It simulates potential fire behavior under constant environmental conditions, including spatially resolved outputs such as rate of spread, flame length, fireline intensity, and crown fire activity across a landscape grid (Finney, 2006). The model accounts for topographic shading, slope, elevation, and aspect to compute moisture conditioning of dead fuels and leverages established sub-models, including Rothermel's surface fire spread (Rothermel, 1972), Van Wagner's crown fire initiation (Van Wagner, 1977), Rothermel's crown fire spread (Rothermel, 1991), Albini's spotting model (Albini, 1979), and Nelson's dead fuel moisture model (Nelson Jr, 2000).

FlamMap produces raster maps that represent fire behavior metrics and environmental conditions, such as wind speeds at mid-flame height and solar radiation, which can be exported to use in GIS or image editing software. Including tools like WindNinja facilitate the modeling of wind patterns (J. Forthofer, Shannon, & Butler, 2009; J. M. Forthofer, Butler, & Wagenbrenner, 2014a, 2014b), while applications such as SpatialFOFEM offer projections for fuel consumption and emissions (Riley, Grenfell, Shaw, & Finney, 2022).

FARSITE (Fire Area Simulator) extends FlamMap by introducing temporally dynamic fire spread simulation, allowing for heterogeneous temporal sequences of weather, fuel moisture, and terrain conditions, allowing realistic modeling of fire

growth over long periods (Finney, 1998). As a deterministic fire growth model, FARSITE computes the progression and behavior of wildfires and produces output compatible with Geographic Information System (GIS) platforms, supporting simulations of suppression tactics, hypothetical situations, and detailed perimeter tracking (Finney, 1998).

By integrating FARSITE, FlamMap is enhanced to assess wildfire burn probabilities, as well as long-term fire behavior patterns and landscape-level hazard assessments in the context of changing environmental conditions. FlamMap offers detailed high-resolution images of possible fire behavior under static conditions, whereas FARSITE supports dynamic landscape-scale simulations that incorporate environmental changes over time.

ELMFIRE

The Eulerian Level-Set Model of FIRE Spread (ELMFIRE) is an open-source operational wildland fire spread simulator developed to forecast and reconstruct fire behavior, quantify landscape-scale fire potential, and estimate metrics such as burn probability, flame length, and fire severity (Lautenberger, 2013). It has seen applications in real-time wildfire prediction in the Continental United States and supports Monte Carlo simulations for hazard assessment (Lautenberger, 2013).

At its core, ELMFIRE implements an Eulerian level-set method to represent the fire front (Osher & Sethian, 1988; Rehm & McDermott, 2009). The model solves this equation with a narrow-band approach and a second-order Runge–Kutta time integrator, using flux limiters, e.g. Superbee, to avoid numerical oscillations (Lautenberger, 2013). Local spread rates are derived using a vectorized version of the Rothermel surface fire spread model (Rothermel, 1972), corrected for slope, aspect, and crown fire interactions. Crown fires are incorporated by combining the formulations Rothermel (1991) and Cruz, Alexander, and Wakimoto (2005) into an effective wind factor within an elliptical spread model (Richards, 1995). This methodology provides spatially varying fire spread and fireline intensity along the fire perimeter.

Originally implemented with Finite Difference discretization, ELMFIRE uses both GIS inputs (e.g. fuels, topography, weather rasters) and configuration data via input files to drive simulations (Lautenberger, 2025). Users can select a transient mode to simulate the spread of the fire over time or a potential fire mode to calculate the behavior of the fire on the landscape-scale in multiple meteorological scenarios (Lautenberger, 2025). Significantly, ELMFIRE interacts with extensive geospatial processes, since it has facilitated simulations throughout California and is incorporated into systems for live forecasting and hazard assessment. The modeling pipeline supports ensemble runs, Monte Carlo weather scenarios, and rapid post-processing of burned area output (Lautenberger, 2025).

PhyFire

The PhyFire model is a two-dimensional, single-phase, physics-based simulator of wildfire spread developed by the *SINUMCC* group at the University of Salamanca (Asensio, Cascón, Prieto-Herráez, & Ferragut, 2023). It was designed to strike a balance between physical realism and computational efficiency by solving simplified partial differential equations for energy and mass conservation. This approach enables the model to represent wildfire dynamics with greater fidelity than empirical models, while avoiding the prohibitive costs of full CFD simulations.

From a physical perspective, PhyFire captures the main processes that govern fire spread, including convection, radiation, flame tilt due to wind and slope, fuel moisture effects, and pyrolysis through a multi-valued enthalpy operator (Asensio & Ferragut, 2002; Ferragut, Asensio, & Monedero, 2007, 2006). It accounts for non-local radiation using convolution terms, allowing three-dimensional flame effects to be represented within a two-dimensional framework. The model also incorporates stochastic elements such as fire spotting, which improves its ability to replicate ignition dispersion and the complex evolution of fire fronts (Asensio et al., 2023; Serón, Gutiérrez, Magallón, Ferragut, & Asensio, 2005).

Numerically, PhyFire employs a mix of Finite Element and Finite Difference discretizations, predictor-corrector schemes, and adaptive refinement strategies to maintain efficiency and accuracy (Montenegro, Plaza, Ferragut, & Asensio, 1997; Asensio & Ferragut, 2002). Parallel implementations using OpenMP significantly reduce runtime in large-scale simulations (Álvarez, Prieto, Asensio, Cascón, & Ferragut, 2017), while sensitivity analysis and parameter tuning enhance predictive robustness under varying conditions (Prieto, Asensio, Ferragut, & Cascón, 2015). The model is integrated into a GIS workflow that supports pre-processing, simulation, and visualization, with outputs describing fire-front evolution over time. It also supports data assimilation for real-time forecasting (Ferragut, Asensio, Cascón, & Prieto, 2015) and can be coupled with the HDWind solver for high-resolution wind fields, improving the modeling of the fire-atmosphere interaction in complex terrain (Ferragut, Asensio, & Simon, 2011; Asensio, Luis, & Jacques, 2002).

2.4 Models summary

Table 2.1 summarizes the mathematical models revised in this chapter.

Table 2.1: Summary of wildfire models.

Modeling	**Model**	**Keywords**
Coupled	FIRETEC	CFD, compressible flow, LES, combustion, heat transfer
	FIRESTAR	CFD, low-Mach flow, LES, combustion, heat transfer
	FDS	CFD, low-Mach flow, LES, combustion, heat transfer
	OpenFOAM	CFD, multiphysics, LES, combustion, heat transfer
Weather	WRF-Fire	Mesoscale weather, semi-physical fire module
	ForeFire/Meso-NH	Mesoscale, semi-empirical spread, multiphysics
	ARPS/DEVS-Fire	Numerical weather model, raster-based fire model
	CAWFE	Mesoscale weather, semi-physical fire module
Operational	ELMFIRE	Empirical/physics-based hybrid model
	PhyFire	Semi-empirical, simplified physics
	FlamMap	Statistical/empirical, risk analysis

In terms of accessibility, the model implementations are:

- Open source: FDS, OpenFOAM, WRF-Fire, ELMFIRE, ForeFire/Meso-NH
- Freely available but no open source: FlamMap
- Limited or restricted availability: FIRETEC, FIRESTAR, CAWFE, ARPS/DEVS-Fire, PhyFire

Chapter 3

Proposal

This chapter introduces the central proposal of the thesis, which consists of a simplified coupled atmosphere-fire model designed to capture essential wildfire dynamics while maintaining computational efficiency. The proposal builds on the limitations identified in the state-of-the-art review, seeking a balance between physical realism and numerical tractability. The key ideas underlying the mathematical formulation, the numerical approach, and the computational strategies are outlined here, along with the specific objectives and hypotheses that guide the development of the model and its implementation.

3.1 Working Hypotheses

The hypotheses developed in this work are the following.

- *A simplified coupled physical model, with respect to the state-of-the-art fire-atmosphere models, allows the description of the dynamics of a wildfire under adverse meteorological conditions such as high temperatures, low relative humidity, high winds, and complex topography, with greater accuracy in metrics such as fire spread speed and fire line intensity, compared to a simplified two-dimensional fire spread model that includes meteorological information in a fixed or predefined way.*

- *It is possible to perform a parallel implementation of the proposed simplified model using a GPU and considering the associated memory constraints, which will reduce computational times compared to a CPU approach implementation of a more detailed physical model such as those of the state of the art and requiring a higher memory usage, under comparable conditions of spatial resolution and physical domain.*

3.2 Objectives

3.2.1 General Objectives

The general objectives associated with this work are as follows:

1. Design and implement an algorithm using a coupled atmosphere-fire model, a physical approach, and based on partial differential equations.
2. Provide an open-source implementation to support the study of the effects of forest fires focused on affordable computing times with limited hardware.

3.2.2 Specific Objectives

The specific objectives associated with the thesis project are:

1. Propose a simplified coupled atmosphere-fire model to describe the phenomenon.
2. Implement the wildfire numerical model on the CPU.
3. Implement the wildfire numerical model on the GPU.

Chapter 4

Mathematical Model

Most of the coupled atmosphere-fire mathematical models are based on fluid flow equations. According to K. McGrattan and Miles (2016), the governing equations of fluid flow have been used successfully in fire modeling. In particular, R. Linn (2019) highlights the importance of fluid dynamics in the case of wildland fires. These equations enable the characterization of fluid dynamics through the principles of mass, momentum, and energy conservation. Analytically, they are unsolvable for general cases and require the introduction of several assumptions and simplifications (Ferziger, Perić, & Street, 2020).

The mathematical model introduced in this research is essentially based on these equations, specifically involving the Boussinesq and low-Mach number approximations related as presented in Figure 4.1.

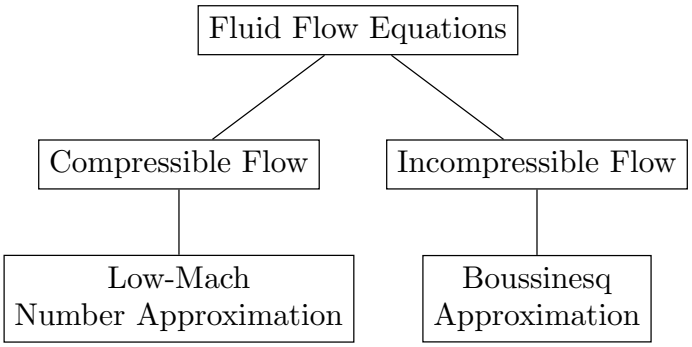

Figure 4.1: Fluid flow approximations.

The next sections will describe the derivation of the model using the governing equations, including the assumptions and simplifications incorporated.

4.1 Governing Equations

Governing equations in fire dynamics are fundamental to understanding the behavior of fire. These equations include a set of physical laws that describe the movement,

heat transfer, and chemical reactions that occur during a fire. The key equations include conservation of mass, momentum, energy, and species (Poinsot & Veynante, 2012; Kuwana, 2020). They describe how the total amount of a conserved property within a control volume evolves due to fluxes across its boundaries and sources or sinks inside, providing a global perspective on physical changes in the system. Understanding and solving these equations allows fire engineers and scientists to accurately simulate fire scenarios and design effective fire protection systems. Appendix B.2 provides the formulation of each conservation equation, beginning with the integral form and proceeding to the corresponding differential form.

The following sub-sections present the main equations in their differential form.

4.1.1 Conservation of mass

The conservation of mass represents the principle that mass is neither created nor destroyed in a closed system during a chemical reaction or physical transformation. In the context of wildfires, mass conservation plays a fundamental role in describing mass transport and transformation within the fire-affected region. This principle ensures that the mass of air, fuel, combustion products, and particulates is accounted for as the fire evolves. As vegetation burns, solid fuel undergoes pyrolysis, releasing gases that mix with ambient air and participate in combustion. The resulting products, including carbon dioxide, water vapor, and soot, are transported by buoyant and wind-driven flows. In computational wildfire modeling, the continuity equation governs this mass balance, ensuring that changes in fluid density and velocity are consistently tracked throughout the domain as the fire interacts with the surrounding environment.

Mathematically, this is described (Batchelor, 2000) by

$$\frac{\partial \rho}{\partial t} + \nabla \cdot (\rho \mathbf{u}) = 0, \tag{4.1}$$

where ρ is the density of the fluid (kg m^{-3}) and $\mathbf{u}$ is the flow velocity (m s^{-1}). Appendix B.2.1 presents the derivation from the integral form.

4.1.2 Conservation of momentum

The conservation of momentum is a principle in physics stating that the total momentum of a closed system remains constant if no external forces are acting on it. It describes the motion of a fluid, taking into account the forces acting on it, represented typically by Newton's second law of motion.

In wildfire dynamics, momentum conservation governs the motion of air and combustion gases driven by thermal buoyancy, wind, and pressure gradients. As fuel burns, intense heat releases generate strong upward motions, creating buoyant plumes that interact with ambient wind fields. This interaction leads to complex flow structures such as vortices, entrainment zones, and turbulent mixing layers. The momentum balance accounts for the forces acting on the fluid, including pressure

gradients, gravitational acceleration, and viscous stresses. In computational wildfire models, the momentum equations describe how the velocity field evolves in response to these forces, capturing key phenomena such as fire-induced winds, plume rise, and feedback between the fire and atmosphere.

Formally, it can be represented by the Cauchy momentum equation (Batchelor, 2000; Pope, 2000),

$$\frac{\partial (\rho \mathbf{u})}{\partial t} + \nabla \cdot (\rho \mathbf{u} \otimes \mathbf{u}) = \nabla \cdot \boldsymbol{\sigma} + \mathbf{f}, \tag{4.2}$$

where $\mathbf{f}$ represents the external forces in the fluid and $\otimes$ represents the outer product (C.4). The stress tensor $\boldsymbol{\sigma}$ (Pa = N m^{-2} = kg m^{-1} s^{-2}) is

$$\boldsymbol{\sigma} = -p\mathbf{I} + \boldsymbol{\tau}, \tag{4.3}$$

where $\boldsymbol{\tau}$ is the viscous stress tensor (kg m^{-1}s^{-2}), p is the pressure (kg m^{-1}s^{-2}), and $\mathbf{I}$ is the identity matrix. The viscous tensor can be defined as

$$\boldsymbol{\tau} = \mu \left(\nabla \mathbf{u} + (\nabla \mathbf{u})^{\top} - \frac{2}{3} (\nabla \cdot \mathbf{u}) \mathbf{I} \right) + \zeta (\nabla \cdot \mathbf{u}) \mathbf{I}, \tag{4.4}$$

where μ is the dynamic viscosity and ζ the bulk viscosity both in kg m^{-1} s^{-1} (Papalexandris, 2020). Appendix B.2.2 presents the derivation from the integral form.

4.1.3 Conservation of energy

Conservation of energy is a fundamental principle that states that energy cannot be created or destroyed but can only be transformed or transferred between different forms, such as kinetic, potential, thermal, and chemical energy.

The conservation of energy is central to understanding and modeling wildfire behavior, as it governs the transformation and transport of thermal energy within the fire environment. During combustion, chemical energy stored in vegetation is released as heat, which in turn heats the surrounding air, drives buoyant flows, and promotes further ignition of nearby fuel. The energy balance accounts for various processes, including convective and radiative heat transfer, conduction through solid materials, and latent heat release from moisture evaporation. In numerical wildfire simulations, the energy equation captures how thermal energy evolves in space and time, influencing temperature fields, fire-induced winds, and the overall dynamics of flame propagation.

Mathematically, it can be expressed in several forms, but in terms of sensible enthalpy h (B.26) (Rohsenow, Hartnett, & Cho, 1998; K. McGrattan & Miles, 2016), it can be described with

$$\frac{\partial (\rho h)}{\partial t} + \nabla \cdot (\rho h \mathbf{u}) = \frac{Dp}{Dt} - \nabla \cdot \mathbf{q} + \boldsymbol{\tau} : \nabla \mathbf{u} + \dot{Q}, \tag{4.5}$$

where $\boldsymbol{\tau} : \nabla \mathbf{u}$ is the viscous dissipation, $\dot{Q}$ is the prescribed heat source (kg m^{-1}s^{-3}), $\mathbf{q}$ the heat flux vector (kg s^{-3}), and D/Dt denotes the material derivative (C.3). Appendix B.2.3 presents the derivation from the integral form.

4.1.4 Conservation of species

The conservation of chemical species is critical in wildfire modeling, as it governs the production, transport, and transformation of gaseous and particulate components generated during combustion. As vegetation burns, complex chemical reactions convert solid and volatile fuels into combustion products such as carbon dioxide, carbon monoxide, water vapor, methane, and various trace gases and aerosols. The species conservation equations track the mass fractions or concentrations of these components as they are advected by the flow, diffused through molecular and turbulent processes, and altered by chemical reactions. Accurate modeling of species transport is essential for understanding fire-atmosphere interactions, radiative heat transfer, and the environmental impact of smoke and emissions. In computational wildfire models, incorporating species conservation allows for realistic simulation of fire chemistry, pollutant dispersion, and the feedback of chemical composition on atmospheric thermodynamics and radiative properties.

Combustion can be represented as the mass conservation equation for chemical species i (Poinsot & Veynante, 2012; Kuwana, 2020) with

$$\frac{\partial(\rho Y_i)}{\partial t} + \nabla \cdot (\rho Y_i \mathbf{u} + \mathbf{J}_i) = \dot{\omega}_i, \tag{4.6}$$

where Y_i is the mass fraction, $\dot{\omega}_i$ is the production rate of species ($\mathrm{kg\,m^{-3}\,s^{-1}}$), $\mathbf{J}_i$ is the diffusive flux defined based on Fick's law,

$$\mathbf{J}_i = -\rho D_i \nabla Y_i, \tag{4.7}$$

with D_i the diffusive coefficient. The term $\dot{\omega}_i$ is modeled using the Arrhenius law,

$$\dot{\omega}_i = M_i \sum_{k=1}^{M} \nu_{ik} A_k T^{\alpha_k} \left(\frac{p}{RT}\right)^{\sum_{j=1}^{N} n_{jk}} \exp\left(-\frac{E_k}{RT}\right) \prod_{j=1}^{N} \left(\frac{Y_j}{M_j}\left(\sum_{l=1}^{N} \frac{Y_l}{M_l}\right)^{-1}\right)^{n_{jk}} \tag{4.8}$$

where M_i is the molar mass of the species, M is the number of reactions considered, ν_{ik} is the stoichiometric coefficient of the specie i in reaction k, E_k is the activation energy of reaction, $\mathcal{R} = 8.314$ J mol^{-1} K^{-1} is the universal gas constant, n_{jk} is the reaction order, X_j is the mole fraction, A_k is the pre-exponential coefficient, and α_k is an exponent for the temperature dependence. The derivation from integral form is detailed in Appendix B.2.4.

4.1.5 Equation of state

The equation of state provides a relationship between thermodynamic variables such as pressure, temperature, and density in wildfire modeling. In most atmospheric fire simulations, the ideal gas law is used to represent the behavior of the gas mixture produced by combustion along with the surrounding air. As the fire develops, the intense heat modifies the surrounding temperature and the composition of the gas

phase, resulting in notable changes in both density and pressure. The equation of state enables the closure of the system of governing equations by relating these quantities in a physically consistent manner. It plays a key role in the capture of buoyancy-driven flows, fire-induced pressure gradients, and the dynamics of plume rise.

Typically, the ideal gas law can be written as

$$p = \rho R T, \tag{4.9}$$

with R the specific gas constant (details in A).

4.2 Compressible Flow

Compressible flow refers to fluid motion in which variations in density play a significant role in the behavior of the flow field. They typically involve gases subjected to substantial changes in pressure and temperature, leading to significant density variations. Viscosity in compressible flows governs momentum diffusion and shear stress generation, especially in regions with strong gradients. It plays a key role in energy dissipation and interacts with thermodynamic variables such as temperature and pressure, which can vary significantly in such flows. There are two main types of viscosity relevant to fluid dynamics, especially in compressible flows: dynamic and bulk viscosity. Dynamic viscosity, denoted by μ, refers to the resistance of a fluid to shear or tangential stress, while bulk viscosity, denoted by ζ, refers to the resistance of a fluid to uniform compression or expansion. A typical assumption introduced is Stokes' hypothesis, which assumes $\zeta = 0$ or relates it to dynamic viscosity, and it is reasonable when the volumetric deformation effects are negligible (Papalexandris, 2020). However, this assumption may break down in flows with strong compressibility or shock waves, where bulk viscosity can significantly influence heat and momentum transfer. This study employs Stokes' hypothesis, noting that the propagation of wildfires is not influenced by shock waves. Then, equation (4.2) can be written as

$$\frac{\partial (\rho \mathbf{u})}{\partial t} + \nabla \cdot (\rho \mathbf{u} \otimes \mathbf{u}) = -\nabla p + \nabla \cdot \boldsymbol{\tau} + \mathbf{f}, \tag{4.10}$$

with the viscous stress tensor denoted as (Batchelor, 2000, p. 147)

$$\boldsymbol{\tau} = 2\mu \left(\mathbf{S} - \frac{1}{3}(\nabla \cdot \mathbf{u})\mathbf{I} \right), \quad \mathbf{S} = \frac{1}{2} \left(\nabla \mathbf{u} + (\nabla \mathbf{u})^{\top} \right). \tag{4.11}$$

$\mathbf{S}$ is known as the strain rate tensor.

4.2.1 Low Mach Number Approximation

In fluid dynamics, the low Mach number approximation applies to flows where the characteristic fluid velocity is much smaller than the speed of sound c, such that the

Mach number satisfies

$$\mathrm{Ma} = \frac{|\mathbf{u}|}{c} \ll 1.$$

In this regime, the compressibility effects associated with acoustic wave propagation become negligible. However, the flow may still exhibit significant density variations due to thermal expansion, chemical reactions, or gravitational stratification. The approximation is particularly beneficial in problems where acoustic phenomena are not central to the dynamics of interest, as it enables larger time steps and significantly reduces computational cost.

This approximation is especially relevant for thermally driven flows, where flow velocities induced by buoyancy or heat release remain well below the speed of sound in air (Rehm & Baum, 1978; Baum, Ezekoye, McGrattan, & Rehm, 1994; Mell, Mcgrattan, & Baum, 1995). In the context of wildland fires, wind speed measurements typically range from 1 to 26 m s^{-1} (Cruz & Alexander, 2019). Taking the upper bound as a representative characteristic velocity, the corresponding Mach number is

$$\mathrm{Ma} = \frac{26}{343} \approx 0.076, \tag{4.12}$$

which clearly satisfies the low Mach number criterion.

The low Mach number approximation has been widely adopted in the modeling of buoyancy-driven flows, combustion processes, both laminar and turbulent (Poinsot & Veynante, 2012), and thermally dominated phenomena such as the propagation of wildland fires (Morvan, 2011). It offers a favorable trade-off between physical fidelity and computational efficiency in situations where full compressibility is unnecessary. However, the approximation is limited to flows lacking strong shocks or significant acoustic transients and where pressure fluctuations remain small relative to the thermodynamic baseline. Consequently, it serves as the foundation for several reduced models in CFD, including anelastic and pseudo-incompressible formulations frequently used in geophysical fluid dynamics.

To derive the formulation of the low Mach number, the governing compressible Navier–Stokes equations are asymptotically expanded in terms of the small parameter Ma. This leads to a modified set of equations in which acoustic waves are effectively filtered out, while the essential thermofluid dynamics are retained. A fundamental feature of this approximation is the decomposition of the pressure field into a spatially uniform thermodynamic component p_0 and a dynamic perturbation p_d, expressed as

$$p(\mathbf{x}, t) = p_0(t) + p_\mathrm{d}(\mathbf{x}, t).$$

Here, p_0 serves as a background reference pressure, evolving slowly and satisfying the equation of state, whereas p_d enforces a velocity divergence constraint in place of the standard continuity equation.

The resulting governing equations for low Mach number flow are:

$$\begin{aligned}
\frac{\partial \rho}{\partial t} + \nabla \cdot (\rho \mathbf{u}) &= 0, \\
\rho \left(\frac{\partial \mathbf{u}}{\partial t} + \mathbf{u} \cdot \nabla \mathbf{u} \right) &= -\nabla p_{\mathrm{d}} + \nabla \cdot \boldsymbol{\tau} + \mathbf{f}, \\
\rho c_p \left(\frac{\partial T}{\partial t} + \mathbf{u} \cdot \nabla T \right) &= \frac{dp_0}{dt} - \nabla \cdot \mathbf{q} + Q, \\
\rho \left(\frac{\partial Y_i}{\partial t} + \mathbf{u} \cdot \nabla Y_i \right) &= -\nabla \cdot \mathbf{J}_i + \dot{\omega}_i, \\
p_0 &= \rho R T,
\end{aligned} \tag{4.13}$$

with the following constraint on the velocity divergence:

$$\nabla \cdot \mathbf{u} = \frac{1}{T} \left(\frac{DT}{Dt} \right) - \frac{1}{\rho T} \frac{dp_0}{dt}. \tag{4.14}$$

The complete derivation of this approximation is included in the Appendix B.2.7.

4.3 Incompressible Flow

The incompressible flow approximation refers to the assumption that the fluid density remains constant throughout the flow, which simplifies the analysis of fluid dynamics. This approximation is valid when the Mach number is less than 0.3. Under these conditions, changes in pressure and temperature do not significantly affect the density of the fluid, making it reasonable to consider the fluid to be incompressible. The primary disadvantage of employing an incompressible model instead of a low-Mach approximation lies in neglecting the significant role of density variations in flows involving considerable heat transfer, chemical reactions, or compositional alterations. This assumption is commonly applied in the analysis of liquid flows and low-speed gas flows.

Considering a strictly incompressible fluid flow, equations (4.1), (4.2), and (4.5) are rewritten as

$$\begin{aligned}
\nabla \cdot \mathbf{u} &= 0, \\
\rho \left(\frac{\partial \mathbf{u}}{\partial t} + (\mathbf{u} \cdot \nabla) \, \mathbf{u} \right) &= -\nabla p + \mu \nabla^2 \mathbf{u} + \mathbf{f}, \\
\rho c_p \left(\frac{\partial T}{\partial t} + \mathbf{u} \cdot \nabla T \right) &= k \nabla^2 T + Q.
\end{aligned} \tag{4.15}$$

The derivation of this approximation from the compressible fluid equations is included in the Appendix B.3.

4.3.1 Boussinesq Approximation

The Boussinesq approximation can be applied to problems where temperature variations are introduced into the fluid dynamics, driving a flow of fluid and heat transfer (Tritton, 1977, p. 127). In this approximation, the density is considered constant except in the force term, specifically because of the gravity effects. Mathematically, it is described with the same equations of an incompressible flow (4.15), except for the pressure and force term. The momentum equation is

$$\frac{\partial \mathbf{u}}{\partial t} + (\mathbf{u} \cdot \nabla)\,\mathbf{u} = -\frac{1}{\rho}\nabla p' + \nu \nabla^2 \mathbf{u} - \alpha_V (T - T_\infty)\mathbf{g}, \tag{4.16}$$

where $\nu = \mu/\rho$ is the dynamic viscosity ($\mathrm{m^2 s^{-1}}$), α_V is the volumetric thermal expansion coefficient ($\mathrm{K^{-1}}$), T_∞ is a reference temperature (K), $\mathbf{g}$ is the acceleration due to gravity ($\mathrm{m\,s^{-2}}$). The term p' is a modified pressure, and according to Tritton (1977, p. 128), is defined as

$$p' = p + \rho_\infty g z, \tag{4.17}$$

with $g \approx 9.81\,\mathrm{m\,s^{-2}}$. Details of the derivation are included in the Appendix A.2.1.

Although this approximation allows the temperature to be directly coupled to the momentum equation, it is considered valid only for small temperature variations (Mayeli & Sheard, 2021). However, it is used in works such as Tang (2017); J. Zhang, Katurji, Zawar-Reza, and Strand (2023); Lin et al. (2024), considering α_V for an ideal gas. According to Kuwana (2020), this approximation is often adopted for a simple estimation of the flow. Furthermore, in the context of outdoor fires, the work of Himoto (2022) considers this approximation for the analysis of the dynamics of hot plumes.

4.4 Turbulence

Fires exhibit a highly turbulent behavior, as illustrated in Figure 4.2. This turbulence is characterized by complex, chaotic movements, and fluctuations in the fire's intensity and direction. This behavior often results from variations in fuel distribution, thermal gradients, and environmental conditions, making accurate prediction and control challenging. Observing and studying these patterns can provide valuable information on fire dynamics and improve fire management strategies.

Turbulent flows exhibit a wide range of dynamically interacting spatial and temporal scales, particularly at high Reynolds (Re) numbers (B.4). Resolving all these scales through *Direct Numerical Simulation* (DNS) is computationally prohibitive for most practical applications because of the enormous resolution required to capture the smallest or Kolmogorov scales (Pope, 2000, p. 344). Formally, for a three-dimensional DNS simulation with N^3 mesh points, this is often reported as

$$N^3 \geq \mathrm{Re}^{9/4}.$$

Figure 4.2: Turbulent nature of fire. Image generated by Google Gemini.

Taking a modest Reynolds number $\mathrm{Re} = 10^6$, the number of points required in one dimension only (N) is

$$N^3 = (10^6)^{9/4} \implies N = 10^{6 \cdot 9/(4 \cdot 3)} \approx 31600,$$

which clearly is not easy to afford.

As alternatives to avoid the prohibitive computational cost of DNS, two main modeling strategies have been developed: the *Reynolds-Averaged Navier–Stokes* equations and *Large Eddy Simulation*. Both approaches rely on applying a filtering operation to the Navier-Stokes equations, but differ in the type of statistical treatment and in the range of turbulence scales they resolve.

Reynolds-Averaged Navier–Stokes

Reynolds-Averaged Navier–Stokes (RANS) methods provide a framework for computing the mean effects of turbulence by modeling the entire spectrum of turbulent fluctuations, offering substantial computational efficiency compared to scale-resolving approaches such as LES or DNS. The formulation is based on the Reynolds decomposition, first introduced by Osborne Reynolds (Reynolds, 1895), in which instantaneous flow variables are separated into mean and fluctuating components. Substituting this decomposition into the Navier–Stokes equations and applying a temporal averaging process eliminates the explicit time dependence of the fluctuations but produces additional correlation terms, known as the Reynolds stresses. These new terms represent momentum transport by turbulent fluctuations and require modeling through turbulence closures such as linear eddy viscosity models or more advanced Reynolds stress models (Pope, 2000).

To address some of the inherent limitations of steady RANS, most notably its inability to represent time-varying behavior in turbulent flows, the Unsteady RANS (URANS) framework was introduced. In URANS, the averaging procedure is performed on a short time scale rather than the entire flow evolution, allowing the equations to retain their unstable character while still generating Reynolds stresses that require turbulence modeling (Pope, 2000). This compromise extends the applicability of RANS methods to mildly unsteady or periodic flows, although the range of resolved turbulence dynamics remains far more limited than in scale-resolving methods such as LES.

Large Eddy Simulation

Large Eddy Simulation (LES) represents a compromise between the high fidelity but prohibitive computational cost of *Direct Numerical Simulation* (DNS) and the lower resolution of *Reynolds-Averaged Navier-Stokes* (RANS) methods. In LES, the dynamically significant large eddies, which contain most of the kinetic energy and are responsible for the bulk of momentum and scalar transport,are explicitly resolved, while the smaller, more isotropic and universal motions are modeled through a subgrid-scale (SGS) closure. The concept of filtering out unresolved turbulent scales was first introduced by Smagorinsky (1963) in the context of atmospheric modeling, with the first three-dimensional implementations later carried out by Deardorff (1970). Since then, LES has evolved into a powerful computational framework capable of capturing unsteady, anisotropic, and strongly nonlinear turbulent features with much higher fidelity than RANS, yet at a fraction of the cost of DNS (Pope, 2000; Sagaut, 2006). Its ability to resolve the spatiotemporal dynamics of turbulence makes LES particularly valuable in complex applications such as combustion, aeroacoustics, environmental and atmospheric flows, and other configurations where transient turbulent structures play a dominant role.

Turbulent flows are characterized by a continuous transfer of kinetic energy across a wide range of spatial and temporal scales, a process known as the *energy cascade*. In this cascade, energy is injected into the flow at large scales, transferred through a hierarchy of intermediate eddies, and finally dissipated as heat at the smallest viscous scales. Figure 4.3 schematically illustrates this cascade, highlighting the broad spectrum of turbulent motions and the corresponding distribution of kinetic energy across scales.

The energy cascade can be described in terms of the turbulent kinetic energy spectrum $E(k)$, which quantifies how the kinetic energy is distributed among the wavenumbers k, inversely proportional to the eddy length scale $l = 2\pi/k$. Energy is injected at large scales (low k), transferred through the inertial subrange with negligible dissipation, and ultimately converted into heat by viscous effects at the smallest scales characterized by the Kolmogorov length η. In DNS, all these scales, from the largest energy-containing eddies to the smallest dissipative ones, are explicitly resolved, providing a complete description of turbulence but at an extremely high computational cost. In contrast, LES resolves only the large-scale motions while

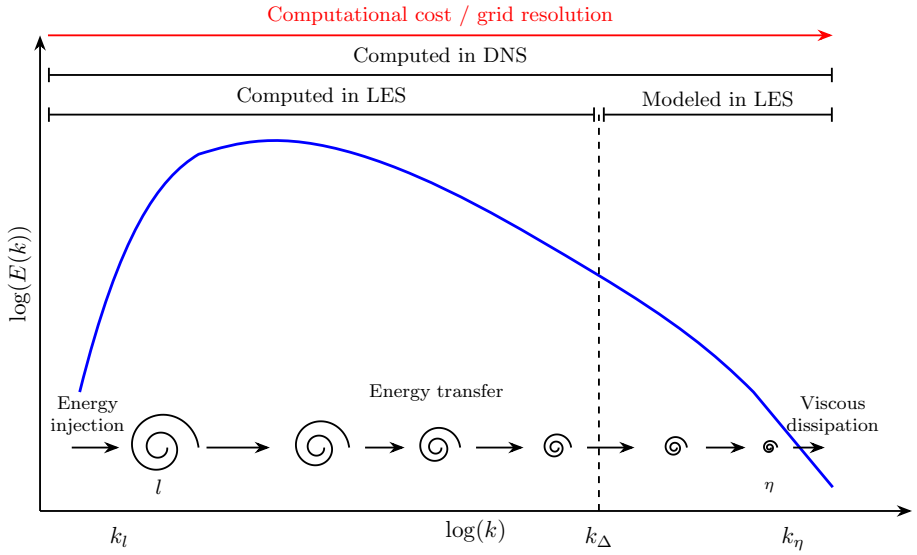

Figure 4.3: Schematic representation of the turbulent energy cascade, illustrating the transfer of kinetic energy from large, energy-containing eddies to progressively smaller scales where viscous dissipation occurs. The relative range of scales resolved by DNS and LES is also indicated.

modeling the subgrid-scale effects occurring below the filter width Δ, which separates the resolved energy-containing motions ($l > \Delta$) from the unresolved dissipative range ($l < \Delta$). This separation, closely linked to the structure of the energy cascade, highlights the fundamental trade-off between physical fidelity and computational efficiency in modern turbulence modeling.

RANS-LES

In between the previous approaches, the RANS-LES represents a hybrid turbulence modeling strategy designed to leverage the advantages of both the RANS and LES methods while mitigating their individual limitations (Benarafa, Cioni, Ducros, & Sagaut, 2006). In this approach, the computational domain is divided into zones or regions where RANS and LES are applied selectively, often based on flow characteristics or mesh resolution. Typically, RANS is used in regions where the flow is near walls or relatively steady, to reduce computational cost, while LES is applied in regions with complex, unsteady turbulence requiring higher fidelity, such as wakes, separated flows, or combustors. This hybrid method aims to optimize accuracy and efficiency by applying the most appropriate model locally, enabling practical simulations of turbulent flows with a high Reynolds number in complex geometries that would be infeasible with LES or DNS alone.

Figure 4.4 summarizes the different approaches for handling turbulence in fluid equations.

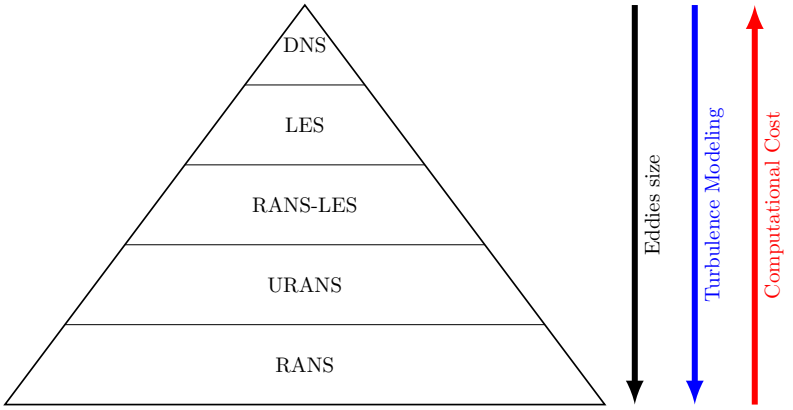

Figure 4.4: Comparison of turbulence approaches. Arrows denote increasing direction.

4.4.1 LES Filtering

Based on the state-of-the-art in wildfire modeling presented in Chapter 2, this work will focus on the LES approach.

The LES formulation relies on the application of a spatial filtering operation to the compressible Navier-Stokes equations. Filtering separates the flow field into large (resolved) and small (unresolved) scales. The filtered variable $\bar{\phi}(\mathbf{x}, t)$ is defined by a convolution with a spatial filter kernel G as follows (Poinsot & Veynante, 2012, p. 169):

$$\bar{\phi}(\mathbf{x}, t) = \int \phi(\mathbf{x}', t)\, G_\Delta(\mathbf{x} - \mathbf{x}')\, d\mathbf{x}'.$$

The filter width Δ is typically related to the local grid size and defines the smallest scale that the LES can resolve. In numerical implementations, the filtering operation is often implicit and is determined by the discretization method and the mesh resolution.

For compressible flows, a *Favre filtering* is typically employed for quantities that depend on density to avoid introducing additional correlations between density and other variables. The Favre-filtered variable $\tilde{\phi}$ is defined as:

$$\tilde{\phi} = \frac{\overline{\rho\phi}}{\bar{\rho}}.$$

Applying the spatial and Favre filtering operations to the compressible Navier-Stokes equations yields the LES equations for mass, momentum, energy, and species. These equations retain their conservative form but include additional terms that account for the effects of unresolved SGS fluctuations.

The governing equations can be written as

$$\begin{aligned}
\frac{\partial \overline{\rho}}{\partial t} + \nabla \cdot (\overline{\rho}\, \widetilde{\mathbf{u}}) &= 0 \\
\frac{\partial (\overline{\rho}\, \widetilde{\mathbf{u}})}{\partial t} + \nabla \cdot (\overline{\rho}\, \widetilde{\mathbf{u}} \otimes \widetilde{\mathbf{u}}) &= -\nabla \overline{p} + \nabla \cdot \left((\mu + \mu_{\mathrm{t}}) \left(2\widetilde{\mathbf{S}} - \frac{2}{3} (\nabla \cdot \widetilde{\mathbf{u}})\, \mathbf{I} \right) \right) + \overline{\mathbf{f}}, \\
\frac{\partial (\overline{\rho}\, \widetilde{h})}{\partial t} + \nabla \cdot \left(\overline{\rho}\, \widetilde{h}\, \widetilde{\mathbf{u}} \right) &= \frac{D\overline{p}}{Dt} + \nabla \cdot \left((k + k_{\mathrm{t}}) \nabla \widetilde{T} \right) + \widetilde{\boldsymbol{\tau}} : \nabla \widetilde{\mathbf{u}} + \overline{Q}, \\
\frac{\partial (\overline{\rho}\, \widetilde{Y_i})}{\partial t} + \nabla \cdot \left(\overline{\rho}\, \widetilde{Y_i}\, \widetilde{\mathbf{u}} \right) &= \nabla \cdot \left(\overline{\rho}\, (D_i + D_{\mathrm{t}}) \nabla \widetilde{Y_i} \right) + \overline{\dot{\omega}_i}, \\
\overline{p} &= \overline{\rho} R \widetilde{T},
\end{aligned} \tag{4.18}$$

where μ_{t}, k_{t}, D_{t} denote turbulent viscosity, thermal conductivity, and diffusivity respectively. The tensor $\widetilde{\mathbf{S}}$ is defined by

$$\tilde{\mathbf{S}} = \frac{1}{2} \left(\nabla \tilde{\mathbf{u}} + (\nabla \tilde{\mathbf{u}})^{\top} \right). \tag{4.19}$$

The presence of the SGS stress tensor and SGS heat fluxes introduces closure problems that must be addressed through appropriate subgrid-scale modeling. These models approximate the impact of unresolved scales on the resolved flow field and are critical to the success of LES. Based on Smagorinsky-Lilly analysis (Smagorinsky, 1963), the turbulent viscosity is modeled as

$$\mu_{\mathrm{t}} = \overline{\rho} (C_{\mathrm{s}} \Delta f_{\mathrm{w}})^2 |\tilde{\mathbf{S}}|, \quad |\tilde{\mathbf{S}}| = \sqrt{2\tilde{\mathbf{S}} : \tilde{\mathbf{S}}}, \tag{4.20}$$

with C_{s} the Smagorinky constant, $\Delta = \sqrt[3]{\Delta x \Delta y \Delta z}$. The Van Driest damping function f_{w} is used to reduce the effect of turbulent viscosity near a solid wall (Sagaut, 2006),

$$f_{\mathrm{w}}(x, y, z) = 1 - \exp\left(-\frac{z \rho u_{\tau}}{26 \mu} \right),$$

with,

$$u_{\tau} = \sqrt{\frac{\tau_{\mathrm{w}}}{\overline{\rho}}}, \quad \tau_{\mathrm{w}} = \sqrt{\left(\mu \frac{\partial u(x, y, 0)}{\partial z} \right)^2 + \left(\mu \frac{\partial v(x, y, 0)}{\partial z} \right)^2}.$$

The turbulent thermal conductivity is modeled using

$$k_{\mathrm{t}} = \frac{\mu_{\mathrm{t}} c_p}{\mathrm{Pr}_{\mathrm{t}}}, \tag{4.21}$$

with Pr_{t} the turbulent Prandtl number (B.5), the turbulent diffusivity is modeled with

$$D_{\mathrm{t}} = \frac{\mu_{\mathrm{t}}}{\overline{\rho}\, \mathrm{Sc}_{\mathrm{t}}}, \tag{4.22}$$

with Sc_{t} the turbulent Schmidt number (B.6).

Appendix B.4 includes the derivation of the filtered equations.

4.5 Simplified coupled wildfire-atmosphere model

The atmosphere-fire model introduced in this thesis employs the low-Mach number approximation, as outlined in Section 4.2.1, focusing on the specific assumptions and applicability discussed therein, as it is well suited for the spatial and temporal scales relevant to this study.

Moreover, further simplifications incorporate means to decrease computational demands and reduce the variables needed for the numerical solution.

The dynamics of the atmosphere is represented by the conservation of momentum from (4.13),

$$\rho\left(\frac{\partial \mathbf{u}}{\partial t} + (\mathbf{u}\cdot\nabla)\mathbf{u}\right) = -\nabla p + \nabla\cdot\boldsymbol{\tau} + \mathbf{f}, \tag{4.23}$$

and the dynamics of fire flames is described using the conservation of energy from (4.13),

$$\rho c_p\left(\frac{\partial T}{\partial t} + \mathbf{u}\cdot\nabla T\right) = \nabla\cdot(\kappa\nabla T) + q. \tag{4.24}$$

In particular, based on Weber (1991) and Asensio and Ferragut (2002), the function $\kappa = \kappa(T)$ is introduced to incorporate the radiation and conduction heat transfer mechanism. From the formulation of (4.5),

$$\mathbf{q} = \mathbf{q}_{\text{conduction}} + \mathbf{q}_{\text{radiation}} = -\kappa(T)\nabla T, \quad \kappa(T) = k + 4\sigma\delta T^3,$$

with k the thermal conductivity of fluid (W $\text{m}^{-1}\text{K}^{-1}$ or kg $\text{m}^2\text{s}^{-3}\text{K}^{-1}$), $\sigma = 5.67\times10^{-8}$ W $\text{m}^{-2}\text{K}^{-4}$ the Stefan–Boltzmann constant, and δ the optical path length (m).

The sources and sinks of temperature are included in the term q. Notice that dp_0/dt is neglected considering that the fires in this work are not in a sealed enclosure (Mell et al., 1995, 2007). The viscous dissipation term $\boldsymbol{\tau} : \nabla\mathbf{u}$, is not explicitly included in (4.24), but is partially incorporated by the turbulence modeling (4.21).

Heat source-induced temperature changes affect the density of the fluid, which manifests itself primarily as buoyant forces. These forces generate flow velocities. The coupling of temperature to the momentum equation is approached through the Boussinesq equations (Rehm & Baum, 1978). Incorporating these equations, following the studies in (Rehm & Baum, 1978; K. B. McGrattan, Rehm, & Baum, 1994; Mell et al., 2007), allows inclusion of the buoyant force as

$$\mathbf{f}_{\text{buoyancy}} = (\rho - \rho_\infty)\mathbf{g}, \tag{4.25}$$

with $\mathbf{g}$ the acceleration due to gravity (m s^{-2}) and ρ_∞ a reference density (kg m^{-3}). Assuming an ideal gas, the density of fluid is computed by the following relationship

$$\rho = \frac{\rho_\infty T_\infty}{T}, \tag{4.26}$$

with T_∞ a reference temperature (K). This expression has been derived or assumed in previous works (Mell et al., 1995; Quintiere, 2006). It is crucial to emphasize that

this expression is employed to calculate the fluid's density rather than resolving the continuity equation. The derivation (4.26) is included in the Appendix A.3.

Based on similar ideas presented by Asensio and Ferragut (2002), Mandel et al. (2008), and Eberle (2014), the consumption of solid fuel is modeled using the following simplification,

$$\frac{\partial Y}{\partial t} = -Y_{\mathrm{f}}\, Y\, K(T), \tag{4.27}$$

where $Y \in [0, 1]$ represents the solid fuel fraction and Y_{f} is the fuel disappearance rate coefficient. It is important to understand that this model represents a significant simplification of (4.6). Consequently, the coefficient Y_{f} encapsulates various characteristics of the fuel, including density and loading. The function $K(T)$ is an Arrhenius-type equation defined as

$$K(T) = A\, H\,(T - T_{\mathrm{pc}}) \exp\left(-\frac{T_{\mathrm{act}}}{T}\right),$$

with A the pre-exponential coefficient (s^{-1}), T_{pc} the phase change temperature (K), and T_{act} the activation temperature (K) (McAllister, Chen, & Fernandez-Pello, 2011, p. 53). The Heaviside step function $H(\cdot)$ is included to model both the solid and gas phases in the phenomenon. This is a rather simple model for the combustion process, and according to Batiot et al. (2021), several limitations must be considered. Despite limitations, it is widely used by simplified reaction models (R. R. Linn & Harlow, 1998; Mandel et al., 2008; Asensio & Ferragut, 2002; Eberle, Freeden, & Matthes, 2015).

Based on (Asensio & Ferragut, 2002; Morvan et al., 2018; K. Zhang et al., 2020), the interaction of temperature and solid fuel is modeled by the term q included in (4.24). In the simplified approach, this term is defined by

$$q = H_{\mathrm{C}}\, K(T) Y \rho - h_{\mathrm{c}} \alpha_{\mathrm{s}} \sigma_{\mathrm{s}}\, (T_{\mathrm{gas}} - T_{\mathrm{solid}}) + q_{\mathrm{B}}, \tag{4.28}$$

where H_{C} is the heat of combustion ($\mathrm{J\ kg}^{-1}$ or $\mathrm{m}^2\mathrm{s}^{-2}$), h_{c} the convective heat transfer coefficient ($\mathrm{kg\ s}^{-3}\mathrm{K}^{-1}$), α_{s} is the solid fuel volume fraction, and σ_{s} the surface-to-volume ratio (m^{-1}). The temperature of gas and solid are determined by the values of Y, considering the location of the solid temperature when $Y > 0$ and gas otherwise. This component of the model is only considered up to the node immediately above the Y location. Moreover, due to the extensive simplifications involved in the modeling process, the source term q_{B} is used in (4.28) to constrain the temperature within physical limits (details in sub-section 5.5.2).

Extending the ideas presented in(Reisner et al., 2000), (Mell et al., 2007), (Morvan et al., 2018), and (K. Zhang et al., 2020), the drag effect arising from the resistance of solid fuel is related to the velocity field $\mathbf{u}$, the magnitude of the speed and the fuel fraction Y, and is modeled with

$$\mathbf{f}_{\mathrm{drag}} = -\frac{1}{2} C_{\mathrm{d}}\, \alpha_{\mathrm{s}} \sigma_{\mathrm{s}}\, Y \rho \|\mathbf{u}\| \mathbf{u},$$

where C_d is the fuel drag coefficient. The momentum equation incorporates the force term $\mathbf{f}_\mathrm{IBM}$ to account for the influence of topography or solid bodies in numerical simulations using the Immersed Boundary Method (details in sub-section 5.5.1), then, the body-force term used is

$$\mathbf{f} = \mathbf{f}_\mathrm{drag} + \mathbf{f}_\mathrm{IBM}.$$

To complete the low-Mach number approximation, the temperature equation (4.24) is used to impose the velocity constraint (4.14),

$$\nabla \cdot \mathbf{u} = \frac{1}{T}\left(\frac{\partial T}{\partial t} + \mathbf{u} \cdot \nabla T\right) = \frac{1}{\rho c_p T}\left(\nabla \cdot (\kappa \nabla T) + q\right). \tag{4.29}$$

It should be highlighted that this represents a simplified form of similar expressions found in Mell et al. (1995); Bell et al. (2000); Mell et al. (2007). The expanded form of (4.29) is

$$\begin{aligned}
\nabla \cdot \mathbf{u} &= \frac{1}{\rho c_p T}\left(\nabla \cdot (\kappa \nabla T) + q\right) \\
&= \frac{1}{\rho c_p T}\left(\nabla \kappa \cdot \nabla T + \kappa \nabla^2 T + q\right) \\
&= \frac{1}{\rho c_p T}\left(\left(12\sigma\delta T^2 \nabla T\right) \cdot \nabla T + \kappa \nabla^2 T + q\right) \\
&= \frac{1}{\rho c_p T}\left(12\sigma\delta T^2 \|\nabla T\|^2 + \left(k + 4\sigma\delta T^3\right)\nabla^2 T + q\right).
\end{aligned} \tag{4.30}$$

It is important to mention that, as a first version of the work, an initial model was developed using incompressible equations (4.15), considering the Boussinesq approximation (4.16) and the simplified combustion model (4.27). This version was discarded considering the temperature restrictions indicated in sub-section 4.3.1.

4.5.1 Summary

Considering all the components described above, the mathematical model is summarized in the following lines. The variables of interest are defined in a three-dimensional space in addition to the time domain. Let $\mathbf{u}(\mathbf{x},t) = (u(\mathbf{x},t), v(\mathbf{x},t), w(\mathbf{x},t))$ and $T(\mathbf{x},t)$ be the velocity and the temperature of the fluid, respectively, and $Y(\mathbf{x},t)$ the fraction of solid fuel, defined in the spatial coordinate $\mathbf{x} = (x,y,z) \in \Omega \subset \mathbb{R}^3$, and temporal $t \in [t_{\min}, t_{\max}] \subseteq \mathbb{R}_0^+$. $\Omega = [x_{\min}, x_{\max}] \times [y_{\min}, y_{\max}] \times [z_{\min}, z_{\max}]$ represents the spatial domain where the problem is defined with boundary $\Gamma = \partial\Omega$. The simplified coupled model is defined in $\Omega \times [t_{\min}, t_{\max}]$ by:

$$\begin{aligned}
\rho\left(\frac{\partial \mathbf{u}}{\partial t} + (\mathbf{u}\cdot\nabla)\,\mathbf{u}\right) &= -\nabla p + \nabla\cdot\boldsymbol{\tau} + \mathbf{f},\\
\rho c_p\left(\frac{\partial T}{\partial t} + \mathbf{u}\cdot\nabla T\right) &= \nabla\cdot(\kappa\nabla T) + q,\\
\frac{\partial Y}{\partial t} &= -Y_{\mathrm{f}}\, Y\, K,\\
\boldsymbol{\tau} &= \mu\left(\nabla\mathbf{u} + (\nabla\mathbf{u})^{\top} - \frac{2}{3}(\nabla\cdot\mathbf{u})\mathbf{I}\right),\\
\nabla\cdot\mathbf{u} &= \frac{1}{\rho c_p T}\left(\nabla\cdot(\kappa\nabla T) + q\right),
\end{aligned} \tag{4.31}$$

with

$$\begin{aligned}
\mathbf{f}(\mathbf{u},T,Y) &= (\rho(T) - \rho_\infty)\mathbf{g} - \frac{1}{2}C_{\mathrm{d}}\,\alpha_{\mathrm{s}}\sigma_{\mathrm{s}}\,Y\rho(T)\|\mathbf{u}\|\mathbf{u} + \mathbf{f}_{\mathrm{IBM}},\\
q(T,Y) &= H_{\mathrm{C}}\,K(T)Y\rho(T) - h_{\mathrm{c}}\alpha_{\mathrm{s}}\sigma_{\mathrm{s}}\,(T_{\mathrm{gas}} - T_{\mathrm{solid}}) + q_{\mathrm{B}},\\
K(T) &= A\,H\,(T - T_{\mathrm{pc}})\exp\left(-\frac{T_{\mathrm{act}}}{T}\right),\\
\kappa(T) &= k + 4\sigma\delta T^3,\\
\rho(T) &= \frac{\rho_\infty T_\infty}{T}.
\end{aligned}$$

The gradient and Laplace operators are defined as

$$\nabla = \left(\frac{\partial}{\partial x}, \frac{\partial}{\partial y}, \frac{\partial}{\partial z}\right), \quad \nabla^2 = \frac{\partial^2}{\partial x^2} + \frac{\partial^2}{\partial y^2} + \frac{\partial^2}{\partial z^2}.$$

Boundary conditions are defined periodic on the x and y directions, with the following in the z direction,

$$\mathbf{u}(\mathbf{x},t) = \mathbf{0}, \quad \frac{\partial T(\mathbf{x},t)}{\partial z} = 0, \quad \frac{\partial Y(\mathbf{x},t)}{\partial z} = 0, \quad \text{at } z = z_{\min}, \tag{4.32}$$

and,

$$\frac{\partial \mathbf{u}(\mathbf{x},t)}{\partial z} = \mathbf{0}, \quad \frac{\partial T(\mathbf{x},t)}{\partial z} = 0, \quad \frac{\partial Y(\mathbf{x},t)}{\partial z} = 0, \quad \text{at } z = z_{\max}. \tag{4.33}$$

The initial conditions,

$$\mathbf{u}(\mathbf{x}, t_{\min}) = \mathbf{u}_0(\mathbf{x}), \quad T(\mathbf{x}, t_{\min}) = T_0(\mathbf{x}), \quad Y(\mathbf{x}, t_{\min}) = Y_0(\mathbf{x}),$$

will depend on the numerical experiments performed.

To address turbulence, the mathematical model (4.31) is solved using LES as described in Section 4.4. Henceforth, the variables in the following sections refer to the filtered variables, but the symbols $-$ and $\tilde{}$ will be omitted.

Figure 4.5 presents a diagram that delineates the components of the mathematical model.

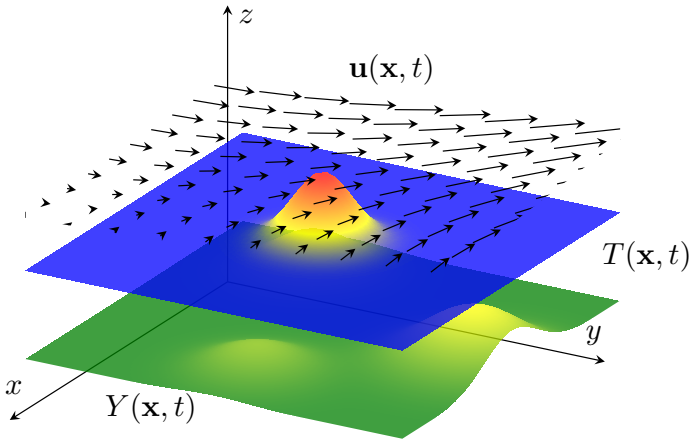

Figure 4.5: Sketch of the mathematical model components.

Chapter 5

Numerical Algorithm

There are several strategies to solve fluid flow equations in various flow regimes, ranging from incompressible to compressible flows (Peyret & Taylor, 1983; Ferziger et al., 2020). As described in Chapter 4, this work employs a numerical approach based on the low-Mach number approximation, which allows capturing variable density effects while filtering out acoustic waves and avoiding the full compressible flow complexity (Schochet, 2005; Yanaoka & Sato, 2025). The numerical solver uses an operator splitting method inspired by Chorin's projection method (Chorin, 1967, 1968) to decouple the velocity and pressure fields. Spatial derivatives are discretized using the Finite Differences Method (FDM), and the time integration can be performed through Euler's method, the Second-Order or Fourth-Order Runge-Kutta (RK) methods for improved accuracy. Furthermore, a pseudo-spectral technique is proposed for numerically solving the pressure problem that arises from the splitting approach. This combination enables efficient and accurate simulation of low-Mach number flows with variable density dynamics.

5.1 Numerical Discretization

The numerical algorithm for solving (4.31) is based on an operator splitting method over the following discrete version of the domain,

$$\begin{aligned}
x_i &= x_{\min} + i\,\Delta x, \quad i = 0, 1, \ldots, N_x, \quad \Delta x = \frac{x_{\max} - x_{\min}}{N_x}, \\
y_j &= y_{\min} + j\,\Delta x, \quad j = 0, 1, \ldots, N_y, \quad \Delta y = \frac{y_{\max} - y_{\min}}{N_y}, \\
z_k &= z_{\min} + k\,\Delta z, \quad k = 0, 1, \ldots, N_z, \quad \Delta z = \frac{z_{\max} - z_{\min}}{N_z}, \\
t_n &= t_{\min} + n\,\Delta t, \quad n = 0, 1, \ldots, N_t, \quad \Delta t = \frac{t_{\max} - t_{\min}}{N_t},
\end{aligned} \tag{5.1}$$

where, N_x, N_y, N_z and N_t are the number of intervals in x, y, z and t respectively. Figure 5.1 sketches the discrete spatial domain and the numerical stencil.

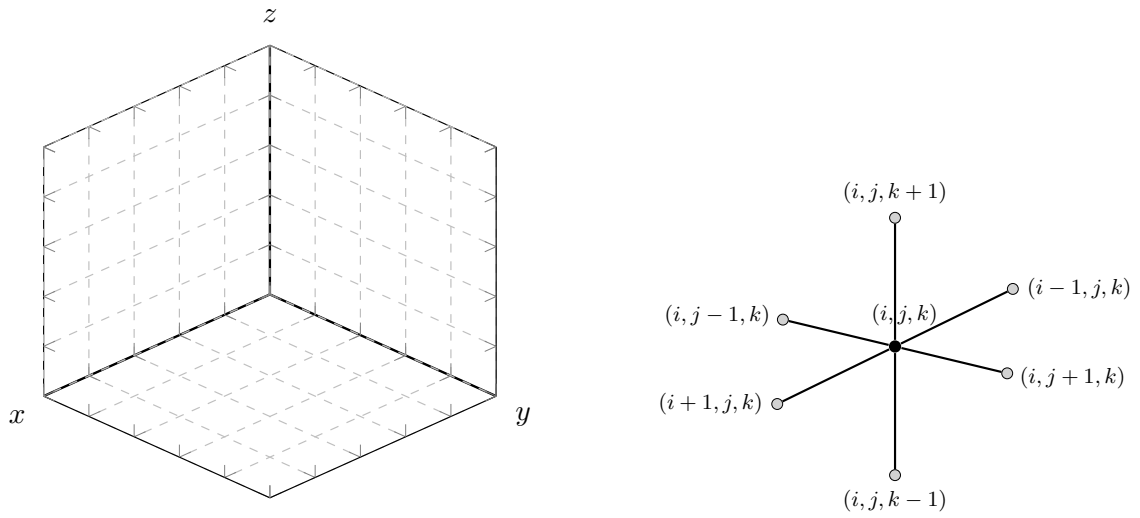

(a) Discrete domain. (b) Stencil used for indexing.

Figure 5.1: Spatial discretization.

The variable of interest ϕ in this discrete domain is defined as $\phi(x_i, y_j, z_k, t_n) = \phi^n_{i,j,k}$. For the sake of notation, subscripts i, j, k are omitted. Based on Chorin's projection method (Chorin, 1967), the following numerical scheme is proposed using a discrete version of (4.31)

$$\frac{\mathbf{u}^{n+1} - \mathbf{u}^n}{\Delta t} = \frac{1}{\rho^n}\left[- \nabla_h p^{n+1} + \nabla_h \cdot \boldsymbol{\tau}^n + \mathbf{f}(\mathbf{u}^n, T^n, Y^n)\right] - (\mathbf{u}^n \cdot \nabla_h)\mathbf{u}^n, \tag{5.2}$$

$$\frac{T^{n+1} - T^n}{\Delta t} = \frac{1}{c_p \rho^n}\left[\nabla_h \cdot (\kappa(T^n)\nabla_h T^n) + q(T^n, Y^n)\right] - \mathbf{u}^n \cdot \nabla_h T^n, \tag{5.3}$$

$$\frac{Y^{n+1} - Y^n}{\Delta t} = -Y_{\mathrm{f}} Y^n K(T^n), \tag{5.4}$$

where ∇_h denotes the discrete version of continuous ∇ operator, and depends on the variable in which they will be applied (it will be detailed in Section 5.2). The computation of (5.3) and (5.4) can be performed directly, but for (5.2) a predictor is employed for a temporal velocity field

$$\frac{\mathbf{u}^* - \mathbf{u}^n}{\Delta t} = \frac{1}{\rho^n}\Big[\nabla_h \cdot \boldsymbol{\tau}^n + \mathbf{f}(\mathbf{u}^n, T^n, Y^n)\Big] - (\mathbf{u}^n \cdot \nabla_h)\mathbf{u}^n, \tag{5.5}$$

and then the corrector step

$$\frac{\mathbf{u}^{n+1} - \mathbf{u}^*}{\Delta t} = -\frac{1}{\rho^n}\nabla_h p^{n+1}. \tag{5.6}$$

The pressure at t_{n+1} is obtained taking the divergence of (5.6),

$$\begin{aligned}
\nabla_h \cdot \left(\frac{1}{\rho^n} \nabla_h p^{n+1} \right) &= \frac{1}{\Delta t} \left(\nabla_h \cdot \mathbf{u}^* - \nabla_h \cdot \mathbf{u}^{n+1} \right) \\
\frac{1}{\rho^n} \nabla_h^2 p^{n+1} - \frac{1}{(\rho^n)^2} \nabla_h \rho^n \cdot \nabla_h p^{n+1} &= \frac{1}{\Delta t} \left(\nabla_h \cdot \mathbf{u}^* - \nabla_h \cdot \mathbf{u}^{n+1} \right) \\
\nabla_h^2 p^{n+1} - \frac{1}{\rho^n} \nabla_h \rho^n \cdot \nabla_h p^{n+1} &= \frac{\rho^n}{\Delta t} \left(\nabla_h \cdot \mathbf{u}^* - \nabla_h \cdot \mathbf{u}^{n+1} \right).
\end{aligned}$$

Since the density, temperature and fuel fraction are known for t_n and t_{n+1}, the restriction (4.29) can be used to obtain $\nabla_h \cdot \mathbf{u}^{n+1}$.

5.2 Spatial Approximation

The approximation of the gradient, divergence, and Laplacian involves spatial partial derivatives that depend on the variable to which the operator is applied. The following sub-sections detail on the discretization techniques employed, which utilize a second-order accuracy approximation. To simplify the explanation, time dependence is omitted.

Velocity

First, the viscous stress tensor is expanded as follows,

$$\nabla_h \cdot \boldsymbol{\tau} = \mu \left(\nabla_h^2 \mathbf{u} + \frac{1}{3} \nabla_h \left(\nabla_h \cdot \mathbf{u} \right) \right) + \nabla_h \mu \cdot \left(\nabla_h \mathbf{u} + \left(\nabla_h \mathbf{u} \right)^\top - \frac{2}{3} \left(\nabla_h \cdot \mathbf{u} \right) \mathbf{I} \right).$$

The Laplacian approximation for $\mathbf{u}$ is

$$\nabla_h^2 \mathbf{u} = \begin{pmatrix} \nabla_h^2 u \\ \nabla_h^2 v \\ \nabla_h^2 w \end{pmatrix},$$

with

$$\nabla_h^2 u = \frac{u_{i+1,j,k} - 2\,u_{i,j,k} + u_{i-1,j,k}}{\Delta x^2} + \frac{u_{i,j+1,k} - 2\,u_{i,j,k} + u_{i,j-1,k}}{\Delta y^2} + \frac{u_{i,j,k+1} - 2\,u_{i,j,k} + u_{i,j,k-1}}{\Delta z^2}$$

$$\nabla_h^2 v = \frac{v_{i+1,j,k} - 2\,v_{i,j,k} + v_{i-1,j,k}}{\Delta x^2} + \frac{v_{i,j+1,k} - 2\,v_{i,j,k} + v_{i,j-1,k}}{\Delta y^2} + \frac{v_{i,j,k+1} - 2\,v_{i,j,k} + v_{i,j,k-1}}{\Delta z^2}$$

$$\nabla_h^2 w = \frac{w_{i+1,j,k} - 2\,w_{i,j,k} + w_{i-1,j,k}}{\Delta x^2} + \frac{w_{i,j+1,k} - 2\,w_{i,j,k} + w_{i,j-1,k}}{\Delta y^2} + \frac{w_{i,j,k+1} - 2\,w_{i,j,k} + w_{i,j,k-1}}{\Delta z^2}.$$

The velocity gradient is approximated with

$$\nabla_h \mathbf{u} = \begin{pmatrix} \nabla_h u \\ \nabla_h v \\ \nabla_h w \end{pmatrix} = \begin{pmatrix} \dfrac{u_{i+1,j,k} - u_{i-1,j,k}}{2\Delta x} & \dfrac{u_{i,j+1,k} - u_{i,j-1,k}}{2\Delta y} & \dfrac{u_{i,j,k+1} - u_{i,j,k-1}}{2\Delta z} \\ \dfrac{v_{i+1,j,k} - v_{i-1,j,k}}{2\Delta x} & \dfrac{v_{i,j+1,k} - v_{i,j-1,k}}{2\Delta y} & \dfrac{v_{i,j,k+1} - v_{i,j,k-1}}{2\Delta z} \\ \dfrac{w_{i+1,j,k} - w_{i-1,j,k}}{2\Delta x} & \dfrac{w_{i,j+1,k} - w_{i,j-1,k}}{2\Delta y} & \dfrac{w_{i,j,k+1} - w_{i,j,k-1}}{2\Delta z} \end{pmatrix}. \tag{5.7}$$

The convective term approximation is based on the second-order upwind scheme,

$$(\mathbf{u} \cdot \nabla_h)\,\mathbf{u} = \begin{pmatrix} u^+_{i,j,k} u^-_x + u^-_{i,j,k} u^+_x + v^+_{i,j,k} u^-_y + v^-_{i,j,k} u^+_y + w^+_{i,j,k} u^-_z + w^-_{i,j,k} u^+_z \\ u^+_{i,j,k} v^-_x + u^-_{i,j,k} v^+_x + v^+_{i,j,k} v^-_y + v^-_{i,j,k} v^+_y + w^+_{i,j,k} v^-_z + w^-_{i,j,k} v^+_z \\ u^+_{i,j,k} w^-_x + u^-_{i,j,k} w^+_x + v^+_{i,j,k} w^-_y + v^-_{i,j,k} w^+_y + w^+_{i,j,k} w^-_z + w^-_{i,j,k} w^+_z \end{pmatrix},$$

where

$$\begin{aligned} u^+_{i,j,k} &= \max(0, u_{i,j,k}), \quad & u^-_{i,j,k} &= \min(0, u_{i,j,k}), \\ v^+_{i,j,k} &= \max(0, v_{i,j,k}), \quad & v^-_{i,j,k} &= \min(0, v_{i,j,k}), \\ w^+_{i,j,k} &= \max(0, w_{i,j,k}), \quad & w^-_{i,j,k} &= \min(0, w_{i,j,k}), \end{aligned}$$

with,

$$\begin{aligned} u^+_x &= \frac{-u_{i+2,j,k} + 4u_{i+1,j,k} - 3u_{i,j,k}}{2\Delta x}, \quad & u^-_x &= \frac{3u_{i,j,k} - 4u_{i-1,j,k} + u_{i-2,j,k}}{2\Delta x}, \\ u^+_y &= \frac{-u_{i,j+2,k} + 4u_{i,j+1,k} - 3u_{i,j,k}}{2\Delta y}, \quad & u^-_y &= \frac{3u_{i,j,k} - 4u_{i,j-1,k} + u_{i,j-2,k}}{2\Delta y}, \\ u^+_z &= \frac{-u_{i,j,k+2} + 4u_{i,j,k+1} - 3u_{i,j,k}}{2\Delta z}, \quad & u^-_z &= \frac{3u_{i,j,k} - 4u_{i,j,k-1} + u_{i,j,k-2}}{2\Delta z}, \\ v^+_x &= \frac{-v_{i+2,j,k} + 4v_{i+1,j,k} - 3v_{i,j,k}}{2\Delta x}, \quad & v^-_x &= \frac{3v_{i,j,k} - 4v_{i-1,j,k} + v_{i-2,j,k}}{2\Delta x}, \\ v^+_y &= \frac{-v_{i,j+2,k} + 4v_{i,j+1,k} - 3v_{i,j,k}}{2\Delta y}, \quad & v^-_y &= \frac{3v_{i,j,k} - 4v_{i,j-1,k} + v_{i,j-2,k}}{2\Delta y}, \\ v^+_z &= \frac{-v_{i,j,k+2} + 4v_{i,j,k+1} - 3v_{i,j,k}}{2\Delta z}, \quad & v^-_z &= \frac{3v_{i,j,k} - 4v_{i,j,k-1} + v_{i,j,k-2}}{2\Delta z}, \end{aligned}$$

and

$$\begin{aligned} w^+_x &= \frac{-w_{i+2,j,k} + 4w_{i+1,j,k} - 3w_{i,j,k}}{2\Delta x}, \quad & w^-_x &= \frac{3w_{i,j,k} - 4w_{i-1,j,k} + w_{i-2,j,k}}{2\Delta x}, \\ w^+_y &= \frac{-w_{i,j+2,k} + 4w_{i,j+1,k} - 3w_{i,j,k}}{2\Delta y}, \quad & w^-_y &= \frac{3w_{i,j,k} - 4w_{i,j-1,k} + w_{i,j-2,k}}{2\Delta y}, \end{aligned}$$

$$w_z^+ = \frac{-w_{i,j,k+2} + 4w_{i,j,k+1} - 3w_{i,j,k}}{2\Delta z}, \quad w_z^- = \frac{3w_{i,j,k} - 4w_{i,j,k-1} + w_{i,j,k-2}}{2\Delta z}.$$

For the right-hand side of (5.21), we approximate the divergence of the temporal velocity $\mathbf{u}^*$ as

$$\nabla_h \cdot \mathbf{u}^* = \frac{{u^*}_{i+\frac{1}{2},j,k} - {u^*}_{i-\frac{1}{2},j,k}}{\Delta x} + \frac{{v^*}_{i,j+\frac{1}{2},k} - {v^*}_{i,j-\frac{1}{2}}, k}{\Delta y} + \frac{{w^*}_{i,j,k+\frac{1}{2}} - {w^*}_{i,j,k-\frac{1}{2}}}{\Delta z},$$

with

$${u^*}_{i+\frac{1}{2},j,k} = \frac{{u^*}_{i+1,j,k} + {u^*}_{i,j,k}}{2}, \quad {u^*}_{i-\frac{1}{2},j,k} = \frac{{u^*}_{i,j,k} + {u^*}_{i-1,j,k}}{2},$$

$${v^*}_{i,j+\frac{1}{2},k} = \frac{{v^*}_{i,j+1,k} + {v^*}_{i,j,k}}{2}, \quad {v^*}_{i,j-\frac{1}{2},k} = \frac{{v^*}_{i,j,k} + {v^*}_{i,j-1,k}}{2},$$

and,

$${w^*}_{i,j,k+\frac{1}{2}} = \frac{{w^*}_{i,j,k+1} + {w^*}_{i,j,k}}{2}, \quad {w^*}_{i,j,k-\frac{1}{2}} = \frac{{w^*}_{i,j,k} + {w^*}_{i,j,k-1}}{2},$$

to reduce the odd-even oscillations.

Temperature

The Laplacian is approximated with

$$\nabla_h^2 T = \frac{T_{i+1,j,k} - 2\,T_{i,j,k} + T_{i-1,j,k}}{\Delta x^2} + \frac{T_{i,j+1,k} - 2\,T_{i,j,k} + T_{i,j-1,k}}{\Delta y^2} + \frac{T_{i,j,k+1} - 2\,T_{i,j,k} + T_{i,j,k-1}}{\Delta z^2}.$$

For the gradient, central difference is used,

$$\nabla_h T = \left(\frac{T_{i+1,j,k} - T_{i-1,j,k}}{2\,\Delta x}, \frac{T_{i,j+1,k} - T_{i,j-1,k}}{2\,\Delta y}, \frac{T_{i,j,k+1} - T_{i,j,k-1}}{2\,\Delta z} \right),$$

Additionally, the convective term is approximated with an upwind-based scheme as used for velocity,

$$\mathbf{u} \cdot \nabla_h T = u_{i,j,k}^+ T_x^- + u_{i,j,k}^- T_x^+ + v_{i,j,k}^+ T_y^- + v_{i,j,k}^- T_y^+ + w_{i,j,k}^+ T_z^- + w_{i,j,k}^- T_z^+$$

where,

$$T_x^+ = \frac{-T_{i+2,j,k} + 4T_{i+1,j,k} - 3T_{i,j,k}}{2\Delta x}, \quad T_x^- = \frac{3T_{i,j,k} - 4T_{i-1,j,k} + T_{i-2,j,k}}{2\Delta x},$$

$$T_y^+ = \frac{-T_{i,j+2,k} + 4T_{i,j+1,k} - 3T_{i,j,k}}{2\Delta y}, \quad T_y^- = \frac{3T_{i,j,k} - 4T_{i,j-1,k} + T_{i,j-2,k}}{2\Delta y},$$

$$T_z^+ = \frac{-T_{i,j,k+2} + 4T_{i,j,k+1} - 3T_{i,j,k}}{2\Delta z}, \quad T_z^- = \frac{3T_{i,j,k} - 4T_{i,j,k-1} + T_{i,j,k-2}}{2\Delta z}.$$

Density

The density gradient is computed using the second-order central finite difference,

$$\nabla_h \rho = \left(\frac{\rho_{i+1,j,k} - \rho_{i-1,j,k}}{2\,\Delta x}, \frac{\rho_{i,j+1,k} - \rho_{i,j-1,k}}{2\,\Delta y}, \frac{\rho_{i,j,k+1} - \rho_{i,j,k-1}}{2\,\Delta z} \right).$$

Pressure

The pressure gradient is computed using the second-order central finite difference as follows,

$$\nabla_h p = \left(\frac{p_{i+1,j,k} - p_{i-1,j,k}}{2\,\Delta x}, \frac{p_{i,j+1,k} - p_{i,j-1,k}}{2\,\Delta y}, \frac{p_{i,j,k+1} - p_{i,j,k-1}}{2\,\Delta z} \right).$$

Boundary nodes

To preserve second-order accuracy in the z direction, the following schemes are used at the boundary nodes and nodes near the boundary. First partial derivative,

$$\left.\frac{\partial \phi}{\partial z}\right|_{(x_i,y_j,z_k)} \approx \frac{-\phi_{i,j,k+2} + 4\phi_{i,j,k+1} - 3\phi_{i,j,k}}{2\Delta z}, \quad \left.\frac{\partial \phi}{\partial z}\right|_{(x_i,y_j,z_k)} \approx \frac{3\phi_{i,j,k} - 4\phi_{i,j,k-1} + \phi_{i,j,k-2}}{2\Delta z}.$$

Second partial derivative,

$$\left.\frac{\partial^2 \phi}{\partial z^2}\right|_{(x_i,y_j,z_k)} \approx \frac{-\phi_{i,j,k+3} + 4\phi_{i,j,k+2} - 5\phi_{i,j,k+1} + 2\phi_{i,j,k}}{\Delta z^2}, \quad \left.\frac{\partial^2 \phi}{\partial z^2}\right|_{(x_i,y_j,z_k)} \approx \frac{2\phi_{i,j,k} - 5\phi_{i,j,k-1} + 4\phi_{i,j,k-2} - \phi_{i,j,}}{\Delta z^2}$$

They are adjusted for each field according to the location of the evaluated node.

Boundary conditions

Regarding boundary conditions, the values for the variable ϕ are assigned based on the specific type of condition applied. In cases using the Dirichlet condition, the values are set directly at the boundary nodes. When employing the Neumann condition, a forward difference scheme with second-order accuracy is utilized for the bottom,

$$\frac{-\phi_{i,j,2} + 4\,\phi_{i,j,1} - 3\,\phi_{i,j,0}}{2\,\Delta z} = 0 \implies \phi_{i,j,0} = \frac{4\,\phi_{i,j,1} - \phi_{i,j,2}}{3},$$

and using the backward difference method in a similar fashion for the top

$$\frac{3\,\phi_{i,j,N_z} - 4\,\phi_{i,j,N_z-1} + \phi_{i,j,N_z-2}}{2\,\Delta z} = 0 \implies \phi_{i,j,N_z} = \frac{4\,\phi_{i,j,N_z-1} - \phi_{i,j,N_z-2}}{3},$$

both approximations for $i = 0, 1, \ldots, N_x$, $j = 0, 1, \ldots, N_y$.

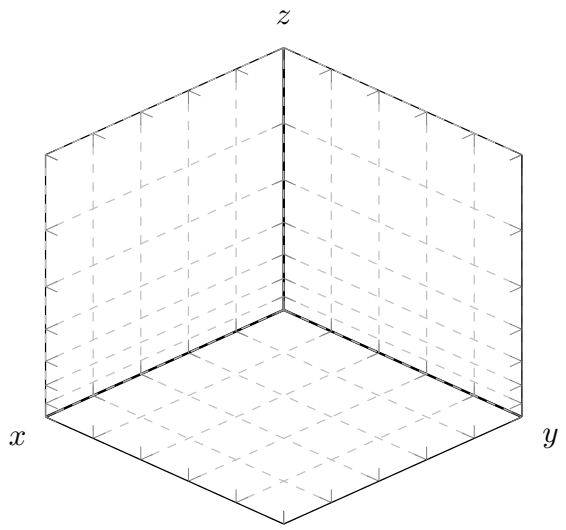

Figure 5.2: Discrete grid with non-uniform vertical axis.

5.2.1 Non-uniform grid

Implementing a non-uniform grid aims to decrease the computational effort required for handling the three-dimensional spatial domain, particularly in the vertical coordinate z. Furthermore, this method improves the resolution details closer to the bottom of the domain, directly influencing the turbulent viscosity. Figure 5.2 presents the non-uniform spatial domain in the vertical axis.

The stencils presented in the next sub-sections, will be used for the numerical approximation of $\partial/\partial z$ and $\partial^2/\partial z^2$ referenced in section 5.2.

Definitions

Let z_k be a set of $N_z{+}1$ nodes. Defining $\Delta z_k = z_{k+1} - z_k$, with $k = 0, \ldots, N_z{-}1$, where Δz_k may differ from Δz_{k+1}. Considering the variable of interest ϕ evaluated at node z_k with the following notation $\phi(z_k) = \phi_k$. It is important to note that for the $N_z + 1$ nodes there are N_z intervals Δz_k. The finite difference schemes have been derived from the Taylor series expansion for central differences and computing the derivatives of Lagrange polynomial interpolation for forward and backward differences (Sauer, 2017). The details of the derivations are given in the Appendix C.3.1.

First derivatives

Following the stated in Section 5.2, the numerical approximation follows a second-order finite differences to approximate the first partial derivatives.

The forward difference is defined as

$$\phi'_k = -\frac{2\Delta z_k + \Delta z_{k+1}}{\Delta z_k\,(\Delta z_k + \Delta z_{k+1})}\phi_k + \frac{\Delta z_k + \Delta z_{k+1}}{\Delta z_k \Delta z_{k+1}}\phi_{k+1} - \frac{\Delta z_k}{\Delta z_{k+1}\,(\Delta z_k + \Delta z_{k+1})}\phi_{k+2}, \tag{5.8}$$

for $k = 0, \ldots, N_z - 2$.

The backward difference is

$$\phi'_k = \frac{\Delta z_{k-1}}{\Delta z_{k-2}\,(\Delta z_{k-2} + \Delta z_{k-1})}\phi_{k-2} - \frac{\Delta z_{k-2} + \Delta z_{k-1}}{\Delta z_{k-2}\Delta z_{k-1}}\phi_{k-1} + \frac{\Delta z_{k-2} + 2\Delta z_{k-1}}{\Delta z_{k-1}\,(\Delta z_{k-2} + \Delta z_{k-1})}\phi_k, \tag{5.9}$$

for $k = 2, \ldots, N_z$.

The central difference is computed with

$$\phi'_k = \frac{\phi_{k+1} - \phi_{k-1}}{\Delta z_{k-1} + \Delta z_k}, \quad k = 1, \ldots, N_z - 1. \tag{5.10}$$

Using (5.8), (5.9), and (5.10), the first derivative is computed with

$$\phi'_0 = -\frac{2\Delta z_0 + \Delta z_1}{\Delta z_0\,(\Delta z_0 + \Delta z_1)}\phi_0 + \frac{\Delta z_0 + \Delta z_1}{\Delta z_0 \Delta z_1}\phi_1 - \frac{\Delta z_0}{\Delta z_1\,(\Delta z_0 + \Delta z_1)}\phi_2,$$

$$\phi'_k = \frac{\phi_{k+1} - \phi_{k-1}}{\Delta z_{k-1} + \Delta z_k}, \quad \text{for } k = 1, \ldots, N_z - 1,$$

and,

$$\begin{aligned}\phi'_{N_z} = &\frac{\Delta z_{N_z-1}}{\Delta z_{N_z-2}\,(\Delta z_{N_z-2} + \Delta z_{N_z-1})}\phi_{N_z-2} \\ &- \frac{\Delta z_{N_z-2} + \Delta z_{N_z-1}}{\Delta z_{N_z-2}\Delta z_{N_z-1}}\phi_{N_z-1} \\ &+ \frac{\Delta z_{N_z-2} + 2\Delta z_{N_z-1}}{\Delta z_{N_z-1}\,(\Delta z_{N_z-2} + \Delta z_{N_z-1})}\phi_{N_z}.\end{aligned}$$

Second derivative

As in the previous sub-section the second-order finite differences are used to approximate the second derivative.

The forward difference is computed as

$$\begin{aligned}\phi''_k = &\frac{6\Delta z_k + 4\Delta z_{k+1} + 2\Delta z_{k+2}}{\Delta z_k(\Delta z_k + \Delta z_{k+1})(\Delta z_k + \Delta z_{k+1} + \Delta z_{k+2})}\phi_k \\ &- \frac{4\Delta z_k + 4\Delta z_{k+1} + 2\Delta z_{k+2}}{\Delta z_k \Delta z_{k+1}(\Delta z_{k+1} + \Delta z_{k+2})}\phi_{k+1} \\ &+ \frac{4\Delta z_k + 2\Delta z_{k+1} + 2\Delta z_{k+2}}{\Delta z_{k+1}\Delta z_{k+2}(\Delta z_k + \Delta z_{k+1})}\phi_{k+2} \\ &- \frac{4\Delta z_k + 2\Delta z_{k+1}}{\Delta z_{k+2}(\Delta z_{k+1} + \Delta z_{k+2})(\Delta z_k + \Delta z_{k+1} + \Delta z_{k+2})}\phi_{k+3},\end{aligned} \tag{5.11}$$

for $k = 0, \ldots, N_z - 3$.

The backward difference is

$$\begin{aligned}\phi''_k = &-\frac{2\Delta z_{k-2} + 4\Delta z_{k-1}}{\Delta z_{k-3}(\Delta z_{k-3} + \Delta z_{k-2})(\Delta z_{k-3} + \Delta z_{k-2} + \Delta z_{k-1})}\phi_{k-3} \\ &+ \frac{2\Delta z_{k-3} + 2\Delta z_{k-2} + 4\Delta z_{k-1}}{\Delta z_{k-3}\Delta z_{k-2}(\Delta z_{k-2} + \Delta z_{k-1})}\phi_{k-2} \\ &- \frac{2\Delta z_{k-3} + 4\Delta z_{k-2} + 4\Delta z_{k-1}}{\Delta z_{k-2}\Delta z_{k-1}(\Delta z_{k-3} + \Delta z_{k-2})}\phi_{k-1} \\ &+ \frac{2\Delta z_{k-3} + 4\Delta z_{k-2} + 6\Delta z_{k-1}}{\Delta z_{k-1}(\Delta z_{k-2} + \Delta z_{k-1})(\Delta z_{k-3} + \Delta z_{k-2} + \Delta z_{k-1})}\phi_k,\end{aligned} \tag{5.12}$$

for $k = 3, \ldots, N_z$.

The central difference is

$$\phi''_k = \frac{2}{\Delta z_{k-1}\left(\Delta z_{k-1} + \Delta z_k\right)}\phi_{k-1} - \frac{2}{\Delta z_{k-1}\Delta z_k}\phi_k + \frac{2}{\Delta z_k\left(\Delta z_{k-1} + \Delta z_k\right)}\phi_{k+1}, \tag{5.13}$$

for $k = 1, \ldots, N_z - 1$.

The discrete second derivative is computed using (5.11), (5.12), and (5.13) as follows,

$$\begin{aligned}\phi''_0 = &\frac{6\Delta z_0 + 4\Delta z_1 + 2\Delta z_2}{\Delta z_0(\Delta z_0 + \Delta z_1)(\Delta z_0 + \Delta z_1 + \Delta z_2)}\phi_0 \\ &- \frac{4\Delta z_0 + 4\Delta z_1 + 2\Delta z_2}{\Delta z_0\Delta z_1(\Delta z_1 + \Delta z_2)}\phi_1 \\ &+ \frac{4\Delta z_0 + 2\Delta z_1 + 2\Delta z_2}{\Delta z_1\Delta z_2(\Delta z_0 + \Delta z_1)}\phi_2 \\ &- \frac{4\Delta z_0 + 2\Delta z_1}{\Delta z_2(\Delta z_1 + \Delta z_2)(\Delta z_0 + \Delta z_1 + \Delta z_2)}\phi_3,\end{aligned}$$

$$\phi''_k = \frac{2}{\Delta z_{k-1}\left(\Delta z_{k-1} + \Delta z_k\right)}\phi_{k-1} - \frac{2}{\Delta z_{k-1}\Delta z_k}\phi_k + \frac{2}{\Delta z_k\left(\Delta z_{k-1} + \Delta z_k\right)}\phi_{k+1},$$

for $k = 1, \ldots, N_z - 1$, and,

$$\begin{aligned}\phi''_{N_z} = &-\frac{2\Delta z_{N_z-2} + 4\Delta z_{N_z-1}}{\Delta z_{N_z-3}(\Delta z_{N_z-3} + \Delta z_{N_z-2})(\Delta z_{N_z-3} + \Delta z_{N_z-2} + \Delta z_{N_z-1})}\phi_{N_z-3} \\ &+ \frac{2\Delta z_{N_z-3} + 2\Delta z_{N_z-2} + 4\Delta z_{N_z-1}}{\Delta z_{N_z-3}\Delta z_{N_z-2}(\Delta z_{N_z-2} + \Delta z_{N_z-1})}\phi_{N_z-2} \\ &- \frac{2\Delta z_{N_z-3} + 4\Delta z_{N_z-2} + 4\Delta z_{N_z-1}}{\Delta z_{N_z-2}\Delta z_{N_z-1}(\Delta z_{N_z-3} + \Delta z_{N_z-2})}\phi_{N_z-1} \\ &+ \frac{2\Delta z_{N_z-3} + 4\Delta z_{N_z-2} + 6\Delta z_{N_z-1}}{\Delta z_{N_z-1}(\Delta z_{N_z-2} + \Delta z_{N_z-1})(\Delta z_{N_z-3} + \Delta z_{N_z-2} + \Delta z_{N_z-1})}\phi_{N_z}.\end{aligned}$$

5.3 Time Approximation

The integration in time is based on numerical methods for dynamical systems or initial value problems. Taking into account equations (5.2), (5.3) and (5.4) the following initial value problem is defined

$$\frac{d}{dt}\boldsymbol{v}(t) = \mathbf{F}\left(t, \boldsymbol{v}(t)\right), \quad \boldsymbol{v}(t) = \left(\mathbf{u}(t), T(t), Y(t)\right)^{\top} \tag{5.14}$$

where $\boldsymbol{v}(t)$ represents the continuous in time variables of interest, and $\mathbf{F}\left(t, \boldsymbol{v}(t)\right)$ is the right-hand side of the proposed numerical scheme. Defining $\mathbf{v}^n = \left(\mathbf{u}^n, T^n, Y^n\right)^{\top}$ as the approximation of $\boldsymbol{v}$ in discrete time t_n, that is, $\mathbf{v}^n \approx \boldsymbol{v}(t_n) = \left(\mathbf{u}(t_n), T(t_n), Y(t_n)\right)^{\top}$. The calculation of $\mathbf{v}^{n+1}$ must consider the intermediate velocity $\mathbf{u}^*$, since the final velocity $\mathbf{u}$ is calculated after the corrector step (5.6). This approximation is denoted as $\mathbf{v}^* = (\mathbf{u}^*, T, Y)$.

There is a wide range of numerical methods to solve (5.14), and the ones implemented in this work are described below.

Euler Method

The Euler Method is the base numerical integration approach used in this work. It computes the values of $\mathbf{v}^*$ as,

$$\mathbf{v}^* = \mathbf{v}^n + \Delta t\, \mathbf{F}\left(t_n, \mathbf{v}^n\right). \tag{5.15}$$

This method has a temporal truncation error of $\mathcal{O}(\Delta t)$ (Sauer, 2017).

Runge-Kutta Method

This study also applies two explicit Runge-Kutta (RK) methods. The initial technique used is the second-order method, which is calculated as

$$\mathbf{v}^* = \mathbf{v}^n + \frac{\Delta t}{2}(\mathbf{k}_1 + \mathbf{k}_2) \tag{5.16}$$

where

$$\begin{aligned} \mathbf{k}_1 &= \mathbf{F}\left(t_n, \mathbf{v}^n\right), \\ \mathbf{k}_2 &= \mathbf{F}\left(t_n + \Delta t, \mathbf{v}^n + \Delta t\, \mathbf{k}_1\right). \end{aligned} \tag{5.17}$$

This method has a temporal truncation error of $\mathcal{O}(\Delta t^2)$ (Sauer, 2017).

Additionally, the fourth-order method is included and computed as

$$\mathbf{v}^* = \mathbf{v}^n + \frac{\Delta t}{6}(\mathbf{k}_1 + 2\,\mathbf{k}_2 + 2\,\mathbf{k}_3 + \mathbf{k}_4) \tag{5.18}$$

where

$$\begin{aligned}
\mathbf{k}_1 &= \mathbf{F}\left(t_n, \mathbf{v}^n\right), \\
\mathbf{k}_2 &= \mathbf{F}\left(t_n + \frac{\Delta t}{2}, \mathbf{v}^n + \frac{\Delta t}{2}\mathbf{k}_1\right), \\
\mathbf{k}_3 &= \mathbf{F}\left(t_n + \frac{\Delta t}{2}, \mathbf{v}^n + \frac{\Delta t}{2}\mathbf{k}_2\right), \\
\mathbf{k}_4 &= \mathbf{F}\left(t_n + \Delta t, \mathbf{v}^n + \Delta t\ \mathbf{k}_3\right).
\end{aligned} \tag{5.19}$$

This method has a temporal truncation error of $\mathcal{O}(\Delta t^4)$ (Sauer, 2017).

It is important to note that the proposed numerical scheme has an order of $\mathcal{O}(\Delta t)$, as the correction step restricts the truncation error associated with the velocity field. However, utilizing higher-order integration methods improves the stability of the approximations, offering flexibility in choosing Δt (Trefethen, 2000).

5.4 Pressure Solver

To address the pressure problem,

$$\nabla_h^2 p^{n+1} - \frac{1}{\rho^n}\nabla_h \rho^n \cdot \nabla_h p^{n+1} = \frac{\rho^n}{\Delta t}\left(\nabla_h \cdot \mathbf{u}^* - \nabla_h \cdot \mathbf{u}^{n+1}\right), \tag{5.20}$$

a hybrid approach is proposed, which employs the Fourier transform for the periodic x-axis and y-axis, and applies FDM for the z-axis. This strategy emerges from the possibility of computing the Fast Fourier Transform (FFT), algorithm implemented by several optimized libraries. This FFT-FD method has been used for weather applications (Schumann & Sweet, 1988; Maronga et al., 2015).

The method derivation starts solving the following Poisson equation,

$$\nabla^2 p = f, \tag{5.21}$$

with periodic boundary conditions in $x - y$ and the following boundary conditions in z

$$\frac{\partial p}{\partial z}(\mathbf{x}, t) = p_{\text{bottom}}, \qquad \text{at } z = z_{\min}, \tag{5.22a}$$

$$p(\mathbf{x}, t) = p_{\text{top}}, \qquad \text{at } z = z_{\max}. \tag{5.22b}$$

The approximation of the variable of interest in the discrete domain (5.1) is denoted by $\phi_{i,j,k} = \phi(x_i, y_j, z_k)$. In this approach, all nodes in the x and y directions are considered in the FFT transform as presented in Figure 5.3.

Then, the Discrete Fourier Transform (DFT) and its inverse (IDFT) are defined as

$$\hat{\phi}_{r,s,k} = \sum_{i=0}^{N_x-1}\sum_{j=0}^{N_y-1} \phi_{i,j,k} \exp\left(-2\pi \mathrm{i}\left(\frac{ir}{N_x} + \frac{js}{N_y}\right)\right), \tag{5.23}$$

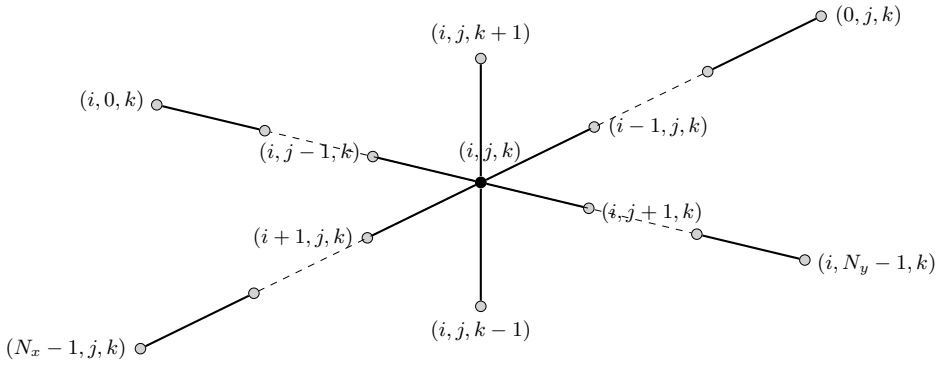

Figure 5.3: FFT-FD stencil

for $r = 0, \ldots, N_x - 1$, $s = 0, \ldots, N_y - 1$, $k = 1, \ldots, N_z - 1$, and,

$$\phi_{i,j,k} = \frac{1}{N_x\, N_y} \sum_{r=0}^{N_x-1} \sum_{s=0}^{N_y-1} \hat{\phi}_{r,s,k} \exp\left(2\pi \mathrm{i} \left(\frac{ir}{N_x} + \frac{js}{N_y}\right)\right), \tag{5.24}$$

for $i = 0, \ldots, N_x - 1$, $j = 0, \ldots, N_y - 1$, $k = 1, \ldots, N_z - 1$, respectively, with $\mathrm{i}^2 = -1$. $\hat{\phi}_{r,s,k}$ represents the function $\phi_{i,j,k}$ in the discrete Fourier domain, but only calculated in the direction of xy. Note that the equations for $k = 0$ and $k = N_z$ are not included because they represent the boundary conditions and their values are incorporated in the equations for $k = 1$ and $k = N_z - 1$. Using this approach, the second derivative with respect to x can be approximated by,

$$\left.\frac{\partial^2 \phi}{\partial x^2}\right|_{(x_i,y_j,z_k)} \approx \frac{1}{N_x\, N_y} \sum_{r=0}^{N_x-1} \sum_{s=0}^{N_y-1} \left(\frac{2\pi \mathrm{i}}{N_x} r\right)^2 \hat{\phi}_{r,s,k} \exp\left(2\pi \mathrm{i} \left(\frac{ir}{N_x} + \frac{js}{N_y}\right)\right), \tag{5.25}$$

and the second derivative with respect to y as,

$$\left.\frac{\partial^2 \phi}{\partial y^2}\right|_{(x_i,y_j,z_k)} \approx \frac{1}{N_x\, N_y} \sum_{r=0}^{N_x-1} \sum_{s=0}^{N_y-1} \left(\frac{2\pi \mathrm{i}}{N_y} s\right)^2 \hat{\phi}_{r,s,k} \exp\left(2\pi \mathrm{i} \left(\frac{ir}{N_x} + \frac{js}{N_y}\right)\right), \tag{5.26}$$

both, (5.25) and (5.26), for $i = 0, \ldots, N_x - 1$, $j = 0, \ldots, N_y - 1$, and $k = 1, \ldots, N_z - 1$. Replacing (5.24), (5.25), and (5.26) into (5.21),

$$\begin{aligned} \frac{1}{N_x\, N_y} \sum_{r=0}^{N_x-1} \sum_{s=0}^{N_y-1} - \left[\left(\frac{2\pi}{N_x} r\right)^2 + \left(\frac{2\pi}{N_y} s\right)^2\right] \hat{p}_{r,s,k} \exp\left(2\pi \mathrm{i} \left(\frac{ir}{N_x} + \frac{js}{N_y}\right)\right) \\ \left.\frac{\partial^2}{\partial z^2}\right|_{(x_i,y_j,z_k)} \left[\frac{1}{N_x\, N_y} \sum_{r=0}^{N_x-1} \sum_{s=0}^{N_y-1} \hat{p}_{r,s,k} \exp\left(2\pi \mathrm{i} \left(\frac{ir}{N_x} + \frac{js}{N_y}\right)\right)\right] \\ = \frac{1}{N_x\, N_y} \sum_{r=0}^{N_x-1} \sum_{s=0}^{N_y-1} \hat{f}_{r,s,k} \exp\left(2\pi \mathrm{i} \left(\frac{ir}{N_x} + \frac{js}{N_y}\right)\right), \end{aligned}$$

and after grouping and reordering terms,

$$\frac{1}{N_x\,N_y}\sum_{r=0}^{N_x-1}\sum_{s=0}^{N_y-1}P_{r,s,k}\exp\left(2\pi\mathrm{i}\left(\frac{ir}{N_x}+\frac{js}{N_y}\right)\right)=0,$$

with

$$P_{r,s,k}=-\left[\left(\frac{2\pi}{N_x}r\right)^2+\left(\frac{2\pi}{N_y}s\right)^2\right]\hat{p}_{r,s,k}+\left.\frac{\partial^2\hat{p}_{r,s,k}}{\partial z^2}\right|_{(x_i,y_j,z_k)}-\hat{f}_{r,s,k}.$$

Notice that the term $P_{r,s,k}$ can be interpreted as the coefficient in the Fourier space for each k. From the orthogonality of the discrete complex exponential, each coefficient $P_{r,s,k}$ must vanish (Trefethen, 2000),

$$P_{r,s,k}=-\left[\left(\frac{2\pi}{N_x}r\right)^2+\left(\frac{2\pi}{N_y}s\right)^2\right]\hat{p}_{r,s,k}+\left.\frac{\partial^2\hat{p}_{r,s,k}}{\partial z^2}\right|_{(x_i,y_j,z_k)}-\hat{f}_{r,s,k}=0,$$

therefore,

$$-\left[\left(\frac{2\pi}{N_x}r\right)^2+\left(\frac{2\pi}{N_y}s\right)^2\right]\hat{p}_{r,s,k}+\left.\frac{\partial^2\hat{p}_{r,s,k}}{\partial z^2}\right|_{(x_i,y_j,z_k)}=\hat{f}_{r,s,k}. \tag{5.27}$$

Now, expanding $\partial^2/\partial z^2$ with second-order finite difference,

$$\begin{aligned}
-\left[\left(\frac{2\pi}{N_x}r\right)^2+\left(\frac{2\pi}{N_y}s\right)^2\right]\hat{p}_{r,s,k}+\frac{\hat{p}_{r,s,k+1}-2\hat{p}_{r,s,k}+\hat{p}_{r,s,k-1}}{\Delta z^2}&=\hat{f}_{r,s,k}\\
\frac{\hat{p}_{r,s,k+1}-\left(2+\left(\frac{2\pi\Delta z}{N_x}r\right)^2+\left(\frac{2\pi\Delta z}{N_y}s\right)^2\right)\hat{p}_{r,s,k}+\hat{p}_{r,s,k-1}}{\Delta z^2}&=\hat{f}_{r,s,k}\\
\frac{\hat{p}_{r,s,k+1}+\gamma_{r,s}\hat{p}_{r,s,k}+\hat{p}_{r,s,k-1}}{\Delta z^2}&=\hat{f}_{r,s,k},
\end{aligned} \tag{5.28}$$

with $\gamma_{r,s}=-\left(2+\left(\frac{2\pi\Delta z}{N_x}r\right)^2+\left(\frac{2\pi\Delta z}{N_y}s\right)^2\right)$. For the boundary condition (5.22a) the following second-order approximation is used,

$$\frac{-\hat{p}_{r,s,2}+4\hat{p}_{r,s,1}-3\hat{p}_{r,s,0}}{2\Delta z}=\hat{f}_{r,s,0}, \tag{5.29}$$

where

$$\hat{f}_{r,s,0}=\sum_{i=0}^{N_x-1}\sum_{j=0}^{N_y-1}p_{\text{bottom}}\exp\left(-2\pi\mathrm{i}\left(\frac{ir}{N_x}+\frac{js}{N_y}\right)\right),$$

for $r=0,\ldots,N_x-1$; $s=0,\ldots,N_y-1$. To implement the boundary condition (5.22b), equation (5.28) is used for $k=N_z-1$, so

$$\begin{aligned}
\frac{\hat{p}_{r,s,N_z}+\gamma_{r,s}\hat{p}_{r,s,k}+\hat{p}_{r,s,N_z-2}}{\Delta z^2}&=\hat{f}_{r,s,N_z-1}\\
\frac{\gamma_{r,s}\hat{p}_{r,s,k}+\hat{p}_{r,s,N_z-2}}{\Delta z^2}&=\hat{f}_{r,s,N_z-1}-\frac{1}{\Delta z^2}\hat{p}_{r,s,N_z}
\end{aligned} \tag{5.30}$$

with

$$\hat{p}_{r,s,N_z} = \sum_{i=0}^{N_x-1}\sum_{j=0}^{N_y-1} p_{\text{top}} \exp\left(-2\pi \mathrm{i}\left(\frac{ir}{N_x}+\frac{js}{N_y}\right)\right),$$

for $r = 0,\ldots,N_x-1$; $s = 0,\ldots,N_y-1$. Now, the following system of linear equations appears when using (5.28), (5.29), and (5.30)

$$\frac{1}{\Delta z^2}\begin{bmatrix} -\frac{3}{2}\Delta z & 2\Delta z & -\frac{1}{2}\Delta z & 0 & \ldots & 0 \\ 1 & \gamma_{r,s} & 1 & 0 & \cdots & 0 \\ 0 & \ddots & \ddots & \ddots & \ddots & \vdots \\ \vdots & \ddots & \ddots & \ddots & \ddots & 0 \\ \vdots & \ddots & \ddots & 1 & \gamma_{r,s} & 1 \\ 0 & \cdots & \cdots & 0 & 1 & \gamma_{r,s} \end{bmatrix}\begin{bmatrix} \hat{p}_{r,s,0} \\ \hat{p}_{r,s,1} \\ \vdots \\ \hat{p}_{r,s,k} \\ \vdots \\ \hat{p}_{r,s,N_z-1} \end{bmatrix} = \begin{bmatrix} \hat{f}_{r,s,0} \\ \hat{f}_{r,s,1} \\ \vdots \\ \hat{f}_{r,s,k} \\ \vdots \\ \hat{f}_{r,s,N_z-1} - \frac{1}{\Delta z^2}\hat{p}_{k,s,N_z} \end{bmatrix}, \tag{5.31}$$

which has to be solved for each $r = 0,\ldots,N_x-1$, $s = 0,\ldots,N_y-1$. The matrix of (5.31) is not singular for $r = s = 0$, since the boundary conditions. Additionally, the following row operation $\text{row}_1 = \text{row}_1 + \text{row}_2 \times(\frac{1}{2}\Delta z)$ in (5.31) is applied to get a tridiagonal matrix, and then solve the system of equations using Thomas' Algorithm (TDMA) (Ferziger et al., 2020; Jiang & Lai, 2009). Thus, the problem (5.31) becomes to

$$\frac{1}{\Delta z^2}\begin{bmatrix} -\Delta z & \Delta z(2+\frac{1}{2}\gamma_{r,s}) & 0 & 0 & \ldots & 0 \\ 1 & \gamma_{r,s} & 1 & 0 & \cdots & 0 \\ 0 & \ddots & \ddots & \ddots & \ddots & \vdots \\ \vdots & \ddots & \ddots & \ddots & \ddots & 0 \\ \vdots & \ddots & \ddots & 1 & \gamma_{r,s} & 1 \\ 0 & \cdots & \cdots & 0 & 1 & \gamma_{r,s} \end{bmatrix}\begin{bmatrix} \hat{p}_{r,s,0} \\ \hat{p}_{r,s,1} \\ \vdots \\ \hat{p}_{r,s,k} \\ \vdots \\ \hat{p}_{r,s,N_z-1} \end{bmatrix} = \begin{bmatrix} \hat{f}_{r,s,0} + \frac{\Delta z}{2}\hat{f}_{r,s,1} \\ \hat{f}_{r,s,1} \\ \vdots \\ \hat{f}_{r,s,k} \\ \vdots \\ \hat{f}_{r,s,N_z-1} - \frac{1}{\Delta z^2}\hat{p}_{k,s,N_z} \end{bmatrix}. \tag{5.32}$$

Appendix C.3.2 presents the characteristics of the matrix shown in equation (5.32). Summarizing the derivation above, the steps to get the pressure are the following:

1. Compute slice-wise $\hat{f}_{r,s} = \text{FFT2D}(f_{i,j})$ for each k, for all i, j. Since in $3D$ the data is stored in a cube, a slice represents the xy domain for each value of z.
2. Solve (5.31) for each $\gamma_{r,s}$.
3. Build $\hat{p}$ using each vector $\hat{p}_{r,s}$
4. Compute p from the real part of $\hat{p}$, i.e., $p = \Re\left(\text{IFFT2D}(\hat{p})\right)$.

It is important to note that FFT and IFFT implementations are used to compute the DFT and IDFT respectively.

For the full pressure problem with variable density, the following fixed-point iteration is used

$$\nabla_h^2 p^{m+1} = \frac{\rho^n}{\Delta t}\left(\nabla_h \cdot \mathbf{u}^* - \nabla_h \cdot \mathbf{u}^{n+1}\right) + \frac{1}{\rho^n}\nabla_h \rho^n \cdot \nabla_h p^m, \tag{5.33}$$

where m represents the iteration step and n denotes the time step of the numerical integration process. p^n is used as the initial guess in $m = 0$. The solution for p^{n+1} is obtained after (5.33) converges.

5.4.1 Non-uniform Version

With the use of non-uniform vertical axis described in sub-section 5.2.1, the approximations for partial derivatives along the z axis result in several modifications to the linear system of equations obtained in the pressure problem. Figure 5.4 presents a sketch of the numerical domain and the stencil used with this type of grid.

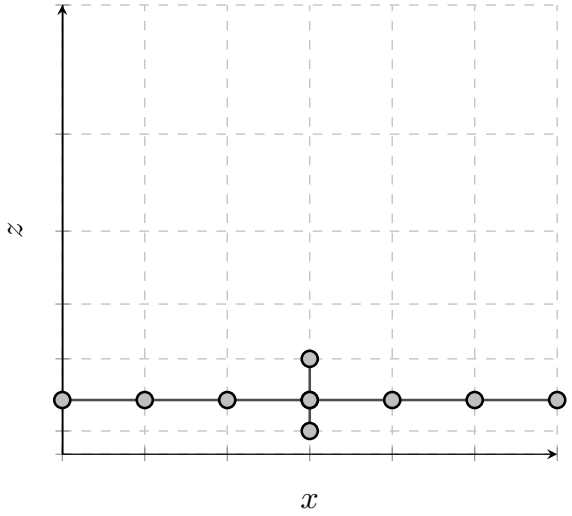

Figure 5.4: Two-dimensional example of the non-uniform domain and the stencil.

The first equation becomes

$$-\frac{(2\Delta z_0 + \Delta z_1)}{\Delta z_0(\Delta z_0 + \Delta z_1)}\hat{p}_{r,s,0} + \frac{\Delta z_0 + \Delta z_1}{\Delta z_0 \Delta z_1}\hat{p}_{r,s,1} - \frac{\Delta z_0}{\Delta z_1(\Delta z_0 + \Delta z_1)}\hat{p}_{r,s,2} = \hat{f}_{r,s,0}. \quad (5.34)$$

The equations for $k = 1$ to $k = N_z - 2$ are

$$\begin{aligned}\frac{2}{\Delta z_{k-1}(\Delta z_{k-1} + \Delta z_k)}\hat{p}_{r,s,k-1} - \left[\left(\frac{2\pi}{N_x}r\right)^2 + \left(\frac{2\pi}{N_y}s\right)^2 + \frac{2}{\Delta z_{k-1}\Delta z_k}\right]\hat{p}_{r,s,k} \\ + \frac{2}{\Delta z_k(\Delta z_{k-1} + \Delta z_k)}\hat{p}_{r,s,k+1} = \hat{f}_{r,s,k}.\end{aligned} \quad (5.35)$$

The last equation for $k = N_z - 1$ is

$$\begin{aligned} &\frac{2}{\Delta z_{N_z-2}(\Delta z_{N_z-2} + \Delta z_{N_z-1})}\hat{p}_{r,s,N_z-2} \\ -\left[\left(\frac{2\pi}{N_x}r\right)^2 + \left(\frac{2\pi}{N_y}s\right)^2 + \frac{2}{\Delta z_{N_z-2}\Delta z_{N_z-1}}\right]&\hat{p}_{r,s,N_z-1} \\ &+\frac{2}{\Delta z_{N_z-1}(\Delta z_{N_z-2} + \Delta z_{N_z-1})}\hat{p}_{r,s,N_z} = \hat{f}_{r,s,N_z-1}. \end{aligned} \tag{5.36}$$

Following the same approach used in the uniform grid domain, equation (5.34) is modified by adding $0.5\Delta z_0$ times the equation for $k = 1$,

$$\begin{aligned} -\frac{1}{\Delta z_0}\hat{p}_{r,s,0} + \left[\frac{\Delta z_0 + \Delta z_1}{\Delta z_0 \Delta z_1} - \frac{\Delta z_0}{2}\left(\left(\frac{2\pi}{N_x}r\right)^2 + \left(\frac{2\pi}{N_y}s\right)^2\right) - \frac{1}{\Delta z_1}\right]\hat{p}_{r,s,1} \\ = \hat{f}_{r,s,0} + \frac{\Delta z_0}{2}\hat{f}_{r,s,1}, \end{aligned} \tag{5.37}$$

to get a tri-diagonal matrix and take advantage of the Thomas algorithm.

5.5 Source Terms

The source terms for the momentum and energy equations, $\mathbf{f}$ and q, are directly computed. Nevertheless, the subsequent sub-sections discuss the additional terms incorporated to enhance the model's capabilities.

5.5.1 Immersed Boundary Method

The Immersed Boundary Method (IBM) is a numerical technique designed to handle complex geometries within a structured computational mesh (Verzicco, 2023). Instead of conforming the grid to the physical boundaries of an object, the method embeds the geometry into a regular grid and imposes boundary conditions through additional forcing terms in the governing equations (Senocak, Ackerman, Stevens, & Mansour, 2004; Fadlun, Verzicco, Orlandi, & Mohd-Yusof, 2000; Chien & Wu, 2016). This approach significantly simplifies the meshing process and reduces computational costs while retaining the ability to capture interactions between solid boundaries and fluid flow.

In the context of wildfire modeling, IBM provides an efficient framework for representing terrain characteristics and obstacles that influence fire behavior and atmospheric dynamics. Within IBM, the solid boundary is characterized by a body force denoted $\mathbf{f}_{\text{IBM}}$ (Senocak et al., 2004). Fire modeling has utilized this concept previously, as evidenced by the FDS software which employed it for handling flow obstructions (K. McGrattan et al., 2012). The discretized form of the momentum

equations can be written as follows

$$\frac{\mathbf{u}^{n+1} - \mathbf{u}^n}{\Delta t} = \mathrm{RHS}_{\mathbf{u}} + \mathbf{f}_{\mathrm{IBM}},$$

where $\mathrm{RHS}_{\mathbf{u}}$ includes the pressure gradient, convection, diffusion, and force terms. $\mathbf{f}_{\mathrm{IBM}}$ denotes the source term that gives the desired velocity at the boundary. Assuming the target velocity at the boundary is $\mathbf{u}^{n+1} = \mathbf{U}^{n+1}$, the explicit expression for the body force can be formulated as

$$\mathbf{f}_{\mathrm{IBM}} = \frac{\mathbf{U}^{n+1} - \mathbf{u}^n}{\Delta t} - \mathrm{RHS}_{\mathbf{u}}.$$

According to (Senocak et al., 2004), the general steps for IBM are:

1. Pre-processing: Determine the Cartesian cells that are cut by the boundary. Tag the nodes as *solid*, *fluid*, and *cut*.

2. Predictor stage: Solve the discretized momentum equations.

3. Set zero velocity field on the *solid* nodes, and apply the reconstruction scheme on the *cut* nodes.

4. Solve the pressure problem.

5. Update the velocity and pressure field and impose the reconstruction on the *cut* nodes.

In this work, the reconstruction method described in step 3 is not used due to the alignment of the boundary nodes with the *cut* nodes. Furthermore, the *cut* nodes were used to determine the correct values in the boundary conditions for both temperature T and fuel Y. Figure 5.5 presents a simple sketch to describe the different types of nodes used by the IBM.

5.5.2 Scalars Bounding

Utilizing a simplified mathematical model in combination with a second-order spatial approximation can lead to non-physical results for both temperature and fuel fraction variables. For example, obtaining a negative fuel fraction, or temperatures lower than 273 K. To address this problem, two additional terms are introduced to restrict the values in a defined range. These components are introduced in each time step as an intermediate procedure to keep the fuel and temperature bounded, and they a work similarly to the IBM procedure.

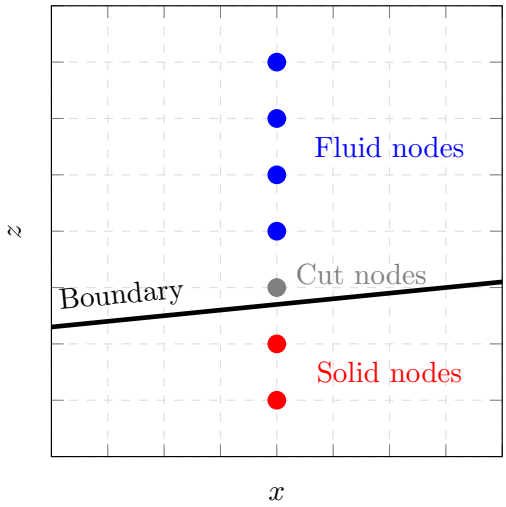

Figure 5.5: Immersed boundary method nodes.

Temperature

For temperature, this bounding term q_{B} is included in the source term q. Following the idea of IBM, the discretized temperature equation is

$$\frac{T^{n+1} - T^n}{\Delta t} = \mathrm{RHS}_T + q_{\mathrm{B}},$$

where RHS_T contains the convection, diffusion, and source terms. Then, q_{B} is defined to force a valid temperature between T_∞ and $T_{\max}$, so

$$q_{\mathrm{B}} = \frac{T^* - T^n}{\Delta t} - \mathrm{RHS}_T$$

where

$$T^* = \begin{cases} T_{\max}, & \text{if } T^{n+1} > T_{\max}, \\ T_\infty, & \text{if } T^{n+1} < T_\infty. \end{cases}$$

Fuel fraction

In a similar fashion, the fuel fraction is

$$\frac{Y^{n+1} - Y^n}{\Delta t} = \mathrm{RHS}_Y + Y_{\mathrm{B}},$$

where RHS_Y includes the Arrhenius-like equation. Then, the value of $Y \in [0, 1]$ is

$$Y_{\mathrm{B}} = \frac{Y^* - Y^n}{\Delta t} - \mathrm{RHS}_Y$$

with

$$Y^* = \begin{cases} 1, & \text{if } Y^{n+1} > 1, \\ 0, & \text{if } Y^{n+1} < 0. \end{cases}$$

5.6 Summary

This section presents a summary of the numerical methods described in previous sections. The main steps for the numerical approximation of the wildfire model (4.31) are presented in Algorithm 1.

Algorithm 1 General steps of the numerical algorithm.

for $n = 0$ to $N_t - 1$ **do**
    $\rho^n \leftarrow \rho(T^n)$.
    $\mathbf{u}^*$, T^{n+1} $Y^{n+1} \leftarrow$ `RHS`$(\mathbf{u}^n, T^n\ Y^n)$.
    $p^{n+1} \leftarrow$ `PressureSolver`$(p^n, \rho^n, \mathbf{u}^*, T^{n+1}, Y^{n+1})$.
    Compute the corrected velocity $\mathbf{u}^{n+1}$ using p^{n+1} with (5.6).
    Impose boundary conditions for $\mathbf{u}^{n+1}$.
    Apply temperature and fuel fraction bounds.
end for

The evaluation on the right-hand side is in Algorithm 2.

Algorithm 2 Computation of right-hand side of the equations.

procedure `RHS`$(\mathbf{u}^n, T^n, Y^n)$
    Compute $\mathbf{u}^*$, T^{n+1} and Y^{n+1} using (5.5), (5.3), and (5.4).
    Impose boundary conditions for $\mathbf{u}^*$, T^{n+1}, and Y^{n+1}.
    return $\mathbf{u}^*$, T^{n+1}, Y^{n+1}
end procedure

The algorithm for solving the full pressure solver is presented in Algorithm 3, and Algorithm 4 describes the procedure for solving the Poisson equation.

Algorithm 3 Pressure solver algorithm.

procedure `PressureSolver`$(p^n, \rho^n, \mathbf{u}^*, T^{n+1}, Y^{n+1})$
    $p^0 \leftarrow p^n$
    for $m = 0$ to N_{iter} **do**
        Compute f using (5.33) with p^m, ρ^n, $\mathbf{u}^*$, T^{n+1}, and Y^{n+1}.
        $p^{m+1} \leftarrow$ `PoissonSolver`(f)
        if $\|p^{m+1} - p^m\|_\infty <$tol **then**
            break
        end if
    end for
    return p
end procedure

Theoretically, the complete numerical algorithm has an error of $\mathcal{O}(\Delta x^2 + \Delta y^2 + \Delta z^2) + \mathcal{O}(\Delta t)$. This bound emerges from the second-order approximation used in the spatial partial derivatives, and the first-order in time approximation used by the

Algorithm 4 Poisson solver.

1: **procedure** PoissonSolver(f)
2: Compute $\hat{f}_{r,s} = \texttt{FFT}(f_{i,j})$ for each k
3: Solve (5.32) for each $\gamma_{r,s}$ using Thomas' Algorithm
4: Build the matrix $\hat{p}$ using each column vector $\hat{p}_{r,s}$
5: Compute the pressure as $p = \Re\left(\texttt{IFFT}(\hat{p})\right)$
6: **return** p
7: **end procedure**

correction step (5.6). In the case of a non-uniform grid, it is bounded by $\mathcal{O}(\Delta x^2 + \Delta y^2 + \max(\Delta z_k)) + \mathcal{O}(\Delta t)$, where the term $\max(\Delta z_k)$ is included due to the different values of Δz_k used in the vertical domain. For the FFT-FD solver, the error is bounded by the approximation of the derivatives with respect to z with $\mathcal{O}(\Delta z^2)$.

Regarding computational complexity, let N_x, N_y, N_z, and N_t denote the number of grid points along each respective coordinate axis. The number of operations are:

- Algorithm 2 has $\sim N_x\, N_y\, N_z$ operations considering the loop on all the points on the grid.
- Algorithm 4 needs $\sim N_x\, N_y\, N_z \log(N_x N_y)$ operations, as it computes N_z FFT and IFFT for matrices of size $N_x\, N_y$. Additionally, it solves $N_x\, N_y$ tridiagonal system of linear equations of size $N_z\, N_z$, which means that $\sim N_x\, N_y\, N_z$ operations are carried out considering that the Thomas algorithm is $\mathcal{O}(N_z)$.
- The algorithm 3 depends on the previous step, as it performs N_{iter} of the constant density pressure solver. In particular, N_{iter} is typically smaller than the grid size.
- Considering that the previous steps are performed N_t times, the overall number of operations is $\sim N_t\,(N_x\, N_y\, N_z \log(N_x N_y) + 2\; N_x\, N_y\, N_z)$.

Using the previous analysis, the complete algorithm has an approximate computational complexity of $\mathcal{O}(N_t\, N_x\, N_y\, N_z \log(N_x N_y))$.

Chapter 6

Implementation

This chapter provides an overview of the hardware and software specifications utilized in the implementations of the CPU and GPU.

6.1 Hardware

The numerical experiments were carried out on a workstation with the following configuration:

- **CPU:** Intel® Core™ i9-13900K Processor, 3.0 GHz
- **Memory (RAM):** 128 GB DDR5 at 5600 MHz (4 × 32 GB)
- **Primary Storage:** Kingston FURY Renegade NVMe SSD, 4 TB
- **Secondary Storage:** Seagate ST12000VN0008 HDD, 12 TB
- **Graphics Processing Unit (GPU):** ASUS TUF Gaming GeForce RTX 4090 OC, 24 GB GDDR6

6.2 Software

The workstation runs on a 64-bit Linux distribution, Ubuntu 22.04 LTS (Jammy Jellyfish). The flexibility and usability of this operating system facilitate the management of latest drivers and package versions for CPU and GPU implementations.

6.2.1 CPU implementation

A CPU-based implementation of the algorithm was developed in *Python*. The core numerical calculations and the manipulation of the vector data structures were carried out using *NumPy*, while *SciPy* was employed for the FFT routines. These libraries rely on a highly optimized linear algebra back-end, primarily implemented in *C/C++*, which provide efficient performance for large-scale numerical operations

(Oliphant, 2007). This version of the code includes the implementation of Algorithms 1, 2, and 3.

To further enhance performance, *Numba* was used to JIT-compile the *TDMA* solver used in the pressure problem, significantly accelerating this computationally intensive step. The spatial partial derivatives were discretized using `numpy.roll`, which provides an efficient array-shifting operation suitable for finite-difference schemes. For time integration, both the Euler method and the second- and fourth-order RK methods were implemented from scratch, allowing flexibility in the numerical treatment of IVP (5.14).

Regarding computational performance, considering a two-dimensional spatial resolution of 512×256 nodes, the solver requires approximately 0.25 seconds per time step. The total run-time may vary due to the iterative procedure employed in the pressure solver, as additional iterations are sometimes necessary to accommodate large temperature fluctuations. For example, executing the entire simulation with 100000 time steps results in a total computational time of about 7 hours.

The source code for this CPU implementation is publicly accessible at `https://github.com/dsanmartin/wildfire`, which facilitates transparency, reproducibility, and accessibility for future research and model development. Appendix D.1 contains detailed information on library installation, library versioning, and how the implementation can be used.

6.2.2 GPU implementation

Graphics Processing Units (GPUs), originally designed to render computer graphics, have become essential tools for scientific computing due to their massive parallel processing capabilities. In particular, they are widely used in the numerical solution of partial Differential Equations and other compute-intensive tasks (Owens et al., 2008; Mattes & Kofuji, 2014).The concept of General-Purpose GPU (GPGPU) computing leverages the highly parallel architecture of GPUs to accelerate applications well beyond graphics, providing significant performance advantages compared to traditional CPU-based approaches (NVIDIA, 2025c; Kirk & Hwu, 2012).

The GPU programming paradigm is based on the *Single Instruction Multiple Threads (SIMT)* model, where a single instruction is executed simultaneously across thousands of lightweight threads. *CUDA* is one of the most widely adopted frameworks for GPU programming, providing an extension of the *C/C++* language along with APIs for other languages such as Python and Fortran. In this model, computations are expressed through *kernels*, which are executed in parallel on threads organized into a hierarchy of grids and blocks. The *host* refers to the CPU and its memory, while the *device* corresponds to the GPU and its dedicated memory space. Execution parameters such as the number of blocks per grid and the number of threads per block must be specified by the user to match the problem size and hardware capabilities.

In the present implementation, a one-dimensional thread organization is adopted for thread indexing and memory storage. The three-dimensional computational do-

main is vectorized, assigning each thread to process the discretized values associated with a node (i, j, k). *CUDA* built-in variables `threadIdx.x`, `blockIdx.x`, and `blockDim.x` are used to compute a unique global thread identifier,

```
idx = threadIdx.x + blockIdx.x * blockDim.x,
```

which allows for direct mapping between threads and data elements. To efficiently handle domains larger than the number of available threads, the *grid-stride loop* pattern is employed (Harris, 2013; NVIDIA, 2025c). This strategy allows each thread to process multiple data points by iterating over indices with a stride equal to the total number of threads in the grid:

```
for (int i = idx; i < N; i += blockDim.x * gridDim.x).
```

This approach ensures scalability across different GPU architectures, improves hardware utilization, and avoids under-subscription of resources, making it a widely recommended best practice in *CUDA* programming (NVIDIA, 2025c; Harris, 2013).

The general procedure used for each *CUDA* kernel is

```
// ...
int i, j, k;
int size = Nx * Ny * Nz;
int idx = threadIdx.x + blockIdx.x * blockDim.x;
int stride = gridDim.x * blockDim.x;
for (int ijk = idx; ijk < size; ijk += stride) {
    i = ijk / (Ny * Nz);
    j = (ijk % (Ny * Nz)) / Nz;
    k = ijk % Nz;
    // Perform the computation for node (i, j, k)
}
// ...
```

The GPU implementation was developed entirely in *CUDA C* and compiled using the *NVIDIA CUDA Compiler Driver* (*NVCC*) (NVIDIA, 2025b). Fast Fourier Transform (FFT) routines were implemented through *cuFFTW* API, a GPU-accelerated library that provides an interface highly compatible with the widely used Fastest Fourier Transform in the West (FFTW) library (NVIDIA, 2025a).

The *cuFFTW* API allows developers to replace existing FFTW calls with minimal modifications, while transparently redirecting the execution of FFTs to the optimized *cuFFT* backend. This ensures that the efficiency of GPU-accelerated FFTs can be leveraged without extensive code restructuring. The cuFFTs itself provides highly optimized implementations of one-, two-, and three-dimensional FFTs for both real and complex data, supporting single and double precision. By combining compatibility with FFTW and the performance benefits of *CUDA*, *cuFFTW* offers a smooth migration path for scientific codes that already rely on FFTW, while exploiting the massive parallelism of modern GPUs.

Another feature to highlight is the TDMA solver. The GPU implementation of the Thomas algorithm solves multiple independent tri-diagonal systems in parallel, with each *CUDA* thread processing one vertical column through forward elimination and back-substitution. A grid-stride loop ensures scalability across problem sizes,

while memory access patterns and indexing macros enable efficient integration with *cuFFT* routines. By performing all operations on-device without inter-thread dependencies, the kernel achieves high throughput and reduced memory overhead (Harris, 2013; NVIDIA, 2025c), making it well suited for the Poisson solver which appears in the constant density pressure problem (Algorithm 4).

For a three-dimensional spatial resolution of $256 \times 256 \times 64$ nodes, the GPU solver requires approximately 0.16 seconds per time step. As in the CPU implementation, the run-time may fluctuate due to the iterative procedure of the pressure solver, which demands additional iterations when strong temperature variations are present. A complete simulation of 100000 time steps is completed in 4.5 hours. This result is significant, as the computational domain contains 32 times more grid points than the CPU-based version, yet the GPU implementation achieves a runtime that is 1.55 times faster overall. When normalized per node, the GPU-based computation delivers an effective speedup of approximately $50\times$, highlighting the substantial performance gains obtained through parallel execution on modern GPU architectures.

The source code for this implementation is also publicly available at the following link: `https://github.com/dsanmartin/wildfires`. Similarly to the previous subsection, Appendix D.2 provides detailed information on installing, library versions, and how to run the GPU implementation.

Chapter 7

Results

This chapter presents the results obtained from the proposed numerical model and its computational implementation. The analysis is structured into four main sections. First, the physical parameters employed in the simulations are outlined, complemented by their theoretical foundations, with particular emphasis on their significance in accurately capturing the interactions between fire and atmosphere. The performance of the numerical solver is then analyzed through validation tests and a study of the effects of spatial discretization on the solution. The third section presents a series of experiments designed to evaluate the model's ability to capture fundamental fire dynamics and compare the results with experimental and numerical references. Finally, a discussion integrates the main findings, emphasizing the advantages and limitations of the proposal and comparing it with other coupled models in terms of its potential use in wildfire modeling.

7.1 Physical parameters

Considering that the mathematical model incorporates multiple parameters, Table 7.1 provides a comprehensive summary of those used in all simulations. It is important to note that most values are derived from the characteristics of air at 1 atm and 15°C (288.15 Kelvin) (Çengel & Cimbala, 2018, p. 956).

Di Blasi et al. (2001) report that the initial phase of solid fuel decomposition occurs between 473 K and 573 K. Therefore, the mean value of these temperatures is taken into account, that is, $T_{\text{pc}} = 523$ K.

As reported in Williams (2020), the heat of combustion of wood ranges from 19 to 23 kJ kg^{-1}. Based on this information, a mean value of $H_{\text{C}} = 21$ kJ kg^{-1} was chosen for the analysis.

The activation temperature is adopted as defined by McAllister et al. (2011, p. 53), $T_{\text{act}} = E_{\text{act}}/\mathcal{R}$, where E_{act} denotes the activation energy expressed in J mol^{-1}, and $\mathcal{R} = 8.3145$ J K^{-1}mol^{-1} represents the universal gas constant. Within the scope of reactions that involve carbonaceous materials interacting with oxygen, the range of values for E_{act} extends from 54000 J mol^{-1} to 237000 J mol^{-1}, as reported in

Table 7.1: Summary of the model's parameters used by the simulations.

Parameter	Value	SI Units	Source
Reference density (ρ_∞)	1.225	kg m^{-3}	Çengel and Cimbala (2018)
Dynamic viscosity (μ)	1.802×10^{-5}	kg m^{-1} s^{-1}	Çengel and Cimbala (2018)
Ambient temperature (T_∞)	288.15	K	Çengel and Cimbala (2018)
Gravity (g)	9.807	m s^{-2}	Çengel and Cimbala (2018)
Solid volume fraction (α_s)	0.002	-	Morvan et al. (2009)
Surface-to-volume ratio (σ_s)	4000	m^{-1}	Morvan et al. (2009)
Smagorinsky constant (C_s)	0.2	-	Typical value
Prandtl number (Pr)	0.7329	-	Çengel and Cimbala (2018)
Thermal conductivity (k)	0.02476	kg m s^{-3} K^{-1}	Çengel and Cimbala (2018)
Specific heat capacity (c_p)	1007	m^{2}s^{-2}K^{-1}	Çengel and Cimbala (2018)
Optical path length (δ)	0.1	m	Mell et al. (2007)
Phase change temperature (T_pc)	523	K	Based on Di Blasi et al. (2001)
Heat of combustion (H_C)	21×10^6	m^{2}s^{-2}	Based on Williams (2020)
Pre-exponential factor (A)	10^9	s^{-1}	Asensio and Ferragut (2002)
Activation temperature (T_act)	18040.85	K	Based on Cuesta et al. (1993)
Fuel drag coefficient (C_d)	0.15	-	Morvan et al. (2009)
Temperature max bound (T_max)	2500	K	Frangieh et al. (2020)
Reference height (z_ref)	2	m	Mell et al. (2007)

Cuesta et al. (1993), and from 125520 J mol^{-1} to 202505 J mol^{-1}, as presented in Westbrook and Dryer (1984). The representative value of $E_\mathrm{act} = 150000$ J mol^{-1} was selected as a reference. Using this value, the activation temperature is

$$T_\mathrm{act} = \frac{150000}{8.3145} \frac{\text{J mol}^{-1}}{\text{J K}^{-1}\text{mol}^{-1}} \approx 18040.85 \text{ K}.$$

The choice of $T_\mathrm{max} = 2500$ K is derived from the temperature of the adiabatic flame resulting from the combustion of carbon monoxide Frangieh et al. (2020).

The fuel consumption parameter Y_f is based on the ideas introduced by Asensio and Ferragut (2002), Mandel et al. (2008), and Eberle et al. (2015). Numerical simulations were performed moving Y_f in the range of 0 to 100, where lower values signify lower fuel consumption rates and higher values indicate an increase in fuel consumption speed. This parameter is selected according to the experiment.

The convective heat transfer coefficient is calculated according to Mell et al. (2007), with

$$h_\mathrm{c} = 1.42 \Delta z \left(\frac{|T_\mathrm{gas} - T_\mathrm{solid}|}{\Delta z} \right)^{1/4}.$$

In terms of spatial domain, a wider extent is used to avoid fluid issues due to periodic boundary conditions in the x and y directions.

While a comprehensive application of physical principles is undertaken, the simplifications introduced require an inevitable calibration of certain parameters, executed and selected through numerical experimentation.

7.2 Numerical Solver Analysis

This section analyzes the numerical solvers employed in the coupled atmosphere–fire spread model, with validation carried out through two academic benchmark problems and an examination of spatial mesh effects.

7.2.1 Full Algorithm

To validate the theoretical computational complexity derived in Section 5.6, a series of numerical experiments were conducted to measure the scaling behavior of the full algorithm. Each configuration was executed between three and five times to minimize the impact of transient performance fluctuations, and the results were averaged to obtain representative timings. The experiments were divided into two main parts: spatial and temporal scaling.

In the first experiment, spatial resolution was systematically increased while keeping the number of time steps constant at $N_t = 10^3$. The dimensions of the grid were defined as $N_x = N_y \in \{32, 64, 128, 256\}$ and $N_z \in \{16, 32, 64, 128\}$, resulting in a total number of nodes $N = N_x N_y N_z$. Figure 7.1a presents the average runtime as a function of N. The results follow the expected asymptotic trend $\mathcal{O}(N_x N_y N_z \log(N_x N_y))$, which is consistent with the theoretical analysis discussed in Section 5.6. This behavior confirms that the dominant computational cost arises from the Fast Fourier Transform (FFT) operations and the three-dimensional spatial discretization. The nearly linear-logarithmic scaling demonstrates that the algorithm remains efficient and well balanced across increasing spatial resolutions.

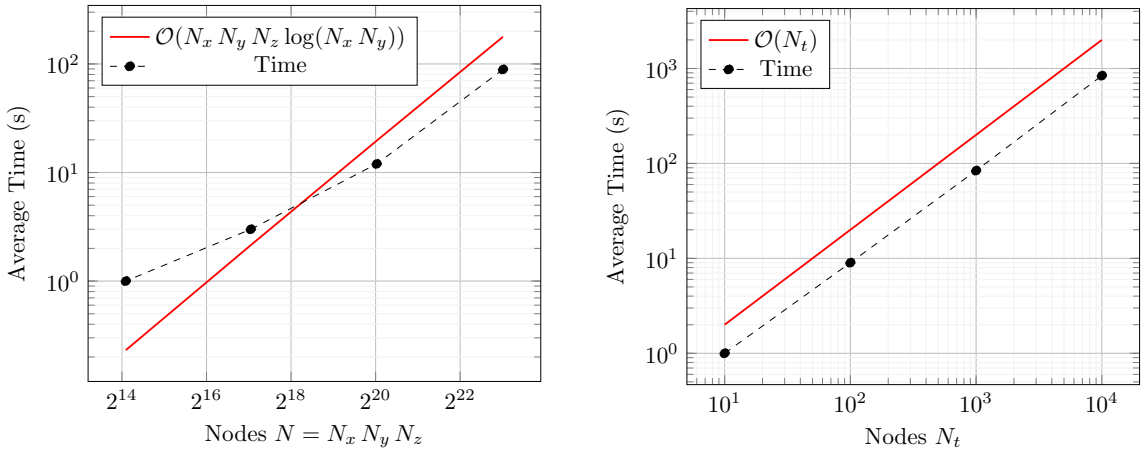

(a) Spatial approximation.

(b) Temporal approximation.

Figure 7.1: Computational complexity of the full algorithm.

In the second experiment, the temporal resolution was varied while keeping the spatial grid fixed at $N_x = N_y = 256$ and $N_z = 128$. The number of time steps was selected as $N_t \in \{10, 10^2, 10^3, 10^4\}$. As shown in Figure 7.1b, the runtime exhibits an almost linear dependence on N_t, consistent with the theoretical complexity

$\mathcal{O}(N_t)$ expected for an explicit time integration scheme. This confirms that the time-stepping implementation scales predictably with the number of iterations, with negligible overhead introduced by memory access or I/O operations.

The experimental results confirm that the overall computational complexity of the algorithm follows the theoretical estimates obtained in Section 5.6. Both spatial and temporal scaling exhibit strong agreement with their respective asymptotic behaviors, demonstrating that the numerical implementation is computationally efficient and free from major bottlenecks. These findings validate the suitability of the algorithm for large-scale simulations, where spatial resolutions and counted time steps can vary by several orders of magnitude.

7.2.2 FFT-FD Solver

The following Poisson problem was solved numerically to study the capabilities of the FFT-FD method. This analysis was performed using a *Python* implementation, and the source code is available in this repository: `https://github.com/dsanmartin/fftfd`.

Let $\mathbf{x} \in \Omega = [0, 2\pi]^3$ be a three-dimensional spatial domain, then Poisson's problem is defined as

$$\begin{aligned} \nabla^2 p &= f, \quad \text{in } \Omega, \\ \frac{\partial p}{\partial z} &= 0, \quad \text{on } z = z_{\min}, \\ p &= 0, \quad \text{on } z = z_{\max}, \end{aligned} \tag{7.1}$$

using periodic boundary conditions in the x and y directions, and

$$f(x, y, z) = \frac{1}{\pi^3} \left(f_1(x, y, z) + f_2(z)\right) G(x, y, z),$$

with

$$f_1(x, y, z) = \left(z^3 - 2\pi z^2\right) \left(\frac{2}{s_x}\left(1 - \frac{2}{s_x}(x - x_0)^2\right) + \frac{2}{s_y}\left(1 - \frac{2}{s_y}(y - y_0)^2\right)\right),$$

$$\begin{aligned} f_2(z) = &-\frac{4}{s_z} z^5 + \left(\frac{8\pi + 8z_0}{s_z^2}\right) z^4 - \left(\frac{16\pi z_0 + 4z_0^2 - 14 s_z}{s_z^2}\right) z^3 \\ &+ \left(\frac{8\pi z_0^2 - 12 s_z z_0 - 20\pi s_z}{s_z^2}\right) z^2 + \left(\frac{16\pi z_0 - 6 s_z}{s_z}\right) z + 4\pi, \end{aligned}$$

and,

$$G(x, y, z) = \exp\left(-\left(\frac{(x - x_0)^2}{s_x} + \frac{(y - y_0)^2}{s_y} + \frac{(z - z_0)^2}{s_z}\right)\right).$$

The following values are used $x_0 = y_0 = z_0 = \pi$, $s_x = s_y = s_z = 0.5$ for the previous functions. The analytical solution to this problem is

$$p(x, y, z) = \frac{1}{\pi^3}(2\pi z^2 - z^3)\, G(x, y, z). \tag{7.2}$$

Several experiments were performed to assess the convergence and computational complexity. Using a regular grid with $N = N_x = N_y = N_z \in \{16, 32, 64, 128, 256\}$, 5 experiments were executed to report the average times. The numerical error is computed using $\|p - p_{\text{app}}\|_2 / \|p\|_2$. The convergence and computational complexity results are presented in Figures 7.2a and 7.2b.

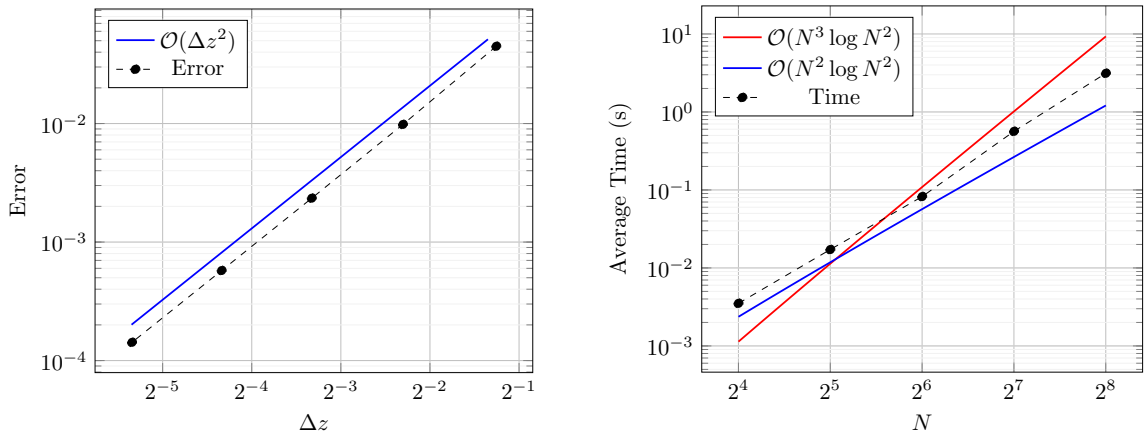

(a) Convergence.

(b) Computational complexity.

Figure 7.2: Analysis of the FFT-FD solver.

As observed in Figure 7.2a, the error aligns with the theoretical prediction derived in sub-section 5.6. Although the method combines spectral differentiation for the x and y axes, the use of FDM on the z axis reduces the order of the method, primarily relying on the dominant term Δz^2. In terms of computational complexity, Figure 7.2b illustrates that the algorithm delivers better performance on smaller problems, but degrades as the size of the problem increases. Nevertheless, as concluded in sub-section 5.6, it remains within the bounds of $\mathcal{O}(N^3 \log N^2)$.

In summary, it can be concluded that the solver has the necessary capabilities to be incorporated into the main solver.

7.2.3 Benchmark problems

The Rayleigh-Bénard convection problem was selected to evaluate the capabilities of the model and its implementation, specifically by solving (4.31) without including the solid fuel equation. These problems were solved using the *Python* CPU implementation described in Sub-section 6.2.1. The physical parameters listed in Table 7.1 were used for the numerical simulation. The computational domain was defined in a two-dimensional spatial region $\Omega = [-1, 2] \times [0, 1]$ m^2, with a total simulation time interval of $t \in [0, 30]$ s. The grid resolution was $N_x \times N_z \times N_t = 511 \times 255 \times 30000$.

For boundary conditions, the velocity field was fixed at $\mathbf{u}(\mathbf{x}, t) = \mathbf{0}$ on the upper and lower boundaries, while periodic conditions were imposed in the x-direction through the "periodic wall" approach within the IBM framework. The initial temperature field was set to $T_0(\mathbf{x}) = T_\infty$ for all $\mathbf{x} \in \Omega$, with the lower and upper boundaries

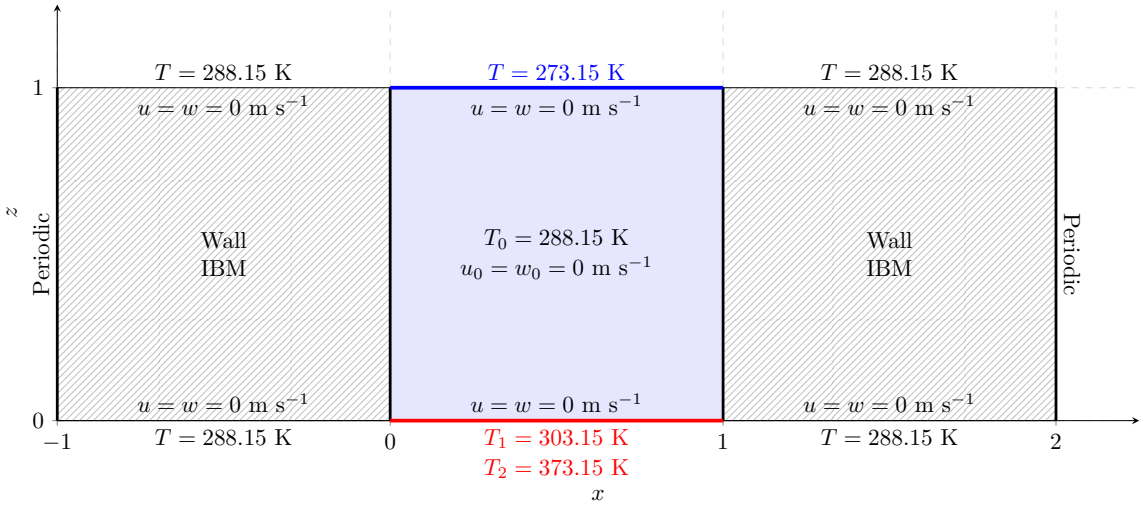

Figure 7.3: Experimental setup description for the Rayleigh-Bénard convection problem.

maintained at constant temperatures of $T(\mathbf{x}) = 303.15$ K and $T(\mathbf{x}) = 273.15$ K, respectively. The velocity field was initialized as $\mathbf{u}_0(\mathbf{x}) = \mathbf{0}$ m s^{-1}. Figure 7.3 summarizes the experimental setup used in the following experiments.

A representative snapshot of the simulation at $t = 25$ s is shown in Figure 7.4.

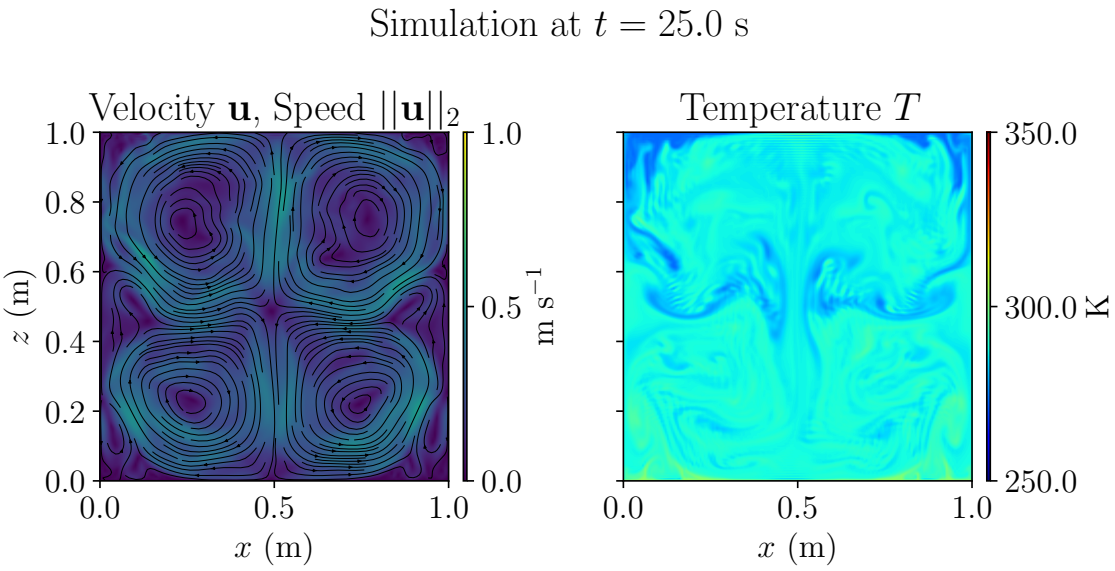

Figure 7.4: First Rayleigh-Bénard convection experiment at $t = 25$ s. The left panel shows the velocity field $\mathbf{u}$ and speed $\|\mathbf{u}\|_2$, and the right panel presents the temperature field T. The characteristic convective rolls are clearly visible, representing the classical steady pattern of buoyancy-driven flow between differentially heated horizontal plates.

A second experiment was designed to analyze the effect of a higher temperature difference, with the bottom boundary set to $T(\mathbf{x}) = 373.15$ K and the top boundary fixed at $T(\mathbf{x}) = 273.15$ K. A maximum simulation time of $t_{\max} = 10$ s and $N_t = 100000$ time steps was used, using the RK2 scheme as the time integration method. The results obtained at the final simulation time are illustrated in Figure 7.5.

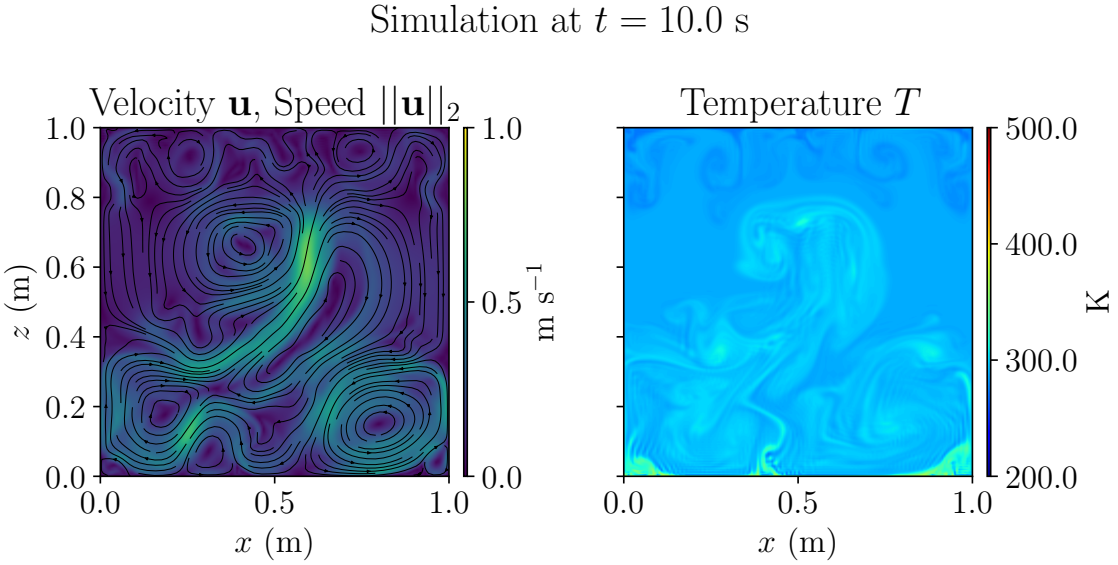

Figure 7.5: Second Rayleigh–Bénard convection experiment at $t = 10$ s. The stronger temperature gradient produces more vigorous convective motion, with the development of small-scale vortices and enhanced plume mixing.

As expected, the larger temperature gradient intensified the buoyancy forces, driving the upward motion of the heated fluid near the lower boundary and the downward motion of the colder fluid near the upper boundary. In the first experiment, the system stabilized into well-defined convective rolls, representative of the steady regime at moderate Rayleigh numbers. In contrast, the second experiment exhibited a transition toward a more dynamic and turbulent state, where the interaction between thermal plumes and vortices led to complex, time-dependent structures. These results are consistent with the expected physical behavior of Rayleigh-Bénard convection (Kästner et al., 2018; Ferialdi & Lappa, 2024), demonstrating that the implemented model correctly reproduces both the laminar and turbulent convective regimes.

7.2.4 Mesh Size effect

Because the LES formulation implemented in this work relies on an implicit filter, the numerical solution is sensitive to mesh resolution (Bose, Moin, & You, 2010; Denaro, 2011). To assess the effect of grid size and domain extent, three numerical experiments were performed in a two-dimensional spatial setup:

1. Experiment 1: $N_x = 512,\ N_z = 256,\ \Omega = [-500, 700] \times [0, 20]$
2. Experiment 2: $N_x = 256,\ N_z = 128,\ \Omega = [-500, 700] \times [0, 20]$
3. Experiment 3: $N_x = 256,\ N_z = 128,\ \Omega = [-250, 350] \times [0, 10]$

Summary of the experimental setup is presented in Figure 7.6.

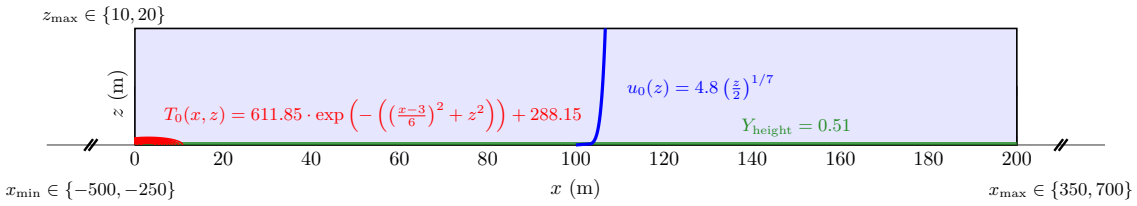

Figure 7.6: Experimental setup of the mesh grid sizes experiment, detailing the domains and initial conditions used.

The comparison of the temperature field at $t = 10$ s is shown in Figure 7.7.

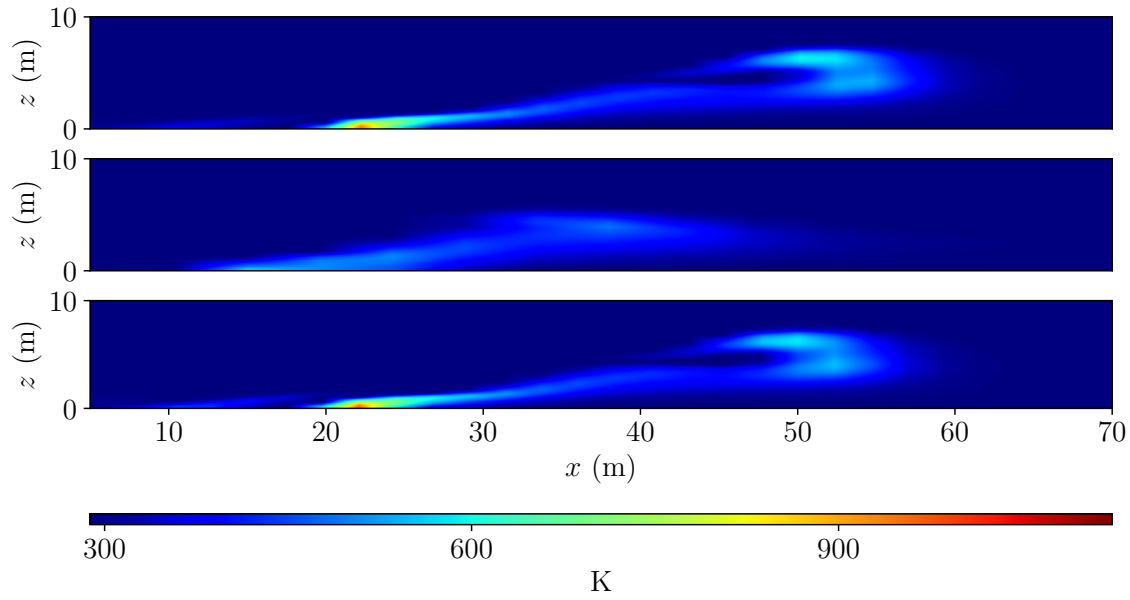

Figure 7.7: Results of different meshes and domain extents. From top to bottom, experiments 1 to 3.

The results highlight the influence of grid resolution on the numerical solution. In particular, maintaining fixed values of Δx and Δz is necessary to achieve comparable results across different configurations. As the grid is refined, smaller turbulent scales and sharper gradients in the flow and temperature fields become better resolved, leading to improved accuracy in capturing buoyancy-driven instabilities and plume dynamics. However, excessively fine grids can increase numerical stiffness and computational cost without significantly altering the large-scale features of the solution,

indicating the presence of a resolution threshold beyond which the solution becomes grid-independent.

Conversely, coarse grids tend to introduce excessive numerical diffusion, which damps small-scale fluctuations and smooths the thermal and velocity fields, potentially suppressing important flow features such as vortex shedding or secondary plume structures. This degradation reflects the implicit filtering inherent in the discretization, where unresolved subgrid-scale motions are artificially dissipated by the numerical scheme rather than being physically modeled.

These findings confirm those of Bose et al. (2010) and Denaro (2011), indicating that the numerical solution utilizing implicit filtering exhibits grid dependency. Therefore, an appropriate grid resolution must be selected to balance accuracy and computational efficiency, ensuring that dominant flow structures are adequately resolved while maintaining numerical stability.

The selection of the mesh grid for the following experiments is based on the results of this sub-section.

7.3 Experiments

The following numerical experiments were conducted to evaluate the model's capabilities:

1. The experiment Case F19 conducted by *CSIRO* which involves a controlled real fire set on flat terrain. The aim is to track the fire front by comparing the actual data and simulated data with the numerical predictions of the proposed model.

2. Four different experiments ranged from a plume-dominated fire to a wind-driven fire, as determined by Byram's convective number criteria. The purpose is to assess the model's ability to handle various fire spread patterns.

3. Two topography experiments were conducted to investigate the impact of slope on the rate of fire spread, as well as a simple hill simulation to understand fire dynamics for this scenario.

4. A three-dimensional experiment on flat terrain. This experiment is intended to evaluate both the fire perimeter patterns and the plume development, considering the full interaction between the fire and the atmosphere.

Experiments 1 to 3 used the CPU implementation in a 2D spatial domain, while the fourth experiment employed the GPU implementation since the 3D computation requirements.

The initial condition for fluid velocity, $\mathbf{u}_0(\mathbf{x}) = (u_0(\mathbf{x}), w_0(\mathbf{x}))$, is based on the power law wind profile,

$$u_0(\mathbf{x}) = u_{\text{ref}} \left(\frac{z}{z_{\text{ref}}} \right)^{1/7}, \; w_0(\mathbf{x}) = 0,$$

where u_{ref} is the reference velocity at height z_{ref} (Mell et al., 1995).

The initial condition for temperature is represented by a half-Gaussian distribution, defined as

$$T_0(\mathbf{x}) = (T_{\text{source}} - T_\infty) \exp\left(-\left(\left(\frac{x - x_T}{s_x}\right)^2 + \left(\frac{z}{s_z}\right)^2\right)\right) + T_\infty,$$

with x_T the center and s_x, s_z parameters used to define the shape of the temperature source. The selection of this configuration seeks to emulate an initial heat source using a differentiable function.

Considering $Z(x)$ as the function to handle the topography effect, the initial condition for the fuel is

$$Y_0(\mathbf{x}) = \begin{cases} 1, & \text{If } z \leq (Z(x) + Y_{\text{height}}), \\ 0, & \text{Otherwise,} \end{cases}$$

where Y_{height} represents a thin layer of fuel over the topography. Observe that the range of values covered by $Z(x)$ includes arbitrary selections for $\mathbf{u}$, T, and Y. However, these selections do not influence the simulation outcome due to the application of IBM. Specifically, the following values are used $\mathbf{u} = \mathbf{0}$, $T = T_\infty$, and $Y = 0$ where $z < Z(x)$.

The Byram's convective number has been employed to categorize experimental fires according to their heat transfer mechanism (Morvan & Frangieh, 2018). This number is computed as follows,

$$N_{\text{C}} = \frac{2gI}{\rho_\infty c_p T_\infty (u_{\text{ref}} - \text{ROS})^3}, \tag{7.3}$$

where g is gravity, I is the intensity of the fireline, ROS is the rate of spread, and u_{ref} is the reference wind speed. The values of N_{C} can suggest the dominance of the heat transfer mechanisms in fires (Frangieh et al., 2020). If N_{C} is less than 2, this implies that convective heat transfer prevails, pointing to a wind-influenced fire. In contrast, when N_{C} exceeds 10, radiative heat transfer takes precedence, suggesting a plume-controlled fire. When N_{C} ranges between 2 and 10, radiative and convective heat transfer play an important role, indicating a mixed heat transfer scenario.

7.3.1 Case F19

The purpose of this experiment is to perform a comparative analysis of the results with experimental and numerical data derived from a real fire event. Initially, the behavior of the Case F19 experiment, which is a controlled fire experiment conducted by the Commonwealth Scientific and Industrial Research Organisation (*CSIRO*) of Australia (Cheney, Gould, & Catchpole, 1993), was documented. Furthermore, numerical simulations of the same experiment as performed by the Fire Dynamics

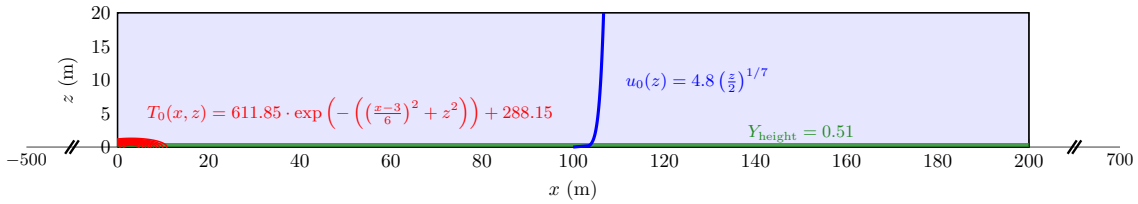

Figure 7.8: Case F19 experimental setup.

Simulator (FDS) (Mell et al., 2007) were also captured. In addition, typical physical quantities reported in other experimental works in the context of fire science are compared. The domain is defined as $\Omega = [-500, 700] \times [0, 20]$ with a grid of $512 \times 256 \times 140000$ nodes. The parameters used are $t_{\max} = 140$ s, $u_{\text{ref}} = 4.8$ ms^{-1}, $Y_{\text{height}} = 0.51$ m, and $Y_{\text{f}} = 70$. The reference velocity and fuel height are based on the values reported in Mell et al. (2007). For the initial ignition temperature, $T_{\text{source}} = 900$ K, $x_T = 3$, $s_x = 6$, and $s_z = 1$ were used. Since the fire spreads over a flat surface, the topography used is $Z(x) = 0$. The experimental setup is detailed in Figure 7.8.

Figure 7.9 presents a snapshot of the numerical simulation.

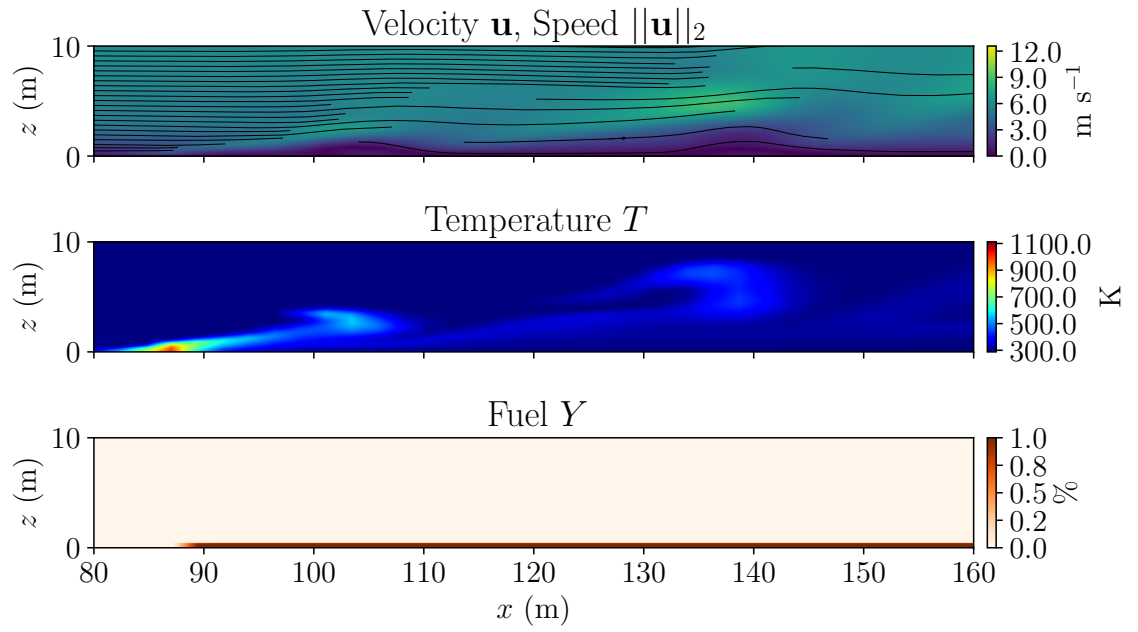

Figure 7.9: Numerical result of the experiment at $t = 56$ s.

Following this, some physical quantities of the simulation are explored.

The Rate of Spread (ROS) in m s^{-1}, as defined in (Byram, 1959; Manzello, 2020), is

$$\text{ROS} = \frac{x_2 - x_1}{t_2 - t_1},$$

where x_1, x_2 are the fire front locations and t_1, t_2 are the times when the location was measured. For the location of the front, two approaches were used: the maximum temperature location and the rightmost x location where $Y < 1$ for each time step. The mean value for both approaches is 1.42 m s^{-1}, which is within the ranges summarized by Speer and Goodrick (2022, p. 220) and Cruz and Alexander (2019). Specifically, the result agrees with the ranges of ROS $\in [0.05, 2.07]$ m s^{-1} presented in Cheney et al. (1993); Cruz et al. (2015); Anderson et al. (2015). To complement the numerical values, the comparison of the fire front between the real experiment, FDS, and the proposed model is summarized in Figure 7.10. The ROS is faster than

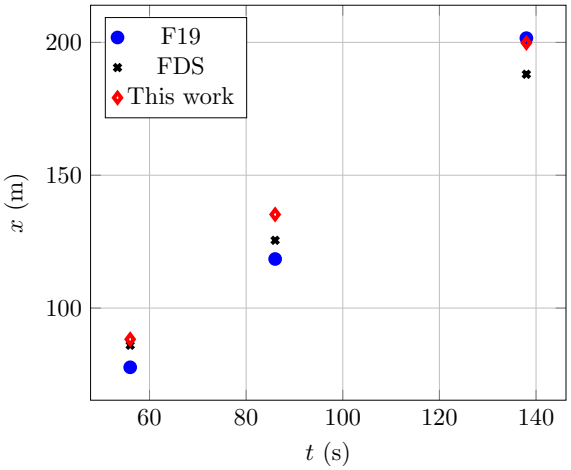

Figure 7.10: Comparison of fire front for times $t \in \{56, 86, 138\}$ s.

the reference data but is still comparable considering the number of simplifications and assumptions made by the proposed model. The Heat Released Rate (HRR) in W is computed according to Himoto (2022); Rangwala and Raghavan (2022) with

$$\text{HRR} = H_C \dot{m}_b,$$

where $\dot{m}_b$ is the fuel consumption rate in kg s^{-1}. Because the fuel density is not directly included and the spatial domain is in the xz plane, the fuel consumption rate is approximated as

$$\dot{m}_b \approx w_s \int_A \frac{\partial Y}{\partial t} dA,$$

with w_s the fuel load in kg m^{-2}, A the solid fuel area, and $dA = \Delta x \Delta z$. Based on Mell et al. (2007), the fuel load is approximated as

$$w_s = \alpha_s Y_{\text{height}} \rho_s,$$

with ρ_s the density of solid fuel. According to Rothermel (1972) and Mell et al. (2007), the density of grass is $\rho_s = 512$ kg m^{-3}, then

$$w_s = 0.002 \times 0.51 \times 512 = 0.52224 \text{ kg m}^{-2}. \tag{7.4}$$

Since Y is available at each time step, $\partial Y/\partial t$ is approximated using finite differences. Taking these values into account, the average fuel consumption rate is $\dot{m}_{\mathrm{b}} = 0.4$ kg s^{-1}, giving an HRR of

$$\mathrm{HRR} \approx 21 \times 10^6 \cdot 0.4 = 8400 \text{ kW},$$

which is in the range of $50 - 20000$ kW according to Z. Wang, Zhang, and Huang (2023).

The geometry of the flame is examined at a threshold of $T \geq 700$ K, based on representative temperature values documented by Finney et al. (2021). Using this threshold, the height and length of the flame were computed at each time step. The height ranged from 0.2 m to 2.9 m, with an average of 0.8 m, which is in agreement with the findings of Y. Zhang and Luo (2024). The flame length ranged from 0.16 m to 12.11 m, with an average of 2.3 m, consistent with Rossa, Davim, Sil, and Fernandes (2024). Finally, the fireline intensity I in kW m^{-1} is calculated using Byram's formula (Alexander & Cruz, 2020),

$$I = H_{\mathrm{C}} w \mathrm{ROS}, \tag{7.5}$$

where w in kg m^{-2} denotes the weight of fuel consumed on the active flame front. The approximation $w = w_{\mathrm{s}} \overline{Y}_{\mathrm{c}}$ is used, where Y_{c} is the representative fuel fraction consumption in the flame front determined from simulations, calculated as

$$Y_{\mathrm{c}}^{n+1} = \int_{\mathrm{FF}^{n+1}} \left(1 - \frac{Y(\mathbf{x}, t^{n+1})}{Y(\mathbf{x}, t^n)}\right) dA,$$

with FF^n the flame front at $t = t_n$. The mean value of Y_{c} is 0.83, giving $w = 0.52 \times 0.83 \approx 0.43$ kg m^{-2}, consistent with the range of 0.1 to 1.0 kg m^{-2} for grasses reported in Finney et al. (2021, p. 37). With a mean ROS of 1.42 m s^{-1},

$$I = 21 \times 10^6 \cdot 0.43 \cdot 1.42 \approx 12823 \text{ kWm}^{-1}.$$

This result falls within the $10 - 100000$ kW m^{-1} range reported in Alexander and Cruz (2020).

Heat fluxes are estimated from the temperature equation as

$$\mathbf{q}_{\text{conduction}} = \kappa \nabla T, \quad \mathbf{q}_{\text{radiation}} = 4\sigma\delta T^3 \nabla T, \quad \mathbf{q}_{\text{convection}} = h_{\mathrm{c}} \alpha_{\mathrm{s}} \sigma_{\mathrm{s}} (T_{\text{gas}} - T_{\text{solid}}).$$

Using the parameters in Table 7.1 and computing $\|\nabla T\|$ in a small neighborhood of the flame, the maximum values are obtained after the outliers are removed. The following values are obtained:

$$\begin{aligned}
\mathbf{q}_{\text{conduction}} &\in [0.01, 0.0464] \text{ kW m}^{-2}, \quad \bar{\mathbf{q}}_{\text{conduction}} = 0.026 \text{ kW m}^{-2}, \\
\mathbf{q}_{\text{radiation}} &\in [3.22, 11.06] \text{ kW m}^{-2}, \quad \bar{\mathbf{q}}_{\text{radiation}} = 6.74 \text{ kW m}^{-2}, \\
\mathbf{q}_{\text{convection}} &\in [7.91, 10.66] \text{ kW m}^{-2}, \quad \bar{\mathbf{q}}_{\text{convection}} = 9.17 \text{ kW m}^{-2}.
\end{aligned}$$

The mean flux is about 15 kW m^{-2}, consistent with the range $5 - 20$ kW m^{-2} reported by Mell et al. (2007) for the same experiment.

Computing Byram's convective number,

$$N_C = \frac{2 \cdot 9.807 \cdot 12823 \times 10^3}{1.225 \cdot 1007 \cdot 288.15 \cdot (4.8 - 1.42)^3} \approx 18.32,$$

classifies the fire as plume-dominated.

Although the mean convective flux is greater than the radiative flux, higher peak radiative fluxes are observed, consistent with the N_C criterion. However, the simplified radiation model can reduce accuracy, and the absence of direct fuel density consideration may overestimate fireline intensity, leading to a higher N_C.

Overall, the model effectively captures the fire propagation behavior, with physical quantities that compare well to experimental studies.

7.3.2 Different fire regimes

To analyze the capabilities of the model, different numerical simulations were conducted based on Byram's criterion. Different values of N_C in equation (7.3) were considered by modifying the reference velocity and fuel height. Both parameters affect N_C, in particular, fuel height influences fuel load w_s when α_s and ρ_s are fixed in (7.4). For these experiments, the domain is $\Omega = [-200, 400] \times [0, 20]$ with a grid of $256 \times 256 \times 30000$ nodes, $t_{max} = 30$ s, $T_{source} = 900$ K, and $Y_f = 70$. The configuration of the experiments is summarized in Figure 7.11,

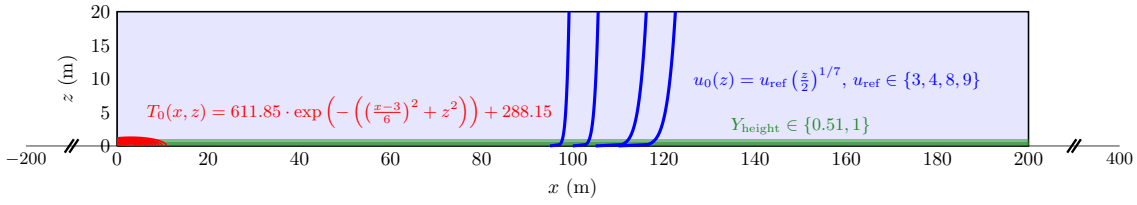

Figure 7.11: Experimental setup to evaluate the model under different fire regimes.

The quantities are computed following the same procedure as indicated in subsection 7.3.1. The summary of the results is presented in Table 7.2 and the fire shapes at the end of the numerical simulations are shown in Figure 7.12.

From Table 7.2, it is apparent that the model effectively represents the dynamics of various fire regimes, ranging from plume-dominated to wind-driven, and produces metrics within the ranges reported. Regarding heat fluxes, the computed values are lower than those of other CFD-based models. However, on average, the results are consistent with Byram's criterion employing the N_C classification.

7.3.3 Topography effect

In the first experiment, the effect of a simple slope on the rate of spread was analyzed. A triangular hill was introduced with its center at $x = 30$ m, and each of its base

Table 7.2: Average quantities for different fire regimes rounded to 0 or 1 decimal respectively. Y_{height} in m, u_{ref} and ROS in m s^{-1}, HRR in kW, I in k Wm^{-1} and heat flux in k Wm^{-2}.

N_{C}	u_{ref}	Y_{height}	ROS	HRR	I	$\mathbf{q}_{\text{radiation}}$, $\mathbf{q}_{\text{convection}}$
283.4	3	1	1.3	25410	24204	10.1, 9.2
104.8	4	1	1.4	27897	28750	10.6, 9.6
5.6	8	1	1.6	29487	28311	13.0, 9.7
1.8	9	0.51	1.6	8784	13591	6.9, 8.5

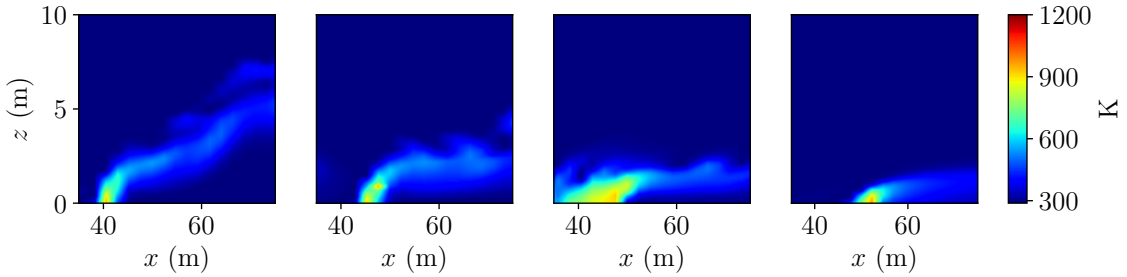

Figure 7.12: Fire shapes for different N_{C} at $t = 30$ s. From left to right $N_{\text{C}} \in \{283.4, 104.8, 5.6, 1.8\}$

angles measuring 10°. Mathematically, the hill is defined by

$$Z(\mathbf{x}) = \begin{cases} x\tan(10°), & \text{If } 0 \leq x < 30, \\ (60 - x)\tan(10°), & \text{If } 30 \leq x \leq 60, \\ 0, & \text{Otherwise.} \end{cases}$$

Figure 7.13 shows the numerical result of this experiment.

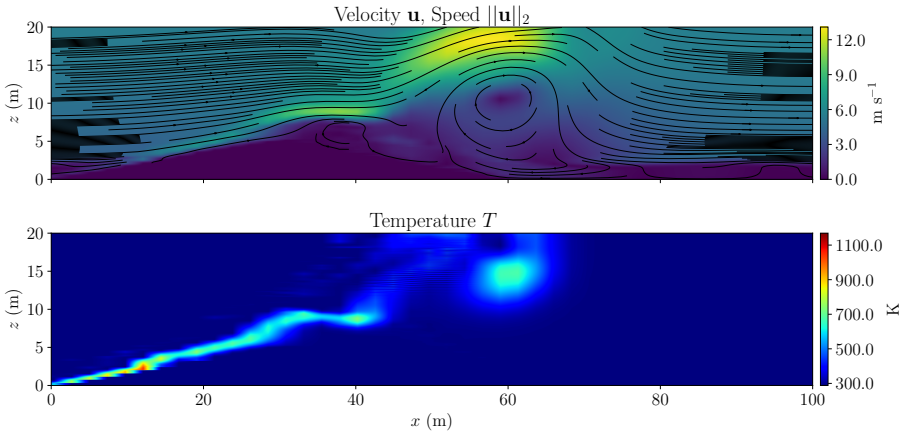

Figure 7.13: Snapshot of the triangular hill experiment at $t = 10$ s.

For comparison, the same experiment was performed without slope. The domain

used is $\Omega = [-200, 400] \times [0, 20]$, $t_{\max} = 15$ s, $256 \times 512 \times 15000$ nodes, $u_{\text{ref}} = 4$ m s^{-1}, $Y_{\text{height}} = 2$ m, $T_{\text{source}} = 900$ K and $Y_{\text{f}} = 100$. The location of the initial temperature source is $x_T = 5$, with $s_x = 10$ and $s_z = 2$. The initial condition for temperature was projected onto the hill, to keep the same shape as used in the flat terrain. The front tracking process adhered to the previously established methodology (experiment in sub-section 7.3.1), but was executed only with the fuel variable in mind. According to McArthur (1967); Opie (2020), *"A head fires' rate of spread doubles for every 10° increase of slope and conversely is halved for backing fires"*.

The flat surface experiment produced an average ROS of 1.31 m s^{-1}. In contrast, the presence of a slope resulted in an average ROS of 1.59 m s^{-1}. The experimental average ROS on the slope was 1.21 times faster than on the flat surface, although it did not reach twice the expected rate as indicated in (McArthur, 1967; Opie, 2020). This discrepancy is attributed to the simplified IBM implementation, which could be improved through alternative boundary representations.

For the second experiment, another topographic effect was examined using a Gaussian-shaped hill defined by

$$Z(x) = 2.5 \exp\left(-\left(\frac{x - 40}{20}\right)^2\right).$$

The domain used was $\Omega = [-500, 700] \times [0, 40]$ with a grid of $256 \times 512 \times 60000$ nodes. The parameters were $t_{\max} = 30$ s, $u_{\text{ref}} = 5$ ms^{-1}, $T_{\text{source}} = 788.15$ K, $Y_{\text{height}} = 1$ m, and $Y_{\text{f}} = 100$. The temperature source was located at $x_T = 3$, with $s_x = 6$, and $s_z = 1$. In addition to the general behavior also exhibited by the simulation without terrain, Figure 7.14 shows how the hill affects the propagation of the fire and the dynamics of the atmosphere.

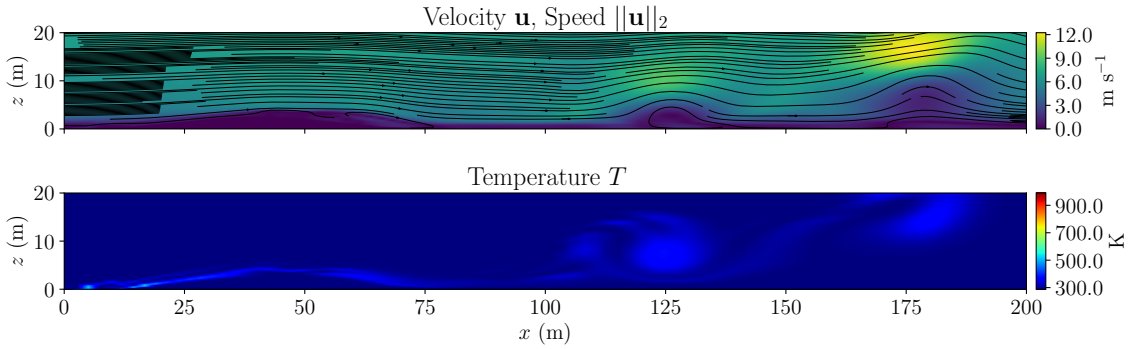

Figure 7.14: Snapshot of the Gaussian hill experiment at $t = 30$ s.

In general, these experiments highlight the significant influence of topography on the dynamics of fire spread. Even in simplified numerical settings, changes in slope and terrain shape lead to measurable differences in the rate of spread and fire–atmosphere interactions. This confirms the importance of incorporating terrain effects into wildfire modeling to achieve realistic predictive capabilities.

7.3.4 3D experiment

A three-dimensional experiment was carried out to demonstrate that the proposed mathematical model can be extended beyond the two-dimensional cases presented in the previous subsections. This experiment illustrates the ability of the formulation and its implementation to capture essential three-dimensional wildfire dynamics, including the interaction between the fire front and the atmosphere.

The initial condition for the fluid velocity $\mathbf{u}_0(\mathbf{x}) = (u_0(\mathbf{x}), v_0(\mathbf{x}), w_0(\mathbf{x}))$ was defined using a power-law wind profile, a widely adopted approach for atmospheric boundary layers. The longitudinal velocity component is prescribed as

$$u_0(\mathbf{x}) = u_{\text{ref}} \left(\frac{z}{z_{\text{ref}}} \right)^{1/7}, \; v_0(\mathbf{x}) = w_0(\mathbf{x}) = 0,$$

while the temperature field is initialized as $T_0(\mathbf{x}) = T_\infty$. A Gaussian-shaped ignition source is introduced between $t = 10$ s and $t = 30$ s, defined by

$$T_0(\mathbf{x}) = (T_{\text{source}} - T_\infty) \exp\left(- \left(\left(\frac{x - x_T}{s_x} \right)^2 + \left(\frac{y - y_T}{s_y} \right)^2 + \left(\frac{z}{s_z} \right)^2 \right) \right) + T_\infty,$$

with $T_{\text{source}} = 2000$ K, $x_T = 5$ m, $y_T = 100$ m, and shape parameters $s_x = 10$, $s_y = 100$, $s_z = 1$.

The computational domain is defined as $\Omega = [-200, 400] \times [-200, 400] \times [0, 40]$ m^3, discretized into $256 \times 256 \times 64$ cells, and numerically integrated for 100000 time steps. The simulation parameters are $t_{\max} = 40$ s, $u_{\text{ref}} = 4.8$ m s^{-1}, $Y_{\text{height}} = 0.51$ m, and $Y_{\text{f}} = 70$. The terrain is assumed to be flat, with $Z(x, y) = 0$. Figure 7.15 summarizes the experimental setup.

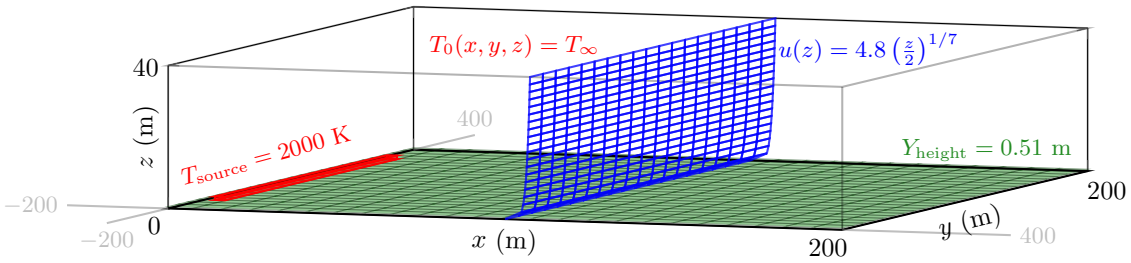

Figure 7.15: Experimental setup used in the three-dimensional wildfire.

A non-uniform mesh is employed in the vertical direction to ensure higher resolution near the ground. The vertical coordinate transformation is given by

$$z(z_{\text{e}}) = \frac{40}{\exp(4) - 1} \left(\exp\left(\frac{z_{\text{e}}}{10} \right) - 1 \right), \qquad z_{\text{e}} \in [0, 40], \tag{7.6}$$

which concentrates nodes close to the surface, allowing for improved resolution of near-ground fire-atmosphere interactions without excessive computational cost.

Representative slices and time steps of the numerical simulation are presented in Figures 7.16 to 7.21. The xz-plane at $y = 100$ m highlights the dynamics of the fire plume and the vertical movement of hot gases, while the xy-plane at $z = 0.05$ m captures the shape of the fire front.

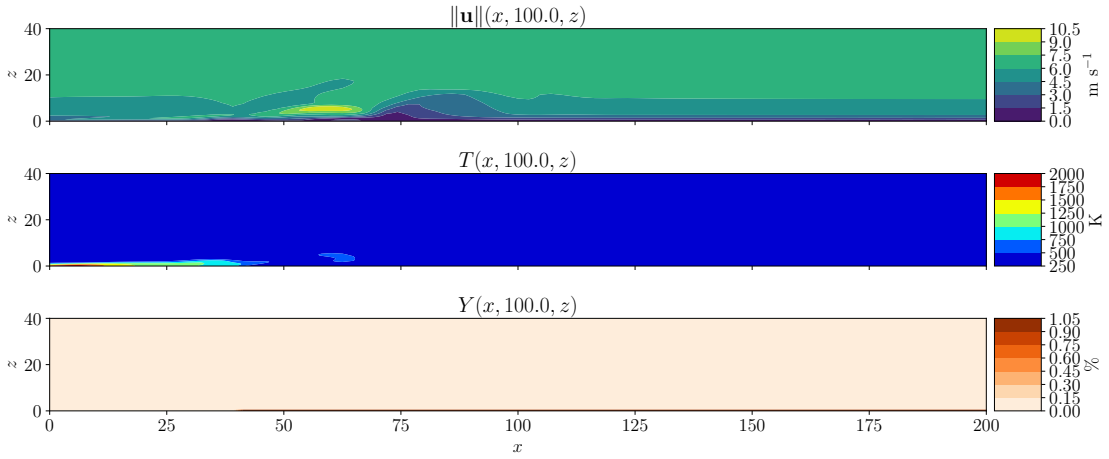

Figure 7.16: Numerical simulation at $y = 100$ m and $t = 20$ s, showing the plume structure in the xz-plane.

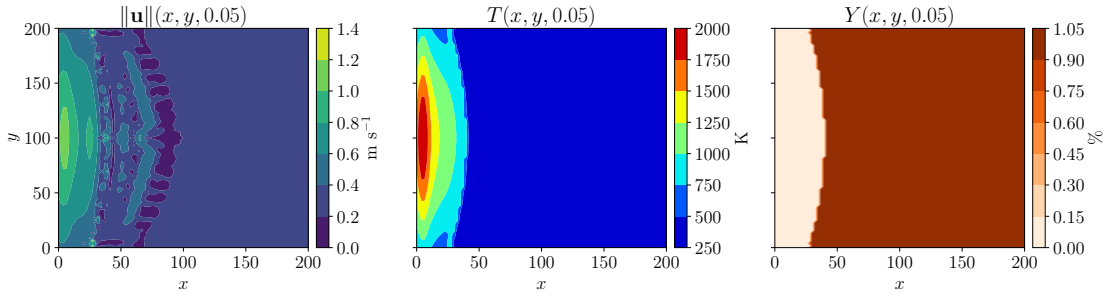

Figure 7.17: Numerical simulation at $z = 0.05$ m and $t = 20$ s, showing the fire front propagation in the xy-plane.

The results clearly reproduce key physical characteristics of a wildfire. Figures 7.17, 7.19, and 7.21 illustrate the evolution and lateral spread of the fire front in the xy-plane, while Figures 7.16, 7.18, and 7.20 reveal the vertical structure of the plume in the xz-plane. The simulation captures the characteristic behavior of buoyancy-driven fire plumes: intense upward motion of hot gases near the ignition region, lateral entrainment of ambient air, and the progressive tilting of the plume under the combined effects of buoyancy and momentum. These features are consistent with experimental and numerical observations reported in the literature (R. Linn et al., 2002; Mell et al., 2007).

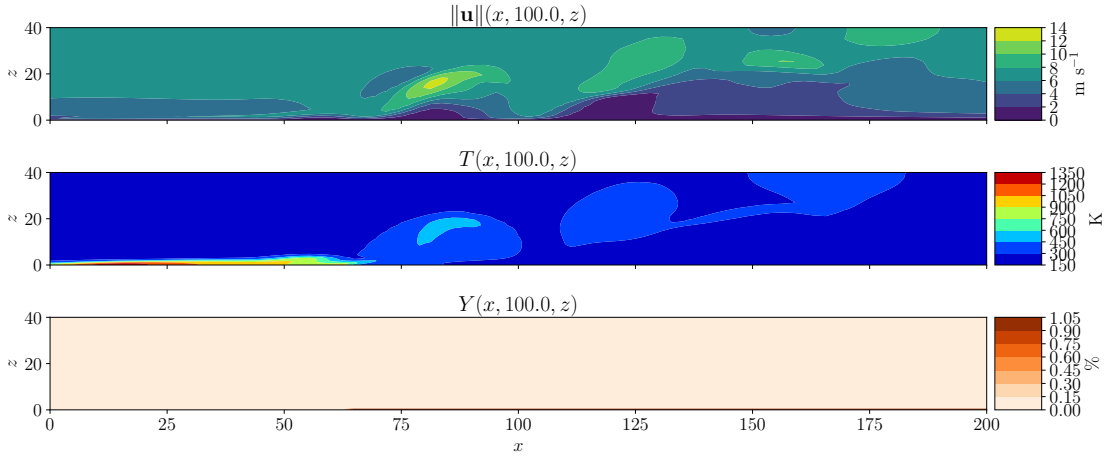

Figure 7.18: Numerical simulation at $y = 100$ m and $t = 32$ s, showing the plume structure in the xz-plane.

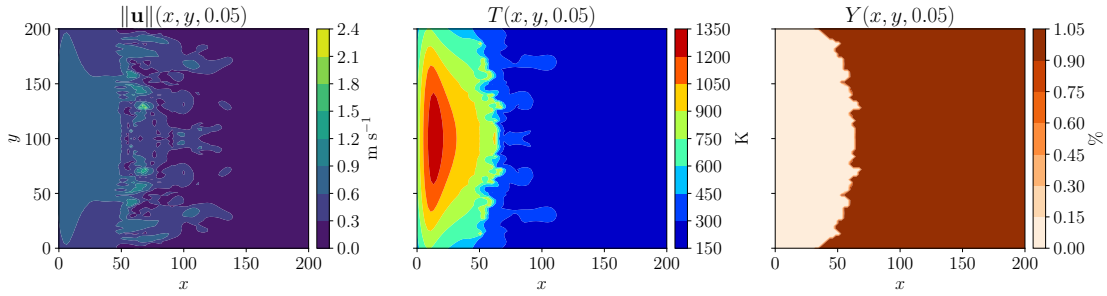

Figure 7.19: Numerical simulation at $z = 0.05$ m and $t = 32$ s, showing the fire front propagation in the xy-plane.

In the early stages of the simulation ($t = 20$ s), the temperature and velocity fields show the formation of a well-defined vertical plume core and the onset of combustion-driven convection. At intermediate times ($t = 32$ s), the plume becomes asymmetric and develops multiple vortical structures, indicating the transition to a more complex, turbulent regime. By $t = 40$ s, strong mixing and entrainment dominate the flow, causing the hot region to expand laterally (Figures 7.20 and 7.21). This evolution is consistent with the typical behavior of buoyant fire plumes, featuring large-scale updrafts and smaller turbulent eddies (Mell et al., 2007).

The corresponding kinetic energy spectrum, shown in Figure 7.22, exhibits a clear inertial subrange that follows the Kolmogorov scaling law $E(k) \propto k^{-5/3}$, demonstrating that the simulation resolves the main inertial and energy-containing scales of turbulence. The drop in spectral energy beyond the cutoff wavenumber k_Δ confirms an adequate numerical dissipation and that the computational grid is sufficiently fine to capture the relevant energy cascade. This spectral behavior is consistent with previous large-eddy simulation (LES) studies of wildfire dynamics (Taha, Zhao,

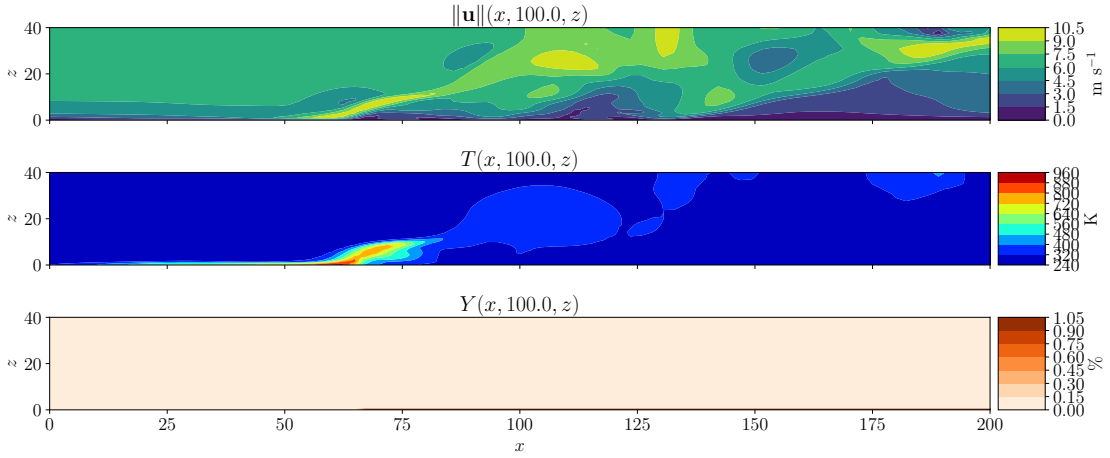

Figure 7.20: Numerical simulation at $y = 100$ m and $t = 40$ s, showing the plume structure in the xz-plane.

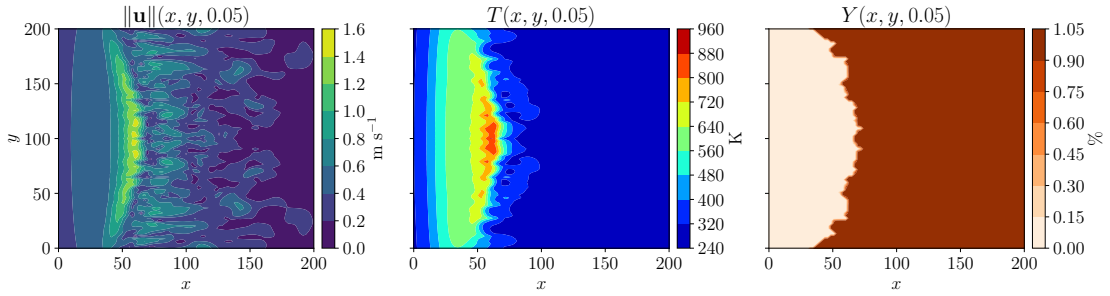

Figure 7.21: Numerical simulation at $z = 0.05$ m and $t = 40$ s, showing the fire front propagation in the xy-plane.

Lamorlette, Consalvi, & Boivin, 2024), where the resolved turbulence range typically spans one to two decades in wavenumber space.

Therefore, the selected grid resolution can be considered appropriate for capturing the dominant turbulent energy transfer in the plume region and the flame-induced flow structures. In general, these results confirm that the proposed three-dimensional implementation preserves the essential physics of the spread of wildfires and provides a reliable foundation for studying more realistic scenarios involving atmospheric coupling and complex terrain.

7.4 Discussion

In terms of the objectives of this work, a coupled atmosphere-fire spread model with a simplified physical formulation is proposed for the numerical simulation of the spread of wildfires. The primary distinction from more detailed CFD models lies

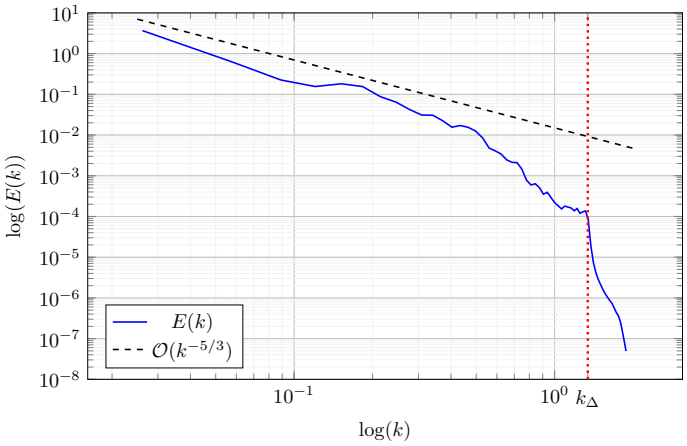

Figure 7.22: Energy cascade of the 3D wildfire simulation. The blue line represents the computed kinetic energy spectrum $E(k)$, while the dashed line shows the theoretical $k^{-5/3}$ slope associated with Kolmogorov turbulence. The vertical dotted line indicates the grid cutoff wavenumber k_Δ.

in the simplifications that reduce the number of variables to be computed. These assumptions partially decrease the accuracy of representing the physical processes, but significantly reduce computational costs, making large-scale simulations feasible.

For example, FIRETEC employs the compressible Navier-Stokes equations with the anelastic approximation of Smolarkiewicz and Margolin (1997), along with simplified combustion (R. Linn, 1997) and radiation transfer models (Dupuy et al., 2011). FDS solves the governing equations of fluid dynamics with the approximation developed by Rehm and Baum (1978), also incorporating simplified combustion and radiation models (K. McGrattan & Miles, 2016). FIRESTAR considers compressible equations for the gas phase, a detailed description of the solid phase, and radiation (Morvan & Dupuy, 2004; Morvan et al., 2018). All of these CFD models employ the full set of fluid flow equations, with variations in the emphasis placed on specific processes, but at a significant computational cost.

In contrast, the model introduced here is based on the low-Mach number approximation, assuming that in wildfire contexts the atmospheric flow is much slower than the speed of sound. This simplification allows for significant variations in density and temperature, while neglecting acoustic pressure waves, a well-established approach in fire modeling (Rehm & Baum, 1978; Mell et al., 1995; Morvan, 2011; K. McGrattan et al., 2012; Morvan et al., 2018). The density of the fluid is computed as a function of temperature using the volumetric thermal expansion of an ideal gas (Tritton, 1977; Batchelor, 2000; Law, 2006), and an expression for the divergence of velocity is derived from the simplified energy equation. Similar formulations exist in the literature (Mell et al., 1995, 2007; Bell et al., 2000), though generally in greater detail in the treatment of mass and temperature sources. This approach avoids solving a transport equation for density while ensuring mass conservation through an equivalent formulation in terms of temperature.

The pressure problem is solved using a pseudo-spectral method enhanced by the Fast Fourier Transform, exploiting periodic boundary conditions in one and two spatial directions. Although initially formulated for constant density, the solver is adapted with an iterative correction that incorporates density variations. This strategy enables the model to capture the effects of buoyancy-driven flows induced by strong temperature gradients, while avoiding the full computational cost of compressible solvers. This constitutes a contribution introduced in the present study. Radiation is not explicitly modeled; instead, it is incorporated into the temperature equation through the diffusion term, following the approaches proposed in (Weber, 1991; Montenegro et al., 1997; Mandel et al., 2008; Eberle et al., 2015).

Despite these simplifications, the model reproduces essential wildfire characteristics and provides estimates for key physical quantities such as the rate of spread, flame geometry, heat flux, heat release rate, and fireline intensity. This balance between computational times and physical realism makes the approach suitable for scenarios where traditional full-physics models are prohibitively expensive.

Chapter 8

Conclusions

This work presents a simplified coupled atmosphere-fire spread model in addition with a numerical method and its open-source implementations. The model employs the low-Mach number approximation for fluid dynamics and a simplified solid fuel formulation, approximations that are well suited to the spatial and temporal scales of wildfire evolution considered in this thesis.

Numerically, the approach is based on operator splitting, with spatial derivatives discretized using Finite Difference methods and time integration performed with explicit schemes. In addition to the first-order Euler method, higher-order Runge-Kutta schemes were implemented, extending the stability domain of the prediction step and permitting larger time steps. For the pressure correction step, a mixed Finite Difference and pseudo-spectral method based on Fourier Transform is employed, combined with an iterative procedure to account for density variations. Topography is represented through the Immersed Boundary Method, while turbulence is modeled using a Large Eddy Simulation with the Smagorinsky closure, enhancing stability and reducing mesh resolution requirements.

The design of the implementation is focused on computational efficiency. A *Python*-based version, optimized with *NumPy*, *SciPy*, and *Numba*, was developed for efficient two-dimensional simulations, enabling rapid prototyping and validation. For three-dimensional simulations, a *CUDA C* implementation was developed, taking advantage of the massive parallelism of GPUs to achieve high performance on modern hardware. This GPU-based solver incorporates grid-stride loops and optimized memory access patterns, providing scalability for large-scale experiments. Additionally, three-dimensional tests included a non-uniform vertical grid, allowing higher resolution near the ground where fire-atmosphere interactions are most intense, while reducing computational cost aloft.

The model successfully captures key wildfire dynamics under conditions such as simple terrain and smooth initial wind and temperature fields. Although simplifications introduce challenges in matching physical parameters with field conditions, the approach achieves competitive predictive capability without the excessive costs of full-physics solvers such as FDS, FIRETEC, FIRESTAR, or OpenFOAM. The results demonstrate that a balance between physical realism and computational ef-

ficiency is attainable. In particular, the integration of operator splitting for the divergence constraint with a pseudo-spectral pressure solver, together with novel algorithms for variable-density treatment and high-performance implementations for both CPUs and GPUs, contributes to advancing the state of reduced-order wildfire modeling. An overview of the state-of-the-art models presented in Chapter 2 and this work in terms of computing and hardware requirements (Table 1.1), is presented in Table 8.1.

Table 8.1: Model comparison in terms of computing and hardware requirements. The computational needs and hardware are determined according to the information provided in the articles detailing the models.

Model	**Computational Requirements**	**Hardware**
FIRETEC	Very High	HPC Cluster
WRF-Fire	Very High	HPC Cluster
ForeFire/Meso-NH	High	HPC Cluster
FIRESTAR	High	HPC Cluster
ARPS/DEVS-Fire	Medium–High	HPC Cluster
FDS	Medium-High	Workstation / HPC Cluster
OpenFOAM	Medium-High	Workstation / HPC Cluster
This Thesis	**Medium–High**	**Workstation (GPU)**
CAWFE	Medium	Workstation
ELMFIRE	Low–Medium	Desktop / Workstation
PhyFire	Low–Medium	Desktop
FlamMap	Low	Desktop

Concerning the hypotheses formulated in this work:

1. The first hypothesis was satisfactorily addressed. The results demonstrate that the proposed model and its implementation are able to reproduce the key metrics commonly used in the fire science community. The supporting evidence for this conclusion is presented in Chapter 7, Section 7.3.

2. The second hypothesis was also satisfactorily addressed. The findings confirm that the model can be implemented efficiently on a GPU, achieving reduced computational times compared to the CPU implementation. The details of this comparison are provided in Chapter 6.

The main contributions of this research are as follows:

1. A simplified coupled atmosphere-fire mathematical model based on the low-Mach number approximation. Although this approach has been used in other state-of-the-art models, the novelty lies in the simplification of certain components based on 2D physics-based models to reduce computing times. The capabilities of the model were presented and published in San Martin and Torres (2025).

2. A numerical solver for low-Mach number fluids has been developed, enabling the inclusion of high-temperature gradients. Moreover, an iterative method utilizing a pseudo-spectral solver is introduced to address the pressure problem, taking into account variable density.

3. Two open-source implementations are publicly available on *GitHub*. The initial version is developed in *Python* for CPUs, using libraries optimized for scientific computation. A second implementation is developed in *CUDA C* specifically for GPUs, employing a parallelization approach that notably decreases the computation times for 3D simulations.

In summary, this thesis delivers a computational framework that incorporates essential fire-atmosphere interactions, making it suitable for research, forecasting, and decision support applications where atmospheric dynamics is important.

8.1 Future Work

Several directions are proposed to extend and improve the present research.

The first direction for future work involves evaluating the model's capabilities using a more extensive data benchmark. This would include utilizing both real and numerical experimental data to gain a comprehensive understanding of the model's performance and potential areas for improvement.

Secondly, the model can be generalized by incorporating the full set of conservation equations for chemical species. This extension would allow for a more detailed representation of combustion processes, enabling the simulation of reactive flows and the transport of combustion products.

Another natural progression is to refine the fluid and solid formulations. The improved governing equations could incorporate more detailed thermophysical properties of the fuels and a more accurate coupling between the gas and solid phases. In parallel, exploring alternative boundary conditions for mathematical formalization would broaden the range of physical scenarios that the model can represent, including more realistic atmospheric and terrain-driven constraints.

From a numerical perspective, future work should emphasize the implementation of high-order discretization methods. In particular, higher-order schemes for both spatial derivatives and time integration could be applied in the corrector step, consequently improving temporal accuracy and enhancing overall numerical stability.

Finally, performance optimization remains a critical aspect for large-scale applications. In-depth performance profiling of GPU and CPU implementations can identify computational bottlenecks and guide targeted improvements, ensuring scalability and efficiency in modern HPC architectures.

Declaration of Generative AI technologies

During the preparation of this work, the author used *Writefull* to improve the readability and language of the manuscript, and *GitHub Copilot* to enhance the code documentation and support in the scripts for visualization and data handling, and *Google Gemini* to generate images. After using these tools, the author reviewed and edited the content as needed and accepts full responsibility for the content of this work.

References

Accary, G., Bessonov, O., Fougère, D., Meradji, S., & Morvan, D. (2007). Optimized Parallel Approach for 3D Modelling of Forest Fire Behaviour. In V. Malyshkin (Ed.), *Parallel Computing Technologies* (pp. 96–102). Berlin, Heidelberg: Springer. doi: 10.1007/978-3-540-73940-1_9

Albini, F. A. (1979). *Spot fire distance from burning trees: A predictive model* (Tech. Rep.). Forest Service, Intermountain Forest and Range Experiment Station.

Alexander, M. E., & Cruz, M. G. (2020). Fireline Intensity. In S. L. Manzello (Ed.), *Encyclopedia of Wildfires and Wildland-Urban Interface (WUI) Fires* (pp. 453–460). Cham: Springer International Publishing. Retrieved 2025-01-08, from https://doi.org/10.1007/978-3-319-52090-2_52 doi: 10.1007/978-3-319-52090-2_52

Anderson, W. R., Cruz, M. G., Fernandes, P. M., McCaw, L., Vega, J. A., Bradstock, R. A., ... Wilgen, B. W. v. (2015, February). A generic, empirical-based model for predicting rate of fire spread in shrublands. *International Journal of Wildland Fire*, *24*(4), 443–460. Retrieved 2024-11-12, from https://www.publish.csiro.au/wf/WF14130 (Publisher: CSIRO PUBLISHING) doi: 10.1071/WF14130

Andrianarivony, H. S., & Akhloufi, M. A. (2024, December). Machine Learning and Deep Learning for Wildfire Spread Prediction: A Review. *Fire*, *7*(12), 482. Retrieved 2025-08-24, from https://www.mdpi.com/2571-6255/7/12/482 doi: 10.3390/fire7120482

Asensio, M. I., Cascón, J. M., Prieto-Herráez, D., & Ferragut, L. (2023, February). An Historical Review of the Simplified Physical Fire Spread Model PhyFire: Model and Numerical Methods. *Applied Sciences*, *13*(4), 2035. Retrieved 2023-02-27, from https://www.mdpi.com/2076-3417/13/4/2035 (Publisher: Multidisciplinary Digital Publishing Institute) doi: 10.3390/app13042035

Asensio, M. I., & Ferragut, L. (2002, May). On a wildland fire model with radiation. *International Journal for Numerical Methods in Engineering*, *54*(1), 137–157. Retrieved 2019-05-16, from https://onlinelibrary.wiley.com/doi/abs/10.1002/nme.420 (Publisher: John Wiley & Sons, Ltd) doi: 10.1002/nme.420

Asensio, M. I., Luis, F., & Jacques, S. (2002). Modelling of convective phenomena in forest fire. *RACSAM*, *96*(3), 299–313. Retrieved from http://eudml.org/doc/40937

Bakhshaii, A., & Johnson, E. A. (2019). A review of a new generation of wild-

fire–atmosphere modeling. *Canadian Journal of Forest Research*, *49*(6), 565–574. doi: 10.1139/cjfr-2018-0138

Balbi, J. H., Morandini, F., Silvani, X., Filippi, J. B., & Rinieri, F. (2009, December). A physical model for wildland fires. *Combustion and Flame*, *156*(12), 2217–2230. (Publisher: Elsevier) doi: 10.1016/j.combustflame.2009.07.010

Batchelor, G. K. (2000). *An Introduction to Fluid Dynamics*. Cambridge University Press. Retrieved 2022-01-14, from https://www.cambridge.org/core/product/identifier/9780511800955/type/book doi: 10.1017/CBO9780511800955

Batiot, B., Rogaume, T., Richard, F., Luche, J., Collin, A., Guillaume, E., & Torero, J. L. (2021). Origin and justification of the use of the arrhenius relation to represent the reaction rate of the thermal decomposition of a solid. *Applied Sciences (Switzerland)*, *11*(9). doi: 10.3390/app11094075

Baum, H. R., Ezekoye, O. A., McGrattan, K. B., & Rehm, R. G. (1994, April). Mathematical modeling and computer simulation of fire phenomena. *Theoretical and Computational Fluid Dynamics 1994 6:2*, *6*(2), 125–139. Retrieved 2022-06-07, from https://link.springer.com/article/10.1007/BF00312345 (Publisher: Springer) doi: 10.1007/BF00312345

Bell, J. B., Brown, N. J., Day, M. S., Frenklach, M., Grcar, J. F., & Tonse, S. R. (2000, January). The dependence of chemistry on the inlet equivalence ratio in vortex-flame interactions. *Proceedings of the Combustion Institute*, *28*(2), 1933–1939. Retrieved 2025-03-07, from https://www.sciencedirect.com/science/article/pii/S0082078400805986 doi: 10.1016/S0082-0784(00)80598-6

Benarafa, Y., Cioni, O., Ducros, F., & Sagaut, P. (2006, April). RANS/LES coupling for unsteady turbulent flow simulation at high Reynolds number on coarse meshes. *Computer Methods in Applied Mechanics and Engineering*, *195*(23), 2939–2960. Retrieved 2025-08-27, from https://www.sciencedirect.com/science/article/pii/S0045782505002343 doi: 10.1016/j.cma.2005.06.007

Bose, S. T., Moin, P., & You, D. (2010, October). Grid-independent large-eddy simulation using explicit filtering. *Physics of Fluids*, *22*(10), 105103. Retrieved 2024-12-20, from https://doi.org/10.1063/1.3485774 doi: 10.1063/1.3485774

Byram, G. M. (1959). Combustion of forest fuels. In K. Davis (Ed.), *Forest fire: control and use* (pp. 61–89). McGraw-Hill: New York.

Cheney, N. P., Gould, J. S., & Catchpole, W. R. (1993). The Influence of Fuel, Weather and Fire Shape Variables on Fire-Spread in Grasslands. *International Journal of Wildland Fire*, *3*(1), 31–44. Retrieved 2023-04-18, from https://www.publish.csiro.au/wf/wf9930031 (Publisher: CSIRO PUBLISHING) doi: 10.1071/WF9930031

Chien, M. H., & Wu, C. M. (2016, March). Representation of topography by partial steps using the immersed boundary method in a vector vorticity equation model (VVM). *Journal of Advances in Modeling Earth Systems*, *8*(1), 212–

223. Retrieved 2022-07-14, from https://onlinelibrary.wiley.com/doi/full/10.1002/2015MS000514 (Publisher: John Wiley & Sons, Ltd) doi: 10.1002/2015MS000514

Chorin, A. J. (1967, August). A numerical method for solving incompressible viscous flow problems. *Journal of Computational Physics*, *2*(1), 12–26. (Publisher: Academic Press) doi: 10.1016/0021-9991(67)90037-X

Chorin, A. J. (1968). Numerical solution of the Navier-Stokes equations. *Mathematics of Computation*, *22*(104), 745–762. Retrieved 2021-12-06, from https://www.ams.org/mcom/1968-22-104/S0025-5718-1968-0242392-2/ (Publisher: American Mathematical Society (AMS)) doi: 10.1090/S0025-5718-1968-0242392-2

Clark, T. L., Coen, J., & Latham, D. (2004). Description of a coupled atmosphere-fire model. *International Journal of Wildland Fire*, *13*(1), 49–63. doi: 10.1071/WF03043

Clark, T. L., Jenkins, M. A., Coen, J., & Packham, D. (1996a, June). A Coupled Atmosphere-Fire Model: Convective Feedback on Fire-Line Dynamics. *Journal of Applied Meteorology*, *35*(6), 875–901. Retrieved from http://journals.ametsoc.org/doi/abs/10.1175/1520-0450%281996%29035%3C0875%3AACAMCF%3E2.0.CO%3B2 doi: 10.1175/1520-0450(1996)035⟨0875:ACAMCF⟩2.0.CO;2

Clark, T. L., Jenkins, M. A., Coen, J. L., & Packham, D. R. (1996b). A coupled atmosphere-fire model: Role of the convective froude number and dynamic fingering at the fireline. *International Journal of Wildland Fire*, *6*(4), 177–190. doi: 10.1071/WF9960177

Coen, J. L. (2005). Simulation of the Big Elk Fire using coupled atmosphere-fire modeling. *International Journal of Wildland Fire*, *14*(1), 49–59. doi: 10.1071/WF04047

Coen, J. L., Cameron, M., Michalakes, J., Patton, E. G., Riggan, P. J., & Yedinak, K. M. (2013, January). WRF-fire: Coupled weather-wildland fire modeling with the weather research and forecasting model. *Journal of Applied Meteorology and Climatology*, *52*(1), 16–38. Retrieved 2021-03-25, from https://journals.ametsoc.org/view/journals/apme/52/1/jamc-d-12-023.1.xml doi: 10.1175/JAMC-D-12-023.1

CONAF. (2025a). *Centro Documental.* Retrieved 2025-09-09, from https://www.conaf.cl/centro-documental/

CONAF. (2025b). *Prevención y mitigación.* Retrieved 2025-09-09, from https://www.conaf.cl/incendios/prevencion-y-mitigacion/

Cruz, M. G., & Alexander, M. E. (2019, June). The 10% wind speed rule of thumb for estimating a wildfire's forward rate of spread in forests and shrublands. *Annals of Forest Science*, *76*(2), 1–11. Retrieved 2021-12-01, from https://link.springer.com/article/10.1007/s13595-019-0829-8 (Publisher: Springer-Verlag France) doi: 10.1007/S13595-019-0829-8/FIGURES/5

Cruz, M. G., Alexander, M. E., & Wakimoto, R. H. (2005, July). Development and

testing of models for predicting crown fire rate of spread in conifer forest stands. *Canadian Journal of Forest Research*, *35*(7), 1626–1639. Retrieved 2025-09-04, from https://cdnsciencepub.com/doi/10.1139/x05-085 (Publisher: NRC Research Press) doi: 10.1139/x05-085

Cruz, M. G., Gould, J. S., Kidnie, S., Bessell, R., Nichols, D., & Slijepcevic, A. (2015, July). Effects of curing on grassfires: II. Effect of grass senescence on the rate of fire spread. *International Journal of Wildland Fire*, *24*(6), 838–848. Retrieved 2024-11-12, from https://www.publish.csiro.au/wf/WF14146 (Publisher: CSIRO PUBLISHING) doi: 10.1071/WF14146

Cuesta, A., Martinez-Alonso, A., & Tascon, J. M. D. (1993, November). Correlation between Arrhenius kinetic parameters in the reaction of different carbon materials with oxygen. *Energy & Fuels*, *7*(6), 1141–1145. Retrieved 2024-11-11, from https://doi.org/10.1021/ef00042a064 (Publisher: American Chemical Society) doi: 10.1021/ef00042a064

Dahl, N., Xue, H., Hu, X., & Xue, M. (2015). Coupled fire–atmosphere modeling of wildland fire spread using DEVS-FIRE and ARPS. *Natural Hazards*, *77*(2), 1013–1035. doi: 10.1007/s11069-015-1640-y

Deardorff, J. W. (1970, April). A numerical study of three-dimensional turbulent channel flow at large Reynolds numbers. *Journal of Fluid Mechanics*, *41*(2), 453–480. Retrieved 2021-04-12, from https://www.cambridge.org/core/journals/journal-of-fluid-mechanics/article/abs/numerical-study-of-threedimensional-turbulent-channel-flow-at-large-reynolds-numbers/D84769F4A3443E4C87E8878303890999 (Publisher: Cambridge University Press) doi: 10.1017/S0022112070000691

Denaro, F. M. (2011, May). What does Finite Volume-based implicit filtering really resolve in Large-Eddy Simulations? *Journal of Computational Physics*, *230*(10), 3849–3883. Retrieved 2024-12-19, from https://www.sciencedirect.com/science/article/pii/S0021999111000933 doi: 10.1016/j.jcp.2011.02.011

Di Blasi, C., Branca, C., Santoro, A., & Gonzalez Hernandez, E. (2001, January). Pyrolytic behavior and products of some wood varieties. *Combustion and Flame*, *124*(1), 165–177. Retrieved 2025-04-16, from https://www.sciencedirect.com/science/article/pii/S0010218000001917 doi: 10.1016/S0010-2180(00)00191-7

Di Virgilio, G., Evans, J. P., Blake, S. A., Armstrong, M., Dowdy, A. J., Sharples, J., & McRae, R. (2019, July). Climate Change Increases the Potential for Extreme Wildfires. *Geophysical Research Letters*, *46*(14), 8517–8526. Retrieved 2023-01-06, from https://onlinelibrary.wiley.com/doi/full/10.1029/2019GL083699 (Publisher: John Wiley & Sons, Ltd) doi: 10.1029/2019GL083699

Drysdale, D. (2011). *An Introduction to Fire Dynamics*. Wiley. Retrieved from https://www.wiley.com/en-be/An+Introduction+to+Fire+Dynamics%2C+3rd+Edition-p-9780470319031

Dupuy, J. L., Linn, R. R., Konovalov, V., Pimont, F., Vega, J. A., & Jiménez, E. (2011). Exploring three-dimensional coupled fireatmosphere interactions downwind of wind-driven surface fires and their influence on backfires using the HIGRAD-FIRETEC model. *International Journal of Wildland Fire*, *20*(6), 734–750. doi: 10.1071/WF10035

Eberle, S. (2014). Modeling and Simulation of Forest Fire Spreading. In Pardo-Igúzquiza Eulogio et al. (Eds.), *Mathematics of Planet Earth* (pp. 811–814). Berlin, Heidelberg: Springer, Berlin, Heidelberg. Retrieved 2019-05-16, from http://link.springer.com/10.1007/978-3-642-32408-6_175 doi: 10.1007/978-3-642-32408-6_175

Eberle, S., Freeden, W., & Matthes, U. (2015). Forest Fire Spreading. In Freeden, Willi, Nashed, M. Zuhair, & Sonar, Thomas (Eds.), *Handbook of Geomathematics* (pp. 1349–1385). Berlin, Heidelberg: Springer Berlin Heidelberg. Retrieved 2019-04-29, from https://link.springer.com/10.1007/978-3-642-54551-1_70 doi: 10.1007/978-3-642-54551-1_70

El Houssami, M., Lamorlette, A., Morvan, D., Hadden, R. M., & Simeoni, A. (2018, April). Framework for submodel improvement in wildfire modeling. *Combustion and Flame*, *190*, 12–24. Retrieved 2025-04-16, from https://www.sciencedirect.com/science/article/pii/S0010218017303760 doi: 10.1016/j.combustflame.2017.09.038

European Court of Auditors. (2025). *Special report 16/2025: EU funding to tackle forest fires.* Retrieved 2025-09-17, from http://www.eca.europa.eu/en/publications/sr-2025-16

Fadlun, E. A., Verzicco, R., Orlandi, P., & Mohd-Yusof, J. (2000, June). Combined Immersed-Boundary Finite-Difference Methods for Three-Dimensional Complex Flow Simulations. *Journal of Computational Physics*, *161*(1), 35–60. (Publisher: Academic Press) doi: 10.1006/JCPH.2000.6484

Ferialdi, H., & Lappa, M. (2024, August). An experimental and numerical investigation into the sensitivity of Rayleigh–Bénard convection to heat loss through the sidewalls. *Physica D: Nonlinear Phenomena*, *464*, 134190. Retrieved 2025-11-05, from https://www.sciencedirect.com/science/article/pii/S0167278924001416 doi: 10.1016/j.physd.2024.134190

Ferragut, L., Asensio, M. I., Cascón, J. M., & Prieto, D. (2015, January). A Wildland Fire Physical Model Well Suited to Data Assimilation. *Pure and Applied Geophysics*, *172*(1), 121–139. Retrieved 2019-05-16, from http://link.springer.com/10.1007/s00024-014-0893-9 (Publisher: Springer Basel) doi: 10.1007/s00024-014-0893-9

Ferragut, L., Asensio, M. I., & Monedero, S. (2006, October). Modelling radiation and moisture content in fire spread. *Communications in Numerical Methods in Engineering*, *23*(9), 819–833. Retrieved from https://onlinelibrary.wiley.com/doi/10.1002/cnm.927 doi: 10.1002/cnm.927

Ferragut, L., Asensio, M. I., & Monedero, S. (2007, June). A numerical method for solving convection-reaction-diffusion multivalued equations in fire spread

modelling. *Advances in Engineering Software*, *38*(6), 366–371. Retrieved 2018-06-01, from https://www.sciencedirect.com/science/article/pii/S096599780600127X (Publisher: Elsevier) doi: 10.1016/j.advengsoft.2006.09.007

Ferragut, L., Asensio, M. I., & Simon, J. (2011, April). High definition local adjustment model of 3D wind fields performing only 2D computations. *International Journal for Numerical Methods in Biomedical Engineering*, *27*(4), 510–523. Retrieved 2023-02-27, from https://onlinelibrary.wiley.com/doi/full/10.1002/cnm.1314 (Publisher: John Wiley & Sons, Ltd) doi: 10.1002/CNM.1314

Ferziger, J. H., Perić, M., & Street, R. L. (2020). *Computational Methods for Fluid Dynamics*. Cham: Springer International Publishing. Retrieved 2021-11-22, from http://link.springer.com/10.1007/978-3-319-99693-6 (Publication Title: Computational Methods for Fluid Dynamics) doi: 10.1007/978-3-319-99693-6

Filippi, J. B., Bosseur, F., Pialat, X., Santoni, P. A., Strada, S., & Mari, C. (2011). Simulation of coupled fire/atmosphere interaction with the MesoNH-ForeFire models. *Journal of Combustion*, *2011*. doi: 10.1155/2011/540390

Finney, M. A. (1998). *FARSITE: Fire Area Simulator-model development and evaluation* (Tech. Rep.). U.S. Department of Agriculture, Forest Service, Rocky Mountain Research Station. Retrieved from https://www.fs.usda.gov/treesearch/pubs/4617 (Volume: 3 Issue: March) doi: 10.2737/RMRS-RP-4

Finney, M. A. (2006, March). An Overview of FlamMap Fire Modeling Capabilities. In *In: Andrews, Patricia L.; Butler, Bret W., comps. 2006. Fuels Management-How to Measure Success: Conference Proceedings. 28-30 March 2006; Portland, OR. Proceedings RMRS-P-41. Fort Collins, CO: U.S. Department of Agriculture, Forest Service, Rocky Mountain Research Station. p. 213-220.* Retrieved 2024-08-28, from https://research.fs.usda.gov/treesearch/25948

Finney, M. A., McAllister, S. S., Grumstrup, T. P., & Forthofer, J. M. (2021). *Wildland Fire Behaviour*. CSIRO Publishing. Retrieved from https://ebooks.publish.csiro.au/content/9781486309092/9781486309092 doi: 10.1071/9781486309092

Forthofer, J., Shannon, K., & Butler, B. (2009). Simulating diurnally driven slope winds with WindNinja..

Forthofer, J. M., Butler, B. W., & Wagenbrenner, N. S. (2014a, August). A comparison of three approaches for simulating fine-scale surface winds in support of wildland fire management. Part I. Model formulation and comparison against measurements. *International Journal of Wildland Fire*, *23*(7), 969–981. Retrieved 2025-09-04, from https://www.publish.csiro.au/wf/WF12089 (Publisher: CSIRO PUBLISHING) doi: 10.1071/WF12089

Forthofer, J. M., Butler, B. W., & Wagenbrenner, N. S. (2014b, August). A comparison of three approaches for simulating fine-scale surface winds in sup-

port of wildland fire management. Part I. Model formulation and comparison against measurements. *International Journal of Wildland Fire*, *23*(7), 969–981. Retrieved 2025-06-20, from https://www.publish.csiro.au/wf/WF12089 (Publisher: CSIRO PUBLISHING) doi: 10.1071/WF12089

Frangieh, N., Accary, G., Morvan, D., Méradji, S., & Bessonov, O. (2020). Wildfires front dynamics: 3D structures and intensity at small and large scales. *Combustion and Flame*, *211*, 54–67. Retrieved from https://doi.org/10.1016/j.combustflame.2019.09.017 (Publisher: Elsevier Inc.) doi: 10.1016/j.combustflame.2019.09.017

Ghaderi, M., Ghodrat, M., & Sharples, J. J. (2021, January). LES Simulation of Wind-Driven Wildfire Interaction with Idealized Structures in the Wildland-Urban Interface. *Atmosphere*, *12*(1), 21. Retrieved 2024-12-17, from https://www.mdpi.com/2073-4433/12/1/21 (Number: 1 Publisher: Multidisciplinary Digital Publishing Institute) doi: 10.3390/atmos12010021

Ghodrat, M., Edalati-Nejad, A., & Simeoni, A. (2022, December). Collective Effects of Fire Intensity and Sloped Terrain on Wind-Driven Surface Fire and Its Impact on a Cubic Structure. *Fire*, *5*(6), 208. Retrieved 2025-01-08, from https://www.mdpi.com/2571-6255/5/6/208 (Number: 6 Publisher: Multidisciplinary Digital Publishing Institute) doi: 10.3390/fire5060208

Ghodrat, M., Edalati-nejad, A., Simeoni, A., Dlugogorski, B. Z., & Masri, A. R. (2023, November). 3D CFD modeling of the Effect of Sloped Terrain on Dynamics of Wildfires in Wildland Urban Interface. In (pp. 78–78). Charles Darwin University. Retrieved 2024-12-17, from http://hdl.handle.net/1959.4/unsworks_85071 (ISSN: 1839-8162) doi: 10.26190/unsworks/28676

Greenshields, C. (2025). *OpenFOAM v13 User Guide*. London, UK: The OpenFOAM Foundation. Retrieved from https://doc.cfd.direct/openfoam/user-guide-v13

Greenshields, C., & Weller, H. (2022). *Notes on Computational Fluid Dynamics: General Principles*. Reading, UK: CFD Direct Ltd.

Harris, M. (2013, April). *CUDA Pro Tip: Write Flexible Kernels with Grid-Stride Loops*. Retrieved 2025-09-09, from https://developer.nvidia.com/blog/cuda-pro-tip-write-flexible-kernels-grid-stride-loops/

Himoto, K. (2022). *Large Outdoor Fire Dynamics*. Boca Raton: CRC Press. doi: 10.1201/9781003096689

Hoover, K., & Hanson, L. A. (2022, December). *Wildfire Statistics* (Tech. Rep.). Congressional Research Service.

Houssami, M. E., Thomas, J. C., Lamorlette, A., Morvan, D., Chaos, M., Hadden, R., & Simeoni, A. (2016, June). Experimental and numerical studies characterizing the burning dynamics of wildland fuels. *Combustion and Flame*, *168*, 113–126. Retrieved 2024-12-17, from https://www.sciencedirect.com/science/article/pii/S0010218016300517 doi: 10.1016/j.combustflame.2016.04.004

Hu, X., Sun, Y., & Ntaimo, L. (2012). DEVS-FIRE: Design and application of formal discrete event wildfire spread and suppression models. *Simulation*, *88*(3), 259–

279. doi: 10.1177/0037549711414592

Jiang, X., & Lai, C.-H. (2009). *Numerical Techniques for Direct and Large-Eddy Simulations*. Boca Raton: CRC Press. Retrieved 2022-05-20, from https://www.taylorfrancis.com/books/9781420075793 (Publication Title: Numerical Techniques for Direct and Large-Eddy Simulations) doi: 10.1201/9781420075793

Kamma, P., Loksupapaiboon, K., Phromjan, J., & Suvanjumrat, C. (2025). Enhancing Combustion Analysis: Implementation and Validation of Laminar Premixed Methane-Air Jet-Impinging Flame Simulation in OpenFOAM. *Journal of Research and Applications in Mechanical Engineering (JRAME)*, *13*, JRAME25. Retrieved 2025-08-24, from http://doi.nrct.go.th/?page=resolve_doi&resolve_doi=10.14456/jrame.2025.22 (Publisher: Thai Society of Mechanical Engineers (TSME)) doi: 10.14456/JRAME.2025.22

Kirk, D. B., & Hwu, W.-m. W. (2012). *Programming Massively Parallel Processors: A Hands-on Approach* (2nd ed.). San Francisco, CA, USA: Morgan Kaufmann Publishers Inc.

Kuwana, K. (2020). Fluid Mechanics. In S. L. Manzello (Ed.), *Encyclopedia of Wildfires and Wildland-Urban Interface (WUI) Fires* (pp. 483–490). Cham: Springer International Publishing. Retrieved 2025-01-13, from https://doi.org/10.1007/978-3-319-52090-2_149 doi: 10.1007/978-3-319-52090-2_149

Kästner, C., Resagk, C., Westphalen, J., Junghähnel, M., Cierpka, C., & Schumacher, J. (2018, October). Assessment of horizontal velocity fields in square thermal convection cells with large aspect ratio. *Experiments in Fluids*, *59*(11), 171. Retrieved 2025-11-05, from https://doi.org/10.1007/s00348-018-2626-9 doi: 10.1007/s00348-018-2626-9

Lafore, J. P., Stein, J., Asencio, N., Bougeault, P., Ducrocq, V., Duron, J., ... Vilà-Guerau de Arellano, J. (1998, January). The Meso-NH Atmospheric Simulation System. Part I: adiabatic formulation and control simulations. *Annales Geophysicae*, *16*(1), 90–109. (Publisher: Copernicus GmbH) doi: 10.1007/s00585-997-0090-6

Lapointe, C., Wimer, N. T., Simons-Wellin, S., Glusman, J. F., Rieker, G. B., & Hamlington, P. E. (2021). Efficient Simulations of Propagating Flames and Fire Suppression Optimization Using Adaptive Mesh Refinement. *Fluids*, *6*(9). Retrieved from https://www.mdpi.com/2311-5521/6/9/323 doi: 10.3390/fluids6090323

Lautenberger, C. (2013, November). Wildland fire modeling with an Eulerian level set method and automated calibration. *Fire Safety Journal*, *62*(PART C), 289–298. doi: 10.1016/J.FIRESAF.2013.08.014

Lautenberger, C. (2025). *ELMFIRE- Eulerian Level Set Model of FIRE spread.* Retrieved 2025-09-04, from https://elmfire.io

Law, C. K. (2006). *Combustion Physics*. Cambridge: Cambridge University Press. Retrieved 2023-10-05, from https://www.cambridge.org/core/

books/combustion-physics/8259DA7A712262E03DD72C365F89F32E doi: 10.1017/CBO9780511754517

Lin, D., Katurji, M., Zawar-Reza, P., Malyarenko, A., Valencia, A., & Zhang, J. (2024, August). *Fire-Atmosphere Interactions in the Wildland-Urban Interface Using High-Fidelity Experimental Simulations.* Retrieved 2024-11-07, from https://www.authorea.com/users/813986/articles/1215184-fire-atmosphere-interactions-in-the-wildland-urban-interface-using-high-fidelity-experimental-simulations doi: 10.22541/essoar.172374094.40776483/v1

Linn, R. (1997). *A transport model for prediction of wildfire behavior* (Doctoral dissertation, Los Alamos National Laboratory (LANL), Los Alamos, NM). doi: 10.2172/505313

Linn, R. (2019). Fluid dynamics of wildfires. *Physics Today*, *72*(11), 70–71. doi: 10.1063/PT.3.4350

Linn, R., Reisner, J., Colman, J. J., & Winterkamp, J. (2002). Studying wildfire behavior using FIRETEC. *International Journal of Wildland Fire*, *11*(3-4), 233–246. Retrieved 2023-05-03, from https://doi.org/10.1071/WF02007 doi: 10.1071/wf02007

Linn, R. R., & Harlow, F. (1998). FIRETEC: A transport description of wildfire behavior. *Second Symposium on Fire and Forest Meteorology*, *836*(1 046), 14–19. Retrieved from http://www.osti.gov/energycitations/product.biblio.jsp?osti_id=563175

Liu, N., Lei, J., Gao, W., Chen, H., & Xie, X. (2021, January). Combustion dynamics of large-scale wildfires. *Proceedings of the Combustion Institute*, *38*(1), 157–198. (Publisher: Elsevier) doi: 10.1016/J.PROCI.2020.11.006

Mandel, J., Beezley, J. D., & Kochanski, A. K. (2011). Coupled atmosphere-wildland fire modeling with WRF 3.3 and SFIRE 2011. *Geoscientific Model Development*, *4*(3), 591–610. (arXiv: 1102.1343) doi: 10.5194/gmd-4-591-2011

Mandel, J., Bennethum, L. S., Beezley, J. D., Coen, J. L., Douglas, C. C., Kim, M., & Vodacek, A. (2008, December). A wildland fire model with data assimilation. *Mathematics and Computers in Simulation*, *79*(3), 584–606. (arXiv: 0709.0086 Publisher: North-Holland ISBN: 0378-4754) doi: 10.1016/j.matcom.2008.03.015

Manzello, S. L. (2020). *Encyclopedia of wildfires and wildland-urban interface (WUI) fires*. Springer.

Maronga, B., Gryschka, M., Heinze, R., Hoffmann, F., Kanani-Sühring, F., Keck, M., ... Raasch, S. (2015, August). The Parallelized Large-Eddy Simulation Model (PALM) version 4.0 for atmospheric and oceanic flows: model formulation, recent developments, and future perspectives. *Geoscientific Model Development*, *8*(8), 2515–2551. Retrieved 2024-10-04, from https://gmd.copernicus.org/articles/8/2515/2015/ (Publisher: Copernicus GmbH) doi: 10.5194/gmd-8-2515-2015

Mattes, L., & Kofuji, S. T. (2014). The efficient use of graphic accelerators to im-

plement high accuracy FDTD algorithms. *IEEE Latin America Transactions*, *12*(4), 825–830. doi: 10.1109/TLA.2014.6868889

Mayeli, P., & Sheard, G. J. (2021). Buoyancy-driven flows beyond the Boussinesq approximation: A brief review. *International Communications in Heat and Mass Transfer*, *125*, 105316. Retrieved 2022-06-14, from https://doi.org/10.1016/j.icheatmasstransfer.2021.105316 doi: 10.1016/j.icheatmasstransfer.2021.105316

McAllister, S., Chen, J.-Y., & Fernandez-Pello, A. C. (2011). *Fundamentals of Combustion Processes*. New York, NY: Springer. Retrieved 2024-11-11, from https://link.springer.com/10.1007/978-1-4419-7943-8 doi: 10.1007/978-1-4419-7943-8

McArthur, A. G. (1967). *Fire Behaviour in Eucalypt Forests*. Forestry and Timber Bureau. Retrieved from https://books.google.cl/books?id=YO32GwAACAAJ (Series Title: Australia. Forestry and Timber Bureau. Leaflet no. 107)

McGrattan, K., McDermott, R., Floyd, J., Hostikka, S., Forney, G., & Baum, H. (2012, July). Computational fluid dynamics modelling of fire. *International Journal of Computational Fluid Dynamics*, *26*(6-8), 349–361. Retrieved from 10.1080/10618562.2012.659663 doi: 10.1080/10618562.2012.659663

McGrattan, K., & Miles, S. (2016). Modeling Fires Using Computational Fluid Dynamics (CFD). In M. J. Hurley et al. (Eds.), *SFPE Handbook of Fire Protection Engineering* (pp. 1034–1065). New York, NY: Springer New York. Retrieved from https://doi.org/10.1007/978-1-4939-2565-0_32 doi: 10.1007/978-1-4939-2565-0_32

McGrattan, K. B., & Forney, G. P. (2025). *Fire Dynamics Simulator User's Guide* (Tech. Rep. No. NIST SP 1019). Gaithersburg, MD: National Institute of Standards and Technology. Retrieved 2025-09-02, from http://dx.doi.org/10.6028/NIST.SP.1019

McGrattan, K. B., Hostikka, S., Floyd, J., McDermott, R., Vanella, M., Mueller, E., & Paul, C. (2025, April). *Fire Dynamics Simulator Technical Reference Guide Volume 1: Mathematical Model* (Tech. Rep. No. NIST SP 1018). Gaithersburg, MD: National Institute of Standards and Technology. Retrieved 2025-04-17, from http://dx.doi.org/10.6028/NIST.SP.1018

McGrattan, K. B., Rehm, R. G., & Baum, H. R. (1994, February). Fire-Driven Flows in Enclosures. *Journal of Computational Physics*, *110*(2), 285–291. (Publisher: Academic Press) doi: 10.1006/JCPH.1994.1025

Meacham, B. J., & McNamee, M. (Eds.). (2023). *Handbook of Fire and the Environment: Impacts and Mitigation*. Cham: Springer International Publishing. Retrieved 2025-01-20, from https://link.springer.com/10.1007/978-3-030-94356-1 doi: 10.1007/978-3-030-94356-1

Mell, W., Jenkins, M. A., Gould, J., & Cheney, P. (2007). A physics-based approach to modelling grassland fires. *International Journal of Wildland Fire*, *16*(1), 1–22. Retrieved from https://doi.org/10.1071/WF06002 doi: 10.1071/WF06002

Mell, W., Mcgrattan, K. B., & Baum, H. R. (1995, August). Large eddy simulations of fire-driven flows. In *National Heat Transfer Conference* (Vol. 304, pp. 73–77). Portland, Oregon: National Institute of Standards and Technology. Retrieved from https://www.researchgate.net/publication/238577221

Montenegro, R., Plaza, A., Ferragut, L., & Asensio, M. I. (1997, December). Application of a nonlinear evolution model to fire propagation. *Nonlinear Analysis, Theory, Methods and Applications*, *30*(5), 2873–2882. (Publisher: Pergamon) doi: 10.1016/S0362-546X(97)00341-6

Morvan, D. (2011). Physical Phenomena and Length Scales Governing the Behaviour of Wildfires: A Case for Physical Modelling. *Fire Technology*, *47*(2), 437–460. (ISBN: 1069401001602) doi: 10.1007/s10694-010-0160-2

Morvan, D., Accary, G., Meradji, S., Frangieh, N., & Bessonov, O. (2018, October). A 3D physical model to study the behavior of vegetation fires at laboratory scale. *Fire Safety Journal*, *101*, 39–52. Retrieved 2024-12-21, from https://www.sciencedirect.com/science/article/pii/S0379711218300225 doi: 10.1016/j.firesaf.2018.08.011

Morvan, D., & Dupuy, J. L. (2004, August). Modeling the propagation of a wildfire through a Mediterranean shrub using a multiphase formulation. *Combustion and Flame*, *138*(3), 199–210. (Publisher: Elsevier) doi: 10.1016/j.combustflame.2004.05.001

Morvan, D., Dupuy, J. L., Rigolot, E., & Valette, J. C. (2006, November). FIRESTAR: A Physically based model to study wildfire behaviour. *Forest Ecology and Management*, *234*, S114. Retrieved 2024-11-08, from https://www.sciencedirect.com/science/article/pii/S0378112706006645 doi: 10.1016/j.foreco.2006.08.155

Morvan, D., & Frangieh, N. (2018, August). Wildland fires behaviour: wind effect versus Byram's convective number and consequences upon the regime of propagation. *International Journal of Wildland Fire*, *27*(9), 636–641. Retrieved 2025-04-20, from https://www.publish.csiro.au/wf/WF18014 (Publisher: CSIRO PUBLISHING) doi: 10.1071/WF18014

Morvan, D., Hoffman, C., Rego, F., & Mell, W. (2011, November). Numerical simulation of the interaction between two fire fronts in grassland and shrubland. *Fire Safety Journal*, *46*(8), 469–479. Retrieved 2024-11-08, from https://www.sciencedirect.com/science/article/pii/S0379711211001068 doi: 10.1016/j.firesaf.2011.07.008

Morvan, D., Méradji, S., & Accary, G. (2009, January). Physical modelling of fire spread in Grasslands. *Fire Safety Journal*, *44*(1), 50–61. Retrieved 2019-05-29, from https://www.sciencedirect.com/science/article/pii/S0379711208000234 (Publisher: Elsevier) doi: 10.1016/J.FIRESAF.2008.03.004

Nadiga, B. T., Hecht, M. W., Margolin, L. G., & Smolarkiewicz, P. K. (1997). On simulating flows with multiple time scales using a method of averages. *Theoretical and Computational Fluid Dynamics*, *9*(3-4), 281–292. Re-

trieved 2021-03-24, from https://link-springer-com.usm.idm.oclc.org/article/10.1007/s001620050045 (Publisher: Springer New York) doi: 10.1007/s001620050045

National Interagency Fire Center. (2025). *Wildfires and Acres | National Interagency Fire Center.* Retrieved 2025-09-09, from https://www.nifc.gov/fire-information/statistics/wildfires

Nelson Jr, R. M. (2000, July). Prediction of diurnal change in 10-h fuel stick moisture content. *Canadian Journal of Forest Research*, *30*(7), 1071–1087. Retrieved 2025-09-04, from https://cdnsciencepub.com/doi/10.1139/x00-032 (Publisher: NRC Research Press) doi: 10.1139/x00-032

Ntaimo, L., Zeigler, B. P., Khargharia, B., & Vasconcelos, M. J. (2004). Forest Fire Spread and Suppression in DEVS. *Simulation*, *80*(10), 479–500. doi: 10.1177/0037549704050918

NVIDIA. (2025a). *1. Introduction — cuFFT 13.0 documentation.* Retrieved 2025-09-09, from https://docs.nvidia.com/cuda/cufft/#

NVIDIA. (2025b). *1. Introduction — NVIDIA CUDA Compiler Driver 13.0 documentation.* Retrieved 2025-09-09, from https://docs.nvidia.com/cuda/cuda-compiler-driver-nvcc/

NVIDIA. (2025c). *CUDA C++ Programming Guide — CUDA C++ Programming Guide.* Retrieved 2025-09-09, from https://docs.nvidia.com/cuda/cuda-c-programming-guide/index.html#

Oliphant, T. E. (2007, May). Python for Scientific Computing. *Computing in Science & Engineering*, *9*(3), 10–20. Retrieved from https://aip.scitation.org/doi/abs/10.1109/MCSE.2007.58 (Publisher: IEEE Computer Society) doi: 10.1109/MCSE.2007.58

Opie, K. (2020). Slope and Terrain. In S. L. Manzello (Ed.), *Encyclopedia of Wildfires and Wildland-Urban Interface (WUI) Fires* (pp. 919–922). Cham: Springer International Publishing. Retrieved 2025-01-08, from https://doi.org/10.1007/978-3-319-52090-2_240 doi: 10.1007/978-3-319-52090-2_240

Osher, S., & Sethian, J. A. (1988, November). Fronts propagating with curvature-dependent speed: Algorithms based on Hamilton-Jacobi formulations. *Journal of Computational Physics*, *79*(1), 12–49. Retrieved 2025-09-04, from https://www.sciencedirect.com/science/article/pii/0021999188900022 doi: 10.1016/0021-9991(88)90002-2

Owens, J. D., Houston, M., Luebke, D., Green, S., Stone, J. E., & Phillips, J. C. (2008, May). GPU Computing. *Proceedings of the IEEE*, *96*(5), 879–899. Retrieved 2025-09-09, from https://ieeexplore.ieee.org/document/4490127 doi: 10.1109/JPROC.2008.917757

Papalexandris, M. V. (2020, July). On the applicability of Stokes' hypothesis to low-Mach-number flows. *Continuum Mechanics and Thermodynamics*, *32*(4), 1245–1249. Retrieved 2025-07-28, from https://doi.org/10.1007/s00161-019-00785-z doi: 10.1007/s00161-019-00785-z

Pastor, E., Zárate, L., Planas, E., & Arnaldos, J. (2003, January). Mathemati-

cal models and calculation systems for the study of wildland fire behaviour. *Progress in Energy and Combustion Science*, *29*(2), 139–153. (Publisher: Pergamon ISBN: 0360-1285) doi: 10.1016/S0360-1285(03)00017-0

Patton, E. G., & Coen, J. L. (2004). WRF-Fire : A Coupled Atmosphere-Fire Module for WRF. *Preprints of Joint MM5/Weather Research and Forecasting Model Users' Workshop, Boulder, CO, 22–25 June, NCAR, 221–223*, 3.

Peyret, R., & Taylor, T. D. (1983). *Computational Methods for Fluid Flow*. Berlin, Heidelberg: Springer Berlin Heidelberg. Retrieved 2022-03-07, from http://link.springer.com/10.1007/978-3-642-85952-6 doi: 10.1007/978-3-642-85952-6

Poinsot, T., & Veynante, D. (2012). *Theoretical and Numerical Combustion* (3rd ed.). T. Poinsot, D. Veynante.

Pope, S. B. (2000). *Turbulent Flows*. Cambridge University Press. Retrieved 2021-04-12, from https://www.cambridge.org/core/product/identifier/9780511840531/type/book doi: 10.1017/CBO9780511840531

Prieto, D., Asensio, M., Ferragut, L., & Cascón, J. (2015, December). Sensitivity analysis and parameter adjustment in a simplified physical wildland fire model. *Advances in Engineering Software*, *90*, 98–106. Retrieved 2019-05-02, from https://www.sciencedirect.com/science/article/pii/S0965997815001131 (Publisher: Elsevier) doi: 10.1016/J.ADVENGSOFT.2015.08.001

Quintiere, J. (2006). *Fundamentals of Fire Phenomena*. Wiley. Retrieved from https://doi.org/10.1002/0470091150 doi: 10.1002/0470091150

Rangwala, A. S., & Raghavan, V. (2022). *Mechanism of Fires: Chemistry and Physical Aspects*. Cham: Springer International Publishing. Retrieved 2024-12-06, from https://link.springer.com/10.1007/978-3-030-75498-3 doi: 10.1007/978-3-030-75498-3

Rehm, R. G., & Baum, H. R. (1978). The Equations of Motion for Thermally Driven, Buoyant Flows. *J Res Natl Bur Stand (US)*, *83*(3), 297–308. doi: 10.6028/jres.083.019

Rehm, R. G., & McDermott, R. J. (2009, April). *Fire-Front Propagation Using the Level Set Method* (Tech. Rep.). NIST. Retrieved 2022-12-08, from https://www.nist.gov/publications/fire-front-propagation-using-level-set-method

Reisner, J., Wynne, S., Margolin, L., & Linn, R. (2000, October). Coupled atmospheric-fire modeling employing the method of averages. *Monthly Weather Review*, *128*(10), 3683–3691. Retrieved 2021-03-23, from https://journals.ametsoc.org/view/journals/mwre/128/10/1520-0493_2001_129_3683_cafmet_2.0.co_2.xml (Publisher: American Meteorological Society) doi: 10.1175/1520-0493(2001)129⟨3683:CAFMET⟩2.0.CO;2

Reynolds, O. (1895, December). IV. On the dynamical theory of incompressible viscous fluids and the determination of the criterion. *Philosophical Transactions*

of the Royal Society of London. (A.), *186*, 123–164. Retrieved 2021-04-12, from https://royalsocietypublishing.org/ (Publisher: The Royal Society) doi: 10.1098/rsta.1895.0004

Richards, G. D. (1995). A General Mathematical Framework For Modelling Two-Dimensional Wildland Fire Spread. *International Journal of Wildland Fire*, *5*(2), 63–72. (Publisher: CSIRO) doi: 10.1071/WF9950063

Riley, K. L., Grenfell, I. C., Shaw, J. D., & Finney, M. A. (2022, November). TreeMap 2016 Dataset Generates CONUS-Wide Maps of Forest Characteristics Including Live Basal Area, Aboveground Carbon, and Number of Trees per Acre. *Journal of Forestry*, *120*(6), 607–632. Retrieved 2025-09-04, from https://doi.org/10.1093/jofore/fvac022 doi: 10.1093/jofore/fvac022

Rohsenow, W. M., Hartnett, J. P., & Cho, Y. I. (1998). *Handbook of Heat Transfer* (3rd ed.). McGraw-Hill Education.

Rossa, C. G., Davim, D. A., Sil, A., & Fernandes, P. M. (2024, January). Field-based generic empirical flame length–fireline intensity relationships for wildland surface fires. *International Journal of Wildland Fire*, *33*(1). Retrieved 2024-11-21, from https://www.publish.csiro.au/wf/WF23127 (Publisher: CSIRO PUBLISHING) doi: 10.1071/WF23127

Rothermel, R. C. (1972). *A mathematical model for predicting fire spread in wildland fuels* (Tech. Rep.). USFS. Retrieved from http://www.srs.fs.usda.gov/pubs/32533 (Publication Title: USDA Forest Service Research Paper INT USA Issue: INT-115 ISBN: Research Paper INT-115) doi: http://www.snap.uaf.edu/webshared/JenNorthway/AKFireModelingWorkshop/AKFireModelingWkshp/FSProAnalysisGuideReferences/Rothermel1972INT-115.pdf

Rothermel, R. C. (1991). Predicting behavior and size of crown fires in the northern Rocky Mountains. *USDA Forest Service, Intermountain Research Station, Research Paper*(January), 46. (ISBN: INT-438)

Sagaut, P. (2006). *Large Eddy Simulation for Incompressible Flows*. Berlin/Heidelberg: Springer-Verlag. Retrieved 2022-05-20, from http://link.springer.com/10.1007/b137536 doi: 10.1007/b137536

San Martin, D. (2021). *Open-source Framework for Chilean Wildfire Spreading and Effects Analysis* (Doctoral dissertation, Universidad Tecnica Federico Santa Maria, Valparaiso). Retrieved 2023-05-25, from https://doi.org/10.71959/rpj9-az53

San Martin, D., & Torres, C. E. (2023, May). 2D Simplified Wildfire Spreading Model in Python: From NumPy to CuPy. *CLEI Electronic Journal*, *26*(1), 5:1–5:18. Retrieved 2023-05-25, from https://www.clei.org/cleiej/index.php/cleiej/article/view/578 doi: 10.19153/CLEIEJ.26.1.5

San Martin, D., & Torres, C. E. (2024). A GPU Numerical Implementation of a 2D Simplified Wildfire Spreading Model. In C. J. Barrios H., S. Rizzi, E. Meneses, E. Mocskos, J. M. Monsalve Diaz, & J. Montoya (Eds.), *High Performance Computing* (pp. 131–145). Cham: Springer Nature Switzerland. doi: 10.1007/

978-3-031-52186-7_9

San Martin, D., & Torres, C. E. (2025, October). Simplified coupled atmosphere-fire model for simulation of 2D wildland fires. *Computer Physics Communications*, *315*, 109746. Retrieved 2025-07-17, from https://www.sciencedirect.com/science/article/pii/S0010465525002486 doi: 10.1016/j.cpc.2025.109746

San Martín, D., & Torres, C. E. (2018, November). Ngen-Kütral: Toward an Open Source Framework for Chilean Wildfire Spreading. In *2018 37th International Conference of the Chilean Computer Science Society (SCCC)* (pp. 1–8). Retrieved 2023-09-28, from https://ieeexplore.ieee.org/document/8705159 (ISSN: 1522-4902) doi: 10.1109/SCCC.2018.8705159

San Martín, D., & Torres, C. E. (2019, November). Exploring a Spectral Numerical Algorithm for Solving a Wildfire Mathematical Model. In *2019 38th International Conference of the Chilean Computer Science Society (SCCC)* (pp. 1–7). Retrieved from https://www.doi.org/10.1109/SCCC49216.2019.8966412 doi: 10.1109/SCCC49216.2019.8966412

Sauer, T. (2017). *Numerical Analysis* (3rd ed.). Boston: Pearson.

Schochet, S. (2005, May). The mathematical theory of low Mach number flows. *ESAIM: Mathematical Modelling and Numerical Analysis*, *39*(3), 441–458. Retrieved 2025-08-26, from https://www.esaim-m2an.org/articles/m2an/abs/2005/03/m2an01EDP/m2an01EDP.html (Publisher: EDP Sciences) doi: 10.1051/m2an:2005017

Schumann, U., & Sweet, R. A. (1988, March). Fast Fourier transforms for direct solution of poisson's equation with staggered boundary conditions. *Journal of Computational Physics*, *75*(1), 123–137. Retrieved 2024-10-04, from https://www.sciencedirect.com/science/article/pii/0021999188901027 doi: 10.1016/0021-9991(88)90102-7

Senocak, I., Ackerman, A. S., Stevens, D. E., & Mansour, N. N. (2004, September). Topography Modeling in Atmospheric Flows Using the Immersed Boundary Method. *Annual Research Briefs, 2004: Center for Turbulence Research*.

Serón, F. J., Gutiérrez, D., Magallón, J., Ferragut, L., & Asensio, M. I. (2005, April). The evolution of a WILDLAND forest FIRE FRONT. *Visual Computer*, *21*(3), 152–169. Retrieved 2023-03-21, from https://link.springer.com/article/10.1007/s00371-004-0278-7 (Publisher: Springer) doi: 10.1007/S00371-004-0278-7/METRICS

Short, K. C. (2022). *Spatial wildfire occurrence data for the United States, 1992-2020 [FPA_fod_20221014] (6th Edition)* (Tech. Rep.). Fort Collins, CO: Forest Service Research Data Archive. Retrieved 2022-12-13, from https://www.fs.usda.gov/rds/archive/catalog/RDS-2013-0009.6 doi: 10.2737/RDS-2013-0009.6

Silva, J., Marques, J., Gonçalves, I., Brito, R., Teixeira, S., Teixeira, J., & Alvelos, F. (2022, December). A Systematic Review and Bibliometric Analysis of Wildland Fire Behavior Modeling. *Fluids 2022, Vol. 7, Page 374*, *7*(12), 374. Retrieved 2023-01-06, from https://www.mdpi.com/2311-5521/7/12/

374/htm (Publisher: Multidisciplinary Digital Publishing Institute) doi: 10.3390/FLUIDS7120374

Smagorinsky, J. (1963, March). General Circulation Experiments with the Primitive Equations. *Monthly Weather Review*, *91*(3), 99–164. Retrieved 2021-04-12, from https://journals.ametsoc.org/view/journals/mwre/91/3/1520-0493_1963_091_0099_gcewtp_2_3_co_2.xml (Publisher: American Meteorological Society) doi: 10.1175/1520-0493(1963)091⟨0099:gcewtp⟩2.3.co;2

Smolarkiewicz, P. K., & Margolin, L. G. (1997, January). On forward-in-time differencing for fluids: An eulerian/semi-lagrangian non-hydrostatic model for stratified flows. *Atmosphere - Ocean*, *35*, 127–152. Retrieved 2021-03-24, from https://www.tandfonline.com/action/journalInformation?journalCode=tato20 (Publisher: Taylor & Francis Group) doi: 10.1080/07055900.1997.9687345

Speer, K., & Goodrick, S. (Eds.). (2022). *Wildland Fire Dynamics*. Cambridge: Cambridge University Press. Retrieved 2024-11-12, from https://www.cambridge.org/core/books/wildland-fire-dynamics/ABB400C822D978A3F4BF02861F5BA5D3 doi: 10.1017/9781108683241

Sullivan, A. L. (2009a). Wildland surface fire spread modelling, 1990 - 2007. 1: Physical and quasi-physical models. *International Journal of Wildland Fire*, *18*(4), 349–368. Retrieved from http://dx.doi.org/10.1071/WF06143 (arXiv: 0706.4128 ISBN: 1049-8001) doi: 10.1071/wf06143

Sullivan, A. L. (2009b). Wildland surface fire spread modelling, 1990 - 2007. 2: Empirical and quasi-empirical models. *International Journal of Wildland Fire*, *18*(4), 369. doi: 10.1071/wf06142

Sullivan, A. L. (2009c). Wildland surface fire spread modelling, 1990 - 2007. 3: Simulation and mathematical analogue models. *International Journal of Wildland Fire*, *18*(4), 387. (Publisher: CSIRO) doi: 10.1071/wf06144

Taha, M., Zhao, S., Lamorlette, A., Consalvi, J.-L., & Boivin, P. (2024, March). Large eddy simulation of fire-induced flows using Lattice-Boltzmann methods. *International Journal of Thermal Sciences*, *197*, 108801. Retrieved 2025-11-06, from https://www.sciencedirect.com/science/article/pii/S1290072923006622 doi: 10.1016/j.ijthermalsci.2023.108801

Tang, T. (2017). *A Physics-based Approach to Modeling Wildland Fire Spread Through Porous Fuel Beds* (Doctoral dissertation, University of Kentucky). doi: https://doi.org/10.13023/ETD.2017.027

Trefethen, L. (2000). *Spectral Methods in MATLAB*. Society for Industrial and Applied Mathematics. (Publication Title: Software, Environments and Tools) doi: 10.1137/1.9780898719598

Tritton, D. J. (1977). *Physical Fluid Dynamics*. Dordrecht: Springer Netherlands. Retrieved from https://books.google.cl/books?id=mrLvCAAAQBAJ (Series Title: The Modern University in Physics Series) doi: 10.1007/978-94-009-9992-3

Tyukavina, A., Potapov, P., Hansen, M. C., Pickens, A. H., Stehman, S. V., Tu-

rubanova, S., ... Harris, N. (2022, March). Global Trends of Forest Loss Due to Fire From 2001 to 2019. *Frontiers in Remote Sensing*, *3*, 9. Retrieved 2022-12-13, from https://www.frontiersin.org/articles/10.3389/frsen.2022.825190/full (Publisher: Frontiers) doi: 10.3389/frsen.2022.825190

U.S. National Science Foundation. (2025). *Fire Science Innovations through Research and Education (FIRE) | NSF - National Science Foundation.* Retrieved 2025-09-17, from https://www.nsf.gov/funding/opportunities/fire-fire-science-innovations-through-research-education

Van Wagner, C. E. (1977, March). Conditions for the start and spread of crown fire. *Canadian Journal of Forest Research*, *7*(1), 23–34. Retrieved 2025-09-04, from https://cdnsciencepub.com/doi/10.1139/x77-004 (Publisher: NRC Research Press) doi: 10.1139/x77-004

Verzicco, R. (2023, January). Immersed Boundary Methods: Historical Perspective and Future Outlook. *Annual Review of Fluid Mechanics*, *55*(Volume 55, 2023), 129–155. Retrieved 2025-09-26, from https://www.annualreviews.org/content/journals/10.1146/annurev-fluid-120720-022129 (Publisher: Annual Reviews) doi: 10.1146/annurev-fluid-120720-022129

Wang, Y., Chatterjee, P., & de Ris, J. L. (2011, January). Large eddy simulation of fire plumes. *Proceedings of the Combustion Institute*, *33*(2), 2473–2480. Retrieved 2025-09-04, from https://www.sciencedirect.com/science/article/pii/S1540748910002944 doi: 10.1016/j.proci.2010.07.031

Wang, Z., Zhang, T., & Huang, X. (2023, January). Predicting real-time fire heat release rate by flame images and deep learning. *Proceedings of the Combustion Institute*, *39*(3), 4115–4123. Retrieved 2025-01-08, from https://www.sciencedirect.com/science/article/pii/S1540748922000918 doi: 10.1016/j.proci.2022.07.062

Weber, R. O. (1991). Toward a comprehensive wildfire spread model. *International Journal of Wildland Fire*, *1*(4), 245–248. Retrieved 2023-05-03, from https://doi.org/10.1071/WF9910245 doi: 10.1071/WF9910245

Wegrzynski, W., & Lipecki, T. (2018). Wind and Fire Coupled Modelling—Part I: Literature Review. *Fire Technology*, *54*(5), 1405–1442. doi: 10.1007/s10694-018-0748-5

Wegrzynski, W., Lipecki, T., & Krajewski, G. (2018). Wind and Fire Coupled Modelling—Part II: Good Practice Guidelines. *Fire Technology*, *54*(5), 1443–1485. doi: 10.1007/s10694-018-0749-4

Westbrook, C. K., & Dryer, F. L. (1984, January). Chemical kinetic modeling of hydrocarbon combustion. *Progress in Energy and Combustion Science*, *10*(1), 1–57. Retrieved 2024-11-11, from https://www.sciencedirect.com/science/article/pii/0360128584901187 doi: 10.1016/0360-1285(84)90118-7

Williams, F. A. (2020). Combustion. In S. L. Manzello (Ed.), *Encyclopedia of Wildfires and Wildland-Urban Interface (WUI) Fires* (pp. 103–114). Cham: Springer International Publishing. Retrieved 2024-11-26, from https://doi

.org/10.1007/978-3-319-52090-2_60 doi: 10.1007/978-3-319-52090-2_60

World Wide Fund, & Boston Consulting Group. (2020). *Fires, forests and the future: a crisis raging out of control?* (Tech. Rep.). Gland, Switzerland: WWF.

Xu, R., Yu, P., Abramson, M. J., Johnston, F. H., Samet, J. M., Bell, M. L., ... Guo, Y. (2020, November). Wildfires, Global Climate Change, and Human Health. *New England Journal of Medicine*, *383*(22), 2173–2181. Retrieved 2023-01-06, from https://www.nejm.org/doi/full/10.1056/NEJMsr2028985 (Publisher: Massachusetts Medical Society) doi: 10.1056/NEJMSR2028985/SUPPL_FILE/NEJMSR2028985_DISCLOSURES.PDF

Xue, M., Droegemeier, K. K., & Wong, V. (2000). The Advanced Regional Prediction System (ARPS) – A multi-scale nonhydrostatic atmospheric simulation and prediction model. Part I: Model dynamics and verification. *Meteorology and Atmospheric Physics*, *75*(3), 161–193. Retrieved from https://doi.org/10.1007/s007030070003 doi: 10.1007/s007030070003

Xue, M., Droegemeier, K. K., Wong, V., Shapiro, A., Brewster, K., Carr, F., ... Wang, D. (2001). The Advanced Regional Prediction System (ARPS) – A multi-scale nonhydrostatic atmospheric simulation and prediction model. Part I: Model dynamics and verification. *Meteorology and Atmospheric Physics*, *76*(3-4), 143–165. doi: 10.1007/s007030170027

Yanaoka, H., & Sato, Y. (2025, February). *A numerical method for low Mach number compressible flows by simultaneous relaxation of dependent variables.* Retrieved 2025-08-26, from https://arxiv.org/abs/2502.08116v1

Zhang, J., Katurji, M., Zawar-Reza, P., & Strand, T. (2023, January). The role of helicity and fire–atmosphere turbulent energy transport in potential wildfire behaviour. *International Journal of Wildland Fire*, *32*(1), 29–42. Retrieved 2024-11-07, from https://www.publish.csiro.au/wf/WF22101 (Publisher: CSIRO PUBLISHING) doi: 10.1071/WF22101

Zhang, K., Verma, S., Trouvé, A., & Lamorlette, A. (2020, March). A study of the canopy effect on fire regime transition using an objectively defined Byram convective number. *Fire Safety Journal*, *112*, 102950. Retrieved 2025-04-07, from https://www.sciencedirect.com/science/article/pii/S0379711219304497 doi: 10.1016/j.firesaf.2020.102950

Zhang, Y., & Luo, A. (2024, February). Applicability analysis of flame height estimation based on Byram's fireline intensity model under flat and windless conditions. *Scientific Reports*, *14*(1), 4441. Retrieved 2024-11-26, from https://www.nature.com/articles/s41598-024-55132-3 (Publisher: Nature Publishing Group) doi: 10.1038/s41598-024-55132-3

Zhuang, Y., Fu, R., Santer, B. D., Dickinson, R. E., & Hall, A. (2021, November). Quantifying contributions of natural variability and anthropogenic forcings on increased fire weather risk over the western United States. *Proceedings of the National Academy of Sciences of the United States of America*, *118*(45), e2111875118. Retrieved 2023-01-06, from https://www.pnas.org/doi/abs/10.1073/pnas.2111875118 (Publisher: National Academy of Sciences) doi:

10.1073/PNAS.2111875118/SUPPL_FILE/PNAS.2111875118.SAPP.PDF

Álvarez, D., Prieto, D., Asensio, M. I., Cascón, J. M., & Ferragut, L. (2017). Parallel implementation of a simplified semi-physical wildland fire spread model using openMP. *Lecture Notes in Computer Science (including subseries Lecture Notes in Artificial Intelligence and Lecture Notes in Bioinformatics)*, *10334 LNCS*, 256–267. (ISBN: 9783319596495) doi: 10.1007/978-3-319-59650-1_22

Çengel, Y. A., & Cimbala, J. M. (2018). *Fluid Mechanics: Fundamentals and Applications*. McGraw-Hill Education. Retrieved from `https://books.google.cl/books?id=DqFJvgAACAAJ`

Appendix A

Ideal Gas Law

A.1 Equation of state

The equation of state for an ideal gas is often written as

$$pV = n\mathcal{R}T, \tag{A.1}$$

where p is the pressure in kg $m^{-1}s^{-2}$, V the volume in m^3, n the number of moles in mol, and T the temperature in K. $\mathcal{R} = 8.31446261815324$ kg $m^{-2}s^{-2}K^{-1}mol^{-1}$ is the universal gas constant.

The molar form of (A.1) can be derived using

$$n = \frac{m}{M}, \tag{A.2}$$

with m the total mass in kg and M the molar mass in kg mol^{-1}. In addition, considering the definition of density

$$\rho = \frac{m}{V}, \tag{A.3}$$

equation (A.1) can be written as

$$\begin{aligned} pV &= n\mathcal{R}T \\ pV &= \frac{m}{M}\mathcal{R}T \\ p &= \frac{m}{V}\frac{\mathcal{R}}{M}T \\ p &= \rho RT \end{aligned} \tag{A.4}$$

with $R = \mathcal{R}/M$ the specific gas constant in J $kg^{-1}K^{-1}$ ($m^2s^{-2}K^{-1}$). For example, for dry air, $R = 287.052874$ J $kg^{-1}K^{-1}$.

A.2 Thermal expansion

Thermal expansion is the phenomenon observed in solids, liquids, and gases, where an object or body expands upon the application of heat. From (A.1), any change in volume, temperature, or pressure is strongly related. In particular, volume expansion is the change in volume as a result of temperature variations.

A.2.1 Thermal expansion coefficient

Considering an isobaric process, that is, p constant, the coefficient of the thermal expansion coefficient (Batchelor, 2000, p. 26) is defined as

$$\alpha_V = \frac{1}{V}\left(\frac{\partial V}{\partial T}\right)_p, \tag{A.5}$$

or (Batchelor, 2000, p. 43),

$$\alpha_V = -\frac{1}{\rho}\left(\frac{\partial \rho}{\partial T}\right)_p, \tag{A.6}$$

where the subscript p denotes that the pressure remains constant during expansion (Batchelor, 2000). The expression (A.6) can be derived written (A.5) as

$$\alpha_V = \frac{1}{V}\left(\frac{\partial V}{\partial T}\right)_p = \frac{1}{V}\left(\frac{\partial V}{\partial \rho}\right)_p \left(\frac{\partial \rho}{\partial T}\right)_p. \tag{A.7}$$

Using the definition of density (A.3),

$$\rho = \frac{m}{V} \implies V = \frac{m}{\rho}, \tag{A.8}$$

and taking the partial derivative of (A.8) with respect to density,

$$\begin{aligned} V &= \frac{m}{\rho} \quad /\frac{\partial}{\partial \rho} \\ \frac{\partial V}{\partial \rho} &= -\frac{m}{\rho^2}\frac{\partial \rho}{\partial \rho} = -\frac{V}{\rho}. \end{aligned} \tag{A.9}$$

Replacing (A.9) in (A.7),

$$\alpha_V = \frac{1}{V}\left(\frac{\partial V}{\partial \rho}\right)_p \left(\frac{\partial \rho}{\partial T}\right)_p = \frac{1}{V}\left(-\frac{V}{\rho}\right)\left(\frac{\partial \rho}{\partial T}\right)_p = -\frac{1}{\rho}\left(\frac{\partial \rho}{\partial T}\right)_p.$$

Considering an ideal gas

$$\begin{aligned} pV &= n\mathcal{R}T \quad /\frac{\partial}{\partial T} \\ p\frac{\partial V}{\partial T} &= n\mathcal{R}\frac{\partial T}{\partial T} \\ \frac{\partial V}{\partial T} &= \frac{n\mathcal{R}}{p} = \frac{V}{T}. \end{aligned} \tag{A.10}$$

Replacing (A.10) in (A.5),

$$\alpha_V = \frac{1}{V}\left(\frac{\partial V}{\partial T}\right)_p = \frac{1}{V}\frac{V}{T} = \frac{1}{T}. \tag{A.11}$$

Similarly, but using (A.4)

$$\begin{aligned} \rho RT &= p \quad / \frac{\partial}{\partial T} \\ R\left(T\frac{\partial \rho}{\partial T} + \rho\frac{\partial T}{\partial T}\right) &= 0 \\ T\frac{\partial \rho}{\partial T} &= -\rho \\ \frac{\partial \rho}{\partial T} &= -\frac{\rho}{T}. \end{aligned} \tag{A.12}$$

Replacing (A.12) in (A.6),

$$\alpha_V = -\frac{1}{\rho}\left(\frac{\partial \rho}{\partial T}\right)_p = -\frac{1}{\rho}\left(-\frac{\rho}{T}\right) = \frac{1}{T}, \tag{A.13}$$

as presented in (Tritton, 1977; Batchelor, 2000; Law, 2006).

A.3 Density expansion

Consider the following expansion of the density depending on the temperature (Mayeli & Sheard, 2021),

$$\rho = \rho_\infty + \left.\frac{\partial \rho}{\partial T}\right|_{T=T_\infty} (T - T_\infty) + \dots.$$

After an algebraic manipulation,

$$\frac{\rho - \rho_\infty}{\rho_\infty} = \frac{1}{\rho_\infty}\left.\frac{\partial \rho}{\partial T}\right|_{T=T_\infty} (T - T_\infty) + \dots \approx -\alpha_V (T - T_\infty), \tag{A.14}$$

where α_V is the volumetric thermal expansion coefficient, defined by (A.5) or (A.6) as reported in Appendix A.2.1. In particular, reordering (A.14),

$$\rho = \rho_\infty (1 - \alpha_V (T - T_\infty)). \tag{A.15}$$

For an ideal gas, $\alpha_V = 1/T$ (A.13), then (A.15), becomes

$$\begin{aligned} \rho &= \rho_\infty (1 - \alpha_V (T - T_\infty)) \\ &= \rho_\infty (1 - \frac{1}{T}(T - T_\infty)) \\ &= \rho_\infty (1 - 1 + \frac{T_\infty}{T})) \\ &= \frac{\rho_\infty T_\infty}{T}. \end{aligned}$$

A.4 Hydrostatic balance

A stratified fluid is said to be in hydrostatic equilibrium if it is at rest ($\mathbf{u} = \mathbf{0}$) and the fluid state variables are simply functions of height z. Let $\rho_0(z)$, $p_0(z)$, $T_0(z)$, $\mathbf{u} = \mathbf{0}$ be the state variables of an atmosphere in hydrostatic equilibrium. Conservation of momentum just reduces to the requirement that such an atmosphere in hydrostatic balance must satisfy static force balance of pressure and gravitational forces:

$$\frac{dp_0}{dz} = -\rho g \implies \nabla p_0 - \rho \mathbf{g} = 0, \quad \mathbf{g} = (0, 0, -g). \tag{A.16}$$

Appendix B

Approximation of Fluid Equations

This chapter outlines the equations and the derivations of the fluid dynamics equations employed in this work.

B.1 Non-dimensional Numbers

In the analysis and scaling of fluid flow problems, several dimensionless numbers arise naturally from the governing equations. These numbers characterize the relative importance of various physical processes and serve as key parameters in similarity analysis, numerical modeling, and experimental design. Below are the most relevant non-dimensional numbers for this study.

Mach Number

The Mach number measures the ratio of the characteristic flow velocity to the speed of sound in the medium:

$$\mathrm{Ma} = \frac{U}{c}, \tag{B.1}$$

where U is the characteristic velocity and c is the speed of sound, given for a perfect gas by

$$c = \sqrt{\gamma R T}, \tag{B.2}$$

with

$$\gamma = \frac{c_p}{c_V}, \tag{B.3}$$

the ratio of specific heats, R the specific gas constant, and T the absolute temperature. The Mach number indicates the importance of compressibility effects. Low Mach values correspond to low-speed, nearly incompressible flows.

Reynolds Number

The Reynolds number quantifies the ratio of inertial forces to viscous forces:

$$\mathrm{Re} = \frac{\rho U L}{\mu}, \tag{B.4}$$

where ρ is the density, L a characteristic length, and μ the dynamic viscosity. High Re indicates turbulence-prone flows dominated by inertial effects, while low Re corresponds to laminar flows dominated by viscosity.

Prandtl Number

The Prandtl number expresses the ratio of momentum diffusivity (viscosity) to thermal diffusivity:

$$\mathrm{Pr} = \frac{\nu}{\alpha} = \frac{\mu c_p}{k}, \tag{B.5}$$

where

$$\nu = \frac{\mu}{\rho},$$

is the kinematic viscosity, and

$$\alpha = \frac{k}{\rho c_p}$$

is the thermal diffusivity, c_p is the specific heat at constant pressure, and k is the thermal conductivity. This number relates the relative thickness of the velocity and thermal boundary layers. Large values indicate that momentum is dominant, and for small values the heat diffusion dominates.

Schmidt Number

The Schmidt number is defined as the ratio between momentum diffusivity and mass diffusivity:

$$\mathrm{Sc} = \frac{\nu}{D} = \frac{\mu}{\rho D}, \tag{B.6}$$

where ν is the kinematic viscosity, μ is the dynamic viscosity, ρ is the density, and D is the mass diffusivity of the species. It characterizes the relative effectiveness of momentum and mass diffusion. High Schmidt numbers indicate that momentum diffuses much faster than mass (typical in liquids), while low Schmidt numbers correspond to faster mass diffusion (common in gases).

Péclet Number

The Péclet number measures the relative importance of advective to diffusive heat transport:

$$\mathrm{Pe} = \frac{UL}{\alpha} = \frac{\rho c_p U L}{k} = \mathrm{Re}\,\mathrm{Pr}, \tag{B.7}$$

where α is the thermal diffusivity. Large values of Pe indicate that advection dominates thermal transport.

In mass transfer, the Péclet number expresses the ratio of the advective transport rate to the diffusive transport rate of a species. It is defined as

$$\mathrm{Pe}_m = \frac{UL}{D} = \mathrm{Re}\,\mathrm{Sc}, \tag{B.8}$$

where D is the mass diffusivity of the species. A large Pe_m indicates that advection dominates over diffusion, while a small Pe_m implies that diffusion is the primary transport mechanism.

Froude Number

The Froude number compares inertial forces with gravitational forces:

$$\mathrm{Fr} = \frac{U}{\sqrt{gL}}, \tag{B.9}$$

where g is the gravitational acceleration. This number is particularly relevant for buoyancy-driven flows and free-surface phenomena. Larger values suggest that inertia prevails, whereas smaller values indicate that gravity significantly affects the behavior.

Eckert Number

The Eckert number relates the kinetic energy to enthalpy:

$$\mathrm{Ec} = \frac{U^2}{c_p \Delta T}, \tag{B.10}$$

where c_p is the specific heat at constant pressure and ΔT is a characteristic temperature difference. This number quantifies the importance of viscous dissipation in the conversion of kinetic energy to internal energy.

Grashof Number

The Grashof number is a dimensionless parameter that quantifies the ratio between buoyancy forces and viscous forces in a fluid flow. It is defined as

$$\mathrm{Gr} = \frac{g\beta\Delta T L^3}{\nu^2} = \frac{g\beta\Delta T L^3 \rho^2}{\mu^2} \tag{B.11}$$

where g is the gravitational acceleration, β is the thermal expansion coefficient, ΔT is the characteristic temperature difference driving buoyancy, L is the characteristic length, and ν is the kinematic viscosity. For and ideal gas, $\beta = 1/T$,

$$\mathrm{Gr} = \frac{g\,\Delta T\,L^3\rho^2}{T\mu^2} \tag{B.12}$$

The Grashof number plays a central role in natural convection: large values of Gr indicate that buoyancy dominates over viscous effects, leading to vigorous convection, while small values imply that viscous diffusion suppresses buoyancy-driven motion.

Rayleigh Number

The Rayleigh number characterizes the competition between buoyancy and dissipative effects (viscous and thermal). It combines the effects of the Grashof and Prandtl numbers:

$$\mathrm{Ra} = \mathrm{Gr}\,\mathrm{Pr} = \frac{g\beta\Delta T L^3}{\nu\alpha}, \tag{B.13}$$

where α is the thermal diffusivity and Pr is the Prandtl number (B.5).

At larger Ra, convective motions become more vigorous and can transition to turbulence.

B.2 Compressible Flow Equations

The compressible flow equations emerge from the idea that the total change of a quantity within a control volume equals the amount that enters or leaves through its surfaces plus any sources or sinks inside. Let V be a fixed control volume with boundary ∂V and outward unit normal vector $\mathbf{n}$. For any conserved or transported quantity ϕ with density $\rho\phi$, advective flux $\rho\phi\,\mathbf{u}$, diffusive flux $\mathbf{j}_\phi$, and volumetric source S_ϕ, the integral balance is

$$\frac{d}{dt}\int_V \rho\,\phi\,dV + \oint_{\partial V} \rho\phi\,(\mathbf{u}\cdot\mathbf{n})\,dS = \oint_{\partial V} \mathbf{j}_\phi\cdot\mathbf{n}\,dS + \int_V S_\phi\,dV. \tag{B.14}$$

Applying the divergence theorem to the surface integrals and using the Reynold's Theorem for the time derivative,

$$\begin{aligned}
\frac{d}{dt}\int_V \rho\,\phi\,dV + \oint_{\partial V} \rho\phi\,(\mathbf{u}\cdot\mathbf{n})\,dS &= \oint_{\partial V} \mathbf{j}_\phi\cdot\mathbf{n}\,dS + \int_V S_\phi\,dV \\
\int_V \frac{\partial}{\partial t}(\rho\,\phi)\,dV + \int_V \nabla\cdot(\rho\phi\,\mathbf{u})dV &= \int_V \nabla\cdot\mathbf{j}_\phi\,dV + \int_V S_\phi\,dV \\
\int_V \left[\frac{\partial}{\partial t}(\rho\,\phi) + \nabla\cdot(\rho\phi\,\mathbf{u})\right] dV &= \int_V \left[\nabla\cdot\mathbf{j}_\phi + S_\phi\right] dV
\end{aligned}$$

For an arbitrary V, the differential or local form is,

$$\frac{\partial}{\partial t}(\rho\,\phi) + \nabla\cdot(\rho\phi\,\mathbf{u}) = \nabla\cdot\mathbf{j}_\phi + S_\phi. \tag{B.15}$$

The governing equations appear after instantiating (B.14)-(B.15) for mass, momentum, sensible enthalpy, and species.

B.2.1 Mass

Defining $\phi = 1$, $\mathbf{j}_\phi = \mathbf{0}$, $S_\phi = 0$, the integral form of conservation of mass is

$$\frac{d}{dt}\int_V \rho\, dV + \oint_{\partial V} \rho\,(\mathbf{u}\cdot\mathbf{n})\, dS = 0,$$

and the differential form,

$$\frac{\partial \rho}{\partial t} + \nabla\cdot(\rho\mathbf{u}) = 0.$$

B.2.2 Momentum

Defining $\phi = \mathbf{u}$, $\mathbf{j}_\phi = \boldsymbol{\sigma} = -p\mathbf{I} + \boldsymbol{\tau}$, $S_\phi = \mathbf{f} = \rho\mathbf{b}$, the integral form of conservation of momentum is,

$$\frac{d}{dt}\int_V \rho\mathbf{u}\, dV + \oint_{\partial V} \rho\mathbf{u}(\mathbf{u}\cdot\mathbf{n})\, dS = \oint_{\partial V} (\boldsymbol{\sigma}\cdot\mathbf{n})\, dS + \int_V \mathbf{f}\, dV,$$

and the differential form,

$$\frac{\partial(\rho\mathbf{u})}{\partial t} + \nabla\cdot(\rho\mathbf{u}\otimes\mathbf{u}) = \nabla\cdot\boldsymbol{\sigma} + \mathbf{f} = -\nabla p + \nabla\cdot\boldsymbol{\tau} + \mathbf{f}\ . \tag{B.16}$$

The term $\boldsymbol{\sigma}\cdot\mathbf{n}$ is known as the traction (Greenshields & Weller, 2022), and p is the pressure. For a Newtonian fluid, with dynamic viscosity μ and bulk viscosity ζ,

$$\boldsymbol{\tau} = \mu\left(\nabla\mathbf{u} + \nabla\mathbf{u}^\top\right) + \left(\zeta - \tfrac{2}{3}\mu\right)(\nabla\cdot\mathbf{u})\,\mathbf{I}. \tag{B.17}$$

Since this work is focused on the low-Mach number approximation, bulk viscosity is neglected and $\zeta = 0$ (Papalexandris, 2020).

B.2.3 Sensible enthalpy

Defining $\phi = h$, $\mathbf{j}_\phi = -\mathbf{q}$, $S_\phi = \dot{Q} + \boldsymbol{\tau} : \nabla\mathbf{u} + \dfrac{Dp}{Dt}$, the integral form of conservation of sensible enthalpy is,

$$\frac{d}{dt}\int_V \rho h\, dV + \oint_{\partial V} \rho h\,(\mathbf{u}\cdot\mathbf{n})\, dS = -\oint_{\partial V} \mathbf{q}\cdot\mathbf{n}\, dS + \int_V \left(\dot{Q} + \boldsymbol{\tau} : \nabla\mathbf{u} + \frac{Dp}{Dt}\right) dV,$$

and the differential form,

$$\frac{\partial(\rho h)}{\partial t} + \nabla\cdot(\rho h\mathbf{u}) = -\nabla\cdot\mathbf{q} + \dot{Q} + \boldsymbol{\tau} : \nabla\mathbf{u} + \frac{Dp}{Dt}.$$

$\mathbf{q}$ is the heat flux, $\dot{Q}$ is the volumetric heat source, $\boldsymbol{\tau} : \nabla\mathbf{u}$ is the viscous dissipation, and $\dfrac{Dp}{Dt}$ represents the pressure-work contribution.

B.2.4 Species

Defining $\phi = Y_i$, $\mathbf{j}_\phi = -\mathbf{J}_i$, $S_\phi = \dot{\omega}_i$, the integral form of the conservation of species is,

$$\frac{d}{dt}\int_V \rho Y_i \, dV + \oint_{\partial V} \rho Y_i \, (\mathbf{u}\cdot\mathbf{n}) \, dS = -\oint_{\partial V} \mathbf{J}_i \cdot \mathbf{n} \, dS + \int_V \dot{\omega}_i \, dV,$$

and the differential form,

$$\partial_t(\rho Y_i) + \nabla\cdot(\rho \mathbf{u} \, Y_i) = -\nabla\cdot\mathbf{J}_i + \dot{\omega}_i.$$

$Y_i = \rho_i/\rho$ represents the fraction of species i, $\mathbf{J}_i$ is the diffusive flux, and $\dot{\omega}_i$ is the production rate. The diffusive flux can be defined as

$$\mathbf{J}_i = \rho_i(\mathbf{V}_i - \mathbf{V}),$$

where $\mathbf{V}_i$ is the diffusion velocity and $\mathbf{V}$ is the mixture velocity defined as

$$\mathbf{V} = \frac{1}{\rho}\sum_{i=1}^{N} \rho_i \mathbf{V}_i.$$

Typically, Fick's law is used to approximate diffusive fluxes (Poinsot & Veynante, 2012; Kuwana, 2020),

$$\mathbf{J}_i = -\rho D_i \nabla Y_i,$$

with D_i the diffusivity of species i.

Furthermore, the following restriction must be met (Poinsot & Veynante, 2012; Kuwana, 2020). The sum of the species fraction must be equal to the unity,

$$\sum_{i=1}^{N} Y_i = \sum_{i=1}^{N} \frac{\rho_i}{\rho} = \frac{1}{\rho}\sum_{i=1}^{N} \rho_i = \frac{\rho}{\rho} = 1.$$

The production rate of species must be equal to zero,

$$\sum_{i=1}^{N} \dot{\omega}_i = 0,$$

since chemical reactions only rearrange atoms and they cannot create or destroy mass. In other words, while the mass of individual species can increase or decrease, the total mass is conserved. The last restriction is that the net diffusive flux is zero,

$$\sum_{i=1}^{N} \mathbf{J}_i = \sum_{i=1}^{N} \rho_i(\mathbf{V}_i - \mathbf{V}) = \sum_{i=1}^{N} \rho_i \mathbf{V}_i - \sum_{i=1}^{N} \rho_i \mathbf{V} = \sum_{i=1}^{N} \rho_i \mathbf{V}_i - \mathbf{V}\sum_{i=1}^{N} \rho_i = \rho\mathbf{V} - \rho\mathbf{V} = \mathbf{0}.$$

B.2.5 Summary

Wrapping up all the previous results, and including the equation of state to close the system A.1, the dimensional compressible Navier-Stokes equations in the differential form are defined as follows

$$\frac{\partial \rho}{\partial t} + \nabla \cdot (\rho \mathbf{u}) = 0, \tag{B.18}$$

$$\frac{\partial (\rho \mathbf{u})}{\partial t} + \nabla \cdot (\rho \mathbf{u} \otimes \mathbf{u}) = -\nabla p + \nabla \cdot \boldsymbol{\tau} + \mathbf{f}, \tag{B.19}$$

$$\frac{\partial (\rho h)}{\partial t} + \nabla \cdot (\rho h \mathbf{u}) = \frac{Dp}{Dt} - \nabla \cdot \mathbf{q} + \boldsymbol{\tau} : \nabla \mathbf{u} + \dot{Q}, \tag{B.20}$$

$$\frac{\partial (\rho Y_i)}{\partial t} + \nabla \cdot (\rho Y_i \mathbf{u}) = -\nabla \cdot \mathbf{J}_i + \dot{\omega}_i, \tag{B.21}$$

$$\boldsymbol{\tau} = \mu \left(\nabla \mathbf{u} + (\nabla \mathbf{u})^\top - \frac{2}{3} (\nabla \cdot \mathbf{u}) \mathbf{I} \right), \tag{B.22}$$

$$p = \rho R T. \tag{B.23}$$

Here, ρ denotes the density, $\mathbf{u}$ the velocity, p the pressure, h the specific enthalpy, Y_i is the mass fraction, $\boldsymbol{\tau}$ the viscous stress tensor, $\mathbf{f}$ the force term, μ the dynamic viscosity, $\mathbf{q}$ the heat flux, $\mathbf{J}_i$ the diffusive flux, T the temperature, R the specific gas constant, Q an external heat source, and $\dot{\omega}_i$ is the production rate.

This set of equations is also written in a different version after a manipulation of the left-hand side of the momentum, energy and species equations.

Using the identity (C.13), the left-hand side of (B.19) is

$$\begin{aligned}
\frac{\partial (\rho \mathbf{u})}{\partial t} + \nabla \cdot (\rho \ \mathbf{u} \otimes \mathbf{u}) &= \frac{\partial \rho}{\partial t} \mathbf{u} + \rho \frac{\partial \mathbf{u}}{\partial t} + \mathbf{u} (\nabla \cdot (\rho \mathbf{u})) + (\rho \mathbf{u} \cdot \nabla) \mathbf{u} \\
&= \mathbf{u} \frac{\partial \rho}{\partial t} + \mathbf{u} (\nabla \cdot (\rho \mathbf{u})) + \rho \frac{\partial \mathbf{u}}{\partial t} + \rho (\mathbf{u} \cdot \nabla) \mathbf{u} \\
&= \mathbf{u} \underbrace{\left(\frac{\partial \rho}{\partial t} + \nabla \cdot (\rho \mathbf{u}) \right)}_{\text{by (B.18)}}^{\to 0} + \rho \left(\frac{\partial \mathbf{u}}{\partial t} + (\mathbf{u} \cdot \nabla) \mathbf{u} \right) \\
&= \rho \left(\frac{\partial \mathbf{u}}{\partial t} + (\mathbf{u} \cdot \nabla) \mathbf{u} \right).
\end{aligned} \tag{B.24}$$

Similarly, for the energy equation,

$$\begin{aligned}\frac{\partial(\rho h)}{\partial t}+\nabla\cdot(\rho h\mathbf{u}) &= \frac{\partial\rho}{\partial t}h+\rho\frac{\partial h}{\partial t}+h(\nabla\cdot(\rho\mathbf{u}))+\rho\mathbf{u}\cdot\nabla h\\ &= h\frac{\partial\rho}{\partial t}+h(\nabla\cdot(\rho\mathbf{u}))+\rho\frac{\partial h}{\partial t}+\rho(\mathbf{u}\cdot\nabla h)\\ &= h\underbrace{\cancelto{0}{\left(\frac{\partial\rho}{\partial t}+\nabla\cdot(\rho\mathbf{u})\right)}}_{\text{by (B.18)}}+\rho\left(\frac{\partial h}{\partial t}+\mathbf{u}\cdot\nabla h\right)\\ &= \rho\left(\frac{\partial h}{\partial t}+\mathbf{u}\cdot\nabla h\right).\end{aligned} \tag{B.25}$$

The definition of sensible enthalpy (Rohsenow et al., 1998; K. McGrattan & Miles, 2016),(Poinsot & Veynante, 2012, p. 7) is,

$$h(T)=\int_{T_0}^{T}c_p(T')dT', \tag{B.26}$$

where T is the temperature of the fluid in Kelvin (K), c_p is the specific heat at constant pressure in J $\mathrm{kg}^{-1}\mathrm{K}^{-1}$ ($\mathrm{m}^2\mathrm{s}^{-2}\mathrm{K}^{-1}$), and T_0 is a reference temperature in K. Using the Leibinz integral and chain rules, the partial derivatives of enthalpy can be rewritten in terms of temperature as follows,

$$\frac{\partial h}{\partial t}=\frac{\partial h}{\partial T}\frac{\partial T}{\partial t}=c_p\frac{\partial T}{\partial t},\quad \nabla h=\frac{\partial h}{\partial T}\nabla T=c_p\nabla T.$$

Replacing both into the energy equation,

$$\frac{\partial(\rho h)}{\partial t}+\nabla\cdot(\rho h\mathbf{u})=\rho c_p\left(\frac{\partial T}{\partial t}+\mathbf{u}\cdot\nabla T\right).$$

For the conservation of species,

$$\begin{aligned}\frac{\partial(\rho Y_i)}{\partial t}+\nabla\cdot(\rho Y_i\mathbf{u}) &= \frac{\partial\rho}{\partial t}Y_i+\rho\frac{\partial Y_i}{\partial t}+Y_i(\nabla\cdot(\rho\mathbf{u}))+\rho\mathbf{u}\cdot\nabla Y_i\\ &= Y_i\frac{\partial\rho}{\partial t}+Y_i(\nabla\cdot(\rho\mathbf{u}))+\rho\frac{\partial Y_i}{\partial t}+\rho(\mathbf{u}\cdot\nabla Y_i)\\ &= Y_i\underbrace{\cancelto{0}{\left(\frac{\partial\rho}{\partial t}+\nabla\cdot(\rho\mathbf{u})\right)}}_{\text{by (B.18)}}+\rho\left(\frac{\partial Y_i}{\partial t}+\mathbf{u}\cdot\nabla Y_i\right)\\ &= \rho\left(\frac{\partial Y_i}{\partial t}+\mathbf{u}\cdot\nabla Y_i\right).\end{aligned} \tag{B.27}$$

Finally, the second version of the compressible Navier-Stokes equations is

$$\begin{aligned}
\frac{\partial \rho}{\partial t} + \nabla \cdot (\rho \mathbf{u}) &= 0, \\
\rho \left(\frac{\partial \mathbf{u}}{\partial t} + (\mathbf{u} \cdot \nabla)\mathbf{u} \right) &= -\nabla p + \nabla \cdot \boldsymbol{\tau} + \mathbf{f}, \\
\rho c_p \left(\frac{\partial T}{\partial t} + \mathbf{u} \cdot \nabla T \right) &= \frac{Dp}{Dt} - \nabla \cdot \mathbf{q} + \boldsymbol{\tau} : \nabla \mathbf{u} + \dot{Q}, \\
\rho \left(\frac{\partial Y_i}{\partial t} + \mathbf{u} \cdot \nabla Y_i \right) &= -\nabla \cdot \mathbf{J}_i + \dot{\omega}_i, \\
\boldsymbol{\tau} &= \mu \left(\nabla \mathbf{u} + (\nabla \mathbf{u})^\top - \frac{2}{3} (\nabla \cdot \mathbf{u}) \mathbf{I} \right), \\
p &= \rho R T.
\end{aligned} \tag{B.28}$$

Another typical version of the equations uses the definition of the material derivative (C.3), rewritten (B.28) as

$$\begin{aligned}
\frac{D\rho}{Dt} &= -\rho \nabla \cdot \mathbf{u}, \\
\rho \frac{D\mathbf{u}}{Dt} &= -\nabla p + \nabla \cdot \boldsymbol{\tau} + \mathbf{f}, \\
\rho c_p \frac{DT}{Dt} &= \frac{Dp}{Dt} - \nabla \cdot \mathbf{q} + \boldsymbol{\tau} : \nabla \mathbf{u} + Q, \\
\rho \frac{DY_i}{Dt} &= -\nabla \cdot \mathbf{J}_i + \dot{\omega}_i, \\
\boldsymbol{\tau} &= \mu \left(\nabla \mathbf{u} + (\nabla \mathbf{u})^\top - \frac{2}{3} (\nabla \cdot \mathbf{u}) \mathbf{I} \right), \\
p &= \rho R T.
\end{aligned} \tag{B.29}$$

B.2.6 Non-dimensionalization

Non-dimensionalization is used to reduce equations to a universal form, making it easier to identify the relative importance of different physical effects through dimensionless numbers. In particular, the numbers described in B.1 emerge from this procedure. The first step is the definition of the reference values for the characteristic scales: length L, velocity U, density ρ_0, temperature T_0, viscosity μ_0, thermal conductivity k_0, shear viscosity τ_0, force f_0, diffusion $D_{i,0}$, heat source $\dot{Q}_0$, and production rate $\dot{\omega}_{i,0}$. Using these scales, the dimensionless variables denoted by a star are

$$\begin{gathered}
\mathbf{x} = L\,\mathbf{x}^*, \quad t = \frac{L}{U}\,t^*, \quad \mathbf{u} = U\,\mathbf{u}^*, \quad \rho = \rho_0\,\rho^*, \quad h = h_0 h^*, \quad Y_i = Y_i^*, \quad T = T_0\,T^*, \\
p = p_0\,p^*, \quad \boldsymbol{\tau} = \tau_0 \boldsymbol{\tau}^*, \quad \mathbf{f} = f_0 \mathbf{f}^*, \quad \mathbf{q} = q_0 \mathbf{q}^*, \quad \dot{Q} = \dot{Q}_0 \dot{Q}^*, \quad \dot{\omega}_i = \dot{\omega}_{i,0} \dot{\omega}_i^*.
\end{gathered} \tag{B.30}$$

The associated scalings for the time derivative and gradient operators follow directly from the change of variables,

$$\frac{\partial}{\partial t} = \frac{U}{L}\frac{\partial}{\partial t^*}, \quad \nabla = \frac{1}{L}\nabla^*, \quad \frac{D}{Dt} = \frac{U}{L}\frac{D}{Dt^*}. \tag{B.31}$$

Starting from conservation of mass, the substitution of (B.31) and (B.30) into (B.18) gives

$$\begin{aligned}
\frac{\partial \rho}{\partial t} + \nabla \cdot (\rho \mathbf{u}) &= 0 \\
\frac{\partial (\rho_0 \rho^*)}{\partial t} + \nabla \cdot \left(\rho_0 \rho^* U \mathbf{u}^*\right) &= 0 \\
\frac{U}{L}\frac{\partial (\rho_0 \rho^*)}{\partial t^*} + \frac{1}{L}\nabla^* \cdot \left(\rho_0 \rho^* U \mathbf{u}^*\right) &= 0 \\
\frac{\rho_0 U}{L}\frac{\partial \rho^*}{\partial t^*} + \frac{\rho_0 U}{L}\nabla^* \cdot \left(\rho^* \mathbf{u}^*\right) &= 0 \\
\frac{\rho_0 U}{L}\left[\frac{\partial \rho^*}{\partial t^*} + \nabla^* \cdot \left(\rho^* \mathbf{u}^*\right)\right] &= 0 \\
\frac{\partial \rho^*}{\partial t^*} + \nabla^* \cdot \left(\rho^* \mathbf{u}^*\right) &= 0.
\end{aligned}$$

This shows that the conservative form is invariant under the chosen scaling, i.e., the non-dimensional equation retains the same structure as the dimensional version.

The same procedure is performed for momentum conservation, replacing (B.31) and (B.30) in (B.19),

$$\begin{aligned}
\frac{\partial (\rho \mathbf{u})}{\partial t} + \nabla \cdot (\rho \mathbf{u} \otimes \mathbf{u}) &= -\nabla p + \nabla \cdot \boldsymbol{\tau} + \mathbf{f} \\
\frac{\partial (\rho_0 \rho^* U \mathbf{u}^*)}{\partial t} + \nabla \cdot (\rho_0 \rho^* U \mathbf{u}^* \otimes U \mathbf{u}^*) &= -\nabla (p_0 p^*) + \nabla \cdot (\tau_0 \boldsymbol{\tau}^*) + f_0 \mathbf{f}^* \\
\frac{U}{L}\frac{\partial (\rho_0 \rho^* U \mathbf{u}^*)}{\partial t^*} + \frac{1}{L}\nabla^* \cdot (\rho_0 \rho^* U \mathbf{u}^* \otimes U \mathbf{u}^*) &= -\frac{1}{L}\nabla^* (p_0 p^*) + \frac{1}{L}\nabla^* \cdot (\tau_0 \boldsymbol{\tau}^*) + f_0 \mathbf{f}^* \\
\frac{\rho_0 U^2}{L}\frac{\partial (\rho^* \mathbf{u}^*)}{\partial t^*} + \frac{\rho_0 U^2}{L}\nabla^* \cdot (\rho^* \mathbf{u}^* \otimes \mathbf{u}^*) &= -\frac{p_0}{L}\nabla^* p^* + \frac{\tau_0}{L}\nabla^* \cdot \boldsymbol{\tau}^* + f_0 \mathbf{f}^* \\
\frac{\rho_0 U^2}{L}\left[\frac{\partial (\rho^* \mathbf{u}^*)}{\partial t^*} + \nabla^* \cdot (\rho^* \mathbf{u}^* \otimes \mathbf{u}^*)\right] &= -\frac{p_0}{L}\nabla^* p^* + \frac{\tau_0}{L}\nabla^* \cdot \boldsymbol{\tau}^* + f_0 \mathbf{f}^* \\
\frac{\partial (\rho^* \mathbf{u}^*)}{\partial t^*} + \nabla^* \cdot (\rho^* \mathbf{u}^* \otimes \mathbf{u}^*) &= -\frac{p_0}{\rho_0 U^2}\nabla^* p^* + \frac{\tau_0}{\rho_0 U^2}\nabla^* \cdot \boldsymbol{\tau}^* + \frac{f_0 L}{\rho_0 U^2}\mathbf{f}^*.
\end{aligned}$$

Considering the characteristic viscous shear stress, force and pressure (using (B.2)),

$$\tau_0 = \frac{\mu_0 U}{L}, \quad p_0 = \rho_0 c^2 = \gamma \rho_0 R T_0, \quad f_0 = \frac{\rho_0 U^2}{L},$$

the non-dimensional momentum equation is

$$\begin{aligned}\frac{\partial(\rho^*\mathbf{u}^*)}{\partial t^*} + \nabla^*\cdot(\rho^*\mathbf{u}^*\otimes\mathbf{u}^*) &= -\frac{p_0}{\rho_0U^2}\nabla^*p^* + \frac{\tau_0}{\rho_0U^2}\nabla^*\cdot\boldsymbol{\tau}^* + \frac{f_0L}{\rho_0U^2}\mathbf{f}^*\\ &= -\frac{\rho_0c^2}{\rho_0U^2}\nabla^*p^* + \frac{\mu_0U}{\rho_0U^2L}\nabla^*\cdot\boldsymbol{\tau}^* + \frac{\rho_0U^2L}{\rho_0U^2L}\mathbf{f}^*\\ &= -\left(\frac{c}{U}\right)^2\nabla^*p^* + \frac{\mu_0}{\rho_0UL}\nabla^*\cdot\boldsymbol{\tau}^* + \mathbf{f}^*\\ &= -\frac{1}{\mathrm{Ma}^2}\nabla^*p^* + \frac{1}{\mathrm{Re}}\nabla^*\cdot\boldsymbol{\tau}^* + \mathbf{f}^*.\end{aligned}$$

For energy conservation, replacing (B.31) and (B.30) in (B.20),

$$\begin{aligned}\frac{\partial(\rho h)}{\partial t} + \nabla\cdot(\rho h\,\mathbf{u}) &= \frac{Dp}{Dt} - \nabla\cdot\mathbf{q} + \boldsymbol{\tau}:\nabla\mathbf{u} + \dot{Q}\\ \frac{\partial(\rho_0\rho^*h_0h^*)}{\partial t} + \nabla\cdot(\rho_0\rho^*h_0h^*\,U\mathbf{u}^*) &= \frac{D(p_0p^*)}{Dt} - \nabla\cdot(q_0\mathbf{q}^*)\\ &\quad + (\tau_0\boldsymbol{\tau}):(\nabla(U\mathbf{u}^*)) + \dot{Q}_0\dot{Q}^*\\ \frac{U}{L}\frac{\partial(\rho_0\rho^*h_0h^*)}{\partial t^*} + \frac{1}{L}\nabla^*\cdot(\rho_0\rho^*h_0h^*\,U\mathbf{u}^*) &= \frac{U}{L}\frac{D(p_0p^*)}{Dt^*} - \frac{1}{L}\nabla^*\cdot(q_0\mathbf{q}^*)\\ &\quad + (\tau_0\boldsymbol{\tau}^*):\left(\frac{1}{L}\nabla^*(U\mathbf{u}^*)\right) + \dot{Q}_0\dot{Q}^*\\ \frac{\rho_0h_0U}{L}\frac{\partial(\rho^*h^*)}{\partial t^*} + \frac{\rho_0h_0U}{L}\nabla^*\cdot(\rho^*h^*\mathbf{u}^*) &= \frac{p_0U}{L}\frac{Dp^*}{Dt^*} - \frac{q_0}{L}\nabla^*\cdot\mathbf{q}^*\\ &\quad + \frac{\tau_0U}{L}\boldsymbol{\tau}^*:\nabla^*\mathbf{u}^* + \dot{Q}_0\dot{Q}^*\\ \frac{\rho_0h_0U}{L}\left[\frac{\partial(\rho^*h^*)}{\partial t^*} + \nabla^*\cdot(\rho^*h^*\mathbf{u}^*)\right] &= \frac{p_0U}{L}\frac{Dp^*}{Dt^*} - \frac{q_0}{L}\nabla^*\cdot\mathbf{q}^*\\ &\quad + \frac{\tau_0U}{L}\boldsymbol{\tau}^*:\nabla^*\mathbf{u}^* + \dot{Q}_0\dot{Q}^*\\ \frac{\partial(\rho^*h^*)}{\partial t^*} + \nabla^*\cdot(\rho^*h^*\mathbf{u}^*) &= \frac{p_0}{\rho_0h_0}\frac{Dp^*}{Dt^*} - \frac{q_0}{\rho_0h_0U}\nabla^*\cdot\mathbf{q}^*\\ &\quad + \frac{\tau_0}{\rho_0h_0}\boldsymbol{\tau}^*:\nabla^*\mathbf{u}^* + \frac{\dot{Q}_0L}{\rho_0h_0U}\dot{Q}^*.\end{aligned}$$

Using (B.26) for a constant specific heat,

$$h = c_pT. \tag{B.32}$$

The heat flux vector can be defined using Fourier's law as follows,

$$\mathbf{q} = -k\nabla T, \tag{B.33}$$

where its non-dimensional form is

$$\mathbf{q} = -k\nabla T \implies q_0\mathbf{q}^* = -\frac{k}{L}\nabla^*(T_0T^*) = -\frac{kT_0}{L}\nabla^*T^*.$$

With (B.32) and (B.33), the following characteristic scales are introduced:

$$h_0 = c_p T_0, \quad q_0 = \frac{kT_0}{L}, \quad \dot{Q}_0 = \frac{\rho_0 h_0 U}{L}.$$

Then, with the previous definitions, the conservation of energy is

$$\begin{aligned}
\frac{\partial(\rho^* h^*)}{\partial t^*} + \nabla^* \cdot (\rho^* h^* \mathbf{u}^*) &= \frac{p_0}{\rho_0 c_p T_0}\frac{Dp^*}{Dt^*} - \frac{q_0}{\rho_0 h_0 U}\nabla^* \cdot \mathbf{q}^* \\
&\quad + \frac{\mu_0 U}{\rho_0 c_p T_0 L}\boldsymbol{\tau}^* : \nabla^* \mathbf{u}^* + \frac{\dot{Q}_0 L}{\rho_0 h_0 U}\dot{Q}^* \\
&= \frac{p_0}{\rho_0 c_p T_0}\frac{Dp^*}{Dt^*} + \frac{kT_0}{\rho_0 c_p T_0 U L}\nabla^* \cdot (\nabla^* T^*) \\
&\quad + \frac{\mu_0 U}{\rho_0 c_p T_0 L}\boldsymbol{\tau}^* : \nabla^* \mathbf{u}^* + \frac{\dot{Q}_0 L}{\rho_0 h_0 U}\dot{Q}^* \\
&= \frac{c^2}{c_p T_0}\frac{Dp^*}{Dt^*} + \frac{k}{\rho_0 c_p U L}\nabla^{*2} T^* \\
&\quad + \frac{\mu_0 U}{\rho_0 c_p T_0 L}\boldsymbol{\tau}^* : \nabla^* \mathbf{u}^* + \frac{\rho_0 h_0 U L}{\rho_0 h_0 U L}\dot{Q}^* \\
&= \frac{c^2}{c_p T_0}\frac{Dp^*}{Dt^*} + \frac{1}{\mathrm{Pe}}\nabla^{*2} T^* + \frac{U^2}{c_p T_0}\frac{\mu}{\rho_0 U L}\boldsymbol{\tau}^* : \nabla^* \mathbf{u}^* + \dot{Q}^* \\
&= (\gamma - 1)\frac{Dp^*}{Dt^*} + \frac{1}{\mathrm{Re}\,\mathrm{Pr}}\nabla^{*2} T^* + \frac{\mathrm{Ec}}{\mathrm{Re}}\boldsymbol{\tau}^* : \nabla^* \mathbf{u}^* + \dot{Q}^*.
\end{aligned}$$

The term $\gamma - 1$ emerges from the approximation $R = c_p - c_V$ and using (B.3),

$$\frac{c^2}{c_p T_0} = \frac{\gamma R T_0}{c_p T_0} = \frac{\gamma R}{c_p} = \frac{c_p}{c_V}\frac{c_p - c_V}{c_p} = \frac{c_p - c_V}{c_V} = \frac{c_p}{c_V} - 1 = \gamma - 1.$$

Following the same procedure for conservation of species using the Fick's law for the mass flux, $\mathbf{J}_i = -\rho D_i \nabla Y_i$,

$$\begin{aligned}
\frac{\partial(\rho Y_i)}{\partial t} + \nabla \cdot (\rho Y_i \mathbf{u}) &= \nabla \cdot (\rho D_i \nabla Y_i) + \dot{\omega}_i \\
\frac{\partial(\rho_0 \rho^* Y_i^*)}{\partial t} + \nabla \cdot (\rho_0 \rho^* Y_i^* U \mathbf{u}^*) &= \nabla \cdot (\rho_0 \rho^* D_{i,0} \nabla Y_i^*) + \dot{\omega}_{i,0}\dot{\omega}_i^* \\
\frac{U}{L}\frac{\partial(\rho_0 \rho^* Y_i^*)}{\partial t^*} + \frac{1}{L}\nabla^* \cdot (\rho_0 \rho^* Y_i^* U \mathbf{u}^*) &= \frac{1}{L}\nabla^* \cdot \left(\rho_0 \rho^* D_{i,0}\frac{1}{L}\nabla^* Y_i^*\right) + \dot{\omega}_{i,0}\dot{\omega}_i^* \\
\frac{\rho_0 U}{L}\frac{\partial(\rho^* Y_i^*)}{\partial t^*} + \frac{\rho_0 U}{L}\nabla^* \cdot (\rho^* Y_i^* \mathbf{u}^*) &= \frac{\rho_0 D_{i,0}}{L^2}\nabla^* \cdot (\rho^* \nabla^* Y_i^*) + \dot{\omega}_{i,0}\dot{\omega}_i^* \\
\frac{\rho_0 U}{L}\left[\frac{\partial(\rho^* Y_i^*)}{\partial t^*} + \nabla^* \cdot (\rho^* Y_i^* \mathbf{u}^*)\right] &= \frac{\rho_0 D_{i,0}}{L^2}\nabla^* \cdot (\rho^* \nabla^* Y_i^*) + \dot{\omega}_{i,0}\dot{\omega}_i^* \\
\frac{\partial(\rho^* Y_i^*)}{\partial t^*} + \nabla^* \cdot (\rho^* Y_i^* \mathbf{u}^*) &= \frac{D_{i,0}}{LU}\nabla^* \cdot (\rho^* \nabla^* Y_i^*) + \frac{\dot{\omega}_{i,0} L}{\rho_0 U}\dot{\omega}_i^*.
\end{aligned}$$

Using (B.8) and defining

$$\dot{\omega}_{i,0} = \frac{\rho_0 L}{U},$$

the non-dimensional conservation of species is,

$$\begin{aligned}
\frac{\partial(\rho^* Y_i^*)}{\partial t^*} + \nabla^* \cdot (\rho^* Y_i^* \mathbf{u}^*) &= \frac{D_{i,0}}{LU} \nabla^* \cdot (\rho^* \nabla^* Y_i^*) + \frac{\dot{\omega}_{i,0} L}{\rho_0 U} \dot{\omega}_i^* \\
\frac{\partial(\rho^* Y_i^*)}{\partial t^*} + \nabla^* \cdot (\rho^* Y_i^* \mathbf{u}^*) &= \frac{1}{\mathrm{Pe}_{m,i}} \nabla^* \cdot (\rho^* \nabla^* Y_i^*) + \frac{\rho_0 U L}{\rho_0 U L} \dot{\omega}_i^* \\
&= \frac{1}{\mathrm{Pe}_{m,i}} \nabla^* \cdot (\rho^* \nabla^* Y_i^*) + \dot{\omega}_i^*.
\end{aligned}$$

The non-dimensional equation of state is obtained straightforwardly using the definition of characteristic lengths and variables,

$$\begin{aligned}
p &= \rho R T \\
p_0 p^* &= \rho_0 \rho^* R T_0 T^* \\
p^* &= \frac{\rho_0 R T_0}{p_0} \rho^* T^* \\
&= \frac{\rho_0 R T_0}{\rho_0 c^2} \rho^* T^* \\
&= \frac{\rho_0 R T_0}{\gamma \rho_0 R T_0} \rho^* T^* \\
&= \frac{1}{\gamma} \rho^* T^*.
\end{aligned}$$

Wrapping up all the derivations of above, the non-dimensional Navier-Stokes equations are:

$$\begin{aligned}
\frac{\partial \rho^*}{\partial t^*} + \nabla^* \cdot (\rho^* \mathbf{u}^*) &= 0 \\
\frac{\partial(\rho^* \mathbf{u}^*)}{\partial t^*} + \nabla^* \cdot (\rho^* \mathbf{u}^* \otimes \mathbf{u}^*) &= -\frac{1}{\mathrm{Ma}^2} \nabla^* p^* + \frac{1}{\mathrm{Re}} \nabla^* \cdot \boldsymbol{\tau}^* + \mathbf{f}^*, \\
\frac{\partial(\rho^* h^*)}{\partial t^*} + \nabla^* \cdot (\rho^* h^* \mathbf{u}^*) &= (\gamma - 1) \frac{D p^*}{D t^*} + \frac{1}{\mathrm{Re}\,\mathrm{Pr}} \nabla^{*2} T^* + \frac{\mathrm{Ec}}{\mathrm{Re}} \boldsymbol{\tau}^* + \dot{Q}^*, \\
\frac{\partial(\rho^* Y_i^*)}{\partial t^*} + \nabla^* \cdot (\rho^* Y_i^* \mathbf{u}^*) &= \frac{1}{\mathrm{Pe}_{m,i}} \nabla^* \cdot (\rho^* \nabla^* Y_i^*) + \dot{\omega}_i^*, \\
p^* &= \frac{1}{\gamma} \rho^* T^*.
\end{aligned} \tag{B.34}$$

B.2.7 Low-Mach number approximation

The low-Mach Number approximation eliminates the propagation of acoustic waves while preserving thermodynamic consistency, making it well suited for modeling

low-speed, variable-density flows. This approximation is obtained from the non-dimensional Navier-Stokes equations (B.34), by performing an asymptotic expansion using powers of $\epsilon = \mathrm{Ma}^2$ and assuming $\mathrm{Ma} \ll 1$. To start, the variables are expanded as follows,

$$\begin{aligned} \rho &= \rho_0 + \epsilon\rho_1 + \mathcal{O}(\epsilon^2), \\ \mathbf{u} &= \mathbf{u}_0 + \epsilon\mathbf{u}_1 + \mathcal{O}(\epsilon^2), \\ p &= p_0 + \epsilon p_1 + \mathcal{O}(\epsilon^2), \\ h &= h_0 + \epsilon h_1 + \mathcal{O}(\epsilon^2), \\ T &= T_0 + \epsilon T_1 + \mathcal{O}(\epsilon^2). \end{aligned} \tag{B.35}$$

Stars in the non-dimensional variables are omitted to simplify the notation, but the derivation is over the non-dimensional equations. The derivation starts by substituting (B.35) in the conservation of momentum of (B.34). For the unsteady term,

$$\begin{aligned} \frac{\partial(\rho\mathbf{u})}{\partial t} &= \frac{\partial}{\partial t}\left((\rho_0 + \epsilon\rho_1 + \mathcal{O}(\epsilon^2))(\mathbf{u}_0 + \epsilon\mathbf{u}_1 + \mathcal{O}(\epsilon^2))\right) \\ &= \frac{\partial}{\partial t}\left(\rho_0\mathbf{u}_0 + \epsilon\rho_1\mathbf{u}_0 + \epsilon\rho_0\mathbf{u}_1 + \epsilon^2\rho_1\mathbf{u}_1 + \mathcal{O}(\epsilon^3)\right) \\ &= \frac{\partial(\rho_0\mathbf{u}_0)}{\partial t} + \mathcal{O}(\epsilon). \end{aligned}$$

As the main assumption, note that $\mathcal{O}(\epsilon) \to 0$ as $\epsilon = \mathrm{Ma}^2 \to 0$ when $\mathrm{Ma} \ll 1$. The full expansion for each component is not detailed, but the idea can be extended from the previous manipulation. In particular, the pressure gradient term is

$$\frac{1}{\mathrm{Ma}^2}\nabla p = \frac{1}{\epsilon}\nabla(p_0 + \epsilon p_1 + \mathcal{O}(\epsilon^2)) = \frac{1}{\epsilon}\nabla p_0 + \frac{1}{\epsilon}\nabla(\epsilon p_1) + \frac{1}{\epsilon}\mathcal{O}(\epsilon^2) = \frac{1}{\epsilon}\nabla p_0 + \nabla p_1 + \mathcal{O}(\epsilon)$$

This result means that the $\mathcal{O}(1)$ term is ∇p_1, and

$$-\nabla p_0 = 0 \implies p_0 = p_0(t),$$

since it does not depend on space. Collecting the leading-order terms $\mathcal{O}(1)$, the conservation of momentum is

$$\frac{\partial(\rho_0\mathbf{u}_0)}{\partial t} + \nabla\cdot(\rho_0\mathbf{u}_0 \otimes \mathbf{u}_0) = -\nabla p_1 + \frac{1}{\mathrm{Re}}\nabla\cdot\boldsymbol{\tau}_0 + \mathbf{f}_0.$$

From a physical meaning, the pressure is decomposed into a spatially uniform thermodynamic component and a dynamic perturbation

$$p(\mathbf{x}, t) = p_0(t) + \epsilon p_1(\mathbf{x}, t) + \mathcal{O}(\epsilon^2). \tag{B.36}$$

Where the thermodynamic pressure scales in $\mathcal{O}(\epsilon^{-1})$, but the other variables, such as density, velocity, and the dynamical perturbation, in $\mathcal{O}(1)$ when the Mach number is small.

In the same fashion, by expanding the mass conservation equation in (B.34),

$$\frac{\partial \rho_0}{\partial t} + \nabla \cdot (\rho_0 \mathbf{u}_0) = 0.$$

This result can be interpreted as the compressibility is governed by thermodynamic changes rather than pressure waves.

The energy equation has the same behavior, but considering

$$\begin{aligned} \frac{Dp}{Dt} = \frac{\partial p}{\partial t} + \mathbf{u} \cdot \nabla p &= \frac{\partial (p_0 + \epsilon p_1 + \mathcal{O}(\epsilon^2))}{\partial t} + \mathbf{u} \cdot \nabla (p_0 + \epsilon p_1 + \mathcal{O}(\epsilon^2)) \\ &= \frac{\partial p_0}{\partial t} + \mathbf{u} \cdot \nabla p_0 + \mathcal{O}(\epsilon). \end{aligned} \tag{B.37}$$

As $\mathrm{Ma} \ll 1$, $\mathcal{O}(\epsilon) \to 0$ and p_0 is spatially uniform, therefore (B.37) can be approximated with

$$\frac{Dp}{Dt} = \frac{\partial p_0}{\partial t} + \mathbf{u} \cdot \nabla p_0 + \mathcal{O}(\epsilon) \approx \frac{dp_0}{dt}.$$

Then,

$$\frac{\partial (\rho_0 h_0)}{\partial t} + \nabla \cdot (\rho_0 h_0 \mathbf{u}) = (\gamma - 1) \frac{dp_0}{dt} + \frac{1}{\mathrm{Re}\,\mathrm{Pr}} \nabla^2 T + \frac{\mathrm{Ec}}{\mathrm{Re}} \boldsymbol{\tau} + \dot{Q}.$$

Regarding the species equation, it does not have any pressure term or Ma scaling term, so the equation follows the same behavior of the mass conservation for the leading-order term,

$$\frac{\partial (\rho_0 Y_{i,0})}{\partial t} + \nabla \cdot (\rho_0 Y_{i,0} \mathbf{u}_0) = \frac{1}{\mathrm{Pe}_{m,i}} \nabla \cdot (\rho_0 \nabla Y_{i,0}) + \dot{\omega}_i.$$

Finally, the equation of state is

$$p_0 = \frac{1}{\gamma} \rho_0 T_0. \tag{B.38}$$

For asymptotic consistency, (B.37) must ensure the combined demands of mass conservation and the equation of state at the limit when $\mathrm{Ma} \to 0$. As a result, an extra restriction using the divergence of velocity is introduced to enforce the latter. Notice that conservation of mass can be expressed as

$$\frac{\partial \rho_0}{\partial t} + \nabla \cdot (\rho_0 \mathbf{u}_0) = \frac{\partial \rho_0}{\partial t} + \rho_0 \nabla \cdot \mathbf{u}_0 + \mathbf{u}_0 \cdot \nabla \rho_0 = \frac{D\rho_0}{Dt} + \rho_0 \nabla \cdot \mathbf{u}_0 = 0.$$

This implies that

$$\nabla \cdot \mathbf{u}_0 = -\frac{1}{\rho_0} \frac{D\rho_0}{Dt}. \tag{B.39}$$

The right-hand side of (B.41) can be obtained from (B.38) computing the total derivative of both sides,

$$\begin{aligned} p_0 &= \frac{1}{\gamma}\rho_0 T_0 \\ \frac{Dp_0}{Dt} &= \frac{1}{\gamma}\left(T_0\frac{D\rho_0}{Dt} + \rho_0\frac{DT_0}{Dt}\right) \\ \gamma\frac{Dp_0}{Dt} &= T_0\frac{D\rho_0}{Dt} + \rho_0\frac{DT_0}{Dt} \\ -T_0\frac{D\rho_0}{Dt} &= \rho_0\frac{DT_0}{Dt} - \gamma\frac{Dp_0}{Dt} \\ -\frac{D\rho_0}{Dt} &= \frac{1}{T_0}\left(\rho_0\frac{DT_0}{Dt} - \gamma\frac{Dp_0}{Dt}\right). \end{aligned} \tag{B.40}$$

Replacing (B.40) in (B.39),

$$\begin{aligned} \nabla\cdot\mathbf{u}_0 &= -\frac{1}{\rho_0}\frac{D\rho_0}{Dt} \\ &= \frac{1}{\rho_0 T_0}\left(\rho_0\frac{DT_0}{Dt} - \gamma\frac{Dp_0}{Dt}\right) \\ &= \frac{1}{T_0}\frac{DT_0}{Dt} - \frac{\gamma}{\rho_0 T_0}\frac{Dp_0}{Dt}. \end{aligned}$$

Finally, after replacing γ with the definition of (B.38),

$$\nabla\cdot\mathbf{u}_0 = \frac{1}{T_0}\frac{DT_0}{Dt} - \frac{1}{p_0}\frac{Dp_0}{Dt} = \frac{1}{T_0}\frac{DT_0}{Dt} - \frac{1}{p_0}\frac{dp_0}{dt}. \tag{B.41}$$

At this point, the derivation of the low-Mach number approximation is complete, and the equations can be returned to the dimensional form, but taking into account the different pressures. In summary, the governing equations, with (B.28) to eliminate the use of sensible enthalpy, are

$$\begin{aligned} \frac{\partial\rho}{\partial t} + \nabla\cdot(\rho\mathbf{u}) &= 0, \\ \rho\left(\frac{\partial\mathbf{u}}{\partial t} + \mathbf{u}\cdot\nabla\mathbf{u}\right) &= -\nabla p_{\mathrm{d}} + \nabla\cdot\boldsymbol{\tau} + \mathbf{f}, \\ \rho c_p\left(\frac{\partial T}{\partial t} + \mathbf{u}\cdot\nabla T\right) &= \frac{dp_0}{dt} - \nabla\cdot\mathbf{q} + \boldsymbol{\tau}:\nabla\mathbf{u} + \dot{Q}, \\ \rho\left(\frac{\partial Y_i}{\partial t} + \mathbf{u}\cdot\nabla Y_i\right) &= -\nabla\cdot\mathbf{J}_i + \dot{\omega}_i, \\ \nabla\cdot\mathbf{u} &= \frac{1}{T}\frac{DT}{Dt} - \frac{1}{p_0}\frac{dp_0}{dt}, \\ p_0 &= \rho RT. \end{aligned}$$

B.3 Incompressible Flow Equations

An incompressible flow can be modeled as strictly incompressible with constant density or variable density involving small perturbations of density, mass, or temperature. For both cases, the divergence of the flow velocity must be zero, or mathematically,

$$\nabla \cdot \mathbf{u} = 0. \tag{B.42}$$

For the constant density, the zero-divergence is a direct consequence from the conservation of mass,

$$\begin{aligned} \frac{\partial \rho}{\partial t} + \nabla \cdot (\rho \mathbf{u}) &= 0 \\ \cancelto{0}{\frac{\partial \rho}{\partial t}} + \rho \nabla \cdot \mathbf{u} &= 0 \\ \nabla \cdot \mathbf{u} &= 0, \end{aligned} \tag{B.43}$$

the last step dividing by $\rho \neq 0$. For a variable density, replacing (B.42) in the conservation of mass (4.1) yields

$$\begin{aligned} \frac{\partial \rho}{\partial t} + \nabla \cdot (\rho \mathbf{u}) &= 0 \\ \frac{\partial \rho}{\partial t} + \nabla \rho \cdot \mathbf{u} + \rho \underbrace{\cancelto{0}{\nabla \cdot \mathbf{u}}}_{\text{by (B.42)}} &= 0 \\ \frac{\partial \rho}{\partial t} + \nabla \rho \cdot \mathbf{u} &= 0. \end{aligned} \tag{B.44}$$

Considering an incompressible flow with constant μ, and using the identity (C.15), the (B.19) simplifies to

$$\begin{aligned} \frac{\partial (\rho \mathbf{u})}{\partial t} + \nabla \cdot (\rho\, \mathbf{u} \otimes \mathbf{u}) &= -\nabla p + \nabla \cdot \left(\mu \left[\nabla \mathbf{u} + (\nabla \mathbf{u})^\top - \frac{2}{3} (\nabla \cdot \mathbf{u}) \mathbf{I} \right] \right) + \mathbf{f} \\ \underbrace{\rho \left(\frac{\partial \mathbf{u}}{\partial t} + (\mathbf{u} \cdot \nabla) \mathbf{u} \right)}_{\text{by (B.24)}} &= -\nabla p + \nabla \cdot \left(\mu \left[\nabla \mathbf{u} + (\nabla \mathbf{u})^\top - \frac{2}{3} \underbrace{\cancelto{0}{(\nabla \cdot \mathbf{u})}}_{\text{by (B.42)}} \mathbf{I} \right] \right) + \mathbf{f} \\ &= -\nabla p + \mu \nabla \cdot \left[\nabla \mathbf{u} + (\nabla \mathbf{u})^\top \right] + \mathbf{f} \\ &= -\nabla p + \underbrace{\mu \left(\nabla^2 \mathbf{u} + \nabla \underbrace{\cancelto{0}{(\nabla \cdot \mathbf{u})}}_{\text{by (B.42)}} \right)}_{\text{by (C.15)}} + \mathbf{f} \\ &= -\nabla p + \mu \nabla^2 \mathbf{u} + \mathbf{f}. \end{aligned}$$

The simplification of the energy equations can be obtained from the sensible enthalpy energy equation:

$$\rho\frac{Dh}{Dt} = \frac{Dp}{Dt} - \nabla\cdot\mathbf{q} + \boldsymbol{\tau} : \nabla\mathbf{u} + Q.$$

Using the thermodynamic identity using the internal energy e,

$$\begin{aligned} h &= e + \frac{p}{\rho} \quad /\frac{D}{Dt} \\ \frac{Dh}{Dt} &= \frac{De}{Dt} + \frac{1}{\rho}\frac{Dp}{Dt} - \frac{p}{\rho^2}\underbrace{\cancelto{0}{\frac{D\rho}{Dt}}}_{\rho \text{ constant}} \\ \frac{Dh}{Dt} &= \frac{De}{Dt} + \frac{1}{\rho}\frac{Dp}{Dt} \\ \rho\frac{Dh}{Dt} &= \rho\frac{De}{Dt} + \frac{Dp}{Dt}. \end{aligned} \tag{B.45}$$

Substituting back into the energy equation yields,

$$\begin{aligned} \rho\frac{Dh}{Dt} &= \frac{Dp}{Dt} - \nabla\cdot\mathbf{q} + \boldsymbol{\tau} : \nabla\mathbf{u} + Q \\ \rho\frac{De}{Dt} + \frac{Dp}{Dt} &= \frac{Dp}{Dt} - \nabla\cdot\mathbf{q} + \boldsymbol{\tau} : \nabla\mathbf{u} + Q \\ \rho\frac{De}{Dt} &= -\nabla\cdot\mathbf{q} + \boldsymbol{\tau} : \nabla\mathbf{u} + Q. \end{aligned}$$

Assuming constant properties, $e = c_V T$ and $c_p \simeq c_V$,

$$\rho c_p\frac{DT}{Dt} = -\nabla\cdot\mathbf{q} + \boldsymbol{\tau} : \nabla\mathbf{u} + Q.$$

Using Fourier's law (B.33) with constant k and neglecting the dissipation term $\boldsymbol{\tau} : \nabla$,

$$\rho c_p\frac{DT}{Dt} = k\nabla^2 T + Q.$$

Finally, considering a strictly incompressible fluid flow, equations (B.18), (B.19) and (B.20) are rewritten as

$$\nabla\cdot\mathbf{u} = 0, \tag{B.46}$$

$$\rho\left(\frac{\partial\mathbf{u}}{\partial t} + (\mathbf{u}\cdot\nabla)\,\mathbf{u}\right) = -\nabla p + \mu\nabla^2\mathbf{u} + \mathbf{f}, \tag{B.47}$$

$$\rho c_p\left(\frac{\partial T}{\partial t} + \mathbf{u}\cdot\nabla T\right) = k\nabla^2 T + Q. \tag{B.48}$$

For small density variations, (B.44), the equations can be written as

$$\begin{aligned}
\nabla \cdot \mathbf{u} &= 0, \\
\frac{\partial \rho}{\partial t} + \nabla \rho \cdot \mathbf{u} &= 0, \\
\rho \left(\frac{\partial \mathbf{u}}{\partial t} + (\mathbf{u} \cdot \nabla)\, \mathbf{u} \right) &= -\nabla p + \mu \nabla^2 \mathbf{u} + \mathbf{f}, \\
\rho c_p \left(\frac{\partial T}{\partial t} + \mathbf{u} \cdot \nabla T \right) &= k \nabla^2 T + Q.
\end{aligned}$$

B.3.1 Boussinesq Approximation

The Boussinesq approximation can be applied to problems where temperature variations are introduced into the fluid dynamics, driving a flow of fluid and heat transfer Tritton (1977, p. 127). In this approximation, the density is considered constant except in the force term, specifically because of the gravity effects. Starting from an approximation of incompressible flow, equations (B.46) and (B.47), the force term is defined by

$$\mathbf{f} = \rho \mathbf{g}, \tag{B.49}$$

where $\mathbf{g}$ represents the gravitational force and is defined as

$$\mathbf{g} = -\nabla \Phi. \tag{B.50}$$

Generally, the potential is $\Phi = gz$, so $\mathbf{g} = -g\hat{\mathbf{z}}$ with $g \approx 9.8$ m s^{-1} and $\hat{\mathbf{z}} = (0, 0, 1)$. The density variations can be considered defining

$$\rho = \rho_\infty + \Delta\rho, \tag{B.51}$$

where ρ_∞ must satisfy the hydrostatic balance (Appendix A.4). Replacing (B.49) and (B.51) in (B.47),

$$(\rho_\infty + \Delta\rho) \left(\frac{\partial \mathbf{u}}{\partial t} + (\mathbf{u} \cdot \nabla)\, \mathbf{u} \right) = -\nabla p + \mu \nabla^2 \mathbf{u} + (\rho_\infty + \Delta\rho)\mathbf{g}.$$

Dividing by ρ_∞,

$$\left(1 + \frac{\Delta\rho}{\rho_\infty} \right) \left(\frac{\partial \mathbf{u}}{\partial t} + (\mathbf{u} \cdot \nabla)\, \mathbf{u} \right) = -\frac{1}{\rho_\infty} \nabla p + \nu \nabla^2 \mathbf{u} + \left(1 + \frac{\Delta\rho}{\rho_\infty} \right) \mathbf{g},$$

where $\nu = \mu / \rho_\infty$ is the kinematic viscosity in m^{2}s^{-1}. Since the Boussinesq assumption states that $\Delta\rho / \rho_\infty \ll 1$ except for the force term,

$$\frac{\partial \mathbf{u}}{\partial t} + (\mathbf{u} \cdot \nabla)\, \mathbf{u} = -\frac{1}{\rho_\infty} \nabla p + \nu \nabla^2 \mathbf{u} + \left(1 + \frac{\Delta\rho}{\rho_\infty} \right) \mathbf{g},$$

Expanding and reordering the last expression,

$$\begin{aligned}
\frac{\partial \mathbf{u}}{\partial t} + (\mathbf{u}\cdot\nabla)\,\mathbf{u} &= -\frac{1}{\rho_\infty}\nabla p + \nu\nabla^2\mathbf{u} + \left(1+\frac{\Delta\rho}{\rho_\infty}\right)\mathbf{g} \\
&= -\frac{1}{\rho_\infty}\nabla p + \nu\nabla^2\mathbf{u} + \mathbf{g} + \frac{\Delta\rho}{\rho_\infty}\mathbf{g} \\
&= -\frac{1}{\rho_\infty}\left(\nabla p - \rho_\infty\mathbf{g}\right) + \nu\nabla^2\mathbf{u} + \frac{\Delta\rho}{\rho_\infty}\mathbf{g} \\
&= -\frac{1}{\rho_\infty}\left(\nabla p + \rho_\infty\nabla\Phi\right) + \nu\nabla^2\mathbf{u} + \frac{\Delta\rho}{\rho_\infty}\mathbf{g} \\
&= -\frac{1}{\rho_\infty}\nabla\left(p + \rho_\infty\Phi\right) + \nu\nabla^2\mathbf{u} + \frac{\Delta\rho}{\rho_\infty}\mathbf{g} \\
&= -\frac{1}{\rho_\infty}\nabla P + \nu\nabla^2\mathbf{u} + \frac{\Delta\rho}{\rho_\infty}\mathbf{g},
\end{aligned} \tag{B.52}$$

where a modified pressure is introduced as

$$P = p + \rho_0\Phi = p + \rho_0\, g\, z. \tag{B.53}$$

According to Tritton (1977, p. 128), the dependence of the density on temperature T, is linearized (derivation in Appendix A.2),

$$\Delta\rho = -\alpha_V\rho_\infty\Delta T \iff \frac{\Delta\rho}{\rho_\infty} = -\alpha_V\Delta T, \tag{B.54}$$

with α_V the coefficient of expansion of the fluid and,

$$T = T_\infty + \Delta T. \tag{B.55}$$

Replacing (B.54), in (B.52),

$$\frac{\partial \mathbf{u}}{\partial t} + (\mathbf{u}\cdot\nabla)\,\mathbf{u} = -\frac{1}{\rho_\infty}\nabla P + \nu\nabla^2\mathbf{u} - \alpha_V\Delta T\mathbf{g}.$$

Restoring P and ρ_∞ as p and ρ,

$$\frac{\partial \mathbf{u}}{\partial t} + (\mathbf{u}\cdot\nabla)\,\mathbf{u} = -\frac{1}{\rho}\nabla p + \nu\nabla^2\mathbf{u} - \alpha_V(T - T_\infty)\mathbf{g}. \tag{B.56}$$

For an ideal gas $\alpha_V = T^{-1}$ (Tritton, 1977, p. 129),(Batchelor, 2000, p. 43), (Law, 2006, p. 556) (see Appendix A.2.1).

B.4 Large-Eddy Simulation

This section details the derivation of the governing equation for Large-Eddy Simulations (LES). The core concept originates from the decomposition and filtering process applied to the variables of interest in fluid flows, as illustrated in Figure B.1.

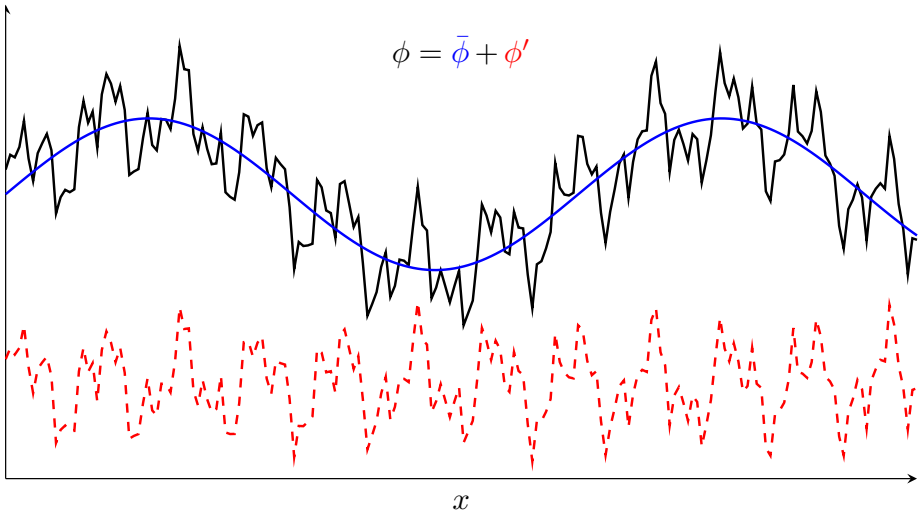

Figure B.1: Decomposition of variable of interest ϕ.

B.4.1 LES spatial filtering

For any scalar, vector, or tensor field ϕ,

$$\overline{\phi}(\mathbf{x}, t) = \int G_\Delta(\mathbf{x} - \mathbf{x}')\, \phi(\mathbf{x}', t)\, \mathrm{d}\mathbf{x}', \tag{B.57}$$

where G_Δ is a filter kernel of characteristic width Δ.

The standard properties of this filtering, assumed in most LES, are:

1. Linearity:
$$\overline{a\,\phi + b\,\psi} = a\,\overline{\phi} + b\,\overline{\psi}$$

2. Normalization. The constants are unchanged by filtering:
$$\int G_\Delta(\mathbf{r})\, d\mathbf{r} = 1.$$

3. Approximate commutation with derivatives. For spatially homogeneous G_Δ and slowly varying Δ:
$$\overline{\frac{\partial \phi}{\partial t}} \approx \frac{\partial \overline{\phi}}{\partial t}, \quad \overline{\nabla \phi} \approx \nabla \overline{\phi}.$$

4. Product not preserved. In general, this is the source of sub-grid (SGS) terms.
$$\overline{\phi\,\psi} \neq \overline{\phi}\,\overline{\psi}$$

5. Idempotence (approximate), for many standard filters on uniform grids:
$$\overline{\overline{\phi}} \approx \overline{\phi}$$

B.4.2 Favre filtering

For any scalar, vector, or tensor field ϕ, the Favre or density-weighted filtering is defined as,

$$\widetilde{\phi} = \frac{\overline{\rho\,\phi}}{\overline{\rho}} \implies \overline{\rho\,\phi} = \overline{\rho}\,\widetilde{\phi}. \tag{B.58}$$

The identities and proprieties of this filtering are:

1. Favre decomposition:

$$\phi = \widetilde{\phi} + \phi'',$$

with,

$$\overline{\rho\,\phi''} = 0.$$

2. Bilinear covariance:

$$\overline{\rho\,\phi\,\psi} = \overline{\rho}\,\widetilde{\phi}\,\widetilde{\psi} + \tau(\phi,\psi),$$

where,

$$\tau(\phi,\psi) \equiv \overline{\rho\,\phi\,\psi} - \overline{\rho}\,\widetilde{\phi}\,\widetilde{\psi}$$

3. Convective flux preservation:

$$\overline{\rho\,\phi\,\mathbf{u}} = \overline{\rho}\,\widetilde{\phi}\,\widetilde{\mathbf{u}} + \text{SGS term}$$

4. Approximate commutation:

$$\widetilde{\frac{\partial\phi}{\partial t}} \approx \frac{\partial\widetilde{\phi}}{\partial t}, \quad \widetilde{\nabla\phi} \approx \nabla\widetilde{\phi},$$

under the same assumptions the previous filtering.

B.4.3 LES equations

The procedure for obtaining the LES equations involves the use of Favre filtering on the governing equations of fluid flow. Starting with conservation of mass, the filters are applied to equation (B.18),

$$\begin{aligned}
&\frac{\partial\rho}{\partial t} + \nabla\cdot(\rho\mathbf{u}) = 0\\
&\overline{\frac{\partial\rho}{\partial t}} + \overline{\nabla\cdot(\rho\mathbf{u})} = 0\\
&\frac{\partial\overline{\rho}}{\partial t} + \nabla\cdot(\overline{\rho}\overline{\mathbf{u}}) = 0\\
&\frac{\partial\overline{\rho}}{\partial t} + \nabla\cdot(\overline{\rho}\widetilde{\mathbf{u}}) = 0.
\end{aligned}$$

Analogously, for conservation of momentum,

$$\begin{aligned}
\frac{\partial(\rho\mathbf{u})}{\partial t} + \nabla\cdot(\rho\mathbf{u}\otimes\mathbf{u}) &= -\nabla p + \nabla\cdot\boldsymbol{\tau} + \mathbf{f} \\
\overline{\frac{\partial(\rho\mathbf{u})}{\partial t}} + \overline{\nabla\cdot(\rho\mathbf{u}\otimes\mathbf{u})} &= -\overline{\nabla p} + \overline{\nabla\cdot\boldsymbol{\tau}} + \overline{\mathbf{f}} \\
\frac{\partial(\overline{\rho}\overline{\mathbf{u}})}{\partial t} + \nabla\cdot(\overline{\rho\mathbf{u}\otimes\mathbf{u}}) &= -\nabla\overline{p} + \nabla\cdot\overline{\boldsymbol{\tau}} + \overline{\mathbf{f}}.
\end{aligned}$$

By the bilinear covariance and the convective flux preservation properties,

$$\overline{\rho\mathbf{u}\otimes\mathbf{u}} = \overline{\rho}\widetilde{\mathbf{u}}\otimes\widetilde{\mathbf{u}} + \text{SGS terms}.$$

Typically, the $\boldsymbol{\tau}^{\text{sgs}}$ term includes all the effects of the sub-grid scale.

$$\begin{aligned}
\frac{\partial(\overline{\rho}\widetilde{\mathbf{u}})}{\partial t} + \nabla\cdot(\overline{\rho}\widetilde{\mathbf{u}}\otimes\widetilde{\mathbf{u}} + \boldsymbol{\tau}^{\text{sgs}}) &= -\nabla\overline{p} + \nabla\cdot\overline{\boldsymbol{\tau}} + \overline{\mathbf{f}} \\
\frac{\partial(\overline{\rho}\widetilde{\mathbf{u}})}{\partial t} + \nabla\cdot(\overline{\rho}\widetilde{\mathbf{u}}\otimes\widetilde{\mathbf{u}}) &= -\nabla\overline{p} + \nabla\cdot\overline{\boldsymbol{\tau}} + \overline{\mathbf{f}} - \nabla\cdot\boldsymbol{\tau}^{\text{sgs}},
\end{aligned}$$

with,

$$\overline{\boldsymbol{\tau}} = 2\overline{\mu}\widetilde{\mathbf{S}} - \frac{2}{3}\overline{\mu}(\nabla\cdot\widetilde{\mathbf{u}})\mathbf{I}, \quad \widetilde{\mathbf{S}} = \frac{1}{2}\left(\nabla\widetilde{\mathbf{u}} + (\nabla\widetilde{\mathbf{u}})^{\top}\right).$$

Many of the LES solvers are based on the model proposed by Smagorinky (Smagorinsky, 1963),

$$\boldsymbol{\tau}^{\text{sgs}} = -2\mu_{\text{t}}\left(\widetilde{\mathbf{S}} - \frac{1}{3}(\nabla\cdot\widetilde{\mathbf{u}})\,\mathbf{I}\right), \quad \mu_{\text{t}} = \rho(C_{\text{s}}\Delta)^2|\widetilde{\mathbf{S}}|, \quad |\widetilde{\mathbf{S}}| = \sqrt{2\widetilde{\mathbf{S}}:\widetilde{\mathbf{S}}}.$$

The term μ_{t} is known as turbulent viscosity. This definition assumes that the filtered pressure is

$$\overline{p}^{*} = \overline{p} + \frac{1}{3}\text{tr}(\boldsymbol{\tau}^{\text{sgs}}),$$

but often is omitted assuming that the pressure absorbs the trace of the sug-grid viscous tensor. Then,

$$\begin{aligned}
\frac{\partial(\overline{\rho}\widetilde{\mathbf{u}})}{\partial t} + \nabla\cdot(\overline{\rho}\tilde{\mathbf{u}}\otimes\tilde{\mathbf{u}}) &= -\nabla\overline{p} + \nabla\cdot\overline{\boldsymbol{\tau}} + \overline{\mathbf{f}} - \nabla\cdot\boldsymbol{\tau}^{\text{sgs}} \\
&= -\nabla\overline{p} + \nabla\cdot(\overline{\boldsymbol{\tau}} - \boldsymbol{\tau}^{\text{sgs}}) + \overline{\mathbf{f}} \\
&= -\nabla\overline{p} + \nabla\cdot\left(2\overline{\mu}\widetilde{\mathbf{S}} - \frac{2}{3}\overline{\mu}(\nabla\cdot\widetilde{\mathbf{u}})\mathbf{I} + 2\mu_{\text{t}}\left(\widetilde{\mathbf{S}} - \frac{1}{3}(\nabla\cdot\widetilde{\mathbf{u}})\,\mathbf{I}\right)\right) + \overline{\mathbf{f}} \\
&= -\nabla\overline{p} + \nabla\cdot\left((\overline{\mu} + \mu_{\text{t}})\left(2\widetilde{\mathbf{S}} - \frac{2}{3}(\nabla\cdot\widetilde{\mathbf{u}})\,\mathbf{I}\right)\right) + \overline{\mathbf{f}}.
\end{aligned} \tag{B.59}$$

The filtering of the conservation of energy follows the same steps

$$\begin{aligned}
\frac{\partial(\rho h)}{\partial t} + \nabla\cdot(\rho h\mathbf{u}) &= \frac{Dp}{Dt} - \nabla\cdot\mathbf{q} + \boldsymbol{\tau}:\nabla\mathbf{u} + Q \\
\overline{\frac{\partial(\rho h)}{\partial t}} + \overline{\nabla\cdot(\rho h\mathbf{u})} &= \overline{\frac{Dp}{Dt}} - \overline{\nabla\cdot\mathbf{q}} + \overline{\boldsymbol{\tau}:\nabla\mathbf{u}} + \overline{Q} \\
\frac{\partial(\overline{\rho}\overline{h})}{\partial t} + \nabla\cdot(\overline{\rho h\mathbf{u}}) &= \frac{D\overline{p}}{Dt} - \nabla\cdot\overline{\mathbf{q}} + \overline{\boldsymbol{\tau}:\nabla\mathbf{u}} + \overline{Q}.
\end{aligned}$$

The filtered quantities add new sub-grid scale terms,

$$\begin{aligned}
\overline{\rho h\mathbf{u}} &= \overline{\rho}\widetilde{h}\widetilde{\mathbf{u}} + \text{SGS enthalpy terms}, \\
\frac{D\overline{p}}{Dt} &= \frac{\partial\overline{p}}{\partial t} + \widetilde{\mathbf{u}}\cdot\nabla\overline{p} + \text{SGS pressure terms}, \\
\nabla\cdot\overline{\mathbf{q}} &= \nabla\cdot\widetilde{\mathbf{q}} + \text{SGS heat flux terms}, \\
\overline{\boldsymbol{\tau}:\nabla\mathbf{u}} &= \widetilde{\tau}:\nabla\widetilde{\mathbf{u}} + \text{SGS viscous terms}.
\end{aligned}$$

In the context of this work, many of these terms can be neglected and grouped into $\mathbf{q}^{\text{sgs}}$, then,

$$\frac{\partial(\overline{\rho}\widetilde{h})}{\partial t} + \nabla\cdot(\overline{\rho}\widetilde{h}\widetilde{\mathbf{u}}) = \frac{D\overline{p}}{Dt} - \nabla\cdot\widetilde{\mathbf{q}} + \widetilde{\boldsymbol{\tau}}:\nabla\widetilde{\mathbf{u}} + \overline{Q} - \nabla\cdot\mathbf{q}^{\text{sgs}}.$$

Considering the Fourier law for the heat flux,

$$\widetilde{\mathbf{q}} = -\overline{k}\nabla\widetilde{T},$$

where $\overline{k}$ is the thermal conductivity. In addition, the sub-grid heat flux term is modeled as

$$\mathbf{q}^{\text{sgs}} = -\frac{\mu_{\text{t}}c_p}{\text{Pr}_{\text{t}}}\nabla\widetilde{T},$$

with μ_{t}, Pr_{t} the turbulent viscosity and Prandtl number, and c_p the specific heat capacity. Using the definition of Prandtl number (B.5),

$$\text{Pr}_{\text{t}} = \frac{\mu_{\text{t}}c_p}{k_{\text{t}}} \implies k_{\text{t}} = \frac{\mu_{\text{t}}c_p}{\text{Pr}_{\text{t}}},$$

thus the conservation of energy can be written as

$$\begin{aligned}
\frac{\partial(\overline{\rho}\widetilde{h})}{\partial t} + \nabla\cdot(\overline{\rho}\widetilde{h}\widetilde{\mathbf{u}}) &= \frac{D\overline{p}}{Dt} - \nabla\cdot\widetilde{\mathbf{q}} + \widetilde{\boldsymbol{\tau}}:\nabla\widetilde{\mathbf{u}} + \overline{Q} - \nabla\cdot\mathbf{q}^{\text{sgs}} \\
&= \frac{D\overline{p}}{Dt} - \nabla\cdot(\widetilde{\mathbf{q}} + \mathbf{q}^{\text{sgs}}) + \widetilde{\boldsymbol{\tau}}:\nabla\widetilde{\mathbf{u}} + \overline{Q} \\
&= \frac{D\overline{p}}{Dt} + \nabla\cdot\left(\overline{k}\nabla\widetilde{T} + k_{\text{t}}\nabla\widetilde{T}\right) + \widetilde{\boldsymbol{\tau}}:\nabla\widetilde{\mathbf{u}} + \overline{Q} \\
&= \frac{D\overline{p}}{Dt} + \nabla\cdot\left(\left(\overline{k} + k_{\text{t}}\right)\nabla\widetilde{T}\right) + \widetilde{\boldsymbol{\tau}}:\nabla\widetilde{\mathbf{u}} + \overline{Q}.
\end{aligned}$$

Finally, the conservation of species,

$$\begin{aligned}
\frac{\partial(\rho Y_i)}{\partial t} + \nabla\cdot(\rho Y_i\mathbf{u}) &= -\nabla\cdot\mathbf{J}_i + \dot{\omega}_i,\\
\overline{\frac{\partial(\rho Y_i)}{\partial t}} + \overline{\nabla\cdot(\rho Y_i\mathbf{u})} &= -\overline{\nabla\cdot\mathbf{J}_i} + \overline{\dot{\omega}_i},\\
\frac{\partial(\overline{\rho Y_i})}{\partial t} + \nabla\cdot\left(\overline{\rho Y_i\mathbf{u}}\right) &= -\nabla\cdot\overline{\mathbf{J}_i} + \overline{\dot{\omega}_i},
\end{aligned}$$

The new sub-grid terms are

$$\begin{aligned}
\overline{\rho Y_i\mathbf{u}} &= \overline{\rho}\widetilde{Y}_i\widetilde{\mathbf{u}} + \text{SGS species flux term},\\
\overline{\mathbf{J}_i} &= \widetilde{\mathbf{J}}_i + \text{SGS diffusive term},
\end{aligned}$$

where,

$$\widetilde{\mathbf{J}}_i = -\overline{\rho}D_i\nabla\widetilde{Y}_i.$$

Grouping all the sub-grid scale terms in $\mathbf{j}^{\text{sgs}}$, which is typically modeled as

$$\mathbf{j}_i^{\text{sgs}} = -\overline{\rho}D_{\text{t}}\nabla\widetilde{Y}_i, \quad D_{\text{t}} = \frac{\mu_{\text{t}}}{\overline{\rho}\,\text{Sc}_{\text{t}}}.$$

$$\begin{aligned}
\frac{\partial(\overline{\rho}\widetilde{Y}_i)}{\partial t} + \nabla\cdot\left(\overline{\rho}\widetilde{Y}_i\widetilde{\mathbf{u}}\right) &= -\nabla\cdot\widetilde{\mathbf{J}}_i + \overline{\dot{\omega}_i} - \nabla\cdot\mathbf{j}_i^{\text{sgs}}\\
&= -\nabla\cdot\left(\widetilde{\mathbf{J}}_i + \mathbf{j}_i^{\text{sgs}}\right) + \overline{\dot{\omega}_i}\\
&= \nabla\cdot\left(\overline{\rho}D_i\nabla\widetilde{Y}_i + \overline{\rho}D_{\text{t}}\nabla\widetilde{Y}_i\right) + \overline{\dot{\omega}_i}\\
&= \nabla\cdot\left(\overline{\rho}\left(D_i + D_{\text{t}}\right)\nabla\widetilde{Y}_i\right) + \overline{\dot{\omega}_i}.
\end{aligned}$$

Wrapping up all the equations,

$$\begin{aligned}
\frac{\partial\overline{\rho}}{\partial t} + \nabla\cdot(\overline{\rho}\widetilde{\mathbf{u}}) &= 0\\
\frac{\partial(\overline{\rho}\widetilde{\mathbf{u}})}{\partial t} + \nabla\cdot(\overline{\rho}\tilde{\mathbf{u}}\otimes\tilde{\mathbf{u}}) &= -\nabla\overline{p} + \nabla\cdot\left(\left(\mu+\mu_{\text{t}}\right)\left(2\widetilde{\mathbf{S}} - \frac{2}{3}\left(\nabla\cdot\widetilde{\mathbf{u}}\right)\mathbf{I}\right)\right) + \overline{\mathbf{f}},\\
\frac{\partial(\overline{\rho}\widetilde{h})}{\partial t} + \nabla\cdot(\overline{\rho}\widetilde{h}\widetilde{\mathbf{u}}) &= \frac{D\overline{p}}{Dt} + \nabla\cdot\left(\left(k+k_{\text{t}}\right)\nabla\widetilde{T}\right) + \widetilde{\boldsymbol{\tau}} : \nabla\widetilde{\mathbf{u}} + \overline{Q},\\
\frac{\partial(\overline{\rho}\widetilde{Y}_i)}{\partial t} + \nabla\cdot\left(\overline{\rho}\widetilde{Y}_i\widetilde{\mathbf{u}}\right) &= \nabla\cdot\left(\overline{\rho}\left(D_i + D_{\text{t}}\right)\nabla\widetilde{Y}_i\right) + \overline{\dot{\omega}_i},\\
\overline{p} &= \overline{\rho}R\widetilde{T}.
\end{aligned}$$

Appendix C

Mathematical definitions and identities

C.1 Definitions

Total derivative

Let f be a function of n variables $x_1, x_2, \ldots, x_n$, each of which depends on a parameter t. The *total derivative* of f with respect to t is defined as

$$\frac{df}{dt} = \sum_{i=1}^{n} \frac{\partial f}{\partial x_i} \frac{dx_i}{dt}. \tag{C.1}$$

If f also depends explicitly on t, i.e. $f = f\big(x_1(t), \ldots, x_n(t), t\big)$, then

$$\frac{df}{dt} = \frac{\partial f}{\partial t} + \sum_{i=1}^{n} \frac{\partial f}{\partial x_i} \frac{dx_i}{dt}. \tag{C.2}$$

Material derivative

For a scalar quantity $\phi = \phi(\mathbf{x}, t)$, the material derivative is defined by

$$\frac{D\phi}{Dt} = \frac{\partial \phi}{\partial t} + \mathbf{u} \cdot \nabla \phi. \tag{C.3}$$

Notice that this is a special case of the total derivative (C.2), since

$$\frac{d\phi}{dt} = \frac{\partial \phi}{\partial t} + \frac{\partial \phi}{\partial x}\frac{dx}{dt} + \frac{\partial \phi}{\partial y}\frac{dy}{dt} + \frac{\partial \phi}{\partial z}\frac{dz}{dt} = \frac{\partial \phi}{\partial t} + \mathbf{u} \cdot \nabla \phi = \frac{D\phi}{Dt}.$$

where,

$$\nabla \phi = \left(\frac{\partial \phi}{\partial x}, \frac{\partial \phi}{\partial y}, \frac{\partial \phi}{\partial z} \right), \quad \mathbf{u} = \frac{d\mathbf{x}}{dt} = \left(\frac{dx}{dt}, \frac{dy}{dt}, \frac{dz}{dt} \right).$$

Outer product

Let $\mathbf{a}$ be a vector, the outer product is defined by

$$\mathbf{a} \otimes \mathbf{a} = \mathbf{a}\mathbf{a}^{\top}. \tag{C.4}$$

Velocity Gradient

Let $\mathbf{u}$ be the velocity field, then the velocity gradient is

$$\nabla \mathbf{u} = \begin{bmatrix} \dfrac{\partial u}{\partial x} & \dfrac{\partial u}{\partial y} & \dfrac{\partial u}{\partial z} \\ \dfrac{\partial v}{\partial x} & \dfrac{\partial v}{\partial y} & \dfrac{\partial v}{\partial z} \\ \dfrac{\partial w}{\partial x} & \dfrac{\partial w}{\partial y} & \dfrac{\partial w}{\partial z} \end{bmatrix}. \tag{C.5}$$

Velocity Laplacian

Let $\mathbf{u}$ be the velocity field, then the velocity laplacian

$$\nabla^2 \mathbf{u} = \begin{pmatrix} \nabla^2 u \\ \nabla^2 v \\ \nabla^2 w \end{pmatrix} = \begin{pmatrix} \dfrac{\partial^2 u}{\partial x^2} + \dfrac{\partial^2 u}{\partial y^2} + \dfrac{\partial^2 u}{\partial z^2} \\ \dfrac{\partial^2 v}{\partial x^2} + \dfrac{\partial^2 v}{\partial y^2} + \dfrac{\partial^2 v}{\partial z^2} \\ \dfrac{\partial^2 w}{\partial x^2} + \dfrac{\partial^2 w}{\partial y^2} + \dfrac{\partial^2 w}{\partial z^2} \end{pmatrix}.$$

Gradient of the velocity divergence

$$\nabla(\nabla \cdot \mathbf{u}) = \begin{pmatrix} \dfrac{\partial}{\partial x}\left(\dfrac{\partial u}{\partial x} + \dfrac{\partial v}{\partial y} + \dfrac{\partial w}{\partial z}\right) \\ \dfrac{\partial}{\partial y}\left(\dfrac{\partial u}{\partial x} + \dfrac{\partial v}{\partial y} + \dfrac{\partial w}{\partial z}\right) \\ \dfrac{\partial}{\partial z}\left(\dfrac{\partial u}{\partial x} + \dfrac{\partial v}{\partial y} + \dfrac{\partial w}{\partial z}\right) \end{pmatrix} \tag{C.6}$$

Strain rate and vorticity tensor

The velocity gradient can be decomposed into

$$\nabla \mathbf{u} = \mathbf{S} + \mathbf{\Omega} \tag{C.7}$$

where $\mathbf{S}$ is the strain-rate tensor

$$\mathbf{S} = \frac{1}{2}\left(\nabla\mathbf{u} + (\nabla\mathbf{u})^\top\right) = \frac{1}{2}\begin{bmatrix} 2\dfrac{\partial u}{\partial x} & \dfrac{\partial u}{\partial y} + \dfrac{\partial v}{\partial x} & \dfrac{\partial u}{\partial z} + \dfrac{\partial w}{\partial x} \\ \dfrac{\partial v}{\partial x} + \dfrac{\partial u}{\partial y} & 2\dfrac{\partial v}{\partial y} & \dfrac{\partial v}{\partial z} + \dfrac{\partial w}{\partial y} \\ \dfrac{\partial w}{\partial x} + \dfrac{\partial u}{\partial z} & \dfrac{\partial w}{\partial y} + \dfrac{\partial v}{\partial z} & 2\dfrac{\partial w}{\partial z} \end{bmatrix}, \tag{C.8}$$

and $\mathbf{\Omega}$ the vorticity tensor

$$\mathbf{\Omega} = \frac{1}{2}\left(\nabla\mathbf{u} - (\nabla\mathbf{u})^\top\right) = \frac{1}{2}\begin{bmatrix} 0 & \dfrac{\partial u}{\partial y} - \dfrac{\partial v}{\partial x} & \dfrac{\partial u}{\partial z} - \dfrac{\partial w}{\partial x} \\ \dfrac{\partial v}{\partial x} - \dfrac{\partial u}{\partial y} & 0 & \dfrac{\partial v}{\partial z} - \dfrac{\partial w}{\partial y} \\ \dfrac{\partial w}{\partial x} - \dfrac{\partial u}{\partial z} & \dfrac{\partial w}{\partial y} - \dfrac{\partial v}{\partial z} & 0 \end{bmatrix}. \tag{C.9}$$

Double dot product

Let $\mathbf{A}, \mathbf{B}$ two second order tensors, then the double dot product or double contraction is

$$\begin{aligned} \mathbf{A} : \mathbf{B} &= \sum_{i=1}^{m}\sum_{j=1}^{n} \mathbf{A}_{ij}\mathbf{B}_{ij} \\ &= A_{11}B_{11} + A_{12}B_{12} + \cdots + A_{1n}B_{1n} + \cdots + A_{m1}B_{m1} + \cdots + A_{mn}B_{mn}. \end{aligned} \tag{C.10}$$

Taylor series expansion

The Taylor series around the point x_0 is defined as (Sauer, 2017)

$$\begin{aligned} f(x) &= f(x_0) + f'(x_0)(x - x_0) + \frac{1}{2!}f''(x_0)(x - x_0)^2 + \dots \\ &= \sum_{n=0}^{\infty} \frac{f^{(n)}(x_0)}{n!}(x - x_0)^n. \end{aligned} \tag{C.11}$$

Lagrange polynomial

For N data points $(x_1, y_1), ..., (x_N, y_N)$, the Lagrange polynomial interpolator (Sauer, 2017) is defined as

$$L(x) = \sum_{i=1}^{N} y_i\, l_i(x), \quad l_i(x) = \frac{x - x_1}{x_i - x_1} \cdots \frac{x - x_{i-1}}{x_i - x_{i-1}} \frac{x - x_{i+1}}{x_i - x_{i+1}} \cdots \frac{x - x_N}{x_i - x_N}. \tag{C.12}$$

C.2 Identities

Divergence of the outer product

Let $\mathbf{a}$, $\mathbf{b}$ be two vectors, the divergence of the outer product is

$$\nabla \cdot (\mathbf{a} \otimes \mathbf{b}) = \nabla \cdot \left(\mathbf{a}\mathbf{b}^\top\right) = \mathbf{b}(\nabla \cdot \mathbf{a}) + (\mathbf{a} \cdot \nabla)\mathbf{b}, \tag{C.13}$$

Divergence of the viscous stress tensor

The viscous stress tensor is defined as

$$\boldsymbol{\tau} = \mu \left(\nabla \mathbf{u} + (\nabla \mathbf{u})^\top - \frac{2}{3} (\nabla \cdot \mathbf{u}) \mathbf{I} \right)$$

The divergence is,

$$\nabla \cdot \boldsymbol{\tau} = \nabla \mu \cdot \left(\nabla \mathbf{u} + (\nabla \mathbf{u})^\top - \frac{2}{3} (\nabla \cdot \mathbf{u}) \mathbf{I} \right) + \mu \nabla \cdot \left(\nabla \mathbf{u} + (\nabla \mathbf{u})^\top - \frac{2}{3} (\nabla \cdot \mathbf{u}) \mathbf{I} \right),$$

or expanded as,

$$\begin{aligned}
(\nabla \cdot \boldsymbol{\tau})_x &= \frac{\partial}{\partial x}\left[\mu\left(2\frac{\partial u}{\partial x} - \tfrac{2}{3}\nabla \cdot \mathbf{u}\right)\right] + \frac{\partial}{\partial y}\left[\mu\left(\frac{\partial u}{\partial y} + \frac{\partial v}{\partial x}\right)\right] + \frac{\partial}{\partial z}\left[\mu\left(\frac{\partial u}{\partial z} + \frac{\partial w}{\partial x}\right)\right], \\
(\nabla \cdot \boldsymbol{\tau})_y &= \frac{\partial}{\partial x}\left[\mu\left(\frac{\partial v}{\partial x} + \frac{\partial u}{\partial y}\right)\right] + \frac{\partial}{\partial y}\left[\mu\left(2\frac{\partial v}{\partial y} - \tfrac{2}{3}\nabla \cdot \mathbf{u}\right)\right] + \frac{\partial}{\partial z}\left[\mu\left(\frac{\partial v}{\partial z} + \frac{\partial w}{\partial y}\right)\right], \\
(\nabla \cdot \boldsymbol{\tau})_z &= \frac{\partial}{\partial x}\left[\mu\left(\frac{\partial w}{\partial x} + \frac{\partial u}{\partial z}\right)\right] + \frac{\partial}{\partial y}\left[\mu\left(\frac{\partial w}{\partial y} + \frac{\partial v}{\partial z}\right)\right] + \frac{\partial}{\partial z}\left[\mu\left(2\frac{\partial w}{\partial z} - \tfrac{2}{3}\nabla \cdot \mathbf{u}\right)\right].
\end{aligned} \tag{C.14}$$

For a constant density,

$$\nabla \cdot \boldsymbol{\tau} = \mu \left(\nabla^2 \mathbf{u} + \tfrac{1}{3} \nabla (\nabla \cdot \mathbf{u}) \right). \tag{C.15}$$

C.3 Derivations

C.3.1 Non-uniform grid schemes

Considering a non-uniform grid x_i, with $i = 0, \ldots, N_x$, $\Delta x_i = x_{i+1} - x_i$ as shown in Figure C.1. The non-uniform finite difference schemes are based on the Lagrange polynomial interpolation using a different number of points. For the first derivative, a 3 points interpolator is used and a 4 points interpolator for the second derivative. The next sub-sections show the interpolator definitions.

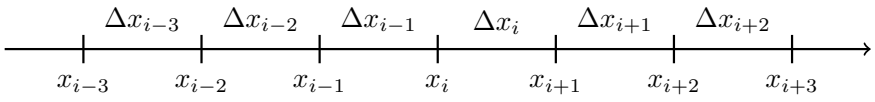

Figure C.1: Non-uniform grid sketch.

3 points

For the following points (x_{i-1}, f_{i-1}), (x_i, f_i), (x_{i+1}, f_{i+1}), the Lagrange polynomial interpolator based on (C.12) is,

$$L(x) = f_{i-1}\frac{(x-x_i)(x-x_{i+1})}{(x_{i-1}-x_i)(x_{i-1}-x_{i+1})} + f_i\frac{(x-x_{i-1})(x-x_{i+1})}{(x_i-x_{i-1})(x_i-x_{i+1})} + f_{i+1}\frac{(x-x_{i-1})(x-x_i)}{(x_{i+1}-x_{i-1})(x_{i+1}-x_i)}. \tag{C.16}$$

Noting that

$$x_{i-1}-x_i = -\Delta x_{i-1}, \quad x_{i-1}-x_{i+1} = -\Delta x_{i-1}-\Delta x_i, \quad x_i - x_{i-1} = \Delta x_{i-1},$$

$$x_i - x_{i+1} = -\Delta x_i, \quad x_{i+1}-x_{i-1} = \Delta x_{i-1}+\Delta x_i, \quad x_{i+1}-x_i = \Delta x_i,$$

and replacing into (C.16),

$$\begin{aligned} L(x) &= f_{i-1}\frac{(x-x_i)(x-x_{i+1})}{-\Delta x_{i-1}(-\Delta x_{i-1}-\Delta x_i)} + f_i\frac{(x-x_{i-1})(x-x_{i+1})}{\Delta x_{i-1}(-\Delta x_i)} + f_{i+1}\frac{(x-x_{i-1})(x-x_i)}{(\Delta x_{i-1}-\Delta x_i)\Delta x_i} \\ &= f_{i-1}\frac{(x-x_i)(x-x_{i+1})}{\Delta x_{i-1}(\Delta x_{i-1}+\Delta x_i)} - f_i\frac{(x-x_{i-1})(x-x_{i+1})}{\Delta x_{i-1}\Delta x_i} + f_{i+1}\frac{(x-x_{i-1})(x-x_i)}{(\Delta x_{i-1}+\Delta x_i)\Delta x_i} \end{aligned}$$

Computing the first derivative with respect to x,

$$\begin{aligned} L'(x) &= f_{i-1}\frac{(x-x_{i+1})+(x-x_i)}{\Delta x_{i-1}(\Delta x_{i-1}+\Delta x_i)} - f_i\frac{(x-x_{i+1})+(x-x_{i-1})}{\Delta x_{i-1}\Delta x_i} + f_{i+1}\frac{(x-x_i)+(x-x_{i-1})}{(\Delta x_{i-1}+\Delta x_i)\Delta x_i} \\ &= f_{i-1}\frac{2x-(x_i+x_{i+1})}{\Delta x_{i-1}\,(\Delta x_{i-1}+\Delta x_i)} - f_i\frac{2x-(x_{i-1}+x_{i+1})}{\Delta x_{i-1}\,\Delta x_i} + f_{i+1}\frac{2x-(x_{i-1}+x_i)}{(\Delta x_{i-1}+\Delta x_i)\,\Delta x_i}, \end{aligned} \tag{C.17}$$

and the second derivative,

$$L''(x) = 2\left(\frac{f_{i-1}}{\Delta x_{i-1}(\Delta x_{i-1}+\Delta x_i)} - \frac{f_i}{\Delta x_{i-1}\Delta x_i} + \frac{f_{i+1}}{(\Delta x_{i-1}+\Delta x_i)\,\Delta x_i}\right). \tag{C.18}$$

4 points

Following the same idea as before, for the following points (x_i, f_i), (x_{i+1}, f_{i+1}), (x_{i+2}, f_{i+2}), (x_{i+3}, f_{i+3}) the Lagrange polynomial interpolator is,

$$\begin{aligned} L(x) = f_i &\frac{(x-x_{i+1})(x-x_{i+2})(x-x_{i+3})}{(x_i-x_{i+1})(x_i-x_{i+2})(x_i-x_{i+3})} \\ &+ f_{i+1}\frac{(x-x_i)(x-x_{i+2})(x-x_{i+3})}{(x_{i+1}-x_i)(x_{i+1}-x_{i+2})(x_{i+1}-x_{i+3})} \\ &+ f_{i+2}\frac{(x-x_i)(x-x_{i+1})(x-x_{i+3})}{(x_{i+2}-x_i)(x_{i+2}-x_{i+1})(x_{i+2}-x_{i+3})} \\ &+ f_{i+3}\frac{(x-x_i)(x-x_{i+1})(x-x_{i+2})}{(x_{i+3}-x_i)(x_{i+3}-x_{i+1})(x_{i+3}-x_{i+2})}. \end{aligned} \tag{C.19}$$

Noting that

$$x_i - x_{i+1} = -\Delta x_i, \quad x_i - x_{i+2} = -\Delta x_i - \Delta x_{i+1}, \quad x_i - x_{i+3} = -\Delta x_i - \Delta x_{i+1} - \Delta x_{i+2},$$

$$x_{i+1} - x_i = \Delta x_i, \quad x_{i+1} - x_{i+2} = -\Delta x_{i+1}, \quad x_{i+1} - x_{i+3} = -\Delta x_{i+1} - \Delta x_{i+2},$$

$$x_{i+2} - x_i = \Delta x_i + \Delta x_{i+1}, \quad x_{i+2} - x_{i+1} = \Delta x_{i+1}, \quad x_{i+2} - x_{i+3} = -\Delta x_{i+2},$$

$$x_{i+3} - x_i = \Delta x_i + \Delta x_{i+1} + \Delta x_{i+2}, \quad x_{i+3} - x_{i+1} = \Delta x_{i+1} + \Delta x_{i+2}, \quad x_{i+3} - x_{i+2} = \Delta x_{i+2},$$

and replacing into (C.19),

$$\begin{aligned} L(x) = f_i &\frac{(x-x_{i+1})(x-x_{i+2})(x-x_{i+3})}{-\Delta x_i(-\Delta x_i - \Delta x_{i+1})(-\Delta x_i - \Delta x_{i+1} - \Delta x_{i+2})} \\ &+ f_{i+1}\frac{(x-x_i)(x-x_{i+2})(x-x_{i+3})}{\Delta x_i(-\Delta x_{i+1})(-\Delta x_{i+1} - \Delta x_{i+2})} \\ &+ f_{i+2}\frac{(x-x_i)(x-x_{i+1})(x-x_{i+3})}{(\Delta x_i + \Delta x_{i+1})\Delta x_{i+1}(-\Delta x_{i+2})} \\ &+ f_{i+3}\frac{(x-x_i)(x-x_{i+1})(x-x_{i+2})}{(\Delta x_i + \Delta x_{i+1} + \Delta x_{i+2})(\Delta x_{i+1} + \Delta x_{i+2})\Delta x_{i+2}} \\ = -f_i &\frac{(x-x_{i+1})(x-x_{i+2})(x-x_{i+3})}{\Delta x_i(\Delta x_i + \Delta x_{i+1})(\Delta x_i + \Delta x_{i+1} + \Delta x_{i+2})} \\ &+ f_{i+1}\frac{(x-x_i)(x-x_{i+2})(x-x_{i+3})}{\Delta x_i \Delta x_{i+1}(\Delta x_{i+1} + \Delta x_{i+2})} \\ &- f_{i+2}\frac{(x-x_i)(x-x_{i+1})(x-x_{i+3})}{(\Delta x_i + \Delta x_{i+1})\Delta x_{i+1}\Delta x_{i+2}} \\ &+ f_{i+3}\frac{(x-x_i)(x-x_{i+1})(x-x_{i+2})}{(\Delta x_i + \Delta x_{i+1} + \Delta x_{i+2})(\Delta x_{i+1} + \Delta x_{i+2})\Delta x_{i+2}}. \end{aligned} \tag{C.20}$$

Computing the first derivative with respect to x,

$$\begin{aligned} L'(x) = &-f_i \frac{(x-x_{i+2})(x-x_{i+3}) + (x-x_{i+1})(x-x_{i+3}) + (x-x_{i+1})(x-x_{i+2})}{\Delta x_i(\Delta x_i + \Delta x_{i+1})(\Delta x_i + \Delta x_{i+1} + \Delta x_{i+2})} \\ &+ f_{i+1} \frac{(x-x_{i+2})(x-x_{i+3}) + (x-x_i)(x-x_{i+3}) + (x-x_i)(x-x_{i+2})}{\Delta x_i\, \Delta x_{i+1}(\Delta x_{i+1} + \Delta x_{i+2})} \\ &- f_{i+2} \frac{(x-x_{i+1})(x-x_{i+3}) + (x-x_i)(x-x_{i+3}) + (x-x_i)(x-x_{i+1})}{(\Delta x_i + \Delta x_{i+1})\, \Delta x_{i+1}\, \Delta x_{i+2}} \\ &+ f_{i+3} \frac{(x-x_{i+1})(x-x_{i+2}) + (x-x_i)(x-x_{i+2}) + (x-x_i)(x-x_{i+1})}{(\Delta x_i + \Delta x_{i+1} + \Delta x_{i+2})(\Delta x_{i+1} + \Delta x_{i+2})\, \Delta x_{i+2}}, \end{aligned} \tag{C.21}$$

and the second derivative,

$$\begin{aligned} L''(x) = &-f_i \frac{2(x-x_{i+1}) + 2(x-x_{i+2}) + 2(x-x_{i+3})}{\Delta x_i(\Delta x_i + \Delta x_{i+1})(\Delta x_i + \Delta x_{i+1} + \Delta x_{i+2})} \\ &+ f_{i+1} \frac{2(x-x_i) + 2(x-x_{i+2}) + 2(x-x_{i+3})}{\Delta x_i\, \Delta x_{i+1}(\Delta x_{i+1} + \Delta x_{i+2})} \\ &- f_{i+2} \frac{2(x-x_i) + 2(x-x_{i+1}) + 2(x-x_{i+3})}{(\Delta x_i + \Delta x_{i+1})\, \Delta x_{i+1}\, \Delta x_{i+2}} \\ &+ f_{i+3} \frac{2(x-x_i) + 2(x-x_{i+1}) + 2(x-x_{i+2})}{(\Delta x_i + \Delta x_{i+1} + \Delta x_{i+2})(\Delta x_{i+1} + \Delta x_{i+2})\, \Delta x_{i+2}}. \end{aligned} \tag{C.22}$$

First derivative

Forward difference

Based on (C.17), the forward difference can be written as,

$$L'(x) = f_i \frac{2x - (x_{i+1} + x_{i+2})}{\Delta x_i\, (\Delta x_i + \Delta x_{i+1})} - f_{i+1} \frac{2x - (x_i + x_{i+2})}{\Delta x_i\, \Delta x_{i+1}} + f_{i+2} \frac{2x - (x_i + x_{i+1})}{(\Delta x_i + \Delta x_{i+1})\, \Delta x_{i+1}}.$$

Evaluating at point x_i,

$$\begin{aligned} L'(x_i) &= f_i \frac{2x_i - (x_{i+1} + x_{i+2})}{\Delta x_i\, (\Delta x_i + \Delta x_{i+1})} - f_{i+1} \frac{2x_i - (x_i + x_{i+2})}{\Delta x_i\, \Delta x_{i+1}} + f_{i+2} \frac{2x_i - (x_i + x_{i+1})}{(\Delta x_i + \Delta x_{i+1})\, \Delta x_{i+1}} \\ &= f_i \frac{(x_i - x_{i+1}) + (x_i - x_{i+2})}{\Delta x_i\, (\Delta x_i + \Delta x_{i+1})} - f_{i+1} \frac{x_i - x_{i+2}}{\Delta x_i\, \Delta x_{i+1}} + f_{i+2} \frac{x_i - x_{i+1}}{(\Delta x_i + \Delta x_{i+1})\, \Delta x_{i+1}} \\ &= f_i \frac{-\Delta x_i - (\Delta x_i + \Delta x_{i+1})}{\Delta x_i\, (\Delta x_i + \Delta x_{i+1})} - f_{i+1} \frac{-(\Delta x_i + \Delta x_{i+1})}{\Delta x_i\, \Delta x_{i+1}} + f_{i+2} \frac{-\Delta x_i}{(\Delta x_i + \Delta x_{i+1})\, \Delta x_{i+1}} \\ &= -\frac{2\Delta x_i + \Delta x_{i+1}}{\Delta x_i\, (\Delta x_i + \Delta x_{i+1})} f_i + \frac{\Delta x_i + \Delta x_{i+1}}{\Delta x_i\, \Delta x_{i+1}} f_{i+1} - \frac{\Delta x_i}{\Delta x_{i+1}(\Delta x_i + \Delta x_{i+1})} f_{i+2} \end{aligned}$$

Backward difference

Based on (C.17), the backward difference can be written as

$$L'(x) = f_{i-2}\,\frac{2x-(x_{i-1}+x_i)}{\Delta x_{i-2}\,(\Delta x_{i-2}+\Delta x_{i-1})} - f_{i-1}\,\frac{2x-(x_{i-2}+x_i)}{\Delta x_{i-2}\,\Delta x_{i-1}} + f_i\,\frac{2x-(x_{i-2}+x_{i-1})}{(\Delta x_{i-2}+\Delta x_{i-1})\,\Delta x_{i-1}}. \tag{C.23}$$

Evaluating at point x_i,

$$\begin{aligned}
L'(x_i) &= f_{i-2}\,\frac{2x_i-(x_{i-1}+x_i)}{\Delta x_{i-2}\,(\Delta x_{i-2}+\Delta x_{i-1})} - f_{i-1}\,\frac{2x_i-(x_{i-2}+x_i)}{\Delta x_{i-2}\,\Delta x_{i-1}} + f_i\,\frac{2x_i-(x_{i-2}+x_{i-1})}{(\Delta x_{i-2}+\Delta x_{i-1})\,\Delta x_{i-1}} \\
&= f_{i-2}\,\frac{x_i-x_{i-1}}{\Delta x_{i-2}\,(\Delta x_{i-2}+\Delta x_{i-1})} - f_{i-1}\,\frac{x_i-x_{i-2}}{\Delta x_{i-2}\,\Delta x_{i-1}} + f_i\,\frac{(x_i-x_{i-2})+(x_i-x_{i-1})}{(\Delta x_{i-2}+\Delta x_{i-1})\,\Delta x_{i-1}} \\
&= f_{i-2}\,\frac{\Delta x_{i-1}}{\Delta x_{i-2}\,(\Delta x_{i-2}+\Delta x_{i-1})} - f_{i-1}\,\frac{\Delta x_{i-2}+\Delta x_{i-1}}{\Delta x_{i-2}\,\Delta x_{i-1}} + f_i\,\frac{(\Delta x_{i-2}+\Delta x_{i-1})+\Delta x_{i-1}}{(\Delta x_{i-2}+\Delta x_{i-1})\,\Delta x_{i-1}} \\
&= \frac{\Delta x_{i-1}}{\Delta x_{i-2}\,(\Delta x_{i-2}+\Delta x_{i-1})} f_{i-2} - \frac{\Delta x_{i-2}+\Delta x_{i-1}}{\Delta x_{i-2}\,\Delta x_{i-1}} f_{i-1} + \frac{\Delta x_{i-2}+2\Delta x_{i-1}}{(\Delta x_{i-2}+\Delta x_{i-1})\,\Delta x_{i-1}} f_i
\end{aligned}$$

Central difference

For the central difference, the scheme is derived using (C.11) with

$$f(x+\Delta x_i) = f(x) + f'(x)\Delta x_i + \mathcal{O}(\Delta x_i^2), \tag{C.24}$$

and

$$f(x-\Delta x_{i-1}) = f(x) - f'(x)\Delta x_{i-1} + \mathcal{O}(\Delta x_{i-1}^2). \tag{C.25}$$

Subtracting (C.25) from (C.24),

$$\begin{aligned}
f(x+\Delta x_i) - f(x-\Delta x_{i-1}) &= f'(x)\Delta x_i + f'(x)\Delta x_{i-1} + \mathcal{O}(\Delta x_i^2 - \Delta x_{i-1}^2) \\
&= (\Delta x_i + \Delta x_{i-1}) f'(x) + \mathcal{O}(\Delta x_i^2 - \Delta x_{i-1}^2),
\end{aligned}$$

then, dividing by $\Delta x_i + \Delta x_{i-1}$,

$$f'(x) = \frac{f(x+\Delta x_i) - f(x-\Delta x_{i-1})}{\Delta x_i + \Delta x_{i-1}} + \mathcal{O}\left(\frac{\Delta x_i^2 - \Delta x_{i-1}^2}{\Delta x_i + \Delta x_{i-1}}\right).$$

For node x_i,

$$f'(x_i) \approx \frac{f(x_{i+1}) - f(x_{i-1})}{\Delta x_i + \Delta x_{i-1}}. \tag{C.26}$$

The truncation error is

$$\mathcal{O}\left(\frac{\Delta x_i^2 - \Delta x_{i-1}^2}{\Delta x_i + \Delta x_{i-1}}\right) = \mathcal{O}\left(\frac{(\Delta x_i + \Delta x_{i-1})(\Delta x_i - \Delta x_{i-1})}{\Delta x_i + \Delta x_{i-1}}\right) = \mathcal{O}(\Delta x_i - \Delta x_{i-1}).$$

Second derivative

Forward difference

The evaluation of x_i at (C.22) is

$$
\begin{aligned}
L''(x_i) = &-2f_i \frac{(x-x_{i+1})+(x-x_{i+2})+(x-x_{i+3})}{\Delta x_i(\Delta x_i+\Delta x_{i+1})(\Delta x_i+\Delta x_{i+1}+\Delta x_{i+2})} \\
&+2f_{i+1}\frac{(x-x_i)+(x-x_{i+2})+(x-x_{i+3})}{\Delta x_i\,\Delta x_{i+1}(\Delta x_{i+1}+\Delta x_{i+2})} \\
&-2f_{i+2}\frac{(x-x_i)+(x-x_{i+1})+(x-x_{i+3})}{(\Delta x_i+\Delta x_{i+1})\,\Delta x_{i+1}\,\Delta x_{i+2}} \\
&+2f_{i+3}\frac{(x-x_i)+(x-x_{i+1})+(x-x_{i+2})}{(\Delta x_i+\Delta x_{i+1}+\Delta x_{i+2})(\Delta x_{i+1}+\Delta x_{i+2})\,\Delta x_{i+2}} \\
= &-2f_i \frac{(x_i-x_{i+1})+(x_i-x_{i+2})+(x_i-x_{i+3})}{\Delta x_i(\Delta x_i+\Delta x_{i+1})(\Delta x_i+\Delta x_{i+1}+\Delta x_{i+2})} \\
&+2f_{i+1}\frac{(x_i-x_i)+(x_i-x_{i+2})+(x_i-x_{i+3})}{\Delta x_i\,\Delta x_{i+1}(\Delta x_{i+1}+\Delta x_{i+2})} \\
&-2f_{i+2}\frac{(x_i-x_i)+(x_i-x_{i+1})+(x_i-x_{i+3})}{(\Delta x_i+\Delta x_{i+1})\,\Delta x_{i+1}\,\Delta x_{i+2}} \\
&+2f_{i+3}\frac{(x_i-x_i)+(x_i-x_{i+1})+(x_i-x_{i+2})}{(\Delta x_i+\Delta x_{i+1}+\Delta x_{i+2})(\Delta x_{i+1}+\Delta x_{i+2})\,\Delta x_{i+2}} \\
= &-2f_i \frac{-\Delta x_i-(\Delta x_i+\Delta x_{i+1})-(\Delta x_i+\Delta x_{i+1}+\Delta x_{i+2})}{\Delta x_i(\Delta x_i+\Delta x_{i+1})(\Delta x_i+\Delta x_{i+1}+\Delta x_{i+2})} \\
&+2f_{i+1}\frac{-(\Delta x_i+\Delta x_{i+1})-(\Delta x_i+\Delta x_{i+1}+\Delta x_{i+2})}{\Delta x_i\,\Delta x_{i+1}(\Delta x_{i+1}+\Delta x_{i+2})} \\
&-2f_{i+2}\frac{-\Delta x_i-(\Delta x_i+\Delta x_{i+1}+\Delta x_{i+2})}{(\Delta x_i+\Delta x_{i+1})\,\Delta x_{i+1}\,\Delta x_{i+2}} \\
&+2f_{i+3}\frac{-\Delta x_i-(\Delta x_i+\Delta x_{i+i})}{(\Delta x_i+\Delta x_{i+1}+\Delta x_{i+2})(\Delta x_{i+1}+\Delta x_{i+2})\,\Delta x_{i+2}} \\
= &\,2\frac{3\Delta x_i+2\Delta x_{i+1}+\Delta x_{i+2}}{\Delta x_i(\Delta x_i+\Delta x_{i+1})(\Delta x_i+\Delta x_{i+1}+\Delta x_{i+2})}f_i \\
&-2\frac{2\Delta x_i+2\Delta x_{i+1}+\Delta x_{i+2}}{\Delta x_i\,\Delta x_{i+1}(\Delta x_{i+1}+\Delta x_{i+2})}f_{i+1} \\
&+2\frac{2\Delta x_i+\Delta x_{i+1}+\Delta x_{i+2}}{(\Delta x_i+\Delta x_{i+1})\,\Delta x_{i+1}\,\Delta x_{i+2}}f_{i+2} \\
&-2\frac{2\Delta x_i+\Delta x_{i+i}}{(\Delta x_i+\Delta x_{i+1}+\Delta x_{i+2})(\Delta x_{i+1}+\Delta x_{i+2})\,\Delta x_{i+2}}f_{i+3}
\end{aligned}
$$

Backward difference

Based on (C.22), for backward difference, the interpolator is

$$\begin{aligned}
L''(x) = &-f_{i-3}\frac{2(x-x_{i-2})+2(x-x_{i-1})+2(x-x_i)}{\Delta x_{i-3}(\Delta x_{i-3}+\Delta x_{i-2})(\Delta x_{i-3}+\Delta x_{i-2}+\Delta x_{i-1})}\\
&+f_{i-2}\frac{2(x-x_{i-3})+2(x-x_{i-1})+2(x-x_i)}{\Delta x_{i-3}\Delta x_{i-2}(\Delta x_{i-2}+\Delta x_{i-1})}\\
&-f_{i-1}\frac{2(x-x_{i-3})+2(x-x_{i-2})+2(x-x_i)}{(\Delta x_{i-3}+\Delta x_{i-2})\Delta x_{i-2}\,\Delta x_{i-1}}\\
&+f_i\frac{2(x-x_{i-3})+2(x-x_{i-2})+2(x-x_{i-1})}{(\Delta x_{i-3}+\Delta x_{i-2}+\Delta x_{i-1})(\Delta x_{i-2}+\Delta x_{i-1})\Delta x_{i-1}}.
\end{aligned}$$

Replacing x_i in the interpolator,

$$\begin{aligned}
L''(x_i) = &-2f_{i-3}\frac{(x_i-x_{i-2})+(x_i-x_{i-1})+(x_i-x_i)}{\Delta x_{i-3}(\Delta x_{i-3}+\Delta x_{i-2})(\Delta x_{i-3}+\Delta x_{i-2}+\Delta x_{i-1})}\\
&+2f_{i-2}\frac{(x_i-x_{i-3})+(x_i-x_{i-1})+(x_i-x_i)}{\Delta x_{i-3}\Delta x_{i-2}(\Delta x_{i-2}+\Delta x_{i-1})}\\
&-2f_{i-1}\frac{(x_i-x_{i-3})+(x_i-x_{i-2})+(x_i-x_i)}{(\Delta x_{i-3}+\Delta x_{i-2})\Delta x_{i-2}\,\Delta x_{i-1}}\\
&+2f_i\frac{(x_i-x_{i-3})+(x_i-x_{i-2})+(x_i-x_{i-1})}{(\Delta x_{i-3}+\Delta x_{i-2}+\Delta x_{i-1})(\Delta x_{i-2}+\Delta x_{i-1})\Delta x_{i-1}}\\
= &-2f_{i-3}\frac{(\Delta x_{i-2}+\Delta x_{i-1})+\Delta x_{i-1}}{\Delta x_{i-3}(\Delta x_{i-3}+\Delta x_{i-2})(\Delta x_{i-3}+\Delta x_{i-2}+\Delta x_{i-1})}\\
&+2f_{i-2}\frac{(\Delta x_{i-3}+\Delta x_{i-2}+\Delta x_{i-1})+\Delta x_{i-1}}{\Delta x_{i-3}\Delta x_{i-2}(\Delta x_{i-2}+\Delta x_{i-1})}\\
&-2f_{i-1}\frac{(\Delta x_{i-3}+\Delta x_{i-2}+\Delta x_{i-1})+(\Delta x_{i-2}+\Delta x_{i-1})}{(\Delta x_{i-3}+\Delta x_{i-2})\Delta x_{i-2}\,\Delta x_{i-1}}\\
&+2f_i\frac{(\Delta x_{i-3}+\Delta x_{i-2}+\Delta x_{i-1})+(\Delta x_{i-2}+\Delta x_{i-1})+\Delta x_{i-1}}{(\Delta x_{i-3}+\Delta x_{i-2}+\Delta x_{i-1})(\Delta x_{i-2}+\Delta x_{i-1})\Delta x_{i-1}}\\
= &-2\frac{\Delta x_{i-2}+2\Delta x_{i-1}}{\Delta x_{i-3}(\Delta x_{i-3}+\Delta x_{i-2})(\Delta x_{i-3}+\Delta x_{i-2}+\Delta x_{i-1})}f_{i-3}\\
&+2\frac{\Delta x_{i-3}+\Delta x_{i-2}+2\Delta x_{i-1}}{\Delta x_{i-3}\Delta x_{i-2}(\Delta x_{i-2}+\Delta x_{i-1})}f_{i-2}\\
&-2\frac{\Delta x_{i-3}+2\Delta x_{i-2}+2\Delta x_{i-1}}{f}_{i-1}(\Delta x_{i-3}+\Delta x_{i-2})\Delta x_{i-2}\,\Delta x_{i-1}\\
&+2\frac{\Delta x_{i-3}+2\Delta x_{i-2}+3\Delta x_{i-1}}{(\Delta x_{i-3}+\Delta x_{i-2}+\Delta x_{i-1})(\Delta x_{i-2}+\Delta x_{i-1})\Delta x_{i-1}}f_i
\end{aligned}$$

Central difference

For the central difference, the scheme is derived in a similar fashion to the first derivative using (C.11) with,

$$f(x+\Delta x_i) = f(x) + f'(x)\Delta x_i + \frac{1}{2}f''(x)\Delta x_i^2 + \mathcal{O}(\Delta x_i^3), \tag{C.27}$$

and,

$$f(x-\Delta x_{i-1}) = f(x) - f'(x)\Delta x_{i-1} + \frac{1}{2}f''(x)\Delta x_{i-1}^2 - \mathcal{O}(\Delta x_{i-1}^3). \tag{C.28}$$

To remove the first derivative, (C.27) is divided by Δx_i, and (C.28) by Δx_{i-1},

$$\begin{aligned} f(x+\Delta x_i) &= f(x) + f'(x)\Delta x_i + \frac{1}{2}f''(x)\Delta x_i^2 + \mathcal{O}(\Delta x_i^3) \quad /\Delta x_i \\ \frac{f(x+\Delta x_i)}{\Delta x_i} &= \frac{f(x)}{\Delta x_i} + f'(x) + \frac{1}{2}f''(x)\Delta x_i + \mathcal{O}(\Delta x_i^2), \end{aligned}$$

and,

$$\begin{aligned} f(x-\Delta x_{i-1}) &= f(x) - f'(x)\Delta x_{i-1} + \frac{1}{2}f''(x)\Delta x_{i-1}^2 - \mathcal{O}(\Delta x_{i-1}^3) \quad /\Delta x_{i-1} \\ \frac{f(x-\Delta x_{i-1})}{\Delta x_{i-1}} &= \frac{f(x)}{\Delta x_{i-1}} - f'(x) + \frac{1}{2}f''(x)\Delta x_{i-1} - \mathcal{O}(\Delta x_{i-1}^2) \end{aligned}$$

Adding both expressions,

$$\begin{aligned} \frac{f(x+\Delta x_i)}{\Delta x_i} + \frac{f(x-\Delta x_{i-1})}{\Delta x_{i-1}} &= \left(\frac{1}{\Delta x_i} + \frac{1}{\Delta x_{i-1}}\right) f(x) \\ &\quad + \frac{1}{2}\left(\Delta x_i + \Delta x_{i-1}\right) f''(x) \\ &\quad + \mathcal{O}(\Delta x_i^2 - \Delta x_{i-1}^2) \\ \frac{f(x+\Delta x_i)}{\Delta x_i} - \left(\frac{1}{\Delta x_i} + \frac{1}{\Delta x_{i-1}}\right) f(x) + \frac{f(x-\Delta x_{i-1})}{\Delta x_{i-1}} &= \frac{1}{2}\left(\Delta x_i + \Delta x_{i-1}\right) f''(x) \\ &\quad + \mathcal{O}(\Delta x_i^2 - \Delta x_{i-1}^2) \\ \frac{f(x+\Delta x_i)}{\Delta x_i} - \left(\frac{\Delta x_{i-1} + \Delta x_i}{\Delta x_i \Delta x_{i-1}}\right) f(x) + \frac{f(x-\Delta x_{i-1})}{\Delta x_{i-1}} &= \frac{1}{2}\left(\Delta x_i + \Delta x_{i-1}\right) f''(x) \\ &\quad + \mathcal{O}(\Delta x_i^2 - \Delta x_{i-1}^2), \end{aligned}$$

then,

$$\begin{aligned} \frac{\Delta x_{i-1} f(x+\Delta x_i) - (\Delta x_{i-1} + \Delta x_i) f(x) + \Delta x_i f(x-\Delta x_{i-1})}{\Delta x_i \Delta x_{i-1}} &= \frac{1}{2}\left(\Delta x_i + \Delta x_{i-1}\right) f''(x) \\ &\quad + \mathcal{O}(\Delta x_i^2 - \Delta x_{i-1}^2) \\ \frac{2\Delta x_{i-1} f(x+\Delta x_i) - 2(\Delta x_{i-1} + \Delta x_i) f(x) + 2\Delta x_i f(x-\Delta x_{i-1})}{\Delta x_i \Delta x_{i-1}(\Delta x_i + \Delta x_{i-1})} &= f''(x) \\ &\quad + \mathcal{O}\left(\frac{\Delta x_i^2 - \Delta x_{i-1}^2}{\Delta x_i + \Delta x_{i-1}}\right). \end{aligned}$$

For node x_i,

$$f''(x_i) \approx \frac{2}{\Delta x_i(\Delta x_i + \Delta x_{i-1})} f_{i-1} - \frac{2}{\Delta x_i \Delta x_{i-1}} f_i, + \frac{2}{\Delta x_{i-1}(\Delta x_i + \Delta x_{i-1})} f_{i+1}.$$

with a truncation error of

$$\mathcal{O}(\Delta x_i - \Delta x_{i-1}).$$

C.3.2 Tridiagonal matrix analysis

This section presents a numerical analysis of the conditioning and diagonal dominance properties of the tridiagonal matrices arising from the discretization of the vertical diffusion operator. The coefficient matrix, prior to applying the scaling factor $1/\Delta z^2$, is defined as

$$\gamma_{r,s} = -\big(2 + \alpha + \beta\big), \qquad \alpha = \left(\frac{2\pi \Delta z\, r}{N_x}\right)^2, \quad \beta = \left(\frac{2\pi \Delta z\, s}{N_y}\right)^2.$$

The structure of this operator yields a tridiagonal matrix whose conditioning depends on the wavenumber indices (r, s) and the vertical resolution Δz. Two representative cases were evaluated to illustrate the sensitivity of the condition number to grid resolution. For a low-resolution configuration ($32 \times 32 \times 16$ nodes), the condition number ranged between $\kappa \in [21, 375]$, whereas for a higher-resolution grid ($256 \times 256 \times 64$ nodes), it increased significantly to $\kappa \in [84, 33541]$. These results, shown in Figure C.2, confirm that the system becomes progressively ill-conditioned as spatial resolution increases, which is typical for elliptic-type operators discretized with small grid spacing.

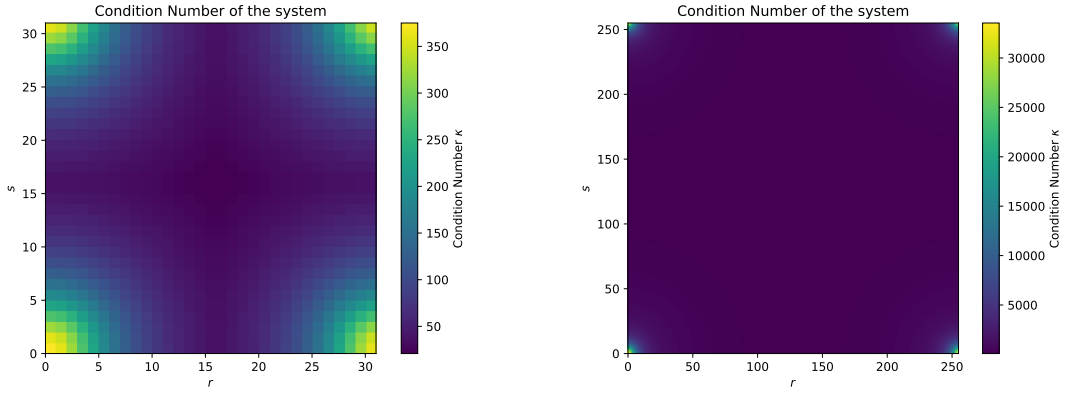

(a) $32 \times 32 \times 16$ nodes. $\kappa \in [21, 375]$. (b) $256 \times 256 \times 64$ nodes. $\kappa \in [84, 33541]$.

Figure C.2: Condition number of the tridiagonal system for different grid resolutions.

A diagonal dominance analysis was also performed to characterize the numerical stability of the tridiagonal solver. A row-by-row examination (Table C.1) shows that

the matrix is diagonally dominant when $\alpha + \beta \leq 4$, ensuring stability for low- to mid-frequency modes. For higher wavenumbers, where $\alpha + \beta > 4$, the first row loses dominance, while the interior rows remain strictly diagonally dominant. This implies that high-frequency modes increase stiffness and condition number without entirely compromising the stability of the solver.

Table C.1: Row-by-row dominance conditions for the tridiagonal coefficient matrix.

Row	**Diagonal term**	**Off-diagonal(s)**	**Condition / Comment**
First	$-\Delta z$	$\Delta z(2 + 0.5\gamma_{r,s}) = \Delta z(1 - 0.5(\alpha + \beta))$	Dominant if $\alpha + \beta \leq 4$
Interior	$\gamma_{r,s} = -(2 + \alpha + \beta)$	1, 1	Always strictly dominant ($\lvert\gamma_{r,s}\rvert \geq 2$)
Last	$\gamma_{r,s}$	1	Always strictly dominant ($\lvert\gamma_{r,s}\rvert \geq 1$)

In summary, the tridiagonal system preserves strong diagonal dominance for most wavenumber combinations, and its conditioning deteriorates predictably with increasing resolution and higher mode contributions. This analysis provides useful insight into the numerical stability of the implicit diffusion solver and justifies the use of double precision arithmetic for high-resolution simulations to mitigate rounding errors.

Appendix D

Open-source implementations

Two open-source implementations have been developed based on the findings discussed in previous chapters. The first implementation is designed for the CPU using Python. This is primarily designed for analyzing the model's capabilities and is also recommended for use in two-dimensional setups. Conversely, a *CUDA C* GPU implementation was developed to enable examination of three-dimensional configurations, required by substantial computational requirements. These resources can be accessed on *GitHub* and are found at `https://github.com/dsanmartin/wildfire` and `https://github.com/dsanmartin/wildfires` respectively.

The sections that follow provide a description of how to utilize the implementations.

D.1 Python

Prerequisites

The following libraries must be installed to execute the *Framework*:

- `Python >= 3.11.8`
- `Numpy >= 1.25.2`
- `Scipy >= 1.11.4`
- `Matplotlib >= 3.8.0`

Installation

Clone the repository to some user-defined directory,

```
user@host:~ $ git clone https://github.com/dsanmartin/wildfire.git
```

Usage

In the cloned folder, execute

```
python bin/main.py path/to/input.ini
```

A base skeleton for the input file is

```
; Physical domain
[domain]
x_min = -500
x_max = 700
y_min = 0
y_max = 20
t_min = 0
t_max = 140

[numerics]
Nx = 512
Ny = 256
Nt = 140000
NT = 1000
time_method = euler

[temperature]
radiation = True
T_hot = 900

[wind]
u_r = 4.8

[fuel]
Y_h = 0.51
C_d = 0.15
alpha_s = 0.002
sigma_s = 4000
Y_f = 70

[topography]
shape = flat
```

The input file options consider the selection of the physical parameters described in Table 7.1, the spatial and temporal domain, the numerical grid, and the methods for approximation. For time integration, the available options are `Euler`, `RK2`, and `RK4`. In addition, the numerical parameters include the number of iterations of the pressure solver and tolerance.

D.2 CUDA C

Prerequisites

The computer must have a compatible *CUDA* version. It depends on the Operating System and the Graphic Card. Please use this link `https://docs.nvidia.com/cuda/` and follow the instructions according to the hardware configuration.

In particular, this work used:

- `nvcc 12.3`
- `cufftw 11.0.2`

Installation

Clone the repository to some user-defined directory,

```
user@host:~ $ git clone https://github.com/dsanmartin/wildfires.git
```

Go inside the folder and compile with `make`

```
cd wildfires && make
```

Usage

Execute the following command

```
./bin/wildfire path/to/input_file.txt
```

A base skeleton for the input file is

```
# Domain
x_min = -200
x_max = 400
y_min = -200
y_max = 400
z_min = 0
z_max = 40
t_min = 0
t_max = 20

# Numerical grid #
Nx = 257
Ny = 257
Nz = 64
Nt = 200000
NT = 20000
```

```
# Time numerical method
method = euler

# Model parameters #
alpha_s = 0.002
sigma_s = 4000
Y_f = 70
T_0 = 288.15
Y_h = 0.51
T_source = 1500

# Temperature source for t time
t_source_start = 5
t_source_end = 10

# Initial conditions parameters #
# Wind
U0_type = power_law
u_r = 4.8
# Temperature
T0_shape = gaussian
T0_x_start = 0
T0_x_end = 10
T0_y_start = 50
T0_y_end = 150
T0_z_start = 0
T0_z_end = 1
# Temperature source
T_source_shape = gaussian
TS_x_start = 0
TS_x_end = 10
TS_y_start = 50
TS_y_end = 150
TS_z_start = 0
TS_z_end = 1
# Fuel
Y0_x_start = 0
Y0_x_end = 200
Y0_y_start = 0
Y0_y_end = 200
```

Similarly to the CPU implementation, the input file options consider the physical parameters presented in Table 7.1, the spatial and temporal domain, the numerical

grid, and the methods of approximation. For time integration, the available options are `Euler`, `RK2`, and `RK4`. Regarding the spatial approximation, this implementation allows the use of a non-uniform grid. Moreover, the numerical parameters include the number of iterations of the pressure solver and tolerance.